Interfaces in Transparent Polycrystalline $MgAl_2O_4$ Spinel

Zur Erlangung des Grades eines Doktors der Naturwissenschaften (Dr. rer. nat.)
Genehmigte Dissertation von Dipl.-Ing. Marc Rubat du Merac aus Calgary, Alberta, Canada 2019 – Darmstadt – D17

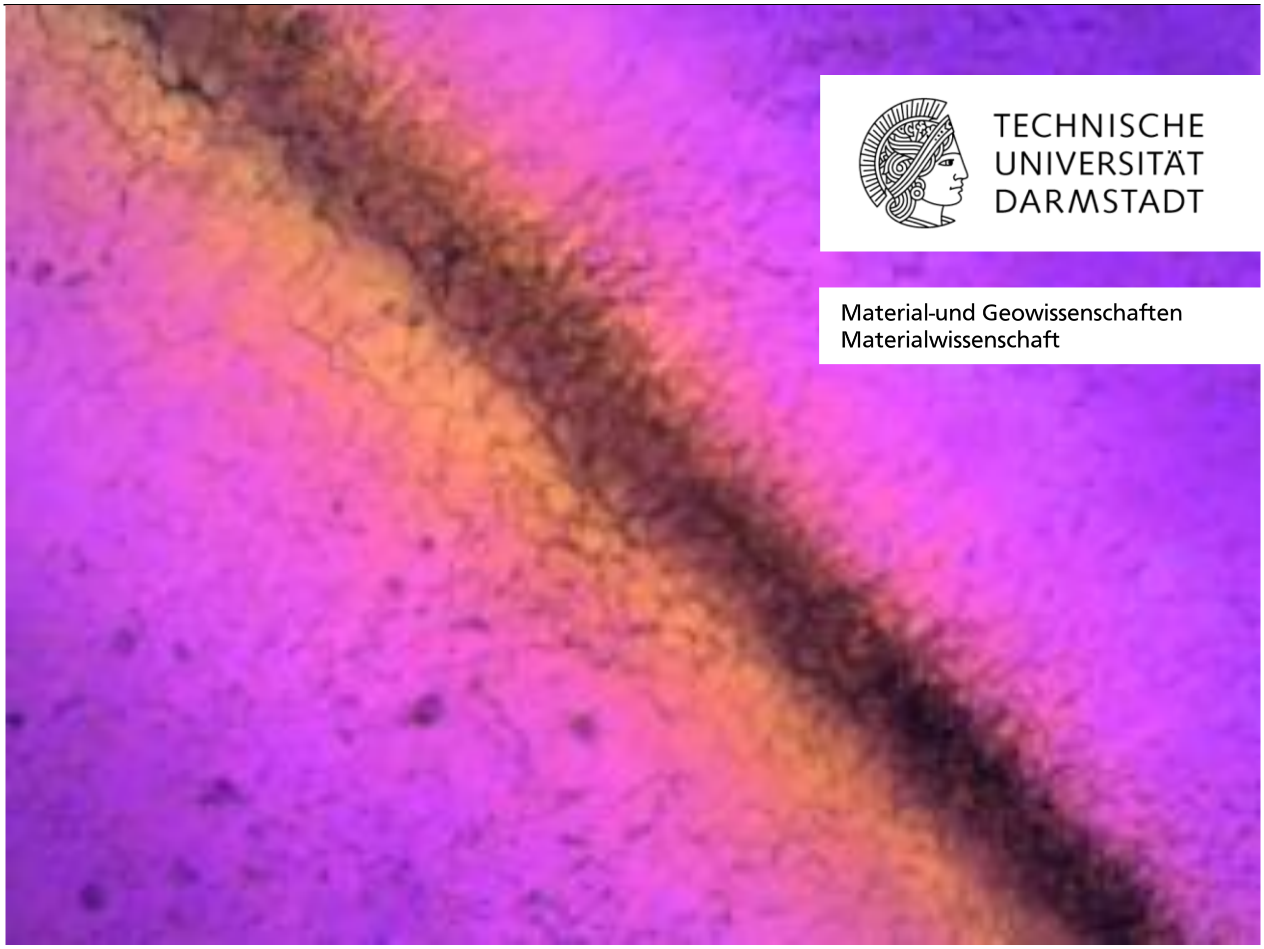

TECHNISCHE UNIVERSITÄT DARMSTADT

Material-und Geowissenschaften
Materialwissenschaft

Interfaces in Transparent Polycrystalline $MgAl_2O_4$ Spinel

Darmstadt, Technische Universität Darmstadt

Gehenmigte Dissertation von Dipl-Ing. Marc Rubat du Merac aus Calgary, Alberta, Canada

Gutatchen: Prof. Dr. rer. nat. Hans-Joachim Kleebe
Gutatchen: Prof. Dr. Anne Leriche

Tag der Einreichnung: 20.09.2018
Tag der Prufung: 14.01.2019

Darmstadt – D17

Veröffentlicht unter CC BY-SA 4.0 International
https://creativecommons.org/licenses/

Cover: A crack that developed during hot-pressing of a high-purity polycrystalline spinel compact. The color change indicates uniaxial tensile stress, likely caused by a combination of differential sintering and preferential MgO evaporation. In turn, this resulted in grain coarsening and a lower CTE offset by a smaller lattice parameter and a volume reduction. Dark spots at lower left are aggregates of abnormal grains radiating from an unknown impurity source (5X obj, 50X mag, polarized light, full-wave retardation plate).

Erklärung zur Dissertation

Hiermit versichere iche die vorliegende Disseration ohne Hilfe Dritter nur mit den angegebenen Quellen und Hilfsmitteln angefertigt zu haben. Alle Stellen, die aus Quellen entnommen wurden, sind als solche kenntlich gemacht. Diese Arbeit hat in gleicher oder ahnlicher Form noch keener Prüfungsbehörde vorgelegen.

Darmstadt, den 20 September 2018

(Marc Rubat du Merac)

Acknowledgments

I sincerely thank my advisor, Hans-Joachim Kleebe for his support and patience, without which this work would not have been completed. I am also deeply indebted to Ivar Reimanis. I thank my wife, Melanie Slemko for her support in difficult times. I thank my parents, Jacques and Adine Rubat du Merac for their support and encouragement, and my grandfather, Jacques Tricand de la Goutte, for inspiration. The research was conducted with the help of many others and I thank Tim Jochum (hot-press, ICP), Scott Pawelka (instrumentation), Anne Cenadella (HIP), Subramanian Ramalingam (particle-size analysis), Shai Meir (spinel articles), Ulrike Kuntz, Gary Zito and John Chandler (electron microscopy), Frank Anderson and Steve Govorchin (LA-ICP), Pat Taylor (HSC), Charlene Smith (fluorescence spectroscopy, WDS), Mike Sanders (dilatometry, STA-MS), Harvey Guthrey (FIB), Brian Gorman and Maria Romanes (STEM-EDS), Leo Molina and Stefan Lauterbach (STEM-EELS), Mathis Müller (TEM specimens), Jason Stoke (ellipsometry), Joseph Tsai and Ingo Sethman (AFM), Yi Ke (Raman spectroscopy), Tod Gross (EFM), Santhana Moorthy (SIMS, PIES), Shen Dillon and Ling Fen (SIMS); Ryan O'Hayre, Jinhua Tong, Chung Min An, and Chan Young Kim (EIS); Aidan Seawalt and Anthony Linenberger (various experiments), Rishi Raj and John Francis (FAST), David Olson and Gerard Martins (scientific advice and inspiration), and to all my colleagues for lively conversations.

Abstract

Transparent ceramics have unique properties that can enable applications that no other materials can and they have recently engendered renewed interest due to scientific and technological advances. Polycrystalline magnesium aluminate spinel is one promising transparent ceramic with an exceptional combination of properties that is at the forefront of these developments. However, the powder-processing-property relationships of transparent spinel fabrication are still poorly understood, precluding repeatably obtaining components with acceptable properties at reasonable cost. In particular, interfaces, such as surfaces and grain boundaries, often govern densification and final properties, yet little is known of how they are affected by stoichiometry, impurities, additives, and processing parameters, and consequently how they affect microstructure during processing. In this light, the interfaces of transparent spinel compacts were studied with the goal of understanding their properties and behaviors.

Spinel powders with different stoichiometries and impurity and LiF additive contents were prepared and extensively characterized. Starting powders were densified into transparent compacts by hot-pressing, hot-isostatic pressing and pressureless sintering under a variety of processing conditions designed to elucidate the behavior of their interfaces, especially in relation to microstructure evolution and opto-electronic properties. Dense compacts were examined by optical and electron microscopy and various spectroscopic methods. Grain boundaries and surfaces were examined by optical microscopy, scanning and transmission electron microscopy, convergent-beam electron diffraction, energy- and wavelength-dispersive X-ray spectroscopy, electron-energy loss spectroscopy, secondary-ion mass spectroscopy, parallel-ion electron spectroscopy, atomic-force microscopy, and electrochemical impedance spectroscopy. In turn, the features of interfaces were related to starting powders, processing, and bulk properties.

Crystallite surfaces and grain boundaries were found to be highly sensitive to small differences in stoichiometry and impurity and additive content, which altered their free energy, diffusion, lattice parameter, and mechanical, optical, and electronic properties. The interface energies of astoichiometric compositions were quantified and found to be more conducive to densification. However, enhanced interface transport for Al_2O_3-rich compositions caused

coarsening, resulting in larger grain size and precluding densification without pressure while assisting it with pressure. Astoichiometry was also observed by way of gradients at interfaces and on a compact scale, which resulted in associated microstructure and property gradients. Impurities in starting powders and carbon contamination from processing segregated at grain boundaries and significantly affected microstructure, were the main source of optical scatter and absorption, and increased conductivity. Dielectric properties were found to be a complex function of microstructure, stoichiometry, impurities, and additives, and higher conductivity for dense compacts compared to single crystals was attributed to conductance along impurity-rich magnesium-depleted grain boundaries, especially for Al_2O_3-rich stoichiometry.

The LiF sintering additive was found to have a powerful, complex, and multi-facetted effect. Fluorine reacted with impurities to form volatile species, which could be removed by careful processing to render transparency, and it also reacted with spinel to form magnesium fluoride and oxide, thus altering stoichiometry. Whereas, lithium incorporated into the lattice and altered interface energies, diffusion, and conductivity. The net effect was (i) a shif towards Al_2O_3-rich composition, (ii) the removal of impurities, (iii) accentuation of grain-boundary and compact-scale stoichiometry and microstructure gradients, (v) enhanced interface transport and grain growth, (vi) reduced densification temperature and enhanced densification with pressure-assisted sintering, (vi) coarsening and inhibited densification without pressure, (vii) grain-boundary embrittlement, (viii) grain-boundary optical scatter, (ix) opacity when processing trapped LiF and its by-products, and (x) lower conductivity due to decreased grain-boundary area and impurities, and the formation of conductance-inhibiting point defects.

The work demonstrated how interfaces were affected by starting powders and processing parameters and in turn how this affected microstructure, fracture behavior, and opto-electronic properties. The findings shed light on many of the intricacies of transparent spinel fabrication, enabling a better understanding of powder-processing-property interactions and giving guidance on how to tailor processing and microstructure to yield desired bulk properties.

Table of Contents

Acknowledgments v

Abstract vii

Table of Contents ix

List of Figures xv

List of Tables xxix

List of Symbols xxxi

Chapter 1 Introduction 39

- 1.1 Motivation 40
- 1.2 Objectives 40
- 1.3 Summary of Work 40
- 1.4 Structure of Thesis 41

Chapter 2 Background 43

- 2.1 Introduction 44
- 2.2 Physical Properties 47
    - 2.2.1 Thermodynamic Properties 47
    - 2.2.2 Crystal Structure and Defects 48
    - 2.2.3 Interface Properties 51
    - 2.2.4 Diffusion Properties 53
    - 2.2.5 Electronic Properties 54
    - 2.2.6 Optical Properties 55

2.2.7 Mechanical Properties 57

2.2.8 Physical Requirements 59

2.3 Processing 61

2.3.1 Key Processing Variables 61

2.3.2 Powder Synthesis 62

2.3.3 Green Body Formation 63

2.3.4 Particle Morphology 64

2.3.5 Microstructure Evolution 66

2.4 Stoichiometry 67

2.4.1 Effect on Properties 67

2.4.2 Stoichiometry Gradients 69

2.4.3 Defect Chemistry and Grain-Boundary Mobility 70

2.4.4 Grain Growth 72

2.4.5 Densification 73

2.5 Impurities & Additives 74

2.5.1 Impurities 74

2.5.2 Sintering Additives 76

2.6 Processing Parameters 81

2.6.1 Temperature and Heating Rate 81

2.6.2 Pressure 81

2.6.3 Atmosphere 83

2.6.4 Electric Fields 84

2.6.5 Absorption 85

2.7 Summary 88

Chapter 3 Experimental Methods 91

3.1 Powder Characterization.. 92

3.2 Powder Treatment Experiments 93

3.3 STA-MS Experiments 93

3.4 Thermodynamic Simulations 94

3.5 Dilatometry Experiments.. 95

3.6 Hot Press Experiments... 97

3.7 Pressureless Sinter - HIP Experiments 101

3.8 Quenching Experiments.. 101

3.9 Density Measurement 101

3.10 Chemical Spectroscopy 101

3.11 Optical Microscopy 102

3.12 Scanning Electron Microscopy.. 103

3.13 Transmission Electron Microscopy 103

3.14 Secondary-Ion Mass Spectroscopy.. 105

3.15 Raman Spectroscopy 106

3.16 Spectrophotometry.. 106

3.17 Thermal Grain-boundary Grooving Experiments.. 107

3.18 Electrochemical Impedance Spectroscopy Experiments 109

Chapter 4 Results and Discussion..115

4.1 Starting Powders... 116

4.1.1 Powder Characterization.. 117

4.1.2 Thermal Analysis 121

4.1.3 Thermodynamic Simulations 124

4.1.4 Dilatometry ... 125
4.2 Bulk Compacts ... 127
4.2.1 Dense Compacts ... 128
4.2.2 Laser-Ablation Inductively-Coupled Plasma (LA-ICP OES/MS) ... 130
4.2.3 Spectrophotometry ... 132
4.2.4 Raman Spectroscopy ... 134
4.3 Interfaces ... 135
4.3.1 Optical Microscopy ... 136
4.3.2 Electron Microscopy ... 141
4.3.3 Electron Energy-Loss Spectroscopy (STEM-EELS) ... 153
4.3.4 Convergent-Beam Electron Diffraction (TEM-CBED) ... 156
4.3.5 Secondary-Ion Mass Spectroscopy (TOF-SIMS) ... 158
4.3.6 Parallel-Ion Electron Spectroscopy (PIES) ... 160
4.3.7 Atomic-Force Microscopy (AFM) ... 162
4.3.8 Electrochemical Impedance Spectroscopy (EIS) ... 165
Chapter 5 General Discussion ... 177
5.1 Interfaces and Starting Powders ... 178
5.2 Interfaces, Stoichiometry and Microstructure Evolution ... 178
5.3 Interfaces, Impurities and Microstructure Evolution ... 180
5.4 Interfaces, LiF and Microsctructure Evolution ... 181
5.5 Interfaces and Combined Effects ... 186
Chapter 6 Summary ... 189
References ... 193
Personal Information ... 219

Curriculum Vitae 220

Publications.. 221

Conferences 222

List of Figures

Fig. 2.1: Spinel phase diagram, adapted with permission. 48

Fig. 2.2: Unit cell of spinel depicting symmetry (shaded) and octahedral and tetrahedral interstices. 49

Fig. 2.3: Diffusion coefficients for spinel species, adapted with permission. 54

Fig. 2.4: Typical transmission spectrum for transparent polycrystalline spinel. 55

Fig. 2.5: Light transmission through a polycrystalline spinel compact. 56

Fig. 2.6: Fracture surfaces of spinel showing mixed-mode inter- and trans-granular fracture for hot-pressed (a) lower-purity powder and (b) higher-purity powder, without additives. With LiF addition, fracture becomes predominantly inter-granular. 58

Fig. 2.7: Fabrication and Key Variables....62

Fig. 2.8: Green bodies made using two different powder/processing routes (pink diamonds represent impurities or additives): (GB1) fine, narrow particle-size distribution powder leading to narrow pore-size distribution, and (GB2) agglomerated, wide particle-size distribution powder leading to wide pore-size distribution, large inter-agglomerate pores, and inhomogeneous additive dispersal. 64

Fig. 2.9: Agglomerates in (a) synthesized, and (b) commercial sulfate-derived powders. 65

Fig. 2.10: (a) Optical microscopy image of microstructure of 2 mm thick hot-pressed stoichiometric spinel compact, and (b) similarly processed compact, but 4 mm thick and with pressure applied at a lower temperature. 67

Fig. 2.11: (a) MgO precipitates (arrows) in x ~0.995 hot-pressed compact and (b) Al_2O_3 precipitates (arrows) and Al_2O_3-rich grain boundaries in HP/HIP compact, reproduced with permission. 68

Fig. 2.12: Composite SEM cross-section of pressureless-sintered stoichiometric spinel compacts, reproduced with permission. 69

Fig. 2.13: (a) Atomic concentration versus distance from grain boundary in $x = 1.05$ PS/HIP spinel compact (adapted with permission), (b) schematic of MgO-depleted grain boundaries. 71

Fig. 2.14: (a) Brouwer diagram and (b) log grain-boundary mobility versus stoichiometry; adapted from Ting & Lu, Chiang & Kingery, and Uematsu et al. with permission. 72

Fig. 2.15: Compact density as a function of time for pressureless-sintered compacts with various stoichiometries ($0.8 < x < 1.5$), adapted with permission. 73

Fig. 2.16: Impurity phases causing opacity in 2 mm thick compact (inset) hot-pressed with high-purity spinel powder; (a) amorphous impurity (C,S,K) phase at grain boundary and (b) decorated grain boundary. (c) Amorphous phase at triple junction in HIP compact (all images TEM-BF). 75

Fig. 2.17: Hot-pressed spinel/LiF/spinel sandwich structure and highly-defected grains revealed by etching. 76

Fig. 2.18: HIP spinel compact with LiF; (a) Fluorine-rich xenomorphic grain (TEM-brightfield) and (b) coffee-bean contrast (arrow, STEM-ABF). 77

Fig. 2.19: Log-log plot of grain-size change versus time for air-sintered spinel powders with 1 wt% LiF at 1000°C, 1100°C, and 1200°C, SEM images of air-sintered spinel powders (a) without LiF and (b) with LiF. 78

Fig. 2.20: Optical defects due to LiF (a) decorated grain boundaries, (b) remnant liquid phase at grain boundaries, (c) amorphous phase at triple-junctions (TEM),

(d) typical mottled-contrast magnesium- and fluorine-rich phase at triple-junction (TEM)....79

Fig. 2.21: Fracture behavior in pressureless sintered high-purity spinel compacts with (a) no LiF 1650°C 10 h (SEM), 1 wt% LiF 1650°C 10 h (SEM). 80

Fig. 2.22: Typical microstructures observed in translucent or transparent spinel; (a) HP/HIP, (b) HP/HIP with LiF, (c) SPS, (d) SPS with LiF, (e) HP, (f) HP with LiF, optical and SEM micrographs, reproduced with permission. 80

Fig. 2.23: Dislocations in a HP stoichiometric spinel compact, adapted with permission. 82

Fig. 2.24: Increased absorption in SPS compacts with; (a) increasing heating rate, (b) sintering temperature, (c) temperature of pressure application, and (d) applied pressure. 86

Fig. 2.25: (a) Carbon-rich phase at triple junction in spinel compact, (b) HRTEM image of graphitic carbon at triple junction in spinel compact. 87

Fig. 3.1: Standard hot-press profile including ramp at 6°C/min to 1550°C with 1 h hold at 400°C, 0.25 h hold at 1200°C, 1 h hold at 1550°C, application of 35 MPa at 1200°C and removal at 900°C. Modified regime with pressure applied at 900°C (dashed line)....99

Fig. 3.2: Schematic of EIS Apparatus. 111

Fig. 3.3: Idealized Nyquist plot (a) and equivalent circuit representing a polycrystalline solid with electrodes (b), dashed line represents additional parallel grain-boundary conductivity and its effect. Z is impedance, f is AC frequency, ω is angular frequency, R is resistance, C is capacitance, and subscripts 'e' refer to electrode, 'gb' to grain boundaries, and '⊥' to field-perpendicular and '∥' to field-parallel boundaries. 112

Fig. 4.1: Sulfate powder (a) agglomerates and (b) crystallites (SEM). 118

Fig. 4.2: Sulfate (a) and alkoxide (b) powder crystallites (TEM-BF). 119

Fig. 4.3: Sulfate (a) and alkoxide (b) powder crystallites (HRTEM). 119

Fig. 4.4: Indexed electron-diffraction patterns for (a) sulfate and (b) alkoxide powder (TEM). 119

Fig. 4.5: Sulfate powder mixed with LiF (a, b) (SEM). 120

Fig. 4.6: Sulfate powder with 1 wt% LiF heated at 1200°C for 1 h in (a) vacuum and (b) air (SEM). 120

Fig. 4.7: STA (DSC + TGA) for sulfate and alkoxide powders in argon at 5K/min ramp. 121

Fig. 4.8: STA for sulfate powders with 0, 1, and 10 wt% LiF addition in argon at 5-20 K/min with LiF DSC at 20% scale superimposed for reference. 122

Fig. 4.9: STA for LiF and $MgF_2 + LiAlO_2$ in argon at 10-20 K/min. 122

Fig. 4.10: STA-MS for *m/z* 32, 48, and 64 shown at a finer scale for (a) sulfate-derived powder without LiF and (b) with 1 wt% LiF in argon. 124

Fig. 4.11: Fractional sintered density relative to theoretical as a function of temperature for dilatometry with cold-pressed sulfate and alkoxide powder samples (inset). 126

Fig. 4.12: Hot-press fractional theoretical sintered density versus temperature corrected for pressure and thermal expansion as a function of powders and LiF addition. Dashed line indicates closed porosity at 92% theoretical density (~1250-1350°C). 127

Fig. 4.13: Compacts hot-pressed using the standard profile with (a) sulfate powder (b) sulfate powder with 1 wt% LiF, (c) sulfate powder with 1 wt% LiF but with pressure applied at 900°C, (d) alkoxide powder and (e) alkoxide powder with 0.25 wt% LiF (compacts 10 mm above template). 128

Fig. 4.14: Samples cut from hot-pressed and HIPed hydroxide powder compacts with *x* = 0.95 (a), 1.0 (b), and 1.5 (c) (10 mm above template). 128

Fig. 4.15: Sulfate (a) and alkoxide (b) powder compacts hot-pressed using the standard profile (10 mm above template). 129

Fig. 4.16: Sulfate powder compacts (a) without and (b) with 1 wt% LiF hot-pressed using the standard profile (10 mm above template). 129

Fig. 4.17: Sulfate powder compacts with 1 wt% LiF hot-pressed with pressure applied at (a) 1200°C and (b) 900°C (10 mm above template). 129

Fig. 4.18: Alkoxide powder compacts hot-pressed using the standard profile with (a) 0 and (b) 0.25 wt% LiF addition (10 mm above template). 130

Fig. 4.19: Total (red) and in-line (dashed red) transmittance, total (blue) and diffuse (dashed blue) reflectance, scatter (dashed green), and absorptance (dashed pink) versus wavelength for sulfate powder compacts hot-pressed with the standard profile. 132

Fig. 4.20: Total (red) and in-line (dashed red) transmittance, total (blue) and diffuse (dashed blue) reflectance, scatter (dashed green), and absorptance (dashed pink) versus wavelength for sulfate powder compacts with 1 wt% LiF hot-pressed with the standard profile. 133

Fig. 4.21: Total (red) and in-line (dashed red) transmittance, total (blue) and diffuse (dashed blue) reflectance, scatter (dashed green), and absorptance (dashed pink) versus wavelength for sulfate powder compacts with 1 wt% LiF hot-pressed with pressure applied at 900°C instead of 1200°C. 133

Fig. 4.22: Total transmittance for hot-pressed and HIPed hydroxide powder compacts with *x* = 0.95 (blue), 1.0 (green), and 1.5 (purple). 133

Fig. 4.23: UV-laser induced fluorescence for a sulfate powder compact hot-pressed with 1 wt% LiF performed with shorter (blue) and longer (pink) integration time. Gaussian fit (black) deconvolution (dotted) yielded two peaks at 710 nm and 757 nm (arrows). 134

Fig. 4.24: Raman spectra for (a) compacts hot-pressed with sulfate powder with and without 1 wt% LiF, and (b) a spinel single crystal and compacts hot-pressed with sulfate powder with 1 wt% LiF and with alkoxide powder (arrows indicate features associated with low inversion). 135

Fig. 4.25: Matrix grains in compacts hot-pressed with pressure applied at 1200°C using (a) sulfate powder and (b) alkoxide powder (optical microscopy 10X, 20X obj.). 136

Fig. 4.26: Abnormal grains in compacts hot-pressed with pressure applied at 1200°C using (a) sulfate powder and (b) alkoxide powder (optical microscopy 10X obj.). 137

Fig. 4.27: Matrix grains in compacts hot-pressed with pressure applied at 1200°C using sulfate powder (a) without and (b) with 1 wt% LiF (optical microscopy 10X, 20X obj.). 137

Fig. 4.28: Matrix grains in compacts hot-pressed with pressure applied at 1200°C using alkoxide powder (a) without and (b) with 0.25 wt% LiF (optical microscopy 20X obj.). 137

Fig. 4.29: Microstructure of compacts hot-pressed using sulfate powder with 1 wt% LiF with pressure applied at (a) 1200°C and (b) 900°C (optical microscopy 20X obj.). 138

Fig. 4.30: Abnormal grains in compacts hot pressed with (a) sulfate powder with 1 wt% LiF (note planar interfaces) and (b) alkoxide powder appearing to originate from a point-source (optical microscopy 20X, 10X obj.). 138

Fig. 4.31: (a) Submicrometer-sized grain-boundary inclusions in compact hot-pressed with sulfate powder using the standard profile and (b) grain-boundary scatter (arrows) in identically-processed compact with 1 wt% LiF (optical microscopy 10X obj.). 139

Fig. 4.32: (a) Submicrometer-sized inclusions and (b) grain-boundary phase in compact hot-pressed with sulfate powder with 1 wt% LiF and pressure applied at 900°C (optical microscopy 50X obj.). 139

Fig. 4.33: (a) Spherical optical defect surrounded by abnormal grains in alkoxide powder compact without LiF, and (b) pore-cluster in sulfate powder compact with LiF (optical microscopy 10X obj.) 140

Fig. 4.34: Crack exhibiting reduced absorption that occurred while hot-pressing an alkoxide powder compact (a, white box), with color-change under polarized light indicating strain birefringence (b) (optical microscopy, 5X obj., full-wavelength filter). 140

Fig. 4.35: Grain-size in the crack region was larger (a, 20X obj.) and boundaries were decorated by a secondary phase (b, optical microscopy, 50X obj.). 141

Fig. 4.36: Fracture surface of compact hot-pressed with sulfate powder with pressure applied at 1200°C exhibiting (a) transgranular fracture (arrows show submicrometer-grain aggregates) and (b) submicrometer-grain aggregate (SEM). 142

Fig. 4.37: Focused ion-beam lift-outs, with only one window usable in each, from compacts hot-pressed at 1200°C with sulfate powder (a) and (b) with 1 wt% LiF (SEM). 142

Fig. 4.38: Submicrometer-grain aggregates in compacts hot-pressed with sulfate powder and pressure applied at 1200°C showing planar interfaces between aggregates and larger matrix grains (arrows) (TEM-BF). 142

Fig. 4.39: Submicrometer-grain aggregate in compact hot-pressed with sulfate powder and pressure applied at 1200°C (a) with amorphous phase at submicrometer grain aggregate-matrix grain interface (white box, b) (TEM-BF)......................143

Fig. 4.40: Partially-filled triple-junction phase in submicrometer grain aggregate in compact hot-pressed with sulfate powder and pressure applied at 1200°C (a, b) (TEM-BF)..143

Fig. 4.41: Near-perpendicular intersection of submicrometer-grain boundary with the interface between matrix grains and submicrometer-grain aggregates (a, arrow) in sulfate powder compact with boundary deviating to intersect at right angles (b, arrow) (TEM-BF). 144

Fig. 4.42: Dark-contrast features resembling dislocation arrays at boundaries of submicrometer grains in compact hot-pressed with sulfate powder and pressure applied at 1200°C (a, b) (TEM-BF). 144

Fig. 4.43: Clean, (a) atomically-rough and (b) smooth matrix grain boundaries in compact hot-pressed with sulfate powder and pressure applied at 1200°C (HRTEM). 144

Fig. 4.44: Fracture surface of compact hot-pressed with sulfate powder with 1 wt% LiF and pressure applied at 1200°C showing (a) matrix grains with interspersed smaller-grain aggregates (arrows, b) (fracture surface, SEM). 145

Fig. 4.45: Polyhedral (a) and partially-wetting (b) Fe, Ni, C, and Ga-rich secondary phases (arrows) in smaller-grain aggregates of compact hot-pressed with sulfate powder with 1 wt% LiF and pressure applied at 1200°C (fracture surface, SEM)..145

Fig. 4.46: Clean grain-boundary (a) and with amorphous phase (b) in compact hot-pressed with 1.5 g of sulfate powder with 1 wt% LiF and pressure applied at 1200°C (HR-TEM, TEM-BF)..146

Fig. 4.47: Clean (a) and mottled-contrast fluorine-rich (MgF_2) phase (b) at matrix-grain triple junctions in compact hot-pressed with sulfate powder with 1 wt% LiF and pressure applied at 900°C (TEM-BF). 146

Fig. 4.48: Matrix grain-boundaries of compact hot-pressed with sulfate powder with 1 wt% LiF and pressure applied at 900°C showing disorder at the interface (a, b) (HRTEM) 147

Fig. 4.49: De-focus (± 3.5 μm) of a grain-boundary of compact hot-pressed with sulfate powder with 1 wt% LiF and pressure applied at 900°C showing Fresnel fringes with reversed contrast (a, b) (TEM) 147

Fig. 4.50: Dislocation arrays (a) and strain-contrast at a grain-boundary (b) in a compact hot-pressed with sulfate powder with 1 wt% LiF and pressure applied at 900°C (TEM) 147

Fig. 4.51: Drift-corrected STEM-EDS profile scan across a matrix grain boundary of a compact hot-pressed with sulfate powder with 1 wt% LiF and pressure applied at 900°C showing C, Ca, and S segregation at the core (~0.035 μm). ..148

Fig. 4.52: Fracture surfaces of compacts hot-pressed with pressure applied at 1200°C with (a) alkoxide powder (a) and alkoxide powder with 0.25 wt% LiF (b) with arrows showing MgO nodules (SEM). 149

Fig. 4.53: Fe-rich phase in compact hot-pressed with alkoxide powder (a) and larger grain-size and absence of Fe-phase in compact hot-pressed with alkoxide powder with 0.25 wt% LiF (b) (SEM). 149

Fig. 4.54: MgO nodules (arrow) surrounded by light-contrast indicative of Mg-depletion in compact hot-pressed with alkoxide powder with 0.25 wt% LiF (SEM) and high-magnification of MgO nodule (b) (TEM-BF). 149

Fig. 4.55: Fracture surfaces for (a) hot-pressed compact with sulfate powder with 1 wt% LiF and (b) same compact after quenching (SEM). 150

Fig. 4.56: Fracture surfaces for (a) hot-pressed alkoxide powder compact with 0.25 wt% LiF and (b) same compact after quenching (SEM). 150

Fig. 4.57: EBSD pole maps for polished sulfate-powder compacts without (a) and with 1 wt% LiF (b) oriented perpendicular to the hot-pressing direction (inset: color-coded pole orientation). 151

Fig. 4.58: EBSD grain misorientation angles for compact hot-pressed with sulfate powder (a) without LiF and (b) with 1 wt% LiF, both showing preferred 45° orientation (first bar in graphs is instrument noise). 151

Fig. 4.59: EBSD grain misorientation angles for compact hot-pressed with sulfate powder without LiF (a) and alkoxide-powder compact with 0.25 wt% LiF (b), exhibiting strikingly similar orientation profiles with preferred 45° orientation (first bar in graphs is instrument noise). 152

Fig. 4.60: Typical zero-loss removed, background-corrected (green line) EELS spectrum with the Mg-$L_{2,3}$ (51 eV), Al-$L_{2,3}$ (73 eV), and Mg-L_1 (88 eV) edges visible (red rectangle indicates selected fit region for background subtraction). 154

Fig. 4.61: Typical low-loss region of zero-loss removed, background-corrected EELS spectrum showing the Mg-$L_{2,3}$ (51 eV), Al-$L_{2,3}$ (73 eV) and Mg-L_1 (88 eV) edges..154

Fig. 4.62: Typical high-loss region of zero-loss removed, background-corrected EELS spectrum showing well-defined C-K (284 eV) and O-K (532 eV) edges. 155

Fig. 4.63: FIB lift-out (a) from a compact hot-pressed with sulfate powder with 1 wt% LiF and standard processing, grain-boundary area scan (b), and STEM-EELS (c) and STEM-EDS (d) intensity ratios across the boundary (dashed line indicates boundary core). 155

Fig. 4.64: FIB lift-outs from compacts hot-pressed with sulfate powder without LiF (a) and with 1 wt% LiF (b). 156

Fig. 4.65: FIB lift-outs from compacts hot-pressed with sulfate powder without LiF oriented along the [011] zone axis (a) and with sulfate powder with 1 wt% LiF oriented along the [001] zone axis (b), with arrows indicating CBED locations. 157

Fig. 4.66: CBED patterns from grain interiors and grain-boundaries for compacts hot-pressed with sulfate powder (a, b), the first-order Laue zones are indicated by the white dashed lines. 157

Fig. 4.67: CBED patterns from grain interiors and grain-boundaries for compacts hot-pressed with sulfate powder with 1 wt% LiF (a, b), the first-order Laue zones are indicated by the white dashed lines. 157

Fig. 4.68: SIMS $^{7}Li^{+}$ maps for a 50 x 50 μm area of a sample hot-pressed with sulfate powder without LiF using the standard profile (a), and a 25 x 25 μm area of a sample hot-pressed with sulfate powder with 1 wt.% LiF (b). 158

Fig. 4.69: SIMS $^{7}Li^{+}$ maps for 25 x 25 μm areas of sample hot-pressed with sulfate powder with 1 wt% LiF with pressure applied at 1100°C (a) and at 900°C (b) during hot-pressing. 158

Fig. 4.70: SIMS $^{7}Li^{+}$ depth profiles corresponding to maps in Fig. 4.68 and Fig. 4.69. 159

Fig. 4.71: 50 x 50 μm SIMS (a) $^{7}Li^{+}$, (b) $^{25}Mg^{2+}$, and (c) $^{27}Al^{3+}$ maps for sulfate powder sample with 1 wt% LiF hot-pressed using the standard profile. 159

Fig. 4.72: Nano-SIMS (a) $^{7}Li^{+}$ and (b) $^{25}Mg^{+}$ maps of a 50 x 50 μm area on the polished surface of a sample hot-pressed with sulfate powder and 1 wt% LiF addition using the standard profile, arrows indicate features consistent with grain-boundaries. 160

Fig. 4.73: (a) Composite TEM brightfield image of a FIB lift-out from sample hot-pressed with sulfate powder with 1 wt% LiF using the standard profile, grain boundaries indicated by arrows, and (b) PIES $^{7}Li^{+}$ map. 161

Fig. 4.74: (a) TEM brightfield image of triple-junction at lower left of FIB lift-out in Fig. 4.73, and (b) intensity map of triple-junction area...162

Fig. 4.75: AFM topography images of (a) calibration grid, showing excellent feature replication, and (b) polished sample surface with minimal roughness..............163

Fig. 4.76: AFM topography image of an optimal thermal grain-boundary groove (x = 1.0)...163

Fig. 4.77: Hot-pressed sulfate powder EIS samples with sputtered gold electrodes (without leads) made from (a) transparent compact with 1 wt% LiF, (b) dark-grey ("dark") opaque compact without LiF (note smaller electrode), and (c) light-grey ("white"), opaque compact without LiF. The alkoxide-powder sample had nearly-identical geometry to (a) and (c). 166

Fig. 4.78: EIS spectra for the dark sulfate-powder sample. Impedance is normalized for geometry (indicating resistivity on the real axis), arrows indicate low-frequency bulges, and Zview® simulation fits are shown as solid red lines. 167

Fig. 4.79: EIS spectra for the light-colored sulfate-powder sample. Arrows show low-frequency bulges and Zivew® simulation fits are shown as solid red lines. 167

Fig. 4.80: EIS spectra for the transparent sulfate-powder sample with 1 wt% LiF. The simulated single-crystal impedance is based on $\sigma = 2.5\cdot10^{-8}$ S/cm at 850°C, Zview® simulation fits are shown as solid red lines with bulk and grain-boundary components noted, and spectra for lower temperatures are not shown due to high scatter...168

Fig. 4.81: Comparison of EIS spectra for sulfate-powder samples at 850°C showing Zview® simulation fits (solid lines) using the series model (ignoring dashed line in equivalent circuit in the inset) and simulated single-crystal impedance based on $\sigma = 2.5\cdot10^{-8}$ S/cm at 850°C (fine dashed line)..................................168

Fig. 4.82: Activation energies for total conductivity for sulfate-powder samples. 169

Fig. 4.83: EIS spectrum for the transparent alkoxide-powder sample at 850°C with EIS spectra for sulfate-powder samples shown for comparison. Spectra for lower temperatures are not shown due to high scatter. 169

Fig. 4.84: Possible conduction mechanisms in polycrystalline spinel, “E” represents the AC field direction. (a) sulfate-powder sample without LiF, (b) sulfate-powder sample with 1 wt% LiF, (c) alkoxide-powder sample without LiF. Dashed arrows indicate current lines. Vertical arrows besides conductivity symbols indicate relative magnitudes. Shaded regions indicate relative effective grain-boundary widths and differing conductivities due to Mg-depletion, V''_{Mg}, and/or Li'_{Mg}. 172

List of Tables

Table 2.1: Calculated Point Defect Formation Energies and Diffusion Barriers.....................51

Table 2.2: Reported Interface Energies for Stoichiometric $MgAl_2O_4$ Spinel. 53

Table 2.3: Physical Properties of Transparent Polycrystalline Spinel...................................60

Table 2.4: Transparent Spinel Processing and Properties..89

Table 3.1: Variation of Processing Parameters...100

Table 4.1: Spinel Powder Properties..117

Table 4.2: LA ICP-OES/MS at the Geometric Center and Exterior Surface of Compacts Hot-Pressed with Sulfate Powder with and without LiF and Pressure Applied at 1200°C. 131

Table 4.3: Grain-boundary to Surface Energy Ratio (γ_{gb}/γ_s) as a Function of Stoichiometry for Hydroxide-powder Compacts...163

Table 4.4: Selected Dielectric Properties of Polycrystalline Samples at 850°C. 170

List of Symbols

(g)	Gas phase
(l)	Liquid phase
(s)	Solid phase
[ ]	Concentration
$\parallel$	Field-parallel
$\perp$	Field-perpendicular
a	Lattice parameter
A	Absorptance, ampere, area, cross-sectional area, interfacial area
Å	Ångström
ABF	Annular brighfield
AC	Alternating current
Ac Mix	Acoustic mix
Add	Addition
AFM	Atomic force microscopy
Ann	Anneal
APS	Average particle size
BET	Brunaeur-Emmett-Teller surface area
BF	Brightfield
BR	Biaxial ring-on-ring flexure test
C	Capacitance
C_0	Open cell capacitance
C_{bulk}	Bulk capacitance
C_{eff}	Effective capacitance
$C_{gb\perp}$	Series grain-boundary capacitance
CBED	Convergent-beam electron diffraction
CCD	Charge couple device
CIP	Cold isostatic press
CP	Cold Press
CPE	Constant phase element

CRSS	Critical resolved shear stress
CTE	Coefficient of thermal expansion
d	Size of scattering center, grain boundary width, groove depth
$d_{\parallel}$	Field-parallel grain-boundary width
$d_{\perp}$	Field-perpendicular grain-boundary width
d_{50}	Average particle diameter
D	Grain size
D_B	Grain boundary diffusivity
D_V	Volume diffusivity
DF	Darkfield
DFT	Density functional theory
DI	Depth-sensitive indentation
dn/dT	Refractive index change with temperature
$dn/d\lambda$	Refractive index homogeneity
DSC	Differential scanning calorimetry
e	Electron, electron charge, base of natural logarithm
E	Modulus of elasticity, electric field
E_a	Activation energy
E_F	Formation energy
E_g	Bandgap energy
EBSD	Electron backscattered diffraction
ED	Electron diffraction
EDS	Energy-dispersive X-ray spectroscopy
EELS	Electron energy loss spectroscopy
EFM	Electrostatic force microscopy
EIS	Electrochemical impedance spectroscopy
erg	10^{-7} Joules
eV	Electron volt
f	Frequency
f_{max}	Resonant frequency
F-	Two trapped electron color center
F+	Single trapped electron color center

FAST	Field-assisted sinter
FD	Freeze dried
FIB	Focused ion beam
FOLZ	First-order Laue zone
g	Gram
GB, gb	Grain boundary
GB1	Green body 1
GB2	Green body 2
GC	Gelcast
GDMS	Gas-discharge mass spectroscopy
GHz	Gigahertz
GPa	Gigapascal
GS	Average grain size
h	Hour, electron hole, Planck's constant
H	Spacing of reciprocal lattice planes
HIP	Hot isostatic press
HK	Hardness Knoop
HP	Hot press
HRTEM	High-resolution transmission electron microscopy
HV	Hardness Vickers
Hz	Hertz
i	Inversion parameter
I	Indentation
I_0	Incident intensity
I_A	Absorption
I_{DT}	Diffuse transmittance
I_{ILT}, ILT	In-line transmittance
I_{RD}	Diffuse reflectance
I_{RS}	Specular reflectance
I_{RT}	Reflected transmittance
I_T, IT	Total forward transmittance
I_{TT}	Total transmittance

IBR	Intrinsic birefringence
ICP	Inductively-coupled plasma
IE	Impulse excitation
Im	Imaginary
IR	Infrared
j	Square root of -1
J	Joule
k	Boltzmann's constant
K	Kelvin
kN	Kilo Newton
L	Camera length, thickness (EIS)
l	Liter
L_0	Initial side length
$L_{compact}$	Length of compact
L_i	Instantaneous side length
L_{std}	Length of standard
LA	Laser ablation
lbs	Pounds
LVDT	Linear variable differential transformer
m	Meter
m_0	Electron mass
M	Modulus (EIS)
m/z	Mass-to-charge ratio
Max	Maximum
mg	Milligram
MHz	Megahertz
min	Minutes
ml	Milliliter
mol%	Mole percent
MPa	Megapascal
mPa	Milli Pascal
MS	Mass spectroscopy

n	Refractive index, neutron
n_c	Constant phase element exponent
N	Newton
NAA	Nuclear activation analysis
NMR	Nuclear magnetic resonance
Null	Perfect lattice
obj	Objective lens
OES	Optical emission spectroscopy
OM	Optical microscopy
P	Pressure application
Pa	Pascal
PC	Polycrystal
PEG	Polyethylene glycol
PIES	Parallel-ion electron spectroscopy
PLM	Polarized light microscopy
pO_2	Oxygen partial pressure
ppm	Parts per million
ppmv	Parts per million volume
ppmw	Parts per million weight
P_S	Fractional sintered density
PS	Pressureless sinter
PVA	Polyvinyl alcohol
p_X	Partial pressure of species formed during reduction
Q	Constant phase element parameter
r	Grain radius, radius of first-order Laue zone
r_0	Initial grain radius
R	Reflectance, resistance, distance between SAD reflections
R’	Thermal shock parameter
R_{bulk}	Bulk resistivity
R_D	Diffuse reflectance
R_S	Specular reflectance
R_{S1}	Reflectance from a single surface

R_{S2}	Reflectance from two surfaces
R_T	Total reflectance
RC	Resistor-capacitor
Re	Real
rel	Relative
RF	Radio frequency
RGA	Residual gas analyser
RIT	Real in-line transmittance
rms	Root-mean squared
RS	Reactive sinter
s	Seconds, inter-ridge distance
S	Seimens, Scatter
SA	Surface area
SAD	Selected-area diffraction
SBR	Stress birefringence
SC	Single crystal, slip cast
SEM	Scanning electron microscopy
SPS	Spark-plasma sinter
STA	Simultaneous thermal analysis
STEM	Scanning transmission electron microscopy
t	Thickness, time
T	Temperature
T_{Amb}	Ambient temperature
TEM	Transmission electron microscopy
TFT	Total forward transmittance
TGA	Thermogravimetric analysis
TOF-SIMS	Time-of-flight secondary-ion mass spectroscopy
u	Anion parameter
US Mix	Ultrasonic mix
UV	Ultraviolet
UV-Vis-IR	Ultraviolet-Visible-Infrared
V	Volts

V-	Trapped hole color center
V_0	Voltage amplitude
Vac	Vacuum
v_{gb}	Grain boundary volume fraction
V_i	Instantaneous volume
Vis	Visible
W	Watt
W_0	Initial weight
WDS	Wavelength-dispersive spectroscopy
wt%	Weight percent
x	Stoichiometry MgO:xAl$_2$O$_3$
XRD	X-ray diffraction
YAG	Yttrium aluminum garnet
Z	Impedance
Z_0	Impedance magnitude
ZA	Zone axis
ZL	Zero-loss
α	Absorption coefficient
α_L	Linear coefficient of thermal expansion
γ	Interfacial energy
γ_{gb}	Grain boundary energy
γ_s	Surface energy
Δ	Change
δ	Loss tangent
ΔL	Linear displacement
$\Delta L/L_0$	Linear shrinkage per unit length
ε	Dielectric constant
ε_0	Permittivity of free space
ε_{bulk}	Bulk permittivity
ε_{gb}	Grain boundary permittivity
θ	Dihedral angle
κ	Thermal expansion coefficient

λ	Wavelength
ξ	Anisotropy ratio
ρ	Resistivity
ρ_{bulk}	Bulk resistivity
ρ_g	Green density
$\rho_{gb\perp\ sp}$	Specific field-perpendicular grain-boundary resistivity
ρ_i	Instantaneous density
ρ_t	Total resistivity
ρ_{th}	Theoretical density
σ	Conductivity, stress
σ_0	Conductivity pre-exponential constant
σ_{bulk}	Bulk conductivity
$\sigma_{bulk\ series}$	Bulk conductivity using the series model
σ_{gb}	Grain boundary conductivity
$\sigma_{gb\parallel\ sp}$	Specific field-parallel grain-boundary conductivity
$\sigma_{gb\perp\ sp}$	Specific field-perpendicular grain-boundary conductivity
σ_{sc}	Single-crystal conductivity
σ_{series}	Conductivity across the bulk and grain boundaries
σ_t	Total conductivity
σ_T	Transition stress
τ	Time constant
υ	Poisson’s ratio, volume fraction (EIS)
φ	Phase shift
Φ	Diameter, phase shift
Φ_f	Final diameter
Φ_i	Instantaneous diameter
Φ_o	Initial diameter
Ψ	Dihedral angle
ω	Angular frequency
ω_{max}	Angular frequency at imaginary maximum

CHAPTER 1 INTRODUCTION

Advances in powder synthesis, processing and scientific understanding have enabled overcoming some of the limitations of polycrystalline ceramics, such as their brittle nature and the difficulty of fabricating dense compacts. In turn, these developments have garnered a renewed interest in transparent ceramics due to their unique functional properties, such as high hardness, chemical inertness, thermal resistance, and high transmission over a wide range of wavelengths. Polycrystalline magnesium aluminate spinel has been at the forefront of these developments due to its isotropic crystal structure and an attractive combination of physical properties. However, there remains a significant lack of understanding of the properties and behaviors of the interfaces of spinel as a function of stoichiometry, impurities, and additives, and how these change during processing. Interfaces, such as surfaces and grain boundaries, largely govern sintering, densification and microstructure evolution in ceramics and other polycrystalline materials, and they can significantly affect the physical properties of bulk compacts. In this light, the properties and behaviors of the interfaces of spinel compacts made using a variety of starting powders with different stoichiometries, impurity contents, additive contents, and using different processing methods and parameters were examined using a wide-range of analytical methods.

1.1 Motivation

The motivation for the research was to understand the structure-processing-property relationships involved in the fabrication of transparent spinel, in order to improve the mechanical and optical properties of bulk compacts and thus widen applications. The goal was to characterize and understand interfaces, in particular how they are affected by stoichiometry, impurities, LiF additive and processing, and in turn, to understand how this affected bulk properties.

1.2 Objectives

Specific objectives included; (i) characterizing interfaces, (ii) determining the effect of stoichiometry, LiF additive, impurities, and processing parameters on their properties, and (iii) determining the effect of interfaces on sintering, densification, microstructure evolution and bulk mechanical, optical, and electronic properties.

1.3 Summary of Work

Experiments were designed to elucidate the role of interfaces in the processing-structure-property relationships of transparent spinel, with attention paid to identifying relationships between variables spanning the entirety of processing. To enable identifying these relationships, starting powders and bulk compacts were extensively characterized. Starting powders with different stoichiometries and impurity and LiF additive contents were characterized by X-ray diffraction, inductively-coupled plasma in combination with optical-emission and mass spectroscopy, carbon-sulfur and nitrogen determination, optical and electron microscopy, particle-size analysis, and Zeta potential. Sintering behavior was assessed by dilatometry and hot-press ram displacement analysis, and chemical interactions by thermal analysis combined with mass spectroscopy and thermodynamic simulations. Compacts were densified by hot-pressing, pressureless sintering and hot-isostatic pressing. Dense compacts and interfaces were characterized using optical microscopy, scanning electron microscopy in combination with energy and wavelength-dispersive spectroscopy and electron-energy backscatter spectroscopy; transmission electron microscopy in combination with convergent-beam electron diffraction, energy-dispersive X-ray spectroscopy, and electron energy-loss spectroscopy; secondary-ion mass spectroscopy, parallel-ion electron spectroscopy, and atomic-force microscopy. Optical properties were assessed by spectrophotometry, ultraviolet laser fluorescence, and Raman spectroscopy, and dielectric properties with electrochemical impedance spectroscopy. Interface properties were then related to starting powder properties, processing parameters, microstructure evolution, and optoelectronic properties.

1.4 Structure of Thesis

The thesis contains six chapters, references, and personal information:

1. Chapter 1 is an introduction consisting of the motivation, goals, and objectives.
2. Chapter 2 is a background on the processing and properties of transparent spinel.
3. Chapter 3 discusses the experimental methods.
4. Chapter 4 presents combined results and discussion.
5. Chapter 5 is a general discussion of the results.
6. Chapter 6 is a summary of the main findings.
7. "References" lists references cited.
8. "Personal Information" contains personal information.

Four articles were published based on the research: "The Role of LiF and Impurities in the Sintering and Optical Properties of Transparent Polycrystalline $MgAl_2O_4$ Spinel",[1] published in the International Journal of Applied Ceramic Technology, "50 Years of Research and Development Coming to Fruition; Understanding the Complex Interactions during Processing of Transparent Magnesium Aluminate ($MgAl_2O_4$) Spinel",[2] published as an invited feature in the Journal of the American Ceramic Society, "Electrochemical Impedance Spectroscopy of Transparent Polycrystalline $MgAl_2O_4$ Spinel",[3] published in the Journal of the American Ceramic Society, and "Interface Energies in Transparent Non-Stoichiometric Spinel Determined by Thermal Grain-Boundary Grooving", to be submitted for publication in the Journal of the European Ceramic Society, and a related article "Enhanced Fracture Toughness in Non-stoichiometric Magnesium Aluminate Spinel through Controlled dissolution of Second Phase Alumina" was published in the Journal of the American Ceramic Society.

CHAPTER 2 BACKGROUND

This chapter provides a detailed background on the processing and properties of polycrystalline transparent spinel, which are crucial to understanding interfaces and their interactions. Section 2.1 is a general introduction, Section 2.2 discusses properties, Section 2.3 discusses processing, Section 2.4 discusses stoichiometry, Section 2.5 discusses impurities and additives, Section 2.6 discusses processing parameters, and Section 2.7 is a summary.

2.1 Introduction

The quest for materials to satisfy demanding optical applications combined with scientific and technological advances have spurred a resurgent interest in transparent polycrystalline ceramics.[4-11] Transparent ceramics have a unique combination of properties that is not obtainable with other materials,[12] and unlike single crystals, they can be formed into complex near-net shapes from commercially-available powders at lower cost.[13] Transparent polycrystalline spinel is an especially promising and rapidly-maturing technology. However, although it has been studied for over 50 years, highly-transparent components with acceptable mechanical properties have only recently been reliably fabricated at reasonable cost.[4,10,13-17] Spinel is difficult to sinter to the near-theoretical density required for transparency and fabrication is complicated by variable stoichiometry and high sensitivity to powder and processing parameters.[1,4,8] These difficulties, combined with a poor of understanding of synthesis-processing-structure-property relationships, have hindered development.[4] Key to recent success is an emerging understanding of complex, multi-scale, multi-variable interactions occurring during green-body formation and sintering.[8,18,19] In particular, particle-size characteristics, stoichiometry, and impurities play a decisive role in determining compact properties and successful fabrication entails tracking these variables from synthesis to the finished product.

Magnesium aluminate spinel ($MgAl_2O_4$, spinel) is a naturally-occurring, often twinned, cubic mineral with octahedral habit.[20] It is transparent to opaque and exhibits various colors, most notably red due to chromium impurity.[20] The general chemical formula $(Mg,Fe)(Al,Cr)_2O_4$ is a common constituent of peridotite, the main mineral comprising the Earth's upper mantle.[21] The spinel structure is the prototype for the larger spinel group, with formula unit AB_2X_4, where A and B are cations with net charges of +2 and +3, respectively, and X is an anion with a net charge of -2.[22] A wide range of cations, including aliovalent substitutions, can occupy the A and B positions, with iron (Fe^{2+} and Fe^{3+}) occupying both in magnetite (Fe_3O_4). The X anion is typically oxygen, but can be occupied by sulfur or other aliovalent anions. This large variety of elemental substitutions leads to a wide range of minerals and compounds with the spinel structure and also to a wide range of substitutions and point-defects in polycrystalline compacts.

Spinel has a combination of isotropic cubic structure, low density, high hardness, erosion resistance, high strength, transparency from the near-UV (ultra-violet) to the mid-IR (infra-red), and high-temperature stability possessed by few materials.[4,23] Transparent non-oxides such as ZnS, ZnSe, Si_3N_4, and SiC possess good IR-transmittance, but have so far exhibited lower visible transmittance.[23] Alkaline and alkali-metal halides like MgF_2, and also glasses and glass-ceramics, have lower mechanical and thermal properties.[23] Competing transparent ceramics include sapphire and polycrystalline $Al_{23}O_{25}N_5$ (AlON), Al_2O_3, MgO, cubic ZrO_2, Y_2O_3, $Y_2Al_5O_{12}$ (YAG), and diamond.[6,11,19,23-30] Sapphire and AlON have excellent mechanical and optical properties, but are denser, harder to polish, more expensive to produce, and birefringence in sapphire requires single crystal use.[4,13,31] In addition, these ceramics have a lower IR absorption edge and transmission at the 4.8 μm exhaust signature wavelength used for IR-sensing, especially at higher temperature.[12] ZrO_2 has a higher IR absorption edge than spinel, but also higher density, and lower hardness, erosion resistance and visible transmittance.[23-25] YAG and Y_2O_3, used in laser applications, both have high transmittance and wider transmission windows than spinel, and Y_2O_3 lower emittance.[6,11,23-26,30] However, they are significantly denser, have lower hardness and erosion resistance, and are more expensive.[6,11,23-26,30] Polycrystalline MgO and Al_2O_3 have excellent mechanical properties, but MgO has poor visible transmittance[23] and polycrystalline Al_2O_3, although showing promise for IR windows and domes, is translucent in thick sections due to birefringence, even with nanometer-sized grains.[23-25,27] Single crystal and polycrystalline diamond produced by chemical vapor deposition have excellent optical and mechanical properties, but they are difficult and expensive to fabricate and are not yet commercially available.[23,28,29]

Until recently, spinel had only been used sporadically in military applications such as transparent armor, IR-transparent windows for missile launchers and reconnaissance pods, and transparent domes for IR-seeking missiles.[4,32,33] However, it is now being used or considered for windows for UV lithography, spacecraft, barcode scanners, watches, night-vision systems, high-temperature sight-glasses, and laser ignitors.[10,13,15,34-40] Moreover; multi-spectral windows for imaging, ranging, and targeting in ground, sea, and air vehicles.[14] In addition; UV, miniaturized, and refractive index lenses; laser and scintillator hosts, and laser Q-switches.[8,10,13,15,34-40]

Spinel was first synthesized accidentally in the mid-18th century[41] but polycrystalline spinel only found commercial use starting in the 1960's, mainly as refractory brick material for the steel-making industry and with limited use as anode and catalyst support material.[19,42] Transparent spinel development began in the 1960's in the U.S. and The General Electric Co. (Fairfield, CT, USA) was first to successfully fabricate visibly transparent material, which also had an IR-transmittance >60% at ~3 mm thickness.[4] Compacts were cold-pressed (CP) from calcined Al_2O_3 and MgO powders with Li_2O and SiO_2 additives, embedded in powder of similar stoichiometry in a molybdenum enclosure, and sequentially pressureless sintered (PS) up to 1900°C in H_2.[12,43,44] Development continued in the 1970's–1990's with hot press (HP), HP/hot isostatic press (HIP), and fusion-cast spinel (which suffered from residual stress), however production was fraught with difficulties.[4] Initially, obtaining high transparency was an issue, but then reproducibility and optical defects became prime concerns.[4] These were attributed to small differences in powder stoichiometry and impurity content that often precluded transparency, a condition which only improved once higher-quality powders became available.[4] Sintering additives were initially necessary for transparency, but they interfered with transmittance, and LiF emerged as the most useful additive.[4] Since the 1990's, many of the inherent issues with achieving transparency were solved and interest shifted towards optimizing processing, lowering cost, and improving mechanical properties, mainly through grain-size reduction.[4,8,45]

Translucent or transparent spinel has since been produced by PS,[43,46-48] HP,[1,33,49,50] HP/HIP,[13,51-57] PS/HIP,[13,34,38.45.54.58-61] spark plasma sintering (SPS),[62-67] field-assisted sintering (FAST),[18] fusion casting,[68] and melt-casting[69] sometimes in combination with reactive sintering (RS).[51,57,58,70] However, nearly all commercial manufacture is currently with HP/HIP or PS/HIP, producing components up to 10 cm thick and 50 cm in diameter, and larger windows up to 0.52 m^2 by diffusion edge-bonding of smaller panes.[16,56] LiF (0.25–4 wt%) is typically required for transparency with pressure-assisted sintering (HP, HP/HIP, and SPS), but with the advent of high-purity nano-powders and improved pre-treatment, the trend is towards not using additives.[4,8,36] The ultimate goal is pressureless sintering without HIP, but only translucency has been achieved and all commercial fabrication uses pressure to increase sintering kinetics (HP, SPS) or close residual pores (HP, HP/HIP, PS/HIP, SPS).[4,8] Electric fields (SPS, FAST) increase kinetics and reduce grain size, but geometry is limited and sintering rates comparable to HP appear necessary for high transparency.[8] Increasing kinetics by irradiating powders and microwave sintering[44,70] have also been attempted without significant success.[71] Despite progress achieved, considerable headway remains, including increasing reproducibility, scaling-up fine grain-size technologies, grain-boundary engineering with new additives, lowering absorption near absorption edges, and lowering cost. In addition, many questions remain only partially answered, such as the causes of grain growth, absorption, and optical defects, as well as the specific role of stoichiometry, defect chemistry, and sintering additives.

2.2 Physical Properties

This section discusses the physical properties of transparent spinel, including thermodynamics (Section 2.2.1), crystal structure (Section 2.2.2), interfaces (Section 2.2.3), diffusion (Section 2.2.4), and electronic (Section 2.2.5), optical (Section 2.2.6), and mechanical properties (Section 2.2.7), and describes the physical requirements for various applications (Section 2.2.8).

2.2.1 Thermodynamic Properties

Spinel is the only intermediate compound of the MgO-Al_2O_3 phase system (Fig. 2.1).[72,73] Formation from its constituents is exothermic and occurs by cation counter-diffusion through a stationary oxygen lattice[71,74] with an accompanying ~5-8 vol% expansion.[19,75] Although spinel forms a line compound of equal mol% MgO and Al_2O_3 at equilibrium below ~1200°C, it has increasing solubility with temperature, especially for Al_2O_3, as described by x in $MgO{:}xAl_2O_3$, with a maximum range of $0.6 \leq x \leq 9.1$.[72] The solid-solubility end-member on the Al_2O_3-rich side is the highly-defected cubic γ-Al_2O_3 polymorph.[76] In practice, single-phase variable stoichiometry $\sim 1 \leq x \leq 3$ is quenched in with moderate cooling rates (<5°C/min).[1,4,73,76,77]

The vapor pressure of Mg or MgO over spinel is up to 10^3 times higher than that of Al_2O_3,[78] resulting in Mg/MgO loss and variable stoichiometry during sintering. Mg/MgO loss is greater at high temperature and low oxygen partial pressure (pO_2),[79-81] and reducing conditions favor the decomposition of MgO(g) into Mg(g) and O_2(g).[75,82] Stoichiometry may also be affected by formation of AlO_2 gas, which is exacerbated by carbon present in graphitic furnaces. Variable stoichiometry affects virtually every property and is both a source of complexity and a key to understanding spinel (Section 2.4).

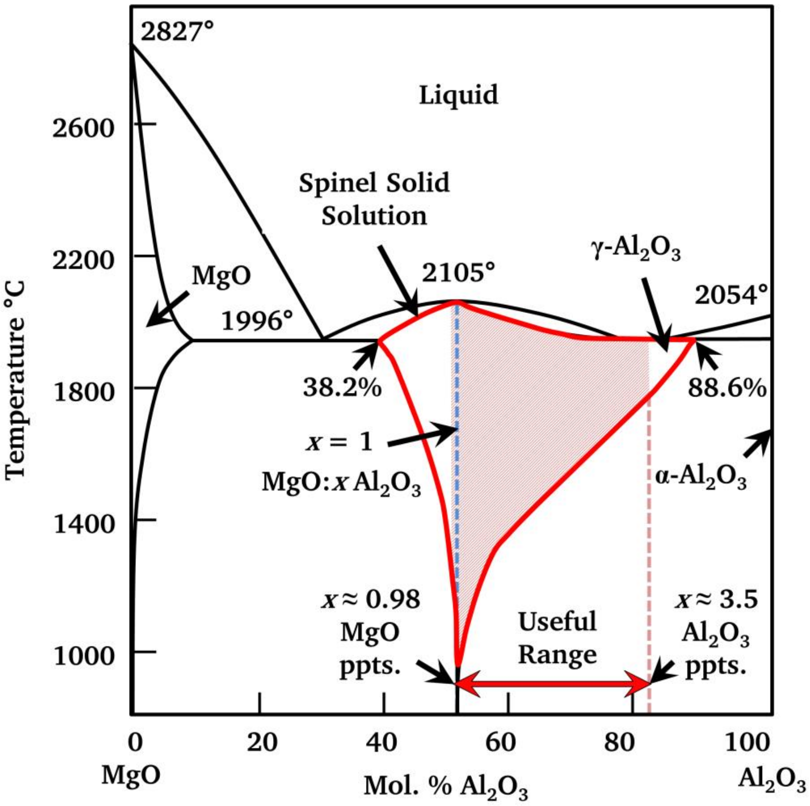

Fig. 2.1: Spinel phase diagram, adapted with permission.[72]

2.2.2 Crystal Structure and Defects

In spinel, the larger O^{2-} anions form a cubic close-packed sub-lattice, rendering isotropic properties, and the cations occupy only ¼ of the interstices (Fig. 2.2). The cubic symmetry is visualized by considering a larger unit cell composed of 8 $MgAl_2O_4$ formula units with the lattice parameter (a) determined by the cations. In normal spinel, larger Mg^{2+} cations occupy ⅛ of the smaller tetrahedral interstices and smaller Al^{3+} cations occupy ½ of the larger octahedral interstices, dilating anions from their ideal cubic arrangement, characterized by the anion parameter (u). The structure can accommodate significant cation site-exchange, characterized by the inversion parameter (0 [normal] $\leq i \leq$ 1 [inverse]), with i ~0.1-0.6 for synthetic spinel.[22,85]

A wide variety of point defects exist in spinel and defect chemistry is a key parameter that influences many properties (Sections 2.4-2.6).[22,76,86-90] In turn, it is affected by stoichiometry, impurities, additives,[36] mechanical treatment,[91] irradiation,[92] sintering atmosphere,[75,79-83] temperature,[93] and applied pressure.[22,76,86-90]

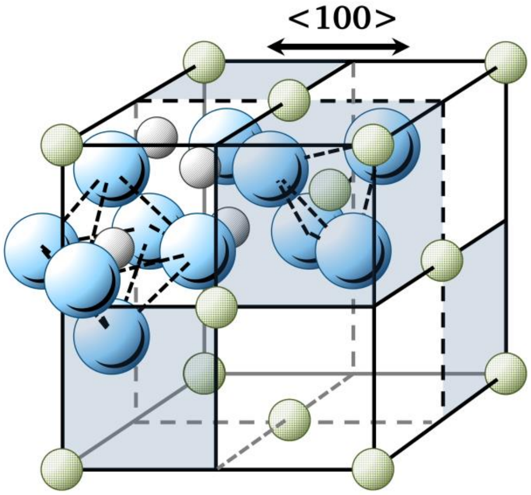

Fig. 2.2: Unit cell of spinel depicting symmetry (shaded) and octahedral and tetrahedral interstices.[15]

Intrinsic point defects in Kroger-Vink notation include:

$$Mg_{Mg}^{x} \rightarrow Mg_{i}^{\bullet\bullet} + V_{Mg}'' \tag{2.1}$$

$$Al_{Al}^{x} \rightarrow Al_{i}^{\bullet\bullet\bullet} + V_{Al}''' \tag{2.2}$$

$$O_{O}^{x} \rightarrow O_{i}'' + V_{O}^{\bullet\bullet} \tag{2.3}$$

$$Null = V_{Mg}'' + 2V_{Al}''' + 4V_{O}^{\bullet\bullet} \tag{2.4}$$

Point defects in high-bandgap ionic compounds like spinel are typically charge-compensated by ionic rather than electronic defects, with interstitial (Frenkel) and anionic defects $(\mathrm{O}_i'', \mathrm{V}_\mathrm{O}^{\bullet\bullet})$ less favorable than Schottky defects due to strain in the close-packed anion lattice.[94] Cation inversion (antisite) is the predominant intrinsic point defect in spinel and is self-compensating:[92]

$$Mg_{Mg}^{x} + Al_{Al}^{x} \rightarrow Mg_{Al}' + Al_{Mg}^{\bullet} \tag{2.5}$$

Inversion causes variation in *u*, affecting the path of diffusing species and altering the equilibria of other defects.[22] For example, Eq. (2.5) combines with Eqs. (2.1-2.4) to replace $\mathrm{V}_\mathrm{Al}'''$ with $\mathrm{V}_\mathrm{Mg}'' + \mathrm{Mg}_\mathrm{Al}'$ or V_Mg'' with $\mathrm{V}_\mathrm{Al}''' + \mathrm{Al}_\mathrm{Mg}^{\bullet}$. Inversion is induced by heating to higher temperature and has been quantified by X-ray diffraction (XRD),[95] nuclear magnetic resonance (NMR),[93,96] electron spin/paramagnetic resonance,[97] neutron diffraction,[98] optical absorption,[99] Raman spectroscopy,[100,101] and simulations.[92,102]

Extrinsic point defects are created by astoichiometry (Eqs. 2.6 and 2.7) introduced during synthesis or caused by Mg/MgO volatilization (Eq. 2.8). Sintering in graphitic furnaces adds an additional reaction affecting defect equilibrium by generating oxygen vacancies (Eq. 2.9).

$$Al_2O_3 - rich \rightarrow Al^{\bullet}_{Mg}\text{, compensated by } V''_{Mg},\ V'''_{Al},\text{ or } O''_i \tag{2.6}$$

$$MgO - rich \rightarrow Mg'_{Al}\text{, compensated by } Mg^{\bullet\bullet}_i,\ Al^{\bullet\bullet\bullet}_i,\text{ or } V^{\bullet\bullet}_O \tag{2.7}$$

$$Null = V''_{Mg} + 2Al^{x}_{Al} + 3O^{x}_{O} + V^{\bullet\bullet}_{O} + MgO_{(g)} \tag{2.8}$$

$$C + O^{x}_{O} \rightarrow V^{\bullet\bullet}_{O} + CO_{(g)} \tag{2.9}$$

The consensus is that excess aluminum occupies magnesium sites and excess magnesium occupies aluminum sites, but experimental studies are contradictory as to compensating defects. XRD and magic-angle NMR indicate V'''_{Al} are preferred in Al_2O_3-rich spinel,[98,103] although V''_{Mg} may exist simultaneously and the viability of O''_i is not addressed. In MgO-rich compositions, enhanced sintering is explained by charge-compensation with $V^{\bullet\bullet}_O$,[50,90,94,104] with possible confirmation by optical methods.[99,105] Simulations also conflict as to compensating defects (Table 2.1), indicating aluminum defects may be even less favorable than oxygen defects. Oxygen interstitials have the highest mobility even though their formation energy is higher and Schottky defects have the lowest formation energy apart from inversion. Simulations also indicate that charged defects attract oppositely-charged defects, leading to defect associates, with lower formation energies noted for defect pairs, trimmers, and cluster.[106,107] Simulations indicate impurities lower defect formation energies, and aliovalent substitutions require charge-compensating defects that likely affect properties similarly to astoichiometry.[108] UV irradiation affects lower-energy defects such as electron-hole recombination, gamma-ray irradiation induces point defects such as inversion, and neutron irradiation induces higher-energy defects such as cation and oxygen vacancies.[92,99,105,109-112]

Line defects such as dislocations are commonly observed and likely serve as pathways for diffusion and have a significant effect on densification during pressure-assisted sintering (Section 2.6.2). Dislocations move primarily on {110}, {111}, and sometimes {100} planes, depending on stoichiometry, and slip occurs along <110> directions,[113,114] while cleavage is typically along {111} planes.[115-119]

Table 2.1: Calculated Point Defect Formation Energies and Diffusion Barriers.

Defect	Formation Energy E_F (eV)	E_F Per Defect (eV)	Diffusion Barrier (eV)	Comments
$MgAl_2O_4$	-21.8[73,108]	-	-	Exothermic, 5-8 vol% increase
MgO	-5.68[108]	-	-	Lowest stability
Al_2O_3	-15.63[108]	-	-	γ–Al_2O_3 also stable
Anti-site	0.48-0.6,[106]	0.32[106]	-	Defect pair, E_F decreases with
	2.3, 4.6[115]	-	-	separation
	0.73[107]	-	-	Defect pair, replacement (Al_{Mg}', $Mg_{Al}^{\bullet}$)
$Mg_i^{\bullet\bullet}$	7.58[106]	2.2[106]	-	Includes isolated V_{Mg}''
	6.6-6.7[106]	-	0.56[116]	Two split $Mg_i^{\bullet\bullet}$ + V_{Mg}''
	-	3.34,[106] 5.46[107]	-	Frenkel (interstitial + vacancy)
$Al_i^{\bullet\bullet\bullet}$	9.7[106]	9.7[106]	0.56[106,116]	Decays → $Al_{Mg}^{\bullet}+2Mg_i^{\bullet\bullet}+V_{Mg}''$
	8.4-8.8[106]	4.4[106]	-	Split ($Al_i^{\bullet\bullet\bullet}+Mg_i^{\bullet\bullet}+V_{Mg}''$)
	7.3-7.7[106]	-	-	Ring defect ($3Al_i^{\bullet\bullet\bullet}+3V_{Al}'''$)
	4.39,[106] 6.93[107]	-	-	Frenkel per defect
O_i''	8.9-9.2[106]	4.5[106]	0.29[116]	Two split O_i including $V_O^{\bullet\bullet}$
	-	4.43,[106] 5.50[107]	-	Frenkel (interstitial + vacancy)
V_{Mg}''	6.65[106]	3.34[106]	0.68[116]	Frenkel (interstitial + vacancy)
V_{Al}'''	8.78,[106] 6.4[89]	4.39[106]	2.00[116]	Frenkel (interstitial + vacancy)
$V_O^{\bullet\bullet}$	8.86[106]	4.43[106]	1.67[116]	Frenkel, E_F reduced by inversion
V_O	1.29-6.73[108]	6.73[108]	1.8-4.3[108]	V_O^x, reduced by pO_2, Ca, Zn, Cu
Schottky	24.7[106,120]	3.5-4.3[86,106]	-	
	-	3.5-5.3[106,107,120]	-	
Bandgap	7.75-7.8[117.118]	-	-	[e' + $h^{\bullet}$], reduced by Ca, Zn, Cu

Density Functional Theory (DFT),[106,108] Temperature Accelerated Dynamics & Kinetic Monte Carlo[116]
Pair Potential Simulations.[107]

2.2.3 Interface Properties

Interfaces comprise the surfaces of powder crystallites and polycrystalline bodies and the internal boundaries between grains and secondary phases. Unlike the bulk, surface atoms have unsatisfied bonds and experience unbalanced attractive forces, resulting in lattice strain, surface reconstruction, and a difference in free energy, which makes them prone to adsorption by impurity species. Grain boundaries are the structural discontinuities between regions with different lattice orientation within polycrystalline bodies and are often likened to arrays of dislocations that accommodate the lattice mismatch. However, grain boundaries also often have associated chemical and defect chemistry gradients, space-charge layers and strain fields, and a difference in free energy, which like surfaces make them prime sites for defect and impurity segregation. Interfaces have a strong and often controlling influence on sintering, microstructure evolution, and mechanical, thermal, optical, and electronic properties. The properties of interfaces of transparent spinel, their interactions with variables that affect them throughout processing, and their effect on bulk properties is the central theme of this work.[120]

Planar defects, such as grain boundaries and surfaces (and their associated energies), can govern sintering, densification, and microstructure evolution while also significantly impacting physical properties (Sections 2.2.8, 2.4.4, 2.5, 2.6.1, 2.7.2).[121] The surface energy (γ_s) of spinel varies with orientation (Table 2.2),[122-129] resulting in the facetted octahedral habit observed for crystallites[122] and polycrystal grains.[119] Recent studies indicate {100} planes have the lowest energy,[123,125,126,128,129] whereas {111} are frequently observed cleavage, twin, and crystal surface planes.[122,130-132] Moreover, simulations predict Mg-terminated surfaces have lower energy,[128] whereas high-temperature annealing in oxygen suggests Al-O terminations are more favorable.[127,133,134] The latter indicates an influence from stoichiometry that also likely applies to grain-boundary energy.[129] The grain-boundary energy (γ_{gb}) of spinel has been estimated based on calorimetry[129] and thermal grooving[135] from which γ_{gb} can be found if γ_s is known (Table 2.2). The γ_{gb} also varies with orientation and {111} grain-boundary plane orientations are observed at twice the frequency of {100} orientations.[119] Published γ_{gb},[129] γ_{gb}/γ_s ratios[135] and recent γ_s[125] values for low-energy planes suggest the grain-boundary energy for pure stoichiometric spinel ranges from 0.5 – 1.6 J/m^2. However, complicating matters is that interface energies are also affected by impurities, additives, and sintering atmosphere.[127,129,135] Grain-boundary mobility is another important variable affecting microstructure evolution and it is generally low in spinel compared to other oxides.[76] Other planar defect such as twins, which are commonly observed in natural spinel, are rarely observed in synthetic material.[136]

Table 2.2: Reported Interface Energies for Stoichiometric $MgAl_2O_4$ Spinel.

Reference	Method	γ_s[a] (J/m^2)		
		{100}	{110}	{111}
Mishra et al. 1977[122]	Calculation (elastic constants)	1.45	2.70	0.30
	Atomistic calculation (unrelaxed)	3.00	4.72	0.62
Stewart et al. 1980[124]	Calculation (single crystal fracture)	3.57	4.07	4.85
Davies et al. 1994[123]	Atomistic simulation (relaxed)	2.28[b]	2.50	2.60
Fang et al. 2000[125]	Atomistic simulation (relaxed)	2.27[b]	2.85	3.07
van der Laag et al. 2005[126]	DFT LDA (relaxed)	1.79[b]	-	-
	DFT GGA (relaxed)	1.61[b]	-	-
Rasmussen et al. 2011[127]	DFT (DACAPO code)	-	-	0.3 – 1.9[d]
Massaro et al. 2014[128]	Empirical force field	2.32[b]	2.75[c]	-
	DFT HF (B3LYP Hamiltonian)	1.60[b]	-	-
Hasan 2016[129]	Calorimetry (plane unspecified)	1.65[e]		
		γ_{gb}/γ_s		
Teevan 2010[135]	Thermal grain-boundary grooves	Undoped		0.26 – 0.53[f]
		TiO_2-doped		0.28 – 0.70[f]
		γ_{gb} (J/m^2)		
Hasan 2016[129]	Calorimetry (nanocrystalline sample)	Undoped		0.53
		Gd-doped		0.32

[a] Minimum surface energies.
[b] Mg-terminated surface.
[c] Al-O-terminated surface.
[d] 0 K, lower values Al-O-termination with H-adsorption, clean Mg-termination lower energy at higher temperature.
[e] Reports {100} have lowest energy based on atomistic calculations.
[f] Average values, relative standard deviations 20-35%, corrected for AFM probe tip, 25 min. H_2 or O_2 etch at 1200°C, some samples pre-annealed 18 h in H_2 at 1100°C or 1400°C.

2.2.4 Diffusion Properties

Mg^{2+} has the highest diffusivity of the constituent ions and Al^{3+} is slightly lower (Fig. 2.3).[137-139] Ionic transport occurs by a defect-assisted interstitial mechanism that is accentuated by V''_{Mg} in Al_2O_3-rich stoichiometry $(2Al_2O_3 \rightarrow 2V''_{Mg} + 4Al^x_{Al} + 6O^x_O + 2V^{\bullet\bullet}_O)$.[138,140-142] O^{2-} diffusivity is orders of magnitude lower than cation diffusivities, as expected for the largest ion and the close-packed lattice.[143-146] Sintering experiments indicate similar activation energies to that of O^{2-} self-diffusion, indicating it is rate-limiting.[50,94,104,147] However, the O^{2-} grain-boundary diffusivity is expected to be rate-limiting as it may be lower.[139] Understanding is complicated because of the dependence of diffusion on stoichiometry and planar defects, which both vary during sintering.[76,86,89,139] O^{2-} diffusion is expected to be higher in MgO-rich compositions due to the higher oxygen vacancy concentration indicated by sintering experiments. However, studies indicate either a slight increase[143] or much higher[145] O^{2-} diffusion for Al_2O_3-rich compositions.

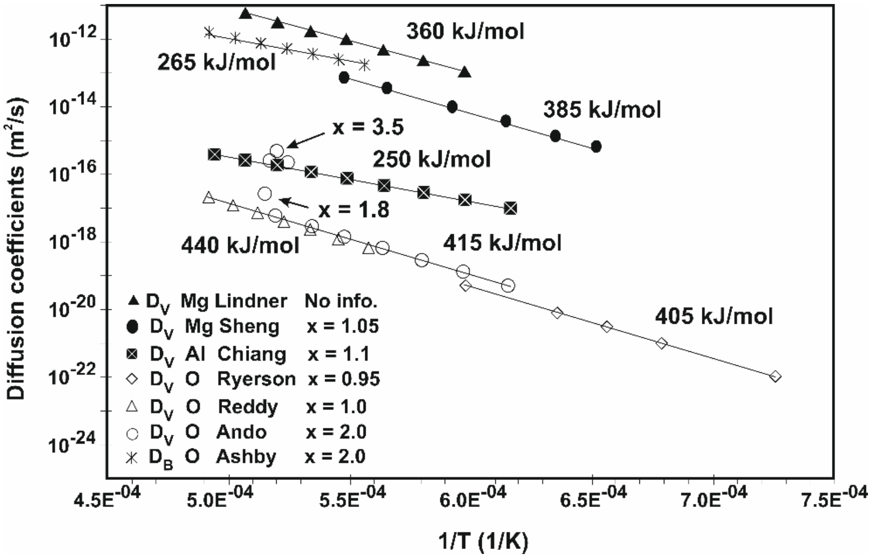

Fig. 2.3: Diffusion coefficients for spinel species, adapted with permission.[139,145]

2.2.5 Electronic Properties

Spinel is a wide, direct band-gap[148-150] insulator with the lowest conductivity of the spinel series.[151] It exhibits mainly ionic, mixed ionic-electronic conduction[137,141,151-154] with transference numbers from 0.5 to 1 reported between 500°C and 1000°C.[137,152] Conductivity varies with an Arrhenius relation from ~10^{-12} S/cm at 500°C to ~10^{-4} S/cm at 1600°C and activation energies vary from 0.4 eV to 2.6 eV.[137,151,154] Although Mg^{2+} ions have the highest self-diffusivity, it is unclear whether they or magnesium vacancies (V_{Mg}'') are the main charge carriers.[137-140,142,152,153,155] Al^{3+} diffusivity is up to several decades lower[138,139,156] and O^{2-} diffusivity is lower still,[139,143-145] with conductivities expected to mirror diffusivities. Polycrystalline conductivity is generally 1-2 decades higher than for single crystals, tentatively attributed to higher conduction along grain-boundaries.[140,142,151,157-159] O^{2-} grain-boundary conductivity is higher than in the bulk[160] but cation grain-boundary conductivities have not been reported.[139] However, cations are likely the main grain-boundary charge carriers as single-crystal and polycrystalline conductivities are not greatly influenced by oxygen partial pressure.[140,142,152] Grain-boundary conductivity is likely affected by Mg-depletion, which is suggested to result in a negative core enriched in V_{Mg}''

compensated by a positive space-charge layer composed of $Al^{\bullet}_{Mg}$.[86,89,161,162] Surface conduction also contributes to conductivity, with protons hopping along surface-adsorbed hydroxyl ions being the main charge carriers at low temperature and high relative humidity in porous oxygen-sensor compacts.[163,164] Conductivity is also highly dependent on porosity, grain size, and impurities.[154]

2.2.6 Optical Properties

Spinel has a wide transmission window (~190 nm < λ < 6000 nm) that is limited by the UV and IR absorption edges (Fig. 2.4). IR transmission decreases starting at ~4-5 μm and reaches zero by ~7 μm, with an IR absorption edge up to ~1 μm lower for Al_2O_3-rich compositions.[4] Some transparency is also exhibited in the microwave range (70 GHz–105 GHz, 2-4 mm).[12]

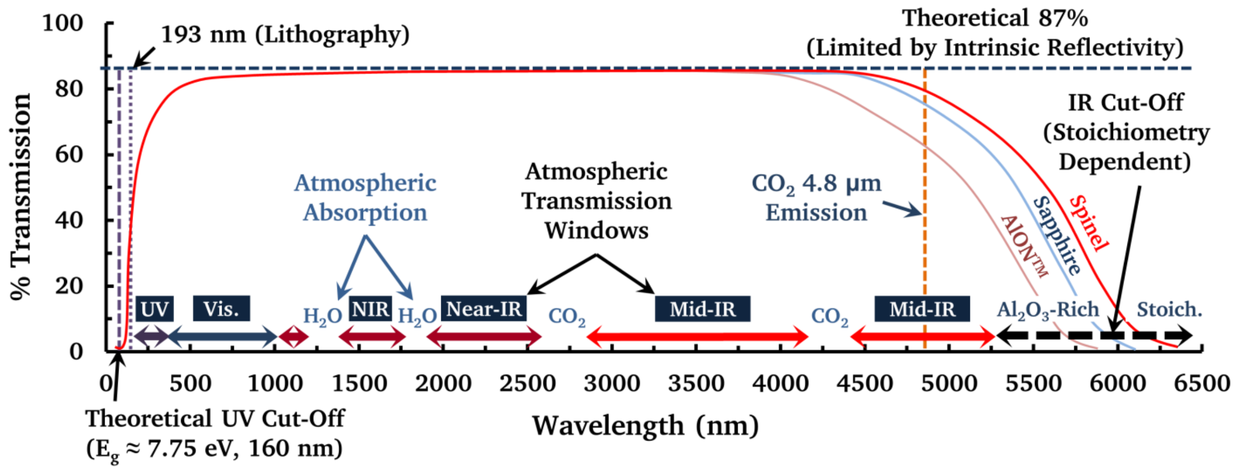

Fig. 2.4: Typical transmission spectrum for transparent polycrystalline spinel.[4,15,165]

The total intensity transmitted through a window is the total forward transmittance (TFT, I_T), while that within a narrow cone (3°–5°) along the incident direction is the in-line transmittance (ILT, I_{ILT}), the difference between the two is the diffuse transmittance (I_{DT}), or forward scatter. The ILT best characterizes the intensity and accuracy with which the spatial relationship and resolution of image details are transmitted. However, most optical imaging applications require high ILT along a narrower cone and the real in-line transmittance (RIT) is defined for an aperture of ~0.5°.[24] In highly transparent compacts with an RIT of >95% theoretical (or >82.2% measured), transmittance becomes nearly thickness-independent as in window glass, with the term translucent used for RIT <95%.[24,61,166] Three main factors reduce transmittance within the transmission window: (i) reflectance (R), (ii) scatter (S), and (iii) absorptance (A) (Fig. 2.5). The relationship between incident radiation of intensity I_0 and transmitted radiation I_T is given by:

$$I_0 = I_T + R + S + A = 1 \tag{2.10}$$

For stoichiometric spinel at $\lambda = 532$ nm, the specular reflectance from a single surface (R_{S1}) is ~7%, implying a minimum theoretical reflectance (R_{S2}, two surfaces including multiple reflections) of ~13% for a window, limiting the maximum theoretical ILT without anti-reflective coatings to ~87%.[23] The diffuse reflectance (R_D) can be minimized by ensuring planarity and smoothness. The refractive index (n) and reflectivity increase with decreasing wavelength, significantly reducing the theoretical ILT below $\lambda \approx 200$ nm.[25]

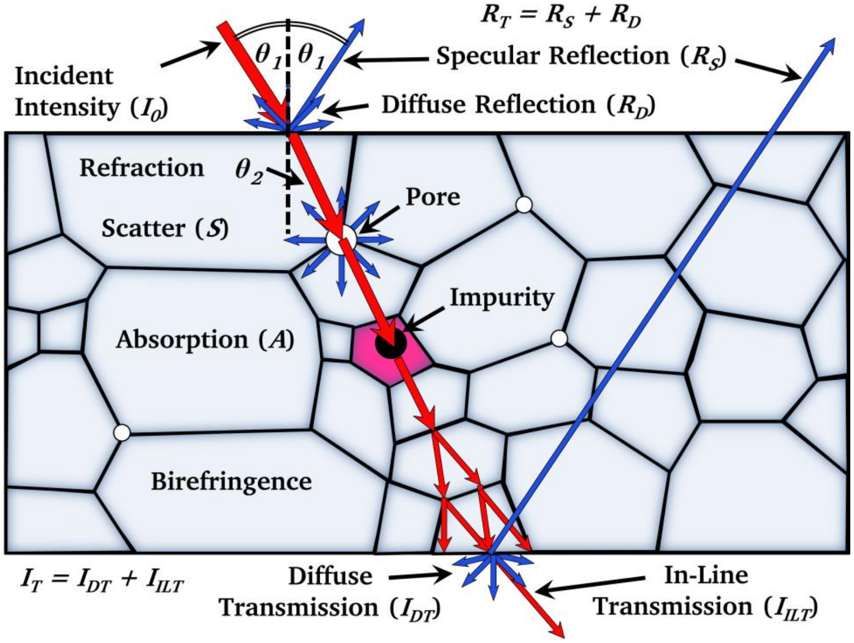
$R_T = R_S + R_D$
Specular Reflection (R_S)
Incident Intensity (I_0)
θ_1
θ_1
Diffuse Reflection (R_D)
Refraction
θ_2
Pore
Scatter (S)
Impurity
Absorption (A)
Birefringence
$I_T = I_{DT} + I_{ILT}$
Diffuse Transmission (I_{DT})
In-Line Transmission (I_{ILT})

Fig. 2.5: Light transmission through a polycrystalline spinel compact.

Scatter is thickness-dependent and caused by phases with different n (pores, precipitates, and impurity and additive phases), regions with variable n (variation in stoichiometry and stress), and variation of n along different crystallographic directions. Light-scattering models are mostly based on Mie theory,[6] with approximations dependent on the size of the scattering center (d) relative to the wavelength (λ): (i) Rayleigh-Gans-Debye scatter ($d > \lambda$), (ii) Mie scatter ($d \approx \lambda$) and (iii) Rayleigh scatter ($d < \lambda/10$). Scatter scales to d^2 for Mie scatter and to d^6/λ^4 for Rayleigh scatter.[25,67] Porosity is a main source of scatter in spinel, the most detrimental being pores the size of the transmitted wavelength.[167] Using a numerical Mie model[168] at λ = 600 nm, 0.1% porosity (1000 parts per million, ppm) of 400 nm diameter pores reduces theoretical ILT to nearly zero for an 0.8 mm thick polycrystalline compact with n = 1.76.[167] Even 0.01% (100 ppm) of 400 nm diameter pores at λ = 600 nm or of 40 nm pores at λ = 200 nm reduces theoretical ILT to ~50% for a 1 mm thick spinel compact.[24,169] For imaging applications, only very thin windows tolerate smaller pores (<100 nm), even at longer IR wavelengths.[170] Reducing the pore size by half reduces Rayleigh scatter by one order of magnitude[6] and thus pore concentration and size reduction are one of the main goals of fabrication. Scatter also occurs due to inclusions, impurity phases, and cracks.[1,4,51] Grain boundaries and point defects contribute minimally to scatter at visible and IR wavelengths due to the small thickness (<5 nm) and size, respectively.[167]

Another source of scatter in spinel is intrinsic birefringence (IBR, ~50 nm/cm) at UV wavelengths due to the refractive index difference along the more densely-packed <111> unit cell cube diagonals versus the <001> cube edges.[25,35] However, IBR is ~0 in polycrystalline compacts.[35] Stress birefringence (SBR) also occurs due to local strain variation and is in the order of ~5 nm/cm.[35] The refractive index of spinel does not change significantly with λ, as indicated by the low Abbé number (~60),[25] resulting in reduced chromatic aberration.[10] Its variation with temperature is also low (dn/dT ~3×10^{-6} K^{-1} from 3 to 5 μm).[10]

Absorption in spinel arises from several sources and even ppm volume fractions of absorbing centers can lead to opacity in thicker compacts. As for scatter, absorption is thickness-dependent and obeys a Beer-Lambert relationship (Eq. 2.11). In the case of scatter, the absorption coefficient (α) is dependent upon a volume fraction and a scattering cross-section. The sensitivity of transmittance to ppm volume fractions of scattering or absorbing centers is arguably the main challenge of transparent spinel fabrication.

$$I_T = I_0 e^{-\alpha t} \tag{2.11}$$

2.2.7 Mechanical Properties

The fracture toughness of spinel ranges between ~1.4-2.0 MPa·m^{½},[7,171-173] with an apparent Hall-Petch dependency for coarse grains (~ >50 μm).[7,39] Lower toughness has been correlated with inter-granular fracture, predominantly in coarse-grained microstructures,[7] probably due to grain-boundary embrittlement by residual LiF, impurities, and residual stress (Fig. 2.6).[1] Somewhat in contrast, coarse-grained microstructures exhibit limited *R*-curve behavior due to frictional grain-bridging and grain-wedging.[172] Thus, strengthening grain boundaries should improve toughness. Strength decreases for inter-granular fracture that persists in coarse-grained microstructures.[114,171,173] In fact, weak boundaries of large grains have been proposed to serve as critical surface flaws.[173,174] Porosity and second phases do not necessarily serve as limiting flaws in highly-transparent compacts as they demand <0.01% porosity and second phases typically smaller than ~50 nm.[8] Coarse-grained microstructures have long been recognized as a source of lower strength, but fine-grained, highly-transparent spinel compacts have only recently been produced.[60,64,175,176] Microstructure refinement exhibits significant hardness increases for grain sizes less than ~1 μm and a Hall-Petch relation is observed.[173,174,177,178] Despite the relevance to projectile erosion during penetration,[10,177] the mechanism for hardness changes in spinel is not known.[179] Nevertheless, reducing grain size is one of the main goals of transparent spinel processing. However, for transparent armor, cost outweighs small additional hardness gains associated with fine grain sizes and sizes in the hundreds of microns are often acceptable.[4] Relatively little is known about the effect of grain size on ballistic performance due to the complexity of failure.[180] Spinel is susceptible to moisture-assisted crack growth, but the effect is significant mainly for coarse-grained microstructures.[7] It appears that no slow crack growth studies for single crystals exist. Nonetheless, the results demonstrate the importance of grain boundaries in dictating strength.

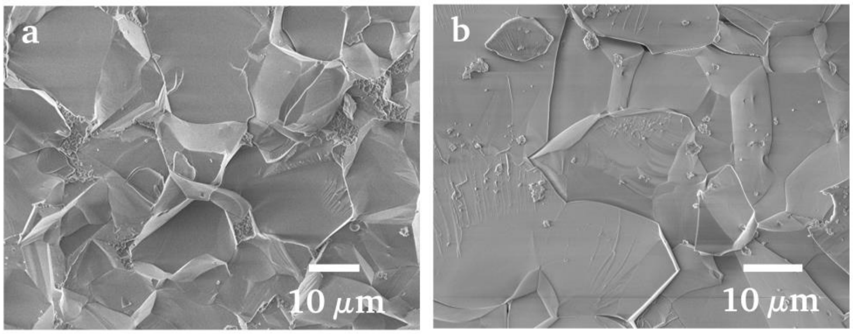

Fig. 2.6: Fracture surfaces of spinel showing mixed-mode inter- and trans-granular fracture for hot-pressed (a) lower-purity powder and (b) higher-purity powder, without additives.[1] With LiF addition, fracture becomes predominantly inter-granular.

2.2.8 Physical Requirements

Spinel physical requirements depend on the application. Requirements for transparent armor are high ILT in the visible range, compatibility with near-IR (0.4-0.92 μm) night-vision and thermal imaging systems,[10] low areal density, high hardness, multi-hit capability, and low cost due to the volumes required.[14,23] In the case of spacecraft windows, fracture strength and toughness are more important.[7] Requirements for IR windows and domes are high RIT in the atmospheric windows from the UV to the mid-IR, possibly transmittance in the microwave region,[13] low absorption near the IR absorption edge and especially at 4.8 μm, low emissivity, flexural strength, impact and erosion resistance, thermo-mechanical stability, low dn/dT, and thermal shock resistance.[10,23] Military requirements are increasingly calling for multi-spectral capability[14] and tri-mode multi-spectral seeker domes satisfying additional RF shielding requirements[181] have been successfully fabricated.[165,182,183] Transmittance requirements are most stringent for imaging applications, with sensor windows requiring error of $<1/10$ of λ over the aperture size.[10] UV lithography components require high RIT, especially near the UV absorption edge but less stringent mechanical properties. UV and IR absorption edges need to be pushed towards theoretical energies and absorption near the edges lowered to enable UV-lithography and increased demands for IR-targeting applications.[35] A combination of low Abbé number combined with a high refractive index compared to glasses can enable miniaturized lenses[10] and refractive index variation with stoichiometry may enable flat graded refractive-index lenses. Properties of polycrystalline spinel compacts are summarized in Table 2.3.

Table 2.3: Physical Properties of Transparent Polycrystalline Spinel.

Property	Value
Melting point (°C)	2105°C–2135°C[19,165,182]
Lattice parameter (a, 3.0 > x > 1.0, Å)	8.797–8.808[22]
Stoichiometry range max. (mol% Al_2O_3, $MgO{:}xAl_2O_3$)	38.2(1996°C)–90.1(1994°C), 0.6–9.1[72]
Stoichiometry range in practice ($MgO{:}xAl_2O_3$)	1.0–3.0[4]
Max. solubility Al_2O_3 in MgO (mol%, 2269K)	9.4[72]
Max. solubility MgO in Al_2O_3 (mol%, 2073K)	0.012[72]
Density (g/cm^3)	3.58 g/cm^3 [23,165]
Young’s modulus (GPa)	193,[193] 260-310[72,165]
Shear modulus (GPa)	192[165]
Poisson’s ratio	0.26[23,165]
Hardness Knoop (GPa, 200 g), (GPa, unspecified 500°C)	1.038,[13] 1.450–1.650[8,23,165]
Hardness Vickers (GPa, 2.5 Kg, 5 Kg, 10 Kg)	12.0–16.8[8,23,174]
Flexure strength (MPa)	70–250,[8,10,23,165,183] 470,[174] (~500)[8,64*]
Fracture toughness ($MPa\sqrt{m}$)	1.4–2.0[23,165]
Dielectric constant (ε, 1 KHz – 1 MHz)	9.19,[23] 8.2[19]
Loss tangent (δ, 1 KHz, 1 MHz, 35 GHz)	0.00025,[19] 0.0002,[19] 0.00022[23]
Refractive Index (n, 532 nm)	1.7108[165]
Abbé number	~60[10,25]
Refractive index homogeneity ($dn/d\lambda$, >3” diameter)	$<5\cdot10^{-6}$ [13]
dn/dT (3-5 μm, 3 GHz) 10^{-6}/K	~3, 20[10,23,39]
Band gap (eV)	7.7^{SC} [35]
Absorption coefficient (3.39 μm, 532 nm, 193 nm, cm^{-1})	0.018,[10] 0.4,[165] 2.7[35]
Absorption coefficient (5 μm, 25°C, 250°C, 500°C, cm^{-1})	0.4, 0.7, 1.3[165]
Intrinsic birefringence (IBR, 193 nm, 365 nm, nm/cm)	51^{SC}, [25,35] 3.6,[25] <2$^{PC(193\ nm)}$ [25,35]
Stress birefringence (SBR, 193 nm, nm/cm)	~3^{SC}, [35] ~5^{PC} [35]
Transmission Window (μm)	~0.19–7.0[34,165]
Theoretical in-line transmittance (window, 532 nm)	87%,[165] typical 70–84%[8]
Emittance (2000K, 1 mm thick)	~0.9 (6-10 μm), ~0 (<3.5 μm)[165]
Thermal expansion (30-200°C, 25°C–1000°C, 30°C–1400°C, range not given, K^{-1})	$6.97\cdot10^{-6}$,[13] $7.90\cdot10^{-6}$, ~$8\cdot10^{-6}$, [23,165] 5.6-$5.9\cdot10^{-6}$ [23,39]
Thermal conductivity ($T_{Amb.}$, W/m-K, 25°C)	13.4,[39] 14.6,[23] 14.7,[165] ~16,[23] 25[10,13]
Thermal shock resistance (R’ = $\sigma(1-\upsilon)\kappa/\alpha E$, kW/m)	1.1,[10] 1.4,[13] 1.9-2.1,[174] 1.9[165]
Chemical resistance	HF, H_2SO_4, HNO_3, NaOH[52,165]
Erosion (rain, 756 km/hr., 20 min, 2 mm drop size)	No damage,[165] High resistance[174]
Erosion (sand, 75 m/s, 3 mg/cm^2 loading, 38-44 μm)	No damage,[165] High resistance[174]

SC (single crystal), PC (polycrystal), all quantities stoichiometric unless indicated, *Unusually high value

2.3 Processing

This section introduces the key processing variables (Section 2.3.1), and describes the effect of powder synthesis (Section 2.3.2), green-body formation (Section 2.3.3), and particle-size characteristics (Section 2.3.4) on microstructure evolution (Section 2.3.5) and compact properties.

2.3.1 Key Processing Variables

Spinel is inherently difficult to sinter due to: (i) low oxygen lattice-diffusion requiring high sintering temperature, (ii) Mg/MgO volatilization causing stoichiometry variation and gradients, (iii) a propensity for coarsening possibly exacerbated by a high grain-boundary to surface-energy ratio, surface-energy anisotropy, and LiF additive, and (iv) extreme sensitivity to impurities, additives, processing parameters, and compact size. These issues accentuate the difficulty in attaining the near-theoretical density required for transparency. In addition, the multitude of fabrication variables combined with property variation with stoichiometry further complicates processing, and in turn understanding. The crux of transparent spinel fabrication lies in understanding the complexities of fabrication, and in particular of green-body formation and of interactions during sintering between material, microstructure, compact, and process variables, from the nanometer to the compact scale (Fig. 2.7). In particular, three variables are key to successful processing: (i) particle-size characteristics, (ii) stoichiometry, and (iii) impurities. Gross deficiencies in these variables cannot be compensated for by adjusting processing parameters and achieving transparency entails controlling them throughout processing. Post-treatment and finishing are not described here, but grinding and polishing can be the most time-consuming and expensive step for components like missile domes[181] and new methods are being explored to reduce costs.[8]

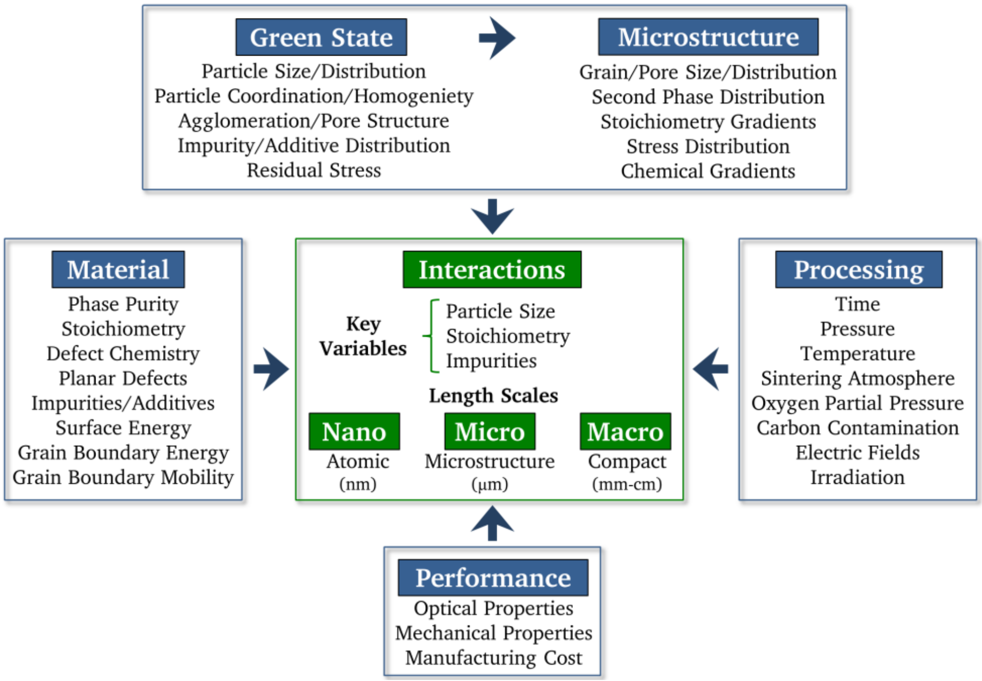
Green State
Particle Size/Distribution
Particle Coordination/Homogeniety
Agglomeration/Pore Structure
Impurity/Additive Distribution
Residual Stress
Microstructure
Grain/Pore Size/Distribution
Second Phase Distribution
Stoichiometry Gradients
Stress Distribution
Chemical Gradients
Material
Phase Purity
Stoichiometry
Defect Chemistry
Planar Defects
Impurities/Additives
Surface Energy
Grain Boundary Energy
Grain Boundary Mobility
Interactions
Key Variables
Particle Size
Stoichiometry
Impurities
Length Scales
Nano
Atomic
(nm)
Micro
Microstructure
(μm)
Macro
Compact
(mm-cm)
Processing
Time
Pressure
Temperature
Sintering Atmosphere
Oxygen Partial Pressure
Carbon Contamination
Electric Fields
Irradiation
Performance
Optical Properties
Mechanical Properties
Manufacturing Cost

Fig. 2.7: Fabrication and Key Variables.

2.3.2 Powder Synthesis

Spinel has been synthesized from a wide variety of precursors (metals, oxides, hydroxides, chlorides, nitrates, carbonates, sulfates, and alkoxides) and methods (mechanical alloying, freeze drying, spray drying, solid-state sintering, sol-gel, hydrothermal, co-precipitation, gelcasting, flame-spray pyrolysis, self-propagating high-temperature synthesis, chemical vapor deposition, atomic layer deposition, and plasma spray).[4,19] Acceptable powders for transparent spinel fabrication typically require nanometer-sized particles with a high surface area (>10 m^2/g)[45] to provide a high driving force for sintering. In addition, it is desirable to have a narrow particle-size distribution, minimal agglomeration,[45] adequate flow properties,[8,34,45] stoichiometry control,[1,77] minimal impurities, and cost matching the intended application. However, powder properties are difficult to characterize in practice. Particle-size analysis by laser scattering can be flawed due to inadequate dispersion and shielding of smaller particles by larger ones,[45] and microscopy samples only small volume fractions, possibly missing large inclusions. Stoichiometry is difficult to quantify by chemical analysis and XRD with an accuracy that reflects the processing sensitivity to it.[1] Volatile impurities such as carbon, nitrogen, and sulfur are difficult to quantify and are often not quoted by suppliers.[1] These issues make it difficult to pinpoint problems caused by starting powders that occur later during processing.[55]

2.3.3 Green Body Formation

The green-body state determines the sintering activity and it is profoundly influenced by particle size characteristics.[45] The goal of synthesis, pre-treatment, and shaping is obtaining green bodies composed of fine, uniformly-sized particles with high coordination and homogeneity.[45] Achieving this may require involved particle sizing, such as centrifugation, filtration, and sedimentation.[45] Perfect packing of spheres yields theoretical pore-size distributions of ~1/5th of particle size. Yet even with optimal processing pore sizes are at least twice that, likely reflecting particle packing resembling GB1 in Fig. 2.8.[45] Nevertheless, defect-free, homogeneous, highly-coordinated green bodies with narrow pore-size distributions like GB1, when obtained with high-purity nano-powders, allow sintering forces alone to achieve high densification (>95%) at temperatures up to 200°C lower than less optimal bodies.[45] With additional pressure, full density has been reached without additives while exhibiting high transparency and nanometer-sized grains.[45] The best results have been obtained using flame-spray pyrolysis powders, whose better flow properties[34] likely contribute to higher coordination and smaller pore-size distributions.[45] Consolidation methods yielding the best results are shaping from aqueous or organic slurries or colloidal suspensions using organic dispersants combined with slip or gel-casting.[6,45] However, these methods require drying, solvent debinding, or lengthy thermal cycles to ensure complete, defect-free organics outgassing.[13,34] Optimal dispersion of binders, dispersants, and sintering additives, typically added during milling or wet processing, is also essential.[36,45] Alternatively to wet processing, high solids-loading slurries have been spray or freeze-dried[184] into better-flowing powders consisting of soft-agglomerate granules,[34] which have been dried and cold-pressed into acceptable green bodies.[34] However, cold-pressing or CIP require high loads (~100-500 MPa) to achieve high green densities, and cold-pressing introduces density gradients due to friction from die walls. Acceptable green bodies have also been obtained by additionally milling or freeze-drying more agglomerated powders followed by dry or wet consolidation.[45]

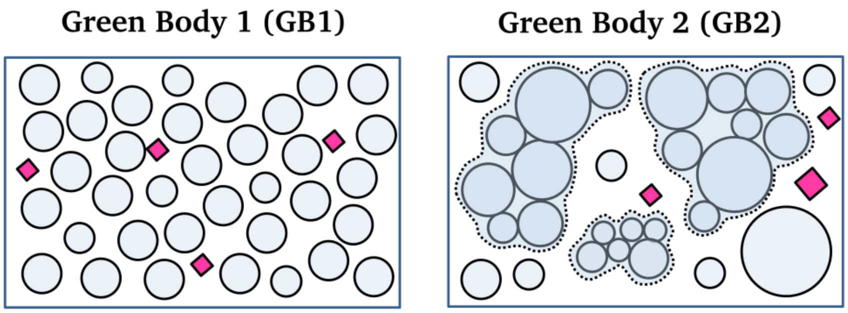

Fig. 2.8: Green bodies made using two different powder/processing routes (pink diamonds represent impurities or additives): (GB1) fine, narrow particle-size distribution powder leading to narrow pore-size distribution, and (GB2) agglomerated, wide particle-size distribution powder leading to wide pore-size distribution, large inter-agglomerate pores, and inhomogeneous additive dispersal.

2.3.4 Particle Morphology

Smaller particles result in smaller green-body inter-particle pores and sizes <50-60 nm decrease PS/HIP temperature <1400°C, improving compact visible and near-IR transmittance and mechanical properties.[45] However, small size and high surface-area increase susceptibility to agglomeration from weak attractive forces, such as friction-induced charging during dry-milling or hydrogen-bonding during aqueous processing.[8,45,49] High surface-area powders also provide more residence sites for adsorbed gases, water, and impurities and may be more susceptible to chemical reactions.[55,185] Nanometer-sized powders are also more expensive, are cumbersome to handle, require large volume reduction, and are difficult to disperse and to sieve to uniform particle-size.[34] In addition, compacts HP/HIPed with nanometer-sized powders (<50 nm) exhibit reduced UV-transmittance and higher refractive-index variation due to a concentration of nanometer-sized pores (<400 nm) that is one order of magnitude higher than for similarly-made compacts using coarser powders (~70-120 nm).[45,170] A balance between particle-size, agglomeration, and attaining high green-body particle-coordination and homogeneity leads to an optimal particle-size.[45] The lower size-limit with HP/HIP using high-purity powders without additives for maximum transmission at low HIP temperatures (<1300°C) and fine grain-size (<500 nm) with current technology is near ~55 nm.[45] However, even with careful processing, 50-200 ppm nanopores have been observed to survive HIP up to 1700°C.[45] For lower-cost, high-volume applications, lower purity powders, or high additive contents, the optimal size for HP or

HP/HIP is perhaps >70-120 nm.[1,45,49] Even larger particle or aggregate size (>1-10 μm) may be desirable as coarser powders attain closed porosity at higher temperatures and enable increased outgassing of volatile impurities and additives.[186]

Agglomeration is the most detrimental powder-size characteristic as inter- and intra-agglomerate pores are frequently orders of magnitude larger than intrinsic crystallites (Fig. 2.9).[45,186] Dense agglomerates differentially sinter; enlarging inter-agglomerate porosity, inducing stresses that can cause cracking, and forming solid skeletons (even during calcining) that limit particle re-arrangement during consolidation and sintering.[185] These can be difficult to remove without resorting to higher pressures or temperatures, where excessive grain growth occurs, and at worst impossible to remove.[185] In addition, lower-temperature sintering and tortuous diffusion paths in dense agglomerates trap volatile species.[184] Some of these features result in optical defects such as pore clusters,[34] large impurity/additive phases,[1] and microstructural inhomogeneity.[186] Agglomerates are best dealt with before green-body formation, and are typically broken down by mechanical milling, ultrasonic or acoustic methods, or removed by sieving.[45] The best case, although difficult to achieve in practice, is forming soft agglomerates that can be broken by sintering stresses alone.[34]

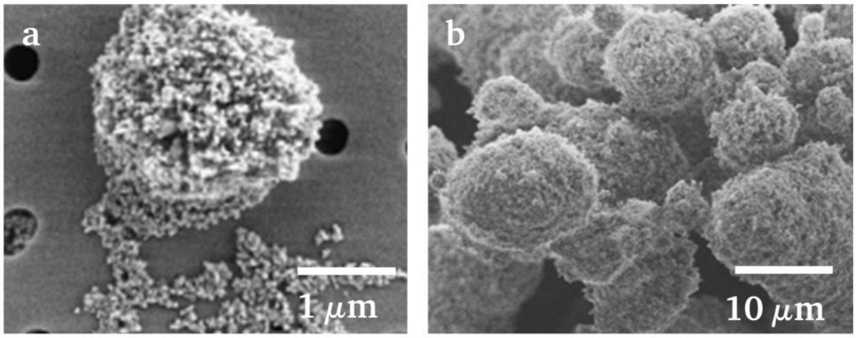

Fig. 2.9: Agglomerates in (a) synthesized,[45] and (b) commercial sulfate-derived powders.

Wide particle-size distributions are also detrimental and result in wide pore-size distributions in green bodies, making it impossible to tailor sintering regimes that close all pores simultaneously.[186] They also exacerbate Ostwald ripening and microstructural coarsening. Conversely, narrow particle-size distributions allow higher green-body coordination and homogeneity, lower sintering temperature, and similar-sized particles have similar driving forces for grain growth, resulting in finer-grain size.[45,186]

2.3.5 Microstructure Evolution

Microstructure evolution during sintering is strongly affected by the green-body state, and also by stoichiometry, impurities, additives, and processing parameters (Sections 2.4-2.6). Particle re-arrangement in the initial sintering stages is inhibited by green bodies like GB2 in Fig. 2.8 and aided by liquid phases (Section 2.5.2) and pressure (Section 2.6.2). Higher surface and vapor transport compared to bulk transport in initial stages result in coarsening, which is exacerbated by green bodies like GB2 and LiF addition, and inhibited by high heating rates (Sections 2.5.2, 2.6.1, 2.6.4). Coarsening is also strongly affected by interface energies. The driving force for sintering is the reduction of excess interfacial energy[186] which is accomplished by transforming surfaces into grain boundaries (resulting in densification), or by reducing surface area by coarsening (without shrinkage);

$$\Delta(\gamma A) = \Delta\gamma A + \gamma\Delta A, \tag{2.4.1}$$

where γ is the interfacial energy and A is the interfacial surface area.[121] High surface energy drives both processes, but high grain boundary versus surface energy favors coarsening and also makes it less favorable for grain boundaries to advance into pores.[121] Interface energies are in turn affected by stoichiometry, impurities, additives, and processing parameters (Sections 2.4-2.6).

Volatile species outgassing during initial and intermediate sintering stages is essential to obtaining transparency (Section 2.5) and is inhibited by differential sintering. Differential sintering occurs on a compact-scale as surfaces sinter more rapidly than the interior due to exposure to higher temperatures and shorter diffusion paths for densification-impeding volatile species to escape.[186] Compact-scale differential sintering traps volatile species in compact interiors, restricting grain size (Fig. 2.10), and if impurity concentration is high enough, scattering second phases form that display as a hazy central region in compacts.[1] Differential sintering is exacerbated by green bodies like GB2 in Fig. 2.8, high heating rates that engender high temperature gradients, large sample size resulting in longer diffusion distances, sintering atmosphere that can cause Mg/MgO loss, and any variable that accelerates sintering or lowers sintering temperatures (Sections 2.4-2.6).[186] Green bodies like GB1 in Fig. 2.8 attain closed porosity homogeneously, but do so at lower temperature and trap higher boiling-point volatiles.

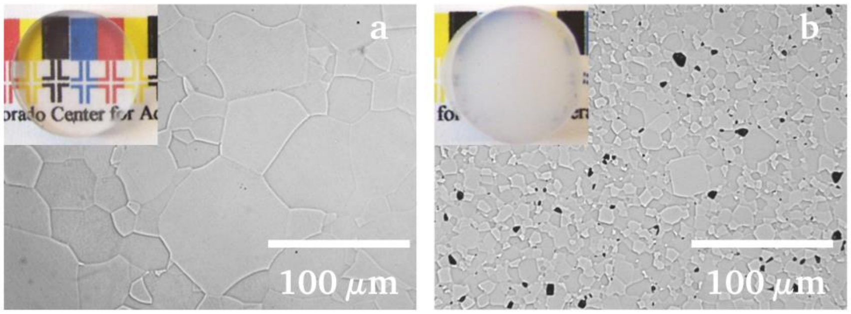

Fig. 2.10: (a) Optical microscopy image of microstructure of 2 mm thick hot-pressed stoichiometric spinel compact, and (b) similarly processed compact, but 4 mm thick and with pressure applied at a lower temperature.[1]

Once closed porosity is attained in the final stage of sintering, densification slows as the sintering stress decreases and mass transport is forced along slower grain boundary and lattice paths. As pore content and size diminish, the pinning effect of remaining porosity on grain boundaries decreases, leading to grain growth. Increasing kinetics with higher temperature (Section 2.6.1) or applied fields (Section 2.6.4) exacerbates grain-boundary mobility and grain growth and can cause pore occlusion, which is virtually impossible to remove. Thus, long sintering times or pressure (Section 2.6.2) are used to close remaining pores.

2.4 Stoichiometry

This section describes; the effect of stoichiometry on properties (Section 2.4.1), stoichiometry gradients (Section 2.4.2), stoichiometry-related defect chemistry (Section 2.4.3), and the effect of stoichiometry on grain growth (Section 2.4.4) and densification (Section 2.4.5).

2.4.1 Effect on Properties

Stoichiometry affects virtually every property of spinel and its spatial and temporal variation during sintering greatly increases processing complexity.[4,8,52,55,61,76,77,86,89,94,99,170,187-191] However, as the cubic structure and transparency are retained,[77] astoichiometry offers opportunities to vary properties[77] and may enable graded-property compacts.[10] Transparent components have successfully been made with $0.98 < x < 3.0$,[4,76,77] with MgO and Al_2O_3 precipitates (Fig. 2.11) typically observed beyond this range.[1,7,73,76] Precipitates scatter wavelengths on the scale of their size and of strain fields that surround them and they also affect mechanical properties.[1]

Mechanical properties comparable to stoichiometric compositions have been observed for $x = 1.2$.[77] However, other studies report increased hardness (up to $x = 2.0$),[192] fracture strength (up to $x = 2.0$),[192] and fracture toughness (up to $x = 1.3$[192] and $x = 2.0$[52,188]) for Al_2O_3-rich stoichiometry. Increased fracture toughness in one case was attributed to transgranular fracture and greater plasticity at grain boundaries,[188] whereas in another increased properties were attributed to hard Al_2O_3 precipitates and associated crack deflection and bridging.[192] However, other studies indicate Al_2O_3 precipitates and Al_2O_3-rich grain boundaries decrease mechanical properties due to residual stress and intergranular fracture,[7] and Al_2O_3-rich compositions exhibit substantial hardness decrease above $x > 2$.[177] Nevertheless, Al_2O_3-rich compositions ($x = 2$) appear less sensitive to microcracking and display higher transmission and fracture toughness compared to stoichiometric compositions when using reactive sintering and HP/HIP.[51,52] High transmittance for Al_2O_3-rich stoichiometry has also been obtained using reactive-sintering with PS/HIP ($2 < x < 2.5$), with opacity observed for $x < 1.8$.[58] However, with HP/HIP of precalcined powders, the best transmittance was noted for $x = 1.2$.[77] Although advantageous in yielding high transparency and fracture toughness in some instances, astoichiometry has major drawbacks of precipitation and scattering for MgO-rich compositions, and a lower IR absorption edge, densification rate, and hardness for Al_2O_3-rich compositions. Stoichiometric compositions likely still yield the best combination of densification and properties.[170]

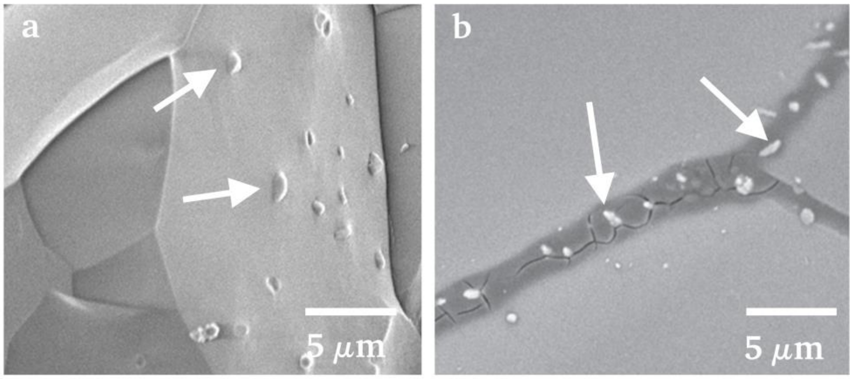

Fig. 2.11: (a) MgO precipitates (arrows) in $x \sim 0.995$ hot-pressed compact[1] and (b) Al_2O_3 precipitates (arrows) and Al_2O_3-rich grain boundaries in HP/HIP compact,[7] reproduced with permission.

2.4.2 Stoichiometry Gradients

Mg/MgO evaporation occurs preferentially at surfaces, causing stoichiometry gradients in grains,[76,86,89] and it is exacerbated by: (i) high temperature, (ii) low pO_2, (iii) reducing conditions, and (iv) LiF addition.[36,93] Stoichiometry gradients between grain boundaries and cores[76,86,89,139] may cause scatter at UV wavelengths as the lattice parameter decreases with Al_2O_3-rich stoichiometry according to Vegard's law,[76] implying a concomitant change in refractive index.[193] Differences in thermal expansion between Al_2O_3-rich boundaries and grain cores may also cause residual stress and grain-boundary embrittlement as Al_2O_3-rich stoichiometry is reported to have a lower coefficient of thermal expansion.[1,194] Preferential Mg/MgO loss at compact surfaces causes compact-scale stoichiometry gradients.[80,81] As Mg/MgO volatilization is compensated by oxygen vacancies [Eq. (2.8)], densification of the compact exterior is enhanced, exerting a backstress that opposes densification of the interior.[81] Interior densification is further inhibited by species diffusing along the slower paths of the densified exterior.[81] With pressureless sintering, by the time Mg/MgO loss leads to Al_2O_3-rich stoichiometry and exterior densification slows, there is already increased porosity in the interior, entrapped pores in the coarsened Al_2O_3-rich zone, and a gradient towards smaller grain size in the compact interior (Fig. 2.12).[81] In addition to porosity, transmittance may be further reduced by refractive index inhomogeneity due to the stoichiometry gradient. The microstructural features that distinguish this effect are obscured in later stages and for thinner compacts.[81] MgO volatilization can be reduced via pressureless sintering in air, embedding compacts in powder of similar stoichiometry, shielding with refractory foils, or introducing inert atmosphere once closed porosity is reached during vacuum sintering.

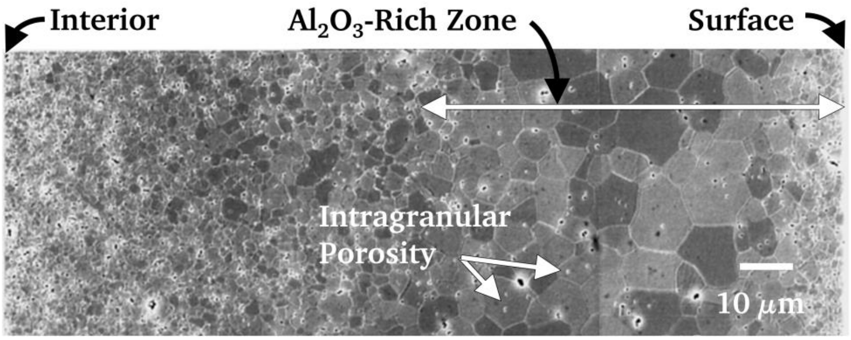

Fig. 2.12: Composite SEM cross-section of pressureless-sintered stoichiometric spinel compacts, reproduced with permission.[81]

2.4.3 Defect Chemistry and Grain-Boundary Mobility

Astoichiometry is especially relevant for interfaces, which are a key determinant of microstructure evolution. Al_2O_3-rich grain boundaries and triple junctions have been observed in polycrystalline compacts (Fig. 2.13a), even for MgO-rich compositions.[18,76,86,89,139] Stoichiometry gradients imply defect-chemistry gradients and suggest a space-charge layer surrounding a charged grain-boundary core (Fig. 2.13b). However, disagreement exists as to the charge-compensating defects.[76,86,89] Chiang and Kingery argued that in stoichiometric and Al_2O_3-rich compositions, anion defects were unlikely due to the close-packed anion lattice and cation interstitials were also unlikely as charge-compensation is expected by cation vacancies.[76,86] As anti-sites are the predominant intrinsic defects, only $Al_{Mg}^{\bullet}$ remain to account for Al_2O_3-rich boundaries. They suggested a positive space-charge layer enriched in $Al_{Mg}^{\bullet}$ adjacent to a negative grain-boundary core, assumed to consist of cation vacancies or oxygen interstitials, as these are more likely to reside there. Based on thermodynamic considerations, Nuns *et al.* also suggested a positive space-charge with segregated $Al_{Mg}^{\bullet}$ and assigned a negative grain-boundary core, but based on simulations[115] assumed it to be composed of V_{Mg}''.[162] For MgO-rich compositions, Chiang and Kingery again assumed a positive space-charge, this time occupied by $Al_i^{\bullet\bullet\bullet}$ to account for Al_2O_3-rich stoichiometry at the boundaries. However, Ting and Lu argued that charge-compensation by cation interstitials in MgO-rich compositions contradicted increased densification[189,195,196] attributed to $V_O^{\bullet\bullet}$.[50,81,104,147] Based on the Brouwer equilibrium diagram (Fig. 2.14a) they argued MgO-rich stoichiometry was charge-compensated by $V_O^{\bullet\bullet}$. Based on proton diffusion experiments, optical absorption, and density measurements, Okuyama suggested that both cation interstitials and $V_O^{\bullet\bullet}$ charge-compensate MgO-rich stoichiometry.[90]

Uncertainty also exists as to grain-boundary mobility variation with stoichiometry. Chiang and Kingery noted 10^2 to 10^3 higher grain-boundary mobility in MgO-rich compositions and decreasing mobility, after a slight initial increase, with increasingly Al_2O_3-rich compositions (Fig. 2.14b).[76,86] Reduced mobility was attributed to solute drag caused by segregated native cation defects. Uematsu *et al.* noted a large initial increase, followed by a decrease in grain-boundary mobility for increasingly MgO-rich compositions and a steadily increasing mobility for Al_2O_3-rich compositions.[197] Chiang and Kingery noted the discrepancy may be due to different experimental conditions; they used reducing H_2 atmosphere and packed compacts in powder of similar stoichiometry enclosed in molybdenum foil, restricting MgO loss and solute segregation, whereas Uematsu *et al.* used open H_2 atmosphere, where Mg/MgO volatilization occurs.[86,198]

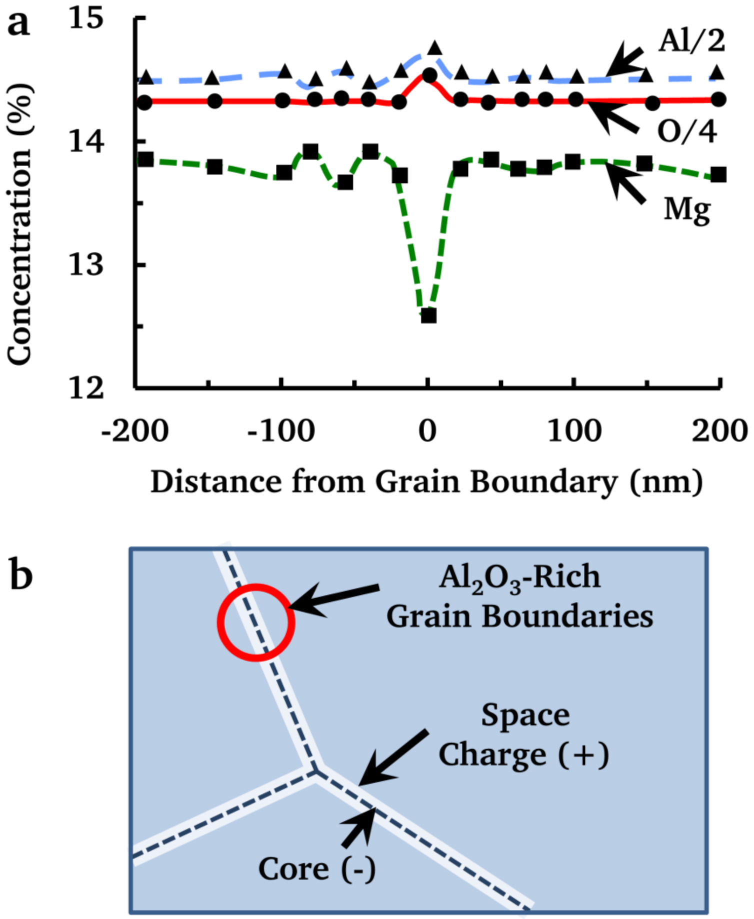

Fig. 2.13: (a) Atomic concentration versus distance from grain boundary in $x = 1.05$ PS/HIP spinel compact[89,162] (adapted with permission), (b) schematic of MgO-depleted grain boundaries.

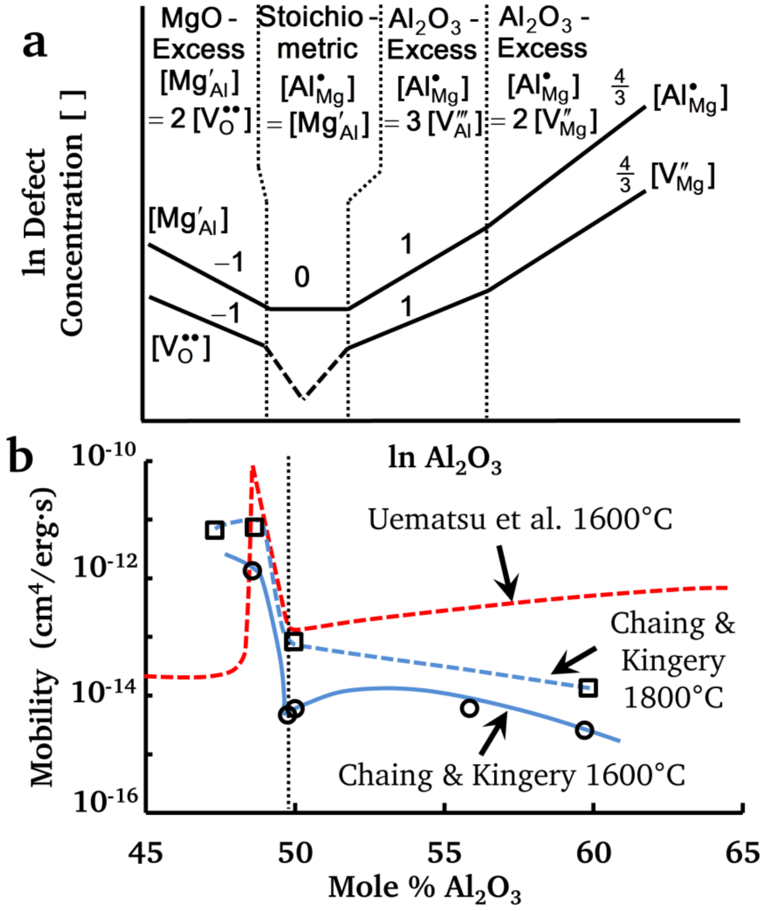

Fig. 2.14: (a) Brouwer diagram and (b) log grain-boundary mobility versus stoichiometry; adapted from Ting & Lu,[81] Chiang & Kingery,[76] and Uematsu et al.[197] with permission.

2.4.4 Grain Growth

Grain-boundary mobility and grain growth are related and abnormal grain growth has been observed in MgO-rich[76,80,86] and more prevalently in Al_2O_3-rich compositions.[47,59,76,80,81,86,196,199] However, it occurs primarily at surfaces, where Mg/MgO volatilization is greater.[76,80,86] MgO-rich compositions generally display smaller grain size, even though mobility is greater,[1,47,59,147,190,196] possibly influenced MgO precipitate drag. On the other hand, smaller grain size is also observed in stoichiometric compositions, where MgO precipitates are not expected.[77] These discrepancies, including those discussed in Section 2.4.2, highlight the sensitivity of spinel to small variations in stoichiometry, processing, and experimental conditions, and indicate a complex defect chemistry. In order for accurate comparisons, stoichiometry, defect chemistry, sintering atmosphere, Mg/MgO outgassing, and impurity content all need accurate spatial and temporal quantification. In the case of grain-boundary mobility and grain growth in ceramics, there is growing evidence that triple junctions and quadruple points play a determining role,[200,201] yet for spinel they are often entirely overlooked. The variation in interface energy with stoichiometry, with relevance to coarsening and densification, has also not been quantified. The remaining uncertainty as to the mechanisms occurring at interfaces requires further research as it precludes enabling greater control over densification and properties.

2.4.5 Densification

Stoichiometry strongly affects densification and deformation, and pressureless-sintered MgO-rich compositions densify one order of magnitude faster[94] and attain higher densities than Al_2O_3-rich compositions (Fig. 2.15),[94,104,189,195,196] attributed to higher oxygen vacancy concentration.[50,81,90,94,104,139,147,189] The effect of stoichiometry in pressure-assisted sintering is discussed in Section 2.6.2.

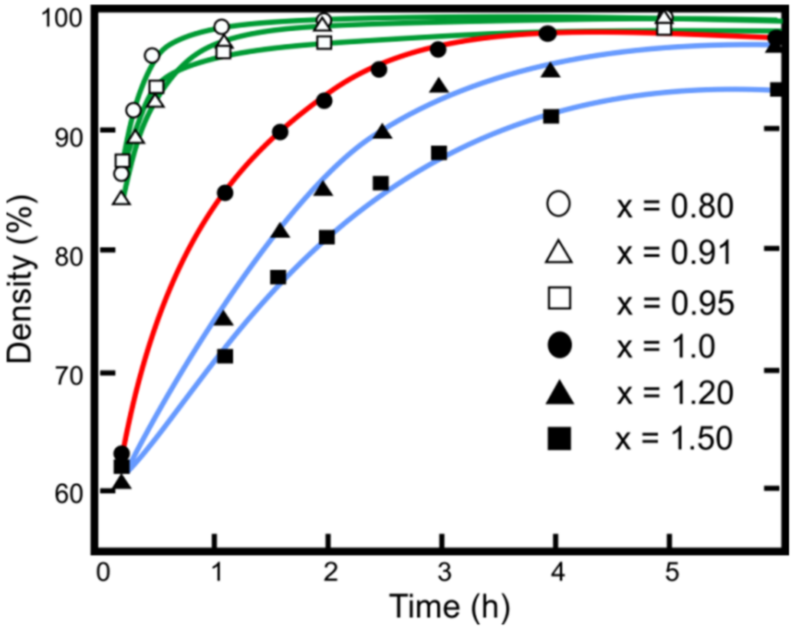

Fig. 2.15: Compact density as a function of time for pressureless-sintered compacts with various stoichiometries ($0.8 < x < 1.5$), adapted with permission.[94]

2.5 Impurities & Additives

This section describes the effect of impurities (Section 2.5.1) and sintering additives (Section 2.5.2) on processing and properties.

2.5.1 Impurities

Impurities affect interface energy and grain-boundary mobility, and are a key determinant of microstructure and properties. Even a few ppm impart color[24] and tens to hundreds of ppm can cause absorption over a broad range.[49,99,109,117,202] The tolerable impurity content depends on the specific impurity, processing, and compact size. Generally, starting powders require ~99.99% purity, <500 ppm cation impurities,[8,46] and removal of higher vapor pressure volatiles.[1] Even in thin compacts (<2 mm), as little as 0.1 wt% of remnant impurity or additive can cause opacity (Fig. 2.16).[1,8,46] Impurities are present in MgO and Al_2O_3 constituents, due to incomplete removal of precursors, binders, and processing fluids, and are inadvertently introduced during processing.[1] As temperature increases during sintering, adsorbed gases, water vapor, organic binders and dispersants, hydroxides, sulfates, sintering additives, and others outgas at different temperatures.[1] Their removal requires knowledge of outgassing behavior, as assessed by vacuum gauge,[12] thermal analysis,[1] or residual gas analysis.[1] Volatiles are more easily trapped when inhomogeneously distributed, present in dense agglomerates (GB1 in Fig. 2.8) or in green bodies that attain closed porosity at lower temperatures (GB2 in Fig. 2.8), in which case powders may need to be pre-coarsened to reduce sintering activity.[1] Incomplete volatile impurity removal is exacerbated by high heating rates, insufficient holds, differential sintering, and larger compacts.[1] Volatile impurities are also trapped by pressure application, use of sintering aids, and applied electric fields, all of which lower densification temperature.[1,186] Vacuum sintering is beneficial in removing most volatiles, whereas air sintering allows formation of volatiles from organics, carbon, and sulfur, although it may result in swelling as in Al_2O_3.[203] High volatilization temperature species like sulfates 1050°C-1250°C require careful attention to remove during pressure-assisted sintering.[1]

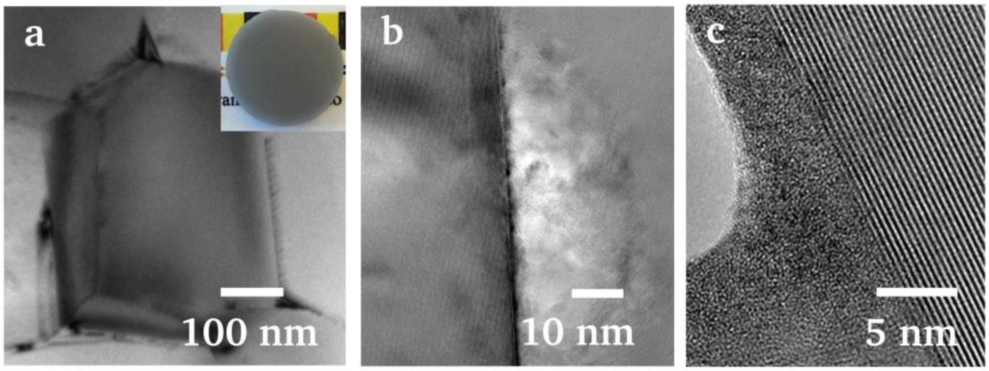

Fig. 2.16: Impurity phases causing opacity in 2 mm thick compact (inset) hot-pressed with high-purity spinel powder; (a) amorphous impurity (C,S,K) phase at grain boundary[1] and (b) decorated grain boundary.[1] (c) Amorphous phase at triple junction in HIP compact (all images TEM-BF).

Impurities (C, S, Si, Ca, Fe, K, Ti, Na, F, Li, lanthanide cations, and likely others) segregate at surfaces and later reside at grain boundaries.[1,18,57,76,86,89,135,139,204] Some studies suggest impurities have little effect on grain-boundary mobility and grain growth.[76,86] However, more recent studies indicate the opposite,[1,8] with some impurities restricting grain growth by solute drag[1] and others forming liquid phases or increasing surface diffusion and enhancing grain growth (LiF, CaO).[1,46] Impurities also modify interface energies. For example, TiO_2 increases the grain boundary relative to surface energy and exacerbates coarsening.[135] As the microstructure coarsens during sintering and grain-boundary area decreases, segregated impurities concentrate[176] and further affect grain-boundary mobility, microstructure evolution, and strength, and can cause fracture behavior to change from transgranular to intergranular.[1] In high concentration, impurities and additives form second phases, especially at triple junctions, pining grain boundaries, opposing densification if they have high vapor pressures, causing scatter and absorption, and reducing mechanical properties.[1] In addition, preferential surface volatilization causes impurity and additive gradients that result in compact-scale microstructure gradients (Fig. 2.12).[1] Impurities like LiF and some transition-metal cations appear to have some solubility in spinel and incorporate into the lattice, creating defects that affect diffusion and optical properties.[1,99] The effect of impurities on grain-boundary strength has not been systematically studied,[135] but additives like Y_2O_3 refine grain size, and increase hardness, flexure strength, and erosion resistance.[174] Composite compacts made with Si_3N_4 nanodispersoids have recently demonstrated enhanced mechanical properties while still retaining >70% IR transmittance.[205]

2.5.2 Sintering Additives

Sintering additives and impurities are inextricably linked, demonstrated by the need for additives with impure powders and the ability to sinter high-purity powders to transparency without them. Many sintering additives have been used to produce translucent or transparent spinel, including Li_2O + SiO_2,[43] CaO,[46,206] LiF + NaF,[204] LiF,[4,50,207] LiF + $CaCO_3$,[208,209] $AlCl_3$,[210] AlF_3,[19] Na_3AlF_6,[211] and B_2O_3.[59] However, LiF (~0.25-4 wt%) is the only sintering aid that consistently enables obtaining highly transparent spinel[212] and likely most commercially manufactured transparent spinel is made with LiF. LiF melts at ~850°C, wets spinel,[65] spreads over surfaces by capillarity,[65] and likely aids densification by particle rearrangement and liquid-phase sintering.[50,212-215] Near its melting point and in sufficient quantity, LiF reacts[216] with spinel and forms a eutectic with MgF_2 at ~740°C.[36,50,215,216] The products may enhance densification by solution re-precipitation (Eqs. 2.12 and 2.13).[50,209] Highly defected reprecipitated grains (Figs. 2.17 and 2.18) may have higher diffusion, enhancing densification.[50,217]

$$3LiF + MgAl_2O_4 \rightarrow LiF : MgF_{2(l)} + 2LiAlO_{2(s)} \tag{2.12}$$

$$MgF_2 + 2LiAlO_2 \rightarrow MgAl_2O_4 + 2LiF \tag{2.13}$$

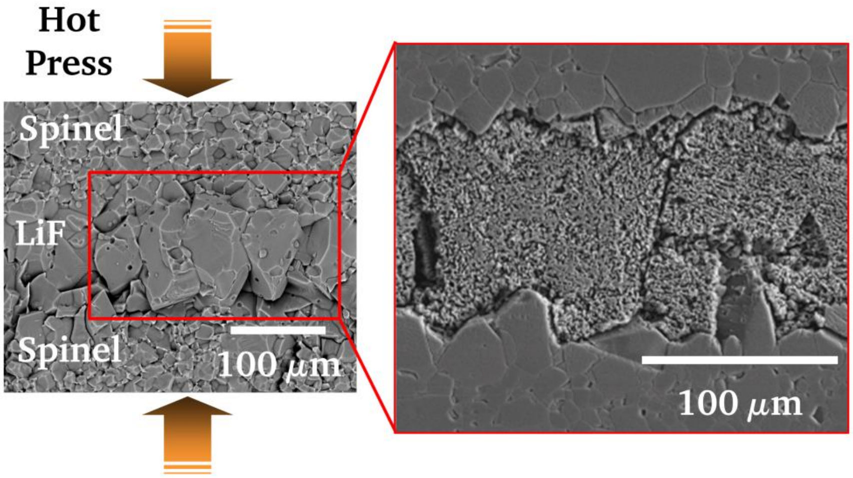

Fig. 2.17: Hot-pressed spinel/LiF/spinel sandwich structure and highly-defected grains revealed by etching.[212]

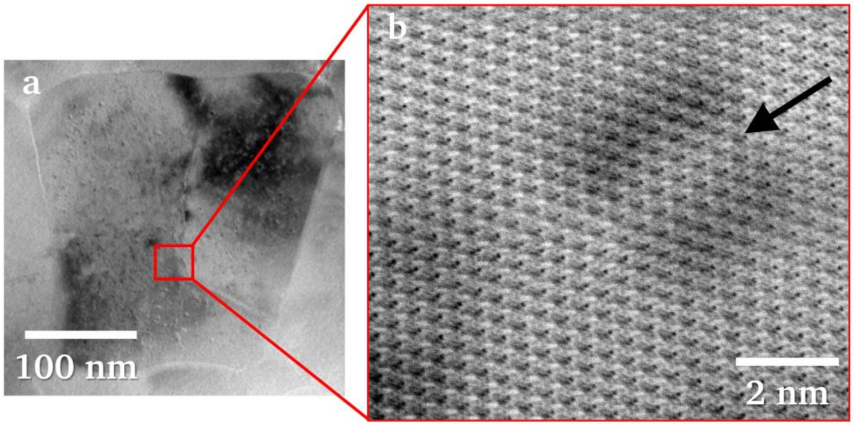

Fig. 2.18: HIP spinel compact with LiF; (a) Fluorine-rich xenomorphic grain (TEM-brightfield) and (b) coffee-bean contrast (arrow, STEM-ABF).[217]

LiF is unique in that lithium and fluorine are highly reactive and can substitute for magnesium and oxygen, respectively, with a valence difference of one. It has even been suggested that a requirement for sintering additives is the ability to create both cation and anion vacancies.[184] Auger electron spectroscopy,[204] optical absorption[218] secondary ion mass spectroscopy, transmission electron microscopy,[217] and sintering experiments[50] indicate lithium and fluorine are both incorporated in the lattice (Eq. 2.14).[215] If fluorine reacts with impurity cations (see below), then only lithium remains to create defects (Eq. 2.15).[65] The resulting oxygen vacancies may explain the ~200 kJ/mol[50,208] and ~200°C[65,208] lower densification activation energy and temperature, respectively. Enhanced formation of spinel during reactive sintering[57,65] has been partially attributed to vacancies caused by lithium incorporation in Al_2O_3 that allow higher cation diffusion.[219]

$$LiF \xrightarrow{MgAl_2O_4} Li'_{Mg} + 2Al^{x}_{Al} + 3O^{x}_{O} + F^{\bullet}_{O} + MgO_{(g)} \tag{2.14}$$

$$2Li \xrightarrow{MgAl_2O_4} 2Li'_{Mg} + 4Al^{x}_{Al} + 7O^{x}_{O} + V^{\bullet\bullet}_{O} + \tfrac{1}{2}O_{2(g)} \tag{2.15}$$

Fluorine forms volatile compounds with many impurity cations, which along with LiF have volatilization temperatures below that at which spinel compacts typically reach closed porosity, enabling their removal. LiF removes carbon,[65,220] sulfur, iron, calcium, and likely other impurities[1] in the vapor phase (Eqs. 2.16-2.18) and hence LiF addition must be tailored to impurity content. Less LiF is also required with alumina-rich powders.[61] LiF also lowers magnesium content[1,208] due to MgF_2 evaporation and perhaps Eq. (2.14).

$$LiF + C \rightarrow Li + (CF)_{(g)} \tag{2.16}$$

$$2LiF + 3(Mg, Al)SO_4 \rightarrow MgAl_2O_4 + 3SO_{2(g)} + O_{2(g)} + LiF_{(g)} \tag{2.17}$$

$$(2yz)LiF + zMe_xO_y \rightarrow yzLi_2O + xzMeF_{\left(2y/x\right)(g)} \tag{2.18}$$

LiF vaporizes between 1000°C and 1400°C and above 1200°C it coarsens spinel crystallites.[221] The slopes of the grain-growth curves in Fig. 2.19 indicate vapor-phase transport,[221] which requires the formation of magnesium and aluminum-containing volatile species, likely similar to that observed for LiCl.[219] Although coarsening is detrimental to densification, it is mitigated in pressure-assisted sintering, especially if surface diffusion or grain-boundary diffusional creep is enhanced[213] and as long as pores migrate as fast as grain boundaries.[184,185,222] Large or exaggerated grain size and lack of intragranular porosity with LiF indeed suggest enhanced surface or vapor-phase diffusion.[49,219] In addition, wetting, reaction with spinel, and defect creation suggest interface-energy modification. High surface energy favors pore-boundary attachment and may decrease the ratio of grain boundary to surface energy, favoring densification.[222] Atomic force microscopy and grain-boundary grooving experiments indicate surface mobility is increased and the interface energy ratio is altered by LiF.

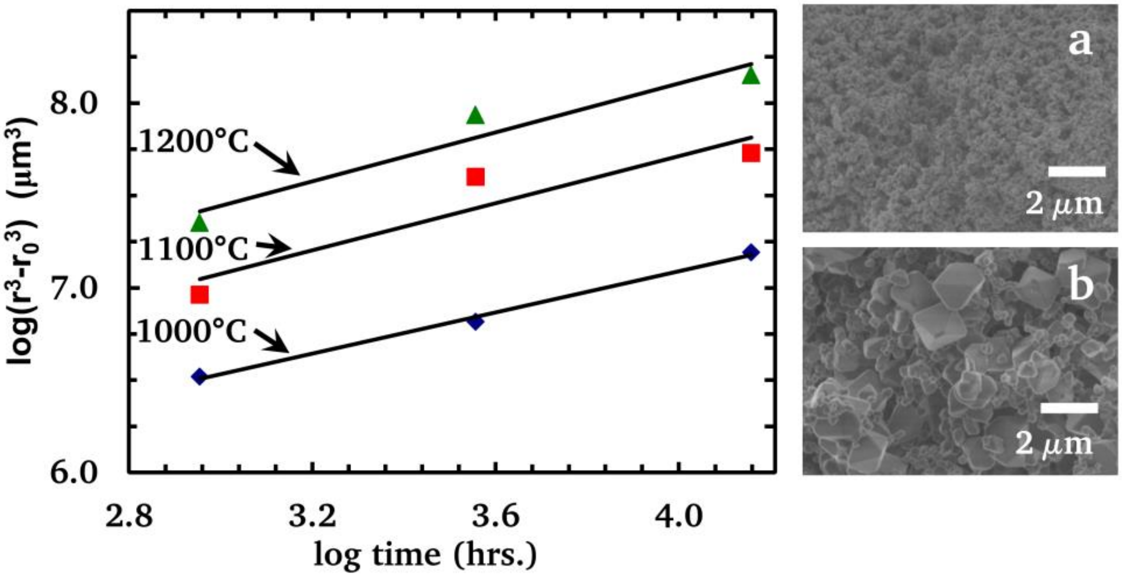

Fig. 2.19: Log-log plot of grain-size change versus time for air-sintered spinel powders with 1 wt% LiF at 1000°C, 1100°C, and 1200°C, SEM images of air-sintered spinel powders (a) without LiF and (b) with LiF.[221]

LiF also counteracts dark color observed in spinel compacts processed in graphitic furnaces by removing carbon and possibly color centers, as suggested by EIS studies.[3,18] To work effectively, LiF must be evenly distributed[213,216] and must leave the compact as it has a different refractive index. LiF can be trapped if too much is used (accelerating sintering)[61] and hold times are insufficient (especially in larger compacts), with high-sintering activity powders, or with pressure application forcing densification to lower temperatures.[1] Excess or trapped LiF accumulates at grain boundaries and triple junctions and results in scatter (Fig. 2.20)[1,53,57,207,214,216] and possibly restricted grain size.[49] Formation of lithium aluminate and/or Mg/MgO evaporation may also result in MgO-rich regions with poor transmission.[207,216]

In addition to coarsening and scatter, a major drawback of LiF is grain-boundary embrittlement and intergranular fracture (Fig. 2.21). Although LiF will likely continue to be used in bulk applications; where lower-cost powders are not required or for more stringent applications the trend is to minimize or eliminate LiF entirely. Figure 2.22 shows typical microstructures with and without LiF for various processing methods.

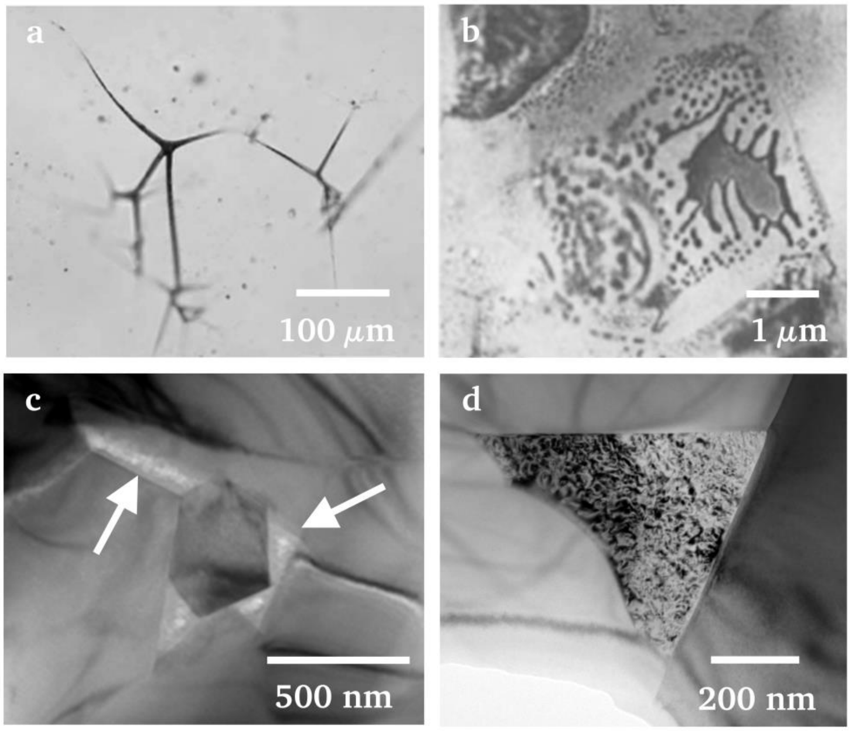

Fig. 2.20: Optical defects due to LiF (a) decorated grain boundaries,[53] (b) remnant liquid phase at grain boundaries,[214] (c) amorphous phase at triple-junctions (TEM), (d) typical mottled-contrast magnesium- and fluorine-rich phase at triple-junction (TEM).

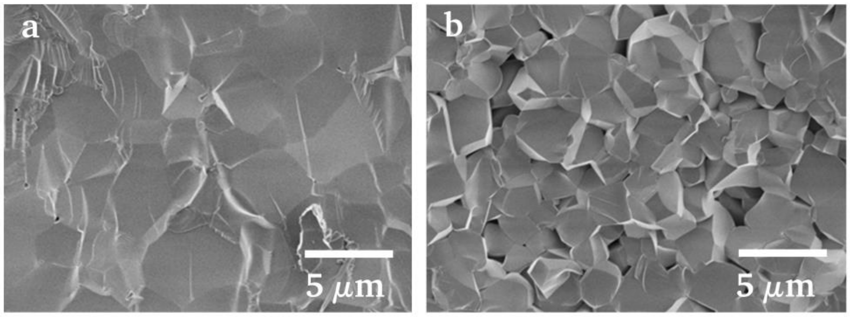

Fig. 2.21: Fracture behavior in pressureless sintered high-purity spinel compacts with (a) no LiF 1650°C 10 h (SEM), 1 wt% LiF 1650°C 10 h (SEM).[221]

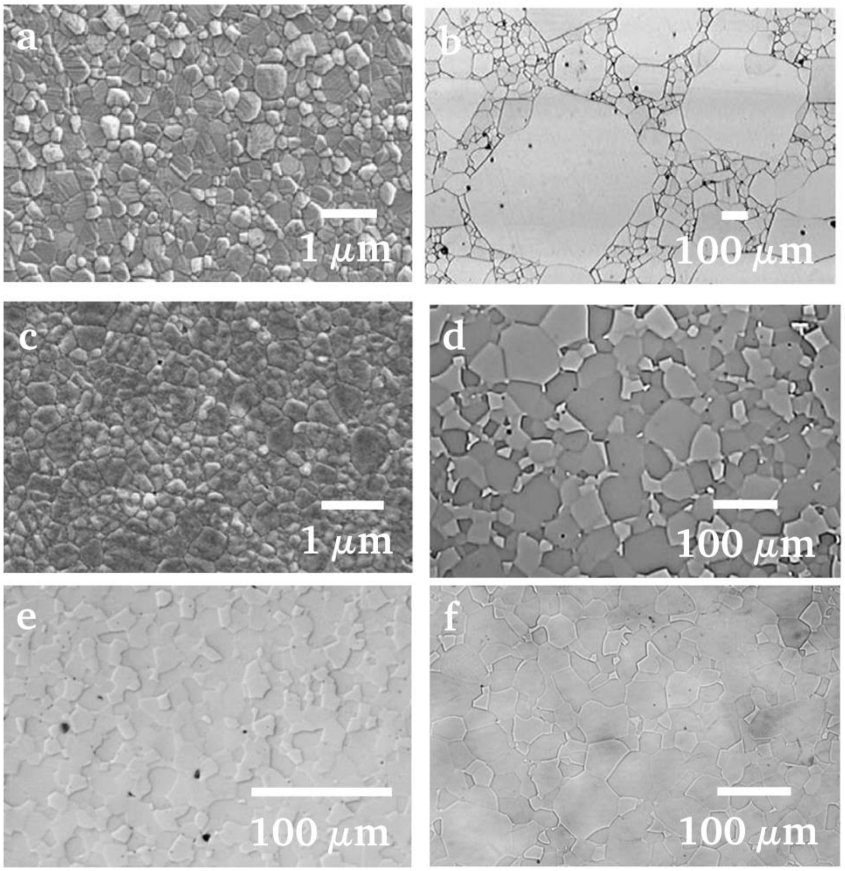
a
1 μm
b
100 μm
c
1 μm
d
100 μm
e
100 μm
f
100 μm

Fig. 2.22: Typical microstructures observed in translucent or transparent spinel; (a) HP/HIP,[60] (b) HP/HIP with LiF,[53] (c) SPS,[176] (d) SPS with LiF,[63] (e) HP,[18] (f) HP with LiF,[1] optical and SEM micrographs, reproduced with permission.

2.6 Processing Parameters

This section describes the effect of temperature (Section 2.6.1), pressure (Section 2.6.2), sintering atmosphere (Section 2.6.3), and electric fields (Section 2.6.4) on processing and properties and also discusses the causes of absorption (Section 2.6.5).

2.6.1 Temperature and Heating Rate

Temperature and heating rate are used to control microstructure evolution during processing.[1] High heating rates are beneficial in attaining temperatures where lattice and grain-boundary diffusion and diffusion-assisted dislocation motion and grain-boundary creep are active, avoiding the formation of densification-resistant sintering necks and grain coarsening by surface or vapor transport mechanisms. However, excessive heating rates provide insufficient time for volatiles removal and enhance compact-scale differential sintering.[1] High cooling rates can also be detrimental by causing residual stress and cracking. High sintering temperatures enable greater diffusion, allowing deformation mechanisms to become active, but are limited by degradation of spinel at ~1650°C in vacuum.[12] To avoid grain growth, carbon contamination, and Mg/MgO volatilization, the lowest possible sintering temperatures are used that still allow densification within reasonable times.

2.6.2 Pressure

Although transparent spinel was first made by PS,[43] to date only small, thin compacts made with high-purity nanometer-sized powders CP at high pressures have been PS to translucency using high temperatures or long sintering times with various atmospheres.[18,46-48] Attempts with larger compacts lead to cracking and opacity, possibly due to density gradients, differential sintering, pore coarsening, and swelling.[18] Consequently, spinel is invariably densified using pressure. Pressure provides an additional driving force for densification, driving mass transport from regions of higher compressive stress at interparticle contacts and adjacent to pores, to regions of lower stress.[186] Densification also occurs by plastic flow assisted by dislocation motion and diffusional creep along dislocations (Fig. 2.23) and grain boundaries.[87] Pressure lowers sintering temperature, allowing finer grain size.[186,223] In PS/HIP, high pressure (>150 MPa) is applied to remove the last few percent porosity at high temperatures (>1600°C), where grain boundary and lattice diffusion and deformation mechanisms are all active, although exaggerated grain growth also occurs. Very high pressures (2-5 GPa) and low temperatures (<800°C) have been used to obtain transparency while maintaining small grain size (<100 nm).[223] However, transparency is degraded by porosity and strain, the latter having low recovery at such temperatures.[38,223] Application of pressure at too low a temperature during sintering traps volatile species.[1,186]

Based on the wide range of stress exponents reported in creep experiments, opinions vary as to the dominant deformation mechanism and the underlying reason for strain softening and hardening. However, there is agreement that dislocations and grain boundaries are critical and oxygen diffusion is in some form rate-limiting. Dominant mechanisms have been attributed to slip,[224] dislocation glide,[191] dislocation creep,[225] grain-boundary sliding,[226,227] diffusional creep,[228] or some combination of these,[227] and control attributed to glide,[224] dislocation climb,[191,225] interface-reaction diffusion,[226] and oxygen-lattice diffusion.[227,228] Lack of consensus as to the dominant deformation mechanism is likely due to its variability, which depends on the densification method and also on the density and distribution of planar defects, grain size, stoichiometry, impurities, additives, temperature, pressure, and strain rate, which all vary during processing.[50,208,229,230] In hot-pressing, Nabarro-Herring diffusional creep dominates at lower temperatures (<1350°C) with a transition to dislocation glide at higher temperatures (> 1450°C).[230] During deformation, the effective pressure changes from an initially high value due to stress concentration at inter-particle contacts (early stage) to a lower value as densification proceeds (late stage).[87] In the case of hot-pressing, the predominant densification mechanism changes at a critical stress (σ_T), from climb-controlled dislocation creep at high effective stress

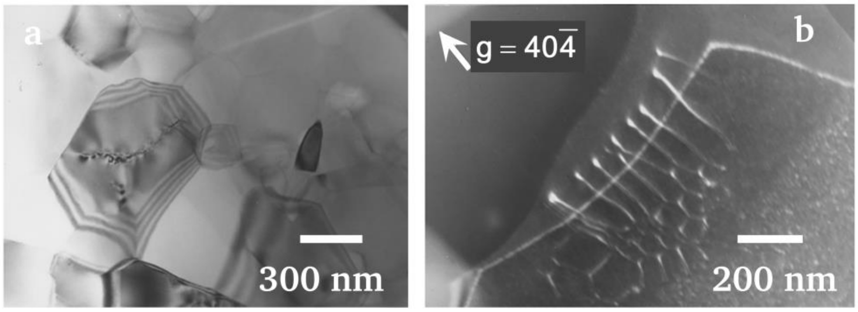

Fig. 2.23: Dislocations in a HP stoichiometric spinel compact, adapted with permission.[88]

(early stage) to Nabarro-Herring diffusional creep controlled by oxygen lattice diffusion, possibly in combination with grain-boundary sliding[229,230] at low effective stress (late stage).[87]

In Al_2O_3-rich stoichiometry, the critical resolved shear stress (CRSS) for dislocation motion is up to several orders of magnitude lower[4,87,113,231] than for stoichiometric compositions. For example, the CRSS drops from ~1 GPa for $x = 1$ to ~100 MPa for $x = 1.7$ and ~20 MPa for $x =$ 3-3.5.[231] Al_2O_3-rich compositions thus give enhanced densification with lower applied stress early during pressure-assisted sintering, so long as the CRSS is within the range of contact stresses. However, as sintering progresses, the effective stress decreases and transition to diffusion control occurs, in which Al_2O_3-rich stoichiometries display lower densification rates (attributed to lower O^{2-} diffusion). During hot-pressing, the transition stress from dislocation to diffusion control decreases with increasing Al_2O_3-rich stoichiometry, consistent with decreased oxygen vacancy concentration ($\sigma_T = 25$ MPa for $x = 1.15$ versus $\sigma_T = 40$ MPa for $x = 0.92$ at 1450°C).[87] Hence, although Al_2O_3-rich stoichiometries initially densify more rapidly, they require longer time, higher temperature, or greater pressure to reach full density (>300 min at 1450°C and 12 MPa, >1500°C and 300 min for 25 MPa, >12 MPa and 300 min for 1550°C).[87] In contrast, for MgO-rich stoichiometry the transition to diffusion control occurs at higher stress (earlier during densification) and as they densify at higher rates in this regime, they achieve full density at even low effective stress within reasonable times (2 h at 12 MPa). For stoichiometric compositions using HP, ~33 MPa is just enough to attain full density at 1550°C.[50] Impurities, additives, and atmosphere likely affect the deformation mechanism, although their effect has not been systematically studied.

2.6.3 Atmosphere

Sintering atmospheres including vacuum, air, oxygen, hydrogen, helium, argon, and combinations have been used to obtain transparent spinel. Vacuum provides a greater driving force for removing volatile species and is typically used with HP, SPS, and with graphitic furnaces. However, vacuum exacerbates Mg/MgO volatilization at higher temperatures. Reducing atmospheres are beneficial in removing sulfur,[1] but exacerbate color center formation, and CO atmosphere causes carbon contamination. Air or oxygen assists in binder burnout and formation of volatile oxide impurities.[24] For PS, higher densification rates initially occur with vacuum sintering compared with air sintering[81] due to Mg/MgO loss and differential sintering, but densification rates are eventually surpassed by air sintering.[45] Sintering atmospheres other than air have found limited benefit in the case of PS.[44,45]

2.6.4 Electric Fields

Applied electric fields enable high heating and densification rates,[232] lower sintering temperature, and attaining fine grain size.[18,67] Many mechanisms have been proposed,[232-235] including enhanced diffusion at grain boundaries early during sintering,[67,232,234,235] although the exact cause is not known with certainty. Applied electric fields lower the flow stress, possibly by reducing the electrochemical potential of rate-controlling vacancies in the space-charge adjacent to grain boundaries,[236] perhaps with relevance to the discussion in Section 2.4.2. SPS is one FAST technique that has enabled the rapid fabrication of transparent spinel compacts with fine grain size. Densification starts as low as ~850°C-950°C and can be complete by ~1200°C.[67,176] The densification mechanism is attributed to grain-boundary sliding accommodated by interface-reaction (controlling) and oxygen-lattice diffusion.[237] However, despite benefits, high heating rates with SPS exacerbate differential sintering and allow insufficient time for pore elimination.[176] In addition, grain-boundary mobility appears to increase, resulting in occluded porosity, a feature not usually observed in HP. The pulsed field also appears to enhance diffusion of carbon and/or CO gas from graphite fixtures, leading to absorption (Section 2.6.5), which in the case of SPS zirconia has been attributed to oxygen vacancies[238] and carbon.[239] LiF addition has been used to counteract dark color, but it requires lower heating rates to ensure its removal. As with hot-pressing, addition of pressure lowers the densification temperature, exacerbating compact-scale differential sintering. In addition, due to increased CO gas concentration, high pressure or application of pressure at too low a temperature traps CO in pores, further increasing absorption.[66,176] Due to enhanced sintering, pressure also forms stronger bonds for a given temperature, making it more difficult to remove intervening porosity.[64] Consequently, applying pressure at higher temperature where increased diffusion and deformation takes places leads to smaller residual pores.[240] Increased trapping of pores, occluded porosity, and absorption with SPS relegates heating rates to those used in hot-pressing.[64,202] In addition, as with HP, shapes and sizes are limited. Thus, although demonstrating promise, SPS has significant hurdles to overcome before becoming competitive. Pressureless FAST suffers from similar problems to SPS as high densification rates trap everything from pores to binders, additives, and impurities.[18]

2.6.5 Absorption

Dark color is observed in spinel compacts sintered in graphitic furnaces (HP, HIP, and SPS, Fig. 2.24),[1,64-66,202] and several sources have been identified;

1. Gross inclusions.
2. Organic additives and binders.
3. Transition metal impurities.
4. Al_2OC formation at spinel-graphite interfaces.
5. Carbon precipitation from trapped CO/CO_2 gas in pores.
6. Diffusion and precipitation of carbon from graphitic components.
7. Color center formation by reduction of spinel in reducing atmospheres.

Gross inclusions in starting powders, graphite foil flakes, atmospheric dust, and remnant organic precursors and binders, can result in significant absorption and/or can decompose into pore clusters.[1,241] As little as 0.01 wt% transition-metal impurities such as Mn, Cr, and Fe cause significant absorption, and even 10-50 ppm can result in color and detrimental absorption at shorter wavelengths.[8,24,49,99,112,117] Absorption occurs due to electronic transitions, charge-transfer transitions, and intervalence charge transfer ($Fe^{2+} \leftrightarrow Fe^{3+}$, absorbs at 194 and 258 nm).[99,109,117] Absorption over the entire visible spectrum requires overlapping absorption bands from multiple impurities present in sufficient quantity; not likely the case for high-purity powders.[8] Charged defects, such as antisites (absorb at 300, 328 nm) and vacancies, can trap electrons or holes, forming F-centers (two trapped electrons, absorbs at 200-233 nm), F+ centers (single trapped electron, absorbs at 260-270 nm) and V-centers (trapped hole, absorbs at 391 nm).[24,99,111,242-244] These defects can interact with impurities and modify absorption characteristics. Vacancies and color centers can form under reducing conditions present in graphitic furnaces,[8,24,66,109,242,243] and their presence is supported by experiments with single and poly-crystals that exhibit dark color when reduced with H_2 under carbon-free conditions.[245]

CO_2 or CO (above ~500°C, depending on pO_2) gas is present in graphitic furnaces[24,79,246,247] and in open porosity early during sintering. It becomes trapped in pores in later stages, and with increased pressure and/or decreasing temperature precipitates as carbon or graphite, possibly by stress graphitization (Eq. 2.19 and Fig. 2.25).[65,202,248,249] Individual carbon atoms may also migrate along grain boundaries, perhaps exacerbated by applied fields during SPS, and accumulate into particles at grain boundaries and triple junctions.[8,202] Spinel also reacts with carbon at interfaces to form Al_2OC, which contributes to absorption.[83] Use of polished vitreous graphite dies alleviates absorption in HP and allows components with modest optical properties to be used without subsequent polishing.[250] Although often only present in detectable quantities at triple junctions, the presence of carbon has been unequivocally demonstrated in alumina and spinel compacts and models confirm absorption between 0.2–2.0 μm.[65,202,248]

$$2CO_{(g)} \rightarrow CO_{2(g)} + C_{(s)} \tag{2.19}$$

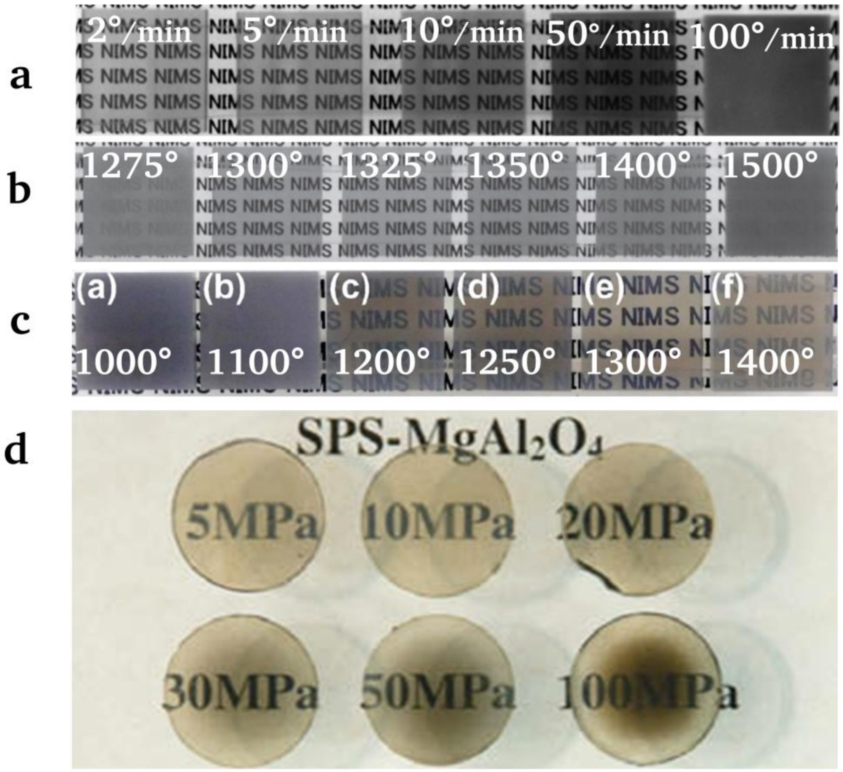
a
2°/min
5°/min
10°/min
50°/min
100°/min
b
1275°
1300°
1325°
1350°
1400°
1500°
c
(a) 1000°
(b) 1100°
(c) 1200°
(d) 1250°
(e) 1300°
(f) 1400°
d
SPS-MgAl₂O₄
5MPa
10MPa
20MPa
30MPa
50MPa
100MPa

Fig. 2.24: Increased absorption in SPS compacts with; (a) increasing heating rate,[64] (b) sintering temperature,[176] (c) temperature of pressure application,[240] and (d) applied pressure.[66]

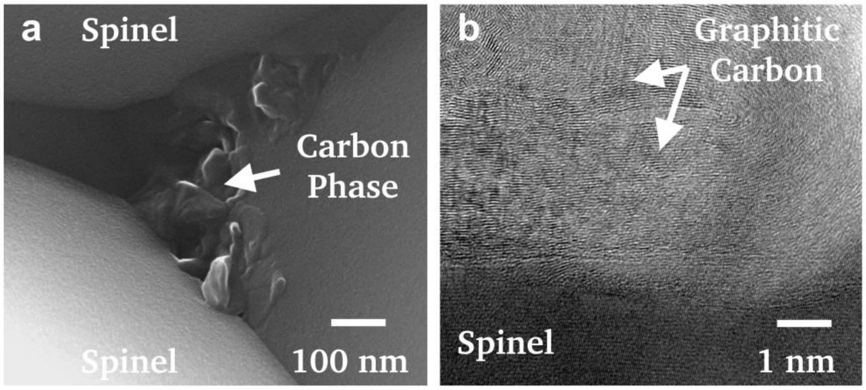

Fig. 2.25: (a) Carbon-rich phase at triple junction in spinel compact, (b) HRTEM image of graphitic carbon at triple junction in spinel compact.[2]

Increasing absorption with temperature in HP and SPS compacts and with Al_2O_3-rich stoichiometry in HP compacts is consistent with increased carbon diffusion and Al_2OC formation, respectively. Absorption is also observed in MgO-rich compositions, possibly at Al_2O_3-rich grain boundaries or due to greater oxygen vacancy and color center concentration. The possibility of absorption due to magnesium and its compounds has not been addressed. Absorption at the periphery of HP compacts and decreased absorption with increased shielding is consistent with carbon contamination from contact with graphite foil or graphitic components. In SPS compacts, increasing absorption with heating rate, with applied pressure, and with decreasing temperature of pressure application is consistent with differential sintering of compact exteriors, trapping CO containing pores, in which CO subsequently transforms to carbon. LiF effectively removes dark color in HP and SPS compacts, with lithium possibly playing a larger role. Pre-heating[58,62] and postannealing in air have been shown to remove dark color in SPS and PS/HIP compacts,[235] indicating either reaction of oxygen with carbon or neutralization of oxygen vacancies with no distinguishing between them.

2.7 Summary

Consensus is emerging that successful fabrication of transparent spinel, and likely transparent ceramics in general, entails a holistic approach. All material and processing variables need consideration, quantification, and tracking, through every step of fabrication. For spinel, increased attention must be paid to three variables that play a critical role during processing: (i) particle-size characteristics, (ii) stoichiometry, and (iii) impurities. In addition, effects that occur from the nanometer-scale to the compact scale must be considered. In this respect, scaling technologies for larger or thicker components is arguably one of the most challenging aspects of fabrication and size is also a major limitation for techniques such as HP and SPS. Although large-scale variables such as agglomeration and gross inclusions are tackled first since they have an immediately visible impact on optical properties, atomic-scale variables such as point defects and color centers, may in some cases be controlling and cannot be overlooked. In between these scales are effects of gradients in stoichiometry, impurities, microstructure, and residual stress. Despite the complexity of the spinel processing system, the identification of key variables, attention to multiscale effects, and understanding of the complexities of green-body formation and interactions that occur during sintering has enabled production of large, transparent components using a variety of methods (Table 2.3). However, significant progress remains, particularly in scaling-up fine grain-size technologies, strengthening grain boundaries, pushing absorption edges towards the theoretical limits, and lowering cost. In addition, understanding still lacks regarding the causes of grain growth and absorption, and the specific role of impurities, additives, and point defects. Variable stoichiometry, although a source of complexity, is a potentially powerful tool to control processing and properties. However, understanding of stoichiometry gradients on microstructural and compact scales also lacks. Perhaps with a deeper knowledge of these issues and with optimal powders and green bodies and careful use of atmosphere, additives, electric fields, and other methods, it may be possible to achieve the ultimate goal of pressureless sintering.

Table 2.4: Transparent Spinel Processing and Properties.

Reference	Process Details	Transmittance	GS(μm)	Young's Modulus (GPa)	Hardness (GPa)	Flexure Strength (MPa)	Fracture Toughness (MPa√m)
	PS						
(43)	CP/PS 1900°C (H_2)	50-62% TFT 2-5 μm (3 mm)	-	-	-	-	-
	2-4 wt.% Li_2O,SiO_2	Translucent Vis. (3 mm)					
(46)	CIP350MPa/PS 1900°C	67-78% TFT Vis. (<1 mm)	-	-	-	-	-
	0.5-1.0 wt.% CaO	79% ILT 5 μm (0.4 mm)					
(47)	CP70MPa/PS 1680°C (H_2)	<50% ILT 2-7 μm (1.9 mm)	-	-	-	-	-
(48)	CIP200MPa/PS 1530°C (Vac.)	Translucent Vis. (1 mm)	-	-	-	-	-
	PS/HIP						
(58)	CIP/(RS)PS/HIP150MPa/ 1750°C (1>x>3)	87-90% ILT 1-5 μm (2.3 mm)	-	-	-	250	2.8
	Ann. 24 h >1000°C						
(34)	CIP/PS/HIP	79% ILT 650 nm (12 mm)	-	-	-	-	
		>82% ILT 1-4 um (12 mm)					
(59)	CIP/HIP150MPa 1300°C	81% TFT(?) 550 nm (1 mm)	1-2	-	-	-	-
	(150 nm APS) 0.15wt.% B_2O_3						
(251)	PS/HIP 1780°C	76% ILT 193 nm (10 mm)	-	-	-	-	-
	(100 nm APS)´0.3wt.% MgF_2, AlF_3						
(252)	HP(RS)/HIP 1800°C 4% LiF	73% ILT 193 nm (4 mm)	-	-	-	-	-
(60)	PS/HIP 1360°C-1440°C <0.5% Add.	81-85% RIT 640 nm (0.8-1.6 mm)	0.4-0.6	-	14.5-15.0	200-250	1.8-2.2^{K1c}
(60)	PS(RS)/HIP 1540°C <0.5% Add.	80% RIT 640 nm (0.8 mm)	3.0-5.0	-	-	-	-
(8)(45)(169)	CP/CIP350MPa/PS/HIP200MPa 4% Binders						
	(53 nm APS) 1260°C	84% RIT 640 nm (4 mm)	0.3-0.6	275	12-16^{HV1,10}	200-250	-
	(57 nm APS) 1440°C-1500°C	81-82% RIT 640 nm (4 mm)	0.8-2.0	275	14-16^{HV1,10}	200-250	-
	(120 nm APS) 1400°C-1580°C	80% RIT 640 nm (4 mm)	3-6	275	14-16^{HV1,10}	200-250	-
	(9 m^2/g) 1730°C	84% RIT 640 nm (4 mm)	-	-		-	-
(169)	GC/PS/HIP200MPa (120 nm) 1700°C-1750°C	83% RIT 640 nm (4 mm)	-	-	-	-	-
(170)	CP/CIP/(RS)PS/HIP						
	1750°C-1850°C *x* = 1.0	>80% Vis. 87% IR ILT (4 mm)	3.0-5.0	-	-	-	-
	1750°C-1850°C *x* = 2.5	>85% Vis. 87% IR ILT (4 mm)					
(174)	PS/HIP?	87% ILT 4 um (1 mm)	2.1	-	15.2^{HV}	364^{BR}	1.4^{I,K1c}
	PS/HIP Y_2O_3 Add.	88% ILT 4 um (1mm)	0.3	-	16.8^{HV}	470^{BR}	1.4^{I,K1c}
(253)	CIP200MPa/PS/HIP200MPa	77% RIT 550 nm (2 mm)	17	300	12.8^{HV5}	-	-
	(20-50 nm APS) 1700°C						
(8)(175)	CIP200MPa/PS/HIP150-220MPa	RIT 75% 550 nm (2mm)	0.45	290	14-14.5^{HV5}	180-220	-
	(20-50 nm APS) 1320°C						
(254)	PS/HIP200MPa						
	(60 nm APS) 1520°C	72% 550 nm 1.7 mm	2.5	-	13.8	200	-
	(60 nm APS) 1580°C	80% 550 nm 1.7 mm	3.5	-	13.8	200	-
(173)(255)	PS/HIP200MPa 1650°C	75% RIT, 83% ILT	5	210^{IE}-270^{I}	15-17$^{I(1-98N)}$	155,169^{BR}	1.6-1.8^{I,BR,4P}

Reference	Process Details	Transmittance	GS(µm)	Young's Modulus (GPa)	Hardness (GPa)	Flexure Strength (MPa)	Fracture Toughness (MPa√m)
	HP						
(256)	HP(RS)75MPa/1400°C	ILT 50% 550 nm (1.2 mm)	1-2	-	-	-	-
(38)(223)	HP3-5GPa 540°C-700°C	~15% TFT 550nm (4 mm)	<0.10	-	-	-	-
		50% TFT 1.5µm (4 mm)					
	HP4GPa 600C (35 nm APS)	~60%,70% TFT 550 nm, 1 µm	0.04				
(53)	HP20MPa/1650C/0.75 wt.% LiF	40% RIT 500 nm (6 mm)	100	-	-	-	-
(1)	HP35MPa/1550°C	ILT 75% 550 nm (2 mm)	25	-	-	-	-
	0.25-1 wt. % LiF	ILT 82% 1-3 um (2 mm)					
(57)	HP(RS)40MPa 1wt. % LiF	77-79% RIT (2mm)	50-300	-	$14^{\mathrm{HV1.0}}$	-	-
	HP/HIP						
(8)	HP/HIP (CoorsTek)	82 TFT	>50	265	$13^{\mathrm{HK0.2}}$	170	
(8)	HP/HIP (NRL/MER)	82 TFT	25	280	16	300	
(8)(13)	CIP/PS or HP/HIP205MPa	ILT 80% 550 nm (3.5 mm)	>50	280	$16.4^{\mathrm{HK0.2}}$	210	
	1750°C-1850°C	ILT 88% 4 um (3.5 mm)					
(257)	HP<41MPa/ HIP207MPa	ILT 72% 700 nm (2 mm)	2	-	-	-	-
	(60 nm APS) 1500°C	ILT 88% 4 um (2 mm)					
(52)	HP(RS)50MPa/HIP189MPa/1900°C x = 1	36% ILT 550 (2 mm)			$15\text{-}16^{\mathrm{HV0.65\text{-}5}}$		$1.5\text{-}1.8^{\mathrm{K1c}}$
	n = 1.5	52% ILT 550 (2mm)			$14\text{-}18^{\mathrm{HV0.65\text{-}5}}$		$1.2\text{-}1.3^{\mathrm{K1c}}$
	n = 2	55% ILT 550 (2mm)			$14\text{-}18^{\mathrm{HV0.65\text{-}5}}$		$1.7\text{-}2.2^{\mathrm{K1c}}$
(53)	HP20MPa/ HIP200MPa	RIT 82.5% 632 nm (6 mm)	200-300	-	-	-	-
	(60 nm APS) 1900°C 0.75 LiF	RIT 87% 3.4 um (6 mm)					
(55)(77)	HP(RS)20MPa/HIP200MPa/1850°C/0.75wt%						
	n = 1.0	84.2% ILT 550 nm (4 mm)	488	287^{US}	12^{HK2}	157^{BR}	
	n = 1.2	84.8% ILT 550 nm (4 mm)	1018	293^{US}	12^{HK2}	177^{BR}	
(39)	HP/HIP206MPa/1600°C LiF(100-200 nm)	>80 IR	25-100	282	16	350	-
(173)	PS or HP/HIP200MPa/1600°C	Transparent (6.2 mm)	5	$270^{\mathrm{IE,I}}$	$13\text{-}17^{\mathrm{DI(1\text{-}98N)}}$	169^{BR}	$1.8^{\mathrm{I,BR,4P}}$
	(70 nm APS)	Transparent (6.2 mm)	60	$270^{\mathrm{IE,I}}$	$9\text{-}16^{\mathrm{DI(1\text{-}98N)}}$	77^{BR}	$1.1^{\mathrm{I,BR,4P}}$
	SPS						
(63)	SPS 1600°C 64 Mpa <20°C/min 1 wt. % LiF	65% ILT 550 nm (2.7 mm)	>20	289^{US}	13^{HV}	-	-
(64)(176)	SPS 1300°C 80 MPa	47% ILT 550 nm (1.8 mm)	0.45	-	15	~500*	-
	<10°C/min	75% ILT >1.4 µm (1.8 mm)				400^{4P}	
(65)	SPS(RS)1600°C/64MPa/100°C/min/1wt%LiF	70% ILT 550 nm (2.1 mm)	~10	-	-	-	-
(66)	SPS 1300°C 5/100 MPa	51% ILT 550 nm (1.8mm)	0.65	-	-	-	-
	100°C/min	>85% ILT >2 m (1.8 mm)					
(240)	SPS 1300°C 80 MPa	35% ILT 550 nm (1.8 mm)	0.4	-	-	-	-
	100°C/min	74% ILT >1.4 µm (1.8 mm)					
(202)	SPS (SC) 1400°C 60 MPa 100°C/min	46% ILT 550 nm (1.2 mm)	0.53	-	-	-	-
(67)	SPS 1300°C 72 MPa	74% RIT 550 nm (2.3 mm)	0.25-0.30	-	$15\text{-}16^{\mathrm{HV3}}$	-	-
	<10°C/min	84% RIT 2 µm (2.3 mm)					

PS Pressureless sinter, HP hot press, HIP hot isostatic press, SPS spark-plasma sinter, RS reactive sinter, CP cold press, CIP cold isostatic press, SC slip cast, GC gelcast, FD freeze dried, APS average particle size (not including agglomerates), Vac. Vacuum, Ann. Anneal, TFT total forward transmission, ILT in-line transmission, RIT real in-line transmission, Vis. visible, IR infra-red, DI depth-sensitive indentation, I Indentation, IE Impulse Excitation, BR Biaxial Ring-on-Ring, HV hardness Vickers, HK hardness Knoop, *unusually high values

CHAPTER 3 EXPERIMENTAL METHODS

Spinel powders were examined by X-ray diffraction (XRD), optical and polarized-light microscopy, scanning electron microscopy (SEM) in combination with energy-dispersive X-ray spectroscopy (EDS), transmission electron microscopy (TEM) in combination with selected-area diffraction (SAD), carbon-sulfur and nitrogen determination, inductively-coupled plasma in combination with mass and optical-emission spectroscopy (ICP MS/OES), laser scattering particle-size analysis, and Zeta potential (Section 3.1). Powders were mixed with additives (Section 3.2) and chemical interactions during thermal treatment were examined by simultaneous thermal analysis in combination with mass spectroscopy (STA-MS) (Section 3.3) and verified with thermodynamic simulations (Section 3.4). Coarsening studies were conducted and densification was assessed by variable-atmosphere dilatometry (Section 3.5) and hot-press displacement analysis (Section 3.6). Dense compacts were made by hot pressing (HP) (Section 3.6) and pressureless-sintering (PS) (Section 3.7), sometimes combined with hot-isostatic pressing (HIP), and were subject to quenching experiments (Section 3.8). Compact density was determined by the Archimedes method and mercury pycnometry (Section 3.9) and chemistry with ICP OES/MS (Section 3.10). Compacts and interfaces were examined with optical and polarized-light microscopy (Section 3.11), SEM in combination with EDS, wavelength-dispersive X-ray spectroscopy (WDS), and electron-backscatter diffraction (EBSD) (Section 3.12), TEM in combination with EDS and convergent-beam electron diffraction (CBED), scanning TEM (STEM) in combination with EDS and electron energy-loss spectroscopy (EELS) (Section 3.13), time-of-flight secondary-ion mass spectroscopy (TOF-SIMS), nano-SIMS, and TEM in combination with SIMS (parallel-ion electron spectroscopy: PIES) (Section 3.14), Raman spectroscopy (Section 3.15), ultraviolet-visible-infrared (UV-Vis-IR) spectrophotometry (Section 3.16), atomic-force (AFM) and electrostatic-force (EFM) microscopy (Section 3.17), and electrochemical impedance spectroscopy (EIS) (Section 3.18).

3.1 Powder Characterization

Spinel powders with x = 0.95, 0.995, 1.0, 1.05, and 1.50 from three different sources were used. S30CR "sulfate powder" (lot #601113, Baikowski, Charlotte, NC, USA) is synthesized from aqueous sulfates and contains ~800 ppm sulfur. Nanocerox "alkoxide powder" (lot #4CZ143B1, Nanocerox, Ann Arbor, MI, USA) is synthesized by flame-spray pyrolysis of metal-organic precursors and contains <100 ppm impurities. Powders "hydroxide powder" with x = 0.95, 1.0, and 1.5 were synthesized by mixing γ-Al_2O_3 (SPA-Gamma, AF grade, SASOL North America, Tuscon, AZ, USA) and $Mg(OH)_2$ (99% grade, Noah Technologies, San Antonio, TX, USA) in an aqueous slurry, drying by rotary evaporation and in vacuum, milling with high-purity alumina media, sieving with 58-mesh nylon screens, and calcining in high-purity alumina crucibles at 1000°C for 2 h.

Powders were examined by XRD (X'Pert, Philips, Eindhoven, The Netherlands). Impurity content was determined by diluting ~0.1 g samples in 4-40 ml of spectroscopic grade H_3PO_4 in Teflon beakers, dissolving by microwave digestion, and examining by ICP-OES (Spectro Arcos, Spectro, Kleve, Germany; 3000 ICP-OES, Perkin Elmer, Waltham, MA, USA). Sulfur and carbon content were determined by placing powder samples into nickel baskets with tungsten-tin and/or iron accelerants in a combustion infrared-absorption analyzer (CS-400, LECO, St. Joseph, MI, USA) that was calibrated with a standard prior to each run. Nitrogen content was determined by placing powder samples in a nitrogen-oxygen thermal conductivity determinator (TC-456, LECO). Powders were also examined using polarized-light microscopy (PMG3, Olympus, Tokyo, Japan).

Powder particle-size was determined by SEM (Quanta 600i, FEI, Hillsboro, OR, USA; JSF-7000, JEOL, Tokyo, Japan), TEM (CM12, CM200, Philips), and laser scattering (S3500, Microtrac, York, PA, USA). The TEM camera length was calibrated with silicon and MoO_3 standards, powders were dispersed in ethanol in glass beakers in an ultrasonic bath and scooped onto lacy polymer/carbon grids, SAD powder ring patterns were indexed, and intensities and lattice spacings calculated and matched to ICDD (International Center for Diffraction Data) PDF files. Average particle size was calculated using diameters for at least 50 particles. The laser scattering analyzer was calibrated with a silica standard and powder samples were dispersed in water using Darvan©C-N (ammonium polymethacrylate). Particle colloid-stability was assessed by dispersing powders in water and measuring the Zeta potential (Zetasizer Nano ZS, Malvern Instruments, Worcestershire, UK).

3.2 Powder Treatment Experiments

Additions of 0.05 – 10 wt% LiF (99.99% metal basis, Lot #20307, Puratronic, Alfa Aesar, Ward Hill, MA, USA) were added to sulfate and alkoxide powders and 0.05 and 0.1 wt% Al_2O_3 (99.99%, 20 nm average particle size, CoorsTek, Golden, CO, USA) was added to alkoxide powder, corresponding to $x = 0.998$ and 0.996, respectively. Additives and powders were weighed to ±0.1 mg, poured into a Nalgene bottle filled with methanol (40 % solids loading), mixed ultrasonically with a tungsten horn (CPX 130, Cole Parmer, Vernon Hills, IL, USA) for 1 min with a power setting of 40 W, solvent was removed by rotary evaporation (R-210, Büchi Labortechnik AG, Flawil, Switzerland), powders were dried in ambient conditions for 3 days and were subsequently ground with an agate mortar and pestle and sieved through 100 or 425 steel mesh sieves using a vibratory mixer. As a control on the mixing method, powders without additives were also similarly processed. Mixing additives by ball-milling in methanol or water with high-purity Al_2O_3 media and dry acoustic mixing (Resodyne, Butte, MT, USA) yielded compacts with poor transmission and so ultrasonic mixing followed by rotary evaporation was selected as standard processing.

3.3 STA-MS Experiments

STA (STA 409, Netzsch, Selb, Germany), combining differential scanning calorimetry (DSC) and thermogravimetric analysis (TGA), was conducted on powder samples to determine thermal behavior. To analyze evolved gases, an atmospheric residual gas analyzer (Cirrus, MKS, Andover, MA, USA) equipped with a 100-channel quadrupole MS operated at 40 eV, was connected to the STA chamber via a 3.175 mm stainless steel capillary heated to ~250°C with resistive tape. Analyte powder was poured into an alumina crucible and weighed to ±0.1 mg. The crucible was placed in the STA chamber, which was filled with air or evacuated and back-filled three times with ultra-high purity argon. The chamber was heated at 5°C/min, 10°C/min, or 20°C/min to 1450°C. The analyzer software output pressures based on calibrated counts for each mass-to-charge (m/z) ratio, which were divided by total pressure to obtain partial pressures and expressed as ideal gas vol% or ppm volume percent (ppmv). Species of equal mass were differentiated based on species known to be present, known chemical interactions, and species predicted by Gibb's energy minimization simulations using thermodynamic software.

Calibration runs were performed with empty crucibles in argon and served as correction files for STA and as a baseline for residual gas analysis. These indicated weak endotherms at 185°C associated with vaporization of adsorbed water and at 425°C associated with organics and an instrument-related endothermic rise above 500°C. STA-MS indicated 99.96 vol% argon species, with the remainder being atmospheric gases and water vapor, confirming effective sealing. Argon species (^{36}Ar, ^{38}Ar, ^{39}Ar, ^{40}Ar) concentrations matched isotopic distributions with weak signals (<0.01 vol%, 100 ppmv total) for charge-to-mass ratios (*m/z)* 20 (Ar^{++}), 41 (ArH^+), and 80 (Ar_2^+).[258-261] Weak signals (<100 ppmv total) for *m/z* 14 (N^+), 16 (O^+), 28 (N_2^+), and 32 (O_2^+) matched atmospheric gas concentrations and fragmentation patterns.[262,263] Weak signals (<200 ppmv total) for *m/z* 17 (OH^+) and 18 (H_2O^+) were consistent with water vapor and increased slightly >1300°C.[263] Weak signals (10 ppmv) for *m/z* 44 (CO_2^+, N_2O^+) between 400°C and 1000°C were likely evaporation or combustion of organics, and for *m/z* 30 (NO^+) and 44 (CO_2^+, N_2O^+) >1000°C were consistent with thermal N_2O formation and fragmentation patterns.[263-267] Small (20-30 ppmv), sharp increases in *m/z* 20 and 32 >1350°C were of unknown origin. STA-MS of empty crucibles in air indicated atmospheric gases and water vapor in expected concentrations. Duplicate runs applying the calibrations were performed in air and in argon for; pure LiF; alkoxide powder with 0 wt%, 1 wt%, and 10 wt% LiF; and sulfate powder with 0 wt% and 1 wt% LiF, and with MgF_2 and $LiAlO_2$, which are products of a reversible reaction between LiF and spinel.

3.4 Thermodynamic Simulations

Thermodynamic simulations were conducted using HSC Chemistry (Outototec, Espoo, Finland) to determine chemical interactions between starting powders, impurities, additives and the processing atmosphere. Simulations are based on thermodynamic equilibrium calculations using an internal thermochemical database. Solid and gaseous species arising from chemical interactions between starting constituents (MgO, Al_2O_3, $MgAl_2O_4$, LiF, Li_2O, AlF_3, $LiAlO_2$, MgF_2), impurities (C, S, Ca, Fe, $MgSO_4$, $Al_2(SO_4)_3$), and atmospheres (air, O_2, N_2, argon), were selected from the software database. Initial species concentrations, atmosphere, pressure, and temperature (typically 25°C to 1500°C) were input, Gibb's energy minimization simulations were conducted, and the software output plots of species concentration as a function of temperature. Simulations did not take into account kinetics, astoichiometry, solubility for species in spinel, or mixed-metal oxides and point defects.

3.5 Dilatometry Experiments

Dilatometry was conducted to assess sintering behavior as a function of powder, LiF addition, and atmosphere. 0.350 g powder samples were weighed with an analytical balance (BA 210S, Sartorius, Elk Grove, IL, USA) with an accuracy of ±0.0001 g, poured into a 6.35 mm diameter cylindrical steel die lubricated with a solution of 5 wt% stearic acid and polyvinyl alcohol, and hydraulically cold-pressed to 530 MPa, yielding cylindrical compacts with an aspect ratio of ~1:1. Cold-pressed compacts were re-weighed and dimensions measured using a micrometer. Compacts were loaded into a horizontal dilatometer (402C, Netzsch) with alumina spacers placed between samples and the alumina pushrod and backrest. A force of 30 mN was applied to the push-rod and temperature was ramped at 2°C/min to 1500°C. Atmosphere was either uncirculated ambient air or argon with 2% H_2 using flow rate of 20 *l*/min, in which case the dilatometer chamber was evacuated with a rotary vacuum pump and backfilled three times prior to starting. Compacts were subsequently re-weighed and dimensions re-measured.

The dilatometer recorded linear displacement (ΔL) as a function of time and temperature. Displacement was corrected for system thermal expansion by applying a calibration correction using an alumina standard. The error due to length and linear coefficient of thermal expansion (linear CTE, α_L) differences between the standard (L_{std} = 10 mm, $\alpha_{L\ Al2O3} = 8.1 \cdot 10^{-6}\ K^{-1}$)[23,268] and samples ($L_{compact}$ = 6 mm, $\alpha_{L\ Spinel} = 8.0 \cdot 10^{-6}\ K^{-1}$)[23] was corrected for. Displacement was normalized by length by dividing by the initial compact length. Sample thermal expansion was subtracted from displacement based on the sintered compact thickness. It was desired to display sintering behavior as a function of temperature (T) in terms of fractional sintered density (P_S) rather than linear shrinkage ($\Delta L/L_0$);[186]

$$P_S = \frac{\rho_i}{\rho_{th}}, \tag{3.5.1}$$

where ρ_i is instantaneous density and ρ_{th} is theoretical density. If no mass loss occurs, then instantaneous density is initial weight (W_0) divided by instantaneous volume (V_i);

$$\rho_i = \frac{W_0}{V_i} \tag{3.5.2}$$

If shrinkage is isotropic, the ratio of initial volume to instantaneous volume (V_0/V_i) is equal to the ratio of the volume of a cube with initial side length (L_0), to that of a cube with instantaneous side length (L_i). Thus,

$$P_S = \frac{\left(\frac{W_0}{V_i}\right)}{\rho_{th}} = \frac{\left(\frac{W_0}{V_0}\right)\times\left(\frac{V_0}{V_i}\right)}{\rho_{th}} = \frac{\left(\frac{W_0}{V_0}\right)\times\left(\frac{L_0}{L_i}\right)^3}{\rho_{th}} \tag{3.5.3}$$

Since (W_0/V_0) is the green density (ρ_g);

$$P_S = \frac{\rho_g}{\rho_{th}}\left(\frac{L_0}{L_i}\right)^3 \tag{3.5.4}$$

Noting that $L_i = L_0 + \Delta L$ and that ΔL is negative for sintering;

$$\frac{L_0}{L_i} = \frac{1}{\left(\frac{L_i}{L_0}\right)} = \frac{1}{\left(\frac{L_0+\Delta L}{L_0}\right)} = \frac{1}{\left(1+\frac{\Delta L}{L_0}\right)} \tag{3.5.5}$$

Thus;

$$P_S = \frac{\rho_g}{\rho_{Th}}\frac{1}{\left(1+\frac{\Delta L}{L_0}\right)^3} \tag{3.5.6}$$

For cylindrical compacts, shrinkage was anisotropic and the thickness (L) shrank more than the diameter (Φ) due to geometry and cold-pressing density gradients. Thus, $L_0/L_i > \Phi_0/\Phi_i$ and $V_0/V_i \neq L_0^3/L_i^3$, so $V_i = L_i \times L_i \times L_i'$, where L_i' is a radial direction with anisotropic shrinkage. If Φ_0 is the initial diameter and Φ_i is the instantaneous diameter;

$$\frac{V_0}{V_i} = \left(\frac{L_0}{L_i}\right)\times\left(\frac{\Phi_0}{\Phi_i}\right)\times\left(\frac{\Phi_0}{\Phi_i}\right) = \left(\frac{L_0}{L_i}\right)^3\times\left(\frac{L_i}{L_0}\times\frac{\Phi_0}{\Phi_i}\right)^2 = \frac{1}{\left(\frac{L_i}{L_0}\right)^3\left(\frac{L_0}{L_i}\times\frac{\Phi_i}{\Phi_0}\right)^2} = \frac{1}{\left(1+\frac{\Delta L}{L_0}\right)^3\xi^2}, \tag{3.5.7}$$

where ξ is the anisotropy parameter. Since Φ changed less per unit increase in temperature (or time) than L, assuming a similar temporal shrinkage behavior for L and Φ;

$$\Phi_{\mathrm{i}} \approx \Phi_0 - \left(\frac{\mathrm{L_i} - \mathrm{L_0}}{\mathrm{L_F} - \mathrm{L_0}}\right)(\Phi_0 - \Phi_{\mathrm{F}}) = \Phi_0 - \left(\frac{\Delta \mathrm{L}}{\mathrm{L_F} - \mathrm{L_0}}\right)(\Phi_0 - \Phi_{\mathrm{F}}) \tag{3.5.8}$$

Thus;

$$\xi = \left(\frac{\mathrm{L_0}}{\mathrm{L_i}} \times \frac{\Phi_{\mathrm{i}}}{\Phi_0}\right) \approx \left(\frac{\mathrm{L_0}}{\mathrm{L_i}} \times \frac{\Phi_0 - \left(\frac{\Delta \mathrm{L}}{\mathrm{L_F} - \mathrm{L_0}}\right)(\Phi_0 - \Phi_{\mathrm{F}})}{\Phi_0}\right) \tag{3.5.9}$$

and

$$P_S = \frac{\rho_G}{\rho_{Th}} \frac{1}{\xi^2 \left(1 + \frac{\Delta L}{L_0}\right)^3} \tag{3.5.10}$$

Eq. (3.5.10) was applied to calculate fractional sintered density as a function of time and temperature. The onset of sintering was determined from the temperature associated with the intersection of tangents to the linear portions of the displacement curves before and after the onset. The temperature of maximum sintering rate was determined by differentiating the normalized displacement versus temperature curves with respect to temperature. Where applicable, the onset of closed porosity was estimated from the attainment of 92% theoretical density for the fractional density versus temperature curves.[186]

3.6 Hot Press Experiments

Hot-pressing was used to achieve densification with a minimum of steps. Powders were poured into a graphite die lined with graphite foil (99.5%, GrafTech, Lakewood, OH, USA) with graphite foil spacers placed above and two below the powder. The graphite foil was cleaned and edges were smoothed to avoid contamination from graphite particles. To study the effect of sample size, three die sizes were used; 12.7 mm, 25.4 mm, and 38.1 mm. Powder amount was varied to study the effect of sample thickness; 1.5 g or 3.5 g (25.4 mm die), 9 g or 12 g (25.4 mm die), and 12 g (38.1 mm die). To eliminate the effect of carbon contamination from graphite foil and dies, a high-purity alumina die was constructed, in which alkoxide powder was hot-pressed with and without molybdenum foil. The graphite or alumina dies were placed in an instrumented hot press (Thermal Technology Inc., Santa Rosa, CA) with a water-cooled, stainless steel chamber and graphitic elements. The hot press chamber was evacuated using rotary and diffusion pumps and vacuum levels were monitored with an ion gauge (Model 563, Varian).

Vacuum levels deteriorated to ~13 mPa between 50°C and 300°C, but were <1.3 mPa for the remainder of the runs. Temperature was recorded with a type C (tungsten/rhenium) hafnia-insulated thermocouple in the hot zone. Ram displacement was measured using a linear variable differential transformer (LVDT). Pressure was measured using a strain-gauge pressure-cell calibrated to a maximum load of 222 kN.

The starting hot-press regime was based on prior research[49,269] and consisted of ramping temperature from ambient to 1550°C. A heating rate of 10°C/min was used to avoid grain growth. The minimum controllable instrument pressure of 3 MPa was applied at the outset to prevent plunger damage during subsequent pressure application. A 60 min hold was used at 400°C to ensure volatile species outgassing. A 5 min hold was used at 900°C, presumably to allow LiF to melt and spread by capillarity.[49,269] A 15 min hold was used at 1200°C, presumably to allow interaction between LiF and spinel.[49,269] A 60 min hold was used at the sintering temperature of 1550°C to ensure complete densification. A slower cooling rate of 6°C/min was used to avoid thermal shock. A pressure of 35 MPa was applied at 1200°C upon heating and maintained during sintering. Reports indicated that applying pressure at lower temperature (1100°C) resulted in opacity, presumably because of trapped volatile impurities and LiF.[49,269] Applying pressure at higher temperature (1300°C) was also reported to result in opacity, presumably due evaporation of LiF without interaction.[49,269] Pressure was maintained until 900°C upon cooling, presumably to avoid pore coarsening.[49,269]

Hot-press parameters from the initial regime were varied and optimized. Heating rates of 2°C/min, 3°C/min, 6°C/min, and 10°C/min were used to optimize volatile species outgassing while minimizing grain growth. High-temperature intermediate holds at 900°C, 1050°C, 1150°C, and 1200°C were used to determine the optimal LiF interaction and outgassing. Maximum sintering temperatures of 1200°C, 1300°C, 1400°C, and 1550°C were used to determine the minimum temperature at which densification could be achieved. The temperature of pressure application was found to be an important parameter[49,269] and temperatures of 800°C, 900°C, 1100°C, 1200°C, 1300°C, and 1400°C were used. A pressure of 60 MPa was also used to gauge the effect on microstructure and optical properties. Although optimal parameters depended on the starting powder and sample size, the regime shown in Fig. 3.1 "standard processing" was generally used. The variation of processing and hot-press parameters is summarized in Table 3.1.

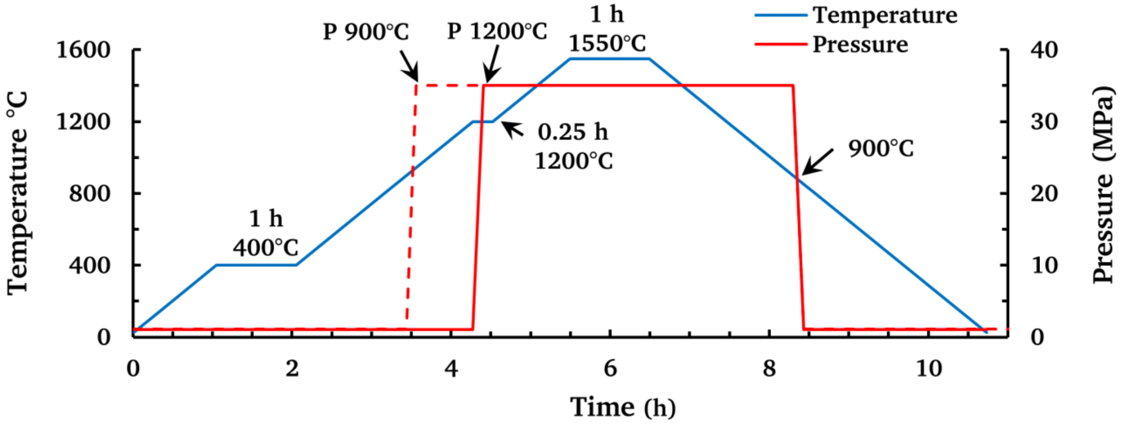

Fig. 3.1: Standard hot-press profile including ramp at 6°C/min to 1550°C with 1 h hold at 400°C, 0.25 h hold at 1200°C, 1 h hold at 1550°C, application of 35 MPa at 1200°C and removal at 900°C. Modified regime with pressure applied at 900°C (dashed line).

Vacuum, temperature, ram displacement, and pressure voltages were acquired and recorded by a data acquisition system every second, averaged to one value per 10 seconds, and imported into Excel. Thermocouple voltage was converted to temperature using a linear best-fit to a Type-C thermocouple voltage calibration.[270] Load-cell strain-gauge voltage was converted to load using a linear best-fit to a manufacturer's calibration and converted to pressure by dividing by the plunger cross-sectional area. LVDT voltage was converted to displacement using a linear best-fit to an empirical calibration, and where necessary corrected for pressure and thermal expansion. Strain due to pressure was assumed to occur mainly in the graphite components due to the lower modulus (E) than the steel rams ($E_{ISO\ 63\ Graphite} \approx$ 12-20 GPa << $E_{Stainless\ Steel} \approx$ 195 GPa),[271,272] and subtracted from displacement. Although the modulus of graphite varies with temperature, a value of 19 GPa correlated well with observations. The system linear thermal expansion was estimated from the displacement for a standard hot press run without a compact, and subtracted from displacement. The calculated system linear CTE ($\alpha_{L\ System} = 5.6 \cdot 10^{-6}\ K^{-1}$) closely matched experimental values. For higher accuracy, displacement values for the standard run without a compact were subtracted from identical standard runs with compacts. Compact linear thermal expansion was estimated based on the fully-densified thickness and $\alpha_{L\ Spinel}$ and subtracted from displacement. Compact density was calculated from corrected displacement, measured compact final thickness and density, and was plotted as percent theoretical. Vacuum thermocouple and ion gauge voltages were converted to pressure based on manufacturer's conversions. For each hot press run, calibrated temperature, pressure, displacement, density, and vacuum levels were plotted as a function of time. The sintering onset temperature and temperature at which closed porosity occurred were determined in the same manner as for dilatometry experiments.

Subsequent to hot-pressing, compacts were ground using SiC grinding discs to 600-grit and polished on glass platens using napless nylon cloths and Al_2O_3 polishing media diluted in water down to 0.05 μm. When higher grain contrast was required, a final polish with colloidal silica and vibratory polishing was used. Compacts had diameters of 12.7 mm or 25.4 mm and were ~2 mm thick (1.5 g of powder) or ~5 mm thick (3.5 g of powder) after polishing.

Table 3.1: Variation of Processing Parameters.

Parameter	**Range**
Powder synthesis	Sulfate, Alkoxide, Hydroxide
LiF Addition (wt%)	0, 0.05, 0.25, 1.0, 10
Al_2O_3 addition (wt%)	0, 0.05, 0.1
Other additives	Li_2O, AlF_3
Mixing method	None, ball mill, acoustic, ultrasonic
Die size (mm)	12.7, 25.4, 38.1
Powder amount (12.7 mm die, g)	1.5, 3.5
Powder amount (25.4 mm die, g)	6, 9 , 12
Powder amount (38.1 mm die, g)	11
Die material	Graphite, Al_2O_3
Shielding type	Graphite foil, molybdenum foil
Sintering method	Pressureless, hot press
Atmosphere	Vacuum, air, argon + 2% H_2
Temp. ramp rate (°C/min)	2, 3, 6, 10
Max. sintering temp. (°C)	1200, 1300, 1400, 1550
Hold at sintering temp. (min)	60, 120, 180
Intermediate hold temp. (°C)	900, 1050, 1150, 1200
Intermediate hold time (min)	15, 60, 120
Temp. pressure applied (°C)	800, 900, 1050, 1100, 1200, 1300, 1400
Max. Pressure (MPa)	35, 60

3.7 Pressureless Sinter - HIP Experiments

Pressureless sintering experiments were conducted to assess scaling-up transparency achieved with dilatometry to larger specimens and to gauge the effect of powder synthesis and properties on subsequent hot-isostatic pressing (HIP). 1.5 g of sulfate or alkoxide powder was poured into a 12.7 mm diameter steel die and cold-pressed at 175 MPa using a hydraulic press. Cold-pressed compacts were sintered in air in a vertical furnace with $MoSi_2$ elements (Deltech, Denver, CO) at 2°C/min to 1550°C, with a 1 hour hold at 1550°C, and a ramp to ambient at 10°C/min. Compacts were cut in half with a diamond saw and HIPed in a graphite furnace in argon at 5°C/min to sintering temperature with a 2 h hold at 300°C. One half of each sample was HIPed at 1550°C for 10 h, and the other at 1650°C for 15 h.

3.8 Quenching Experiments

Quenching experiments were conducted to determine whether impurities and additives segregated at grain boundaries could be re-dissolved into the matrix to alter fracture behavior. Samples from compacts hot pressed with sulfate powder with 1 wt% LiF were heated in an air furnace to 1200°C and quenched in water at ambient temperature. The samples were sectioned with a diamond saw and the slices obtained were fractured and the surfaces examined with SEM and compared to those of un-quenched samples.

3.9 Density Measurement

Compact densities were calculated using the Archimedes method and ASTM B962 and C373. Compacts were boiled in de-ionized water for 5 h, weighed to ±0.1 mg with an analytical balance (BA 210S, Sartorius) with adjustments made for ambient temperature and pressure. Density was also assessed using mercury pycnometry (Spy-2, QuantaChrome, Boynton Beach, FL, USA). However, although relative values between samples appeared accurate, calculated densities were higher than theoretical, likely due to the large chamber size compared to samples.

3.10 Chemical Spectroscopy

Laser ablation inductively coupled plasma optical emission and mass spectroscopy (LA-ICP OES/MS; Spectro-Arcos, Spectro; 820 MS, Varian; LSX-500 LA, Cetac, Omaha, NB) was used to quantify impurity content within and among compacts. Two compacts hot pressed with 3.5 g of sulfate powder and pressure applied at 1200°C were analyzed; one without LiF and one with 1 wt% LiF. Compacts were sectioned using a diamond saw, yielding semi-cylinders. For each compact, two areas were analyzed; the center of a face and the geometric center. Prior to LA-ICP a compact hot pressed so as to maximize retained impurity content was analyzed with LA-ICP and also dissolved using spectroscopic-grade phosphoric acid and microwave digestion for analysis by solution ICP-OES to establish a reference. The spectral counts of the ICP analyses were integrated and the element counts normalized by dividing them by the aluminum, magnesium, or gallium counts. The normalized counts from LA-ICP were compared to those from solution-ICP to establish absolute concentrations. Major species (Na, Mg, Si, S, Ca, and Fe) concentrations were determined by OES and trace species (Li, B, Cu, Zn, Zr, Ga, Se, I, Ba, W) concentrations by MS. Alumina levels were obtained by difference, lithium content was measured directly and LiF content estimated from it, and boron content was too low to establish a calibration curve.

3.11 Optical Microscopy

Compact microstructures were examined using optical microscopy (OM; PMG 3, Olympus), with a 10X eyepiece, 10X-50X objective lenses, and a top-mounted digital camera (PX-CM, Paxcam, Villa Park, IL, USA). Decorated grain boundaries, second phases, inclusions, and other optical defects were observed by focusing the image plane in the interior of transparent compacts. Images with annotated calibrated scale bars were imported into Image J image analysis software (National Institute of Health, Bethesda, MD, USA). Average grain size was calculated using the circle-intercept method and ASTM E112. Grain boundary surface area per unit volume was calculated by modeling grains as tetrakaidecahedrons with diameters equal to the measured average grain size.[273] Total grain boundary area for each grain size type was calculated by multiplying the grain boundary surface area per unit volume for each grain size type (matrix grains, sub-micron grains, abnormal grains) by the area fraction of that type determined from Image J analysis of SEM images. Compacts were also examined with polarized light microscopy (PLM; AxioScope A1, Zeiss, Oberkochen, Germany) using a full-wavelength green-light filter to examine birefringent features and residual stress.

3.12 Scanning Electron Microscopy

The microstructure and chemistry of polished compacts, fracture surfaces (which ensured the retention of brittle second phases and showed fracture mode), and of precipitate collected from the periphery of compacts subsequent to hot-pressing, were examined with SEM (JSF-7000, JEOL) in combination with EDS and WDS. Crystallographic texture in polished compacts was examined using EBSD. The volume percent of phases and fracture features were determined using Image J.

3.13 Transmission Electron Microscopy

Transmission electron microscopy (TEM; CM200, CM12, Phillips; JEM 2100F, JEOL) and scanning TEM (STEM, Tecnai G2 F20 S-Twin, FEI; JEM ARM 200F, JEOL) were performed on specimens that were dimple-ground and ion milled (Duo Mill 600, Gatan, Warrendale, PA, USA) with argon, or alternatively on lift-outs prepared with a dual-beam focused ion beam (FIB; Helios 600i; FEI). To preserve phases that dissolve in water, dimpled specimens were ground using an ethanol-based lubricant (Lubricant Yellow, Cloeren Technology, Wegberg, Germany). Compacts were examined in brightfield (BF) and centered dark-field (DF) modes and by electron diffraction (ED), selected-area electron diffraction (SAD), and convergent beam electron diffraction (CBED), and chemical composition was examined using energy-dispersive X-ray spectroscopy (EDS) and electron energy loss spectroscopy (EELS).

Changes in lattice parameter at grain boundaries were assessed by performing CBED on FIB samples. The TEM cameral length was calibrated with silicon and polycrystalline aluminum standards using;[274]

$$R = \lambda L\,, \tag{3.13.1}$$

where R is the distance between SAD reflections, d is the crystal lattice spacing, λ is the electron wavelength, and L is the camera length. The TEM voltage was determined by collecting CBED patterns for a silicon single crystal and matching central-disc Kikuchi line patterns of low-index zone axes to simulated patterns with JEMS (EPFL, Lausanne, Switzerland) electron diffraction simulation software[275] using;

$$\lambda = \frac{h}{(2m_0 eV)^{1/2}} \quad , \tag{3.13.2}$$

where λ is the electron wavelength, h is Planck's constant, m_0 is the electron mass, e is the charge of one electron, and V is the TEM voltage. CBED patterns were collected at grain interiors and grain boundaries of FIB samples. The relationship between electron wavelength, TEM camera length and voltage, and lattice parameter is given by;

$$\frac{1}{H} = \left(\frac{2}{\lambda}\right)\left(\frac{\lambda L}{r}\right)^2 , \tag{3.13.3}$$

where H is the spacing of reciprocal lattice planes parallel to the electron beam, λ is the electron wavelength, L is the camera length, and r is the measured radius of the first-order Laue zone (FOLZ) ring. The lattice parameter was calculated from;

$$\frac{1}{H} = \frac{a_0 (U^2 + V^2 + W^2)^{1/2}}{P} , \tag{3.13.4}$$

where a_0 is the lattice parameter, U, V, and W are the zone axis plane indices, $P = 1$ when $(U + V + W)$ is odd and $P = 2$ when $(U + V + W)$ is even.

Lattice parameter variation across grain boundaries using TEM-CBED could not be determined with certainty either because the variation gradient was too shallow or too narrow, or because the electron beam probe size was larger than the features being investigated. In addition, accuracy was limited by beam asphericity noted in FOLZ circles.

STEM-EDS/EELS maps were collected at several grain boundaries and triple-junctions of FIB lift-outs from hot-pressed sulfate powder compacts with LiF and were imported into Digital Micrograph (Gatan, Warrendale, PA). Relative intensity ratios for Mg, Al, and O peaks from EDS spectra were plotted versus distance from the grain-boundary core. The zero-loss (ZL) peak was removed and a power-law background subtraction was applied to EELS spectra. The Mg-$L_{2,3}$ (51 eV), Al-$L_{2,3}$ (73 eV), Mg-L_1 (88 eV), Al-L_1 (118 eV), C-K (284 eV), O-K (532 eV), Mg-K (1305 eV), and Al-K (1560 eV) edges were extracted and quantified. The Li-K (55 eV) edge was not identifiable, likely due to the low edge/background ratio intensity combined with low concentration and overlap with the Mg-$L_{2,3}$ edge. The F-K (685 eV) edge was similarly not identified, likely due to low concentration. Mg-K (1305 eV) and Al-K (1560 eV) edges were too weak to be accurately resolved. Edge intensity ratio variation across grain boundaries were plotted versus distance from the grain-boundary core for the following combinations: Mg-$L_{2,3}$/Al-$L_{2,3}$, Mg-L_1/Al-$L_{2,3}$, Mg-$L_{2,3}$7O-K, Mg-L_1/O-K, and Al-$L_{2,3}$/O-K.

3.14 Secondary-Ion Mass Spectroscopy

Knowledge of the distribution of lithium in sintered samples can give insights into its role during densification and how it affects interfaces. However, it is not easily detectable by EDS or TEM-EELS. Time-of-flight secondary-ion mass spectroscopy (TOF-SIMS) is one of few methods capable of quantifying its distribution with relatively high spatial resolution. TOF-SIMS (Phi Thrift III, Physical Electronics, Chanhassen, MN, USA) $^{7}Li^{+}$ mapping was performed on the polished surfaces of samples hot-pressed with sulfate powder with (i) no LiF using the standard profile with 35 MPa applied at 1200°C, (ii) 1 wt% LiF addition and pressure applied at 1100°C during hot-pressing, and (iii) 1 wt% LiF addition and pressure applied at 900°C during hot-pressing. Application of pressure at a lower temperature during hot pressing was expected to trap more LiF and to result in sufficient lithium content for detection. Compacts were coated with 200 nm of copper to reduce charging. A liquid-metal ion (Au, Ce) or oxygen source was used for the ion beam and the manufacturer quoted ~1 ppm species and ~1 μm spatial resolution. For the compact without LiF, SIMS was conducted over an area of 50 μm^2, using 32 s analyze time, 10 s sputter time, and no charge compensation. For compacts with LiF, SIMS was conducted over an area of 25 μm^2, using 16 s analyze time, 10 s sputter time, and charge compensation. Lithium counts were normalized by the sum of magnesium and aluminum counts and plotted as a function of analysis time. Surface scans at the bottom of ion craters were conducted for 30 min for the compact without LiF and for 8 min for compacts with LiF. SIMS $^{7}Li^{+}$, $^{25}Mg^{2+}$, and $^{27}Al^{3+}$ 50 x 50 μm maps were also performed on a polished sample hot-pressed with sulfate powder and 1 wt% LiF addition using the standard profile using a different SIMS instrument (IMS 6f, Cameca, France) and a SIMS instrument with a higher lateral resolution of 50 nm (Nano-SIMS 50L, Cameca, France).

PIES (Parallel-ion electron spectroscopy; LIMS, Esch-sur-Alzette, Luxembourg) consists of a SIMS instrument (with high sensitivity for low atomic-weight elements) placed within a TEM (with high spatial resolution of microstructural and crystallographic features). PIES $^{7}Li^{+}$

mapping was conducted on a FIB lift-out from a sample hot-pressed with sulfate powder and 1 wt% LiF using the standard profile.

3.15 Raman Spectroscopy

Confocal Raman spectroscopy (Alpha 3000, WiTec, Ulm, Germany), using a Nd:YAG laser emitting light at 532 nm, was used to probe point-defect structure, determine the chemistry of second phases and inclusions, and to examine fluorescent behavior, both on the surface and within the interior of polished compacts. Raman shift as a function of wavelength was recorded for various compacts, spinel single crystals, and graphite, and compared to published spectra.

3.16 Spectrophotometry

UV-Vis.-IR Spectrophotometry (Lambda 950, Perkin Elmer; Cary 5G, Varian) was used to measure transmittance, reflectance, and fluorescence of surface ground and polished compacts. In-line transmittance (I_{ILT}) was measured from 175 nm to 3000 nm by placing samples between the radiation source and detector. Total transmittance (I_{TT}), total reflectance (I_{RT}), and diffuse reflectance (I_{RD}) were measured from 175 nm to 3000 nm using an integrating sphere. For total transmittance, samples were placed at the integrating sphere entrance aperture and a reflective plug placed at the sample reflection measurement location. For total and diffuse reflectance, samples were placed at the rear sample reflection measurement location, which was set to include specular reflectance within the sphere for total reflectance measurement, or to reflect it out the entrance aperture for diffuse reflectance measurement. For all measurements, 0% and 100% transmittance baselines were set by measuring transmittance with the source blocked and without a sample, respectively. For the 100% reflectance measurement a highly reflective polytetrafluoroethylene standard was used. Sample fluorescence was measured using a 6 W continuous wave UV source with and without a UV filter (9683) and measurement was made at 90 degrees to the incident light using a fiber-coupled detector.

Incident, transmitted, reflected, and absorbed intensities are related by;

$$I_0 = I_{TT} + I_{RT} + I_A = 1, \qquad (3.16.1)$$

where I_0 is the incident intensity, I_{TT} is the transmitted intensity, I_{RT} is the reflected intensity, and I_A is the absorbed intensity. Total transmittance is the sum of in-line and diffuse transmittance;

$I_{TT} = I_{ILT} + I_{DT}$, and total reflectance is the sum of specular and diffuse reflectance; $I_{RT} = I_{RS} + I_{RD}$. Diffuse transmittance (I_{DT}, or forward scatter) was calculated from the difference between total (I_{TT}) and in-line transmittance (I_{ILT}). Specular reflectance (I_{RS}) was calculated from the difference between total (I_{RT}) and diffuse reflectance (I_{RD}). Absorptance (I_A) was calculated as the incident intensity minus total transmittance and total reflectance. Where different thickness compacts were compared, values were normalized per unit thickness.

3.17 Thermal Grain-boundary Grooving Experiments

Stoichiometry affects nearly every property of spinel (Section 2.4), and it was expected to affect surface[134] (γ_s) and grain-boundary[129] (γ_{gb}) energies, which strongly influence densification.[121] LiF was also expected to influence interface energies due to its reactivity with spinel and its effect on processing and properties (Section 2.5.2). In this vein, the relative γ_{gb}/γ_s ratio was quantified from thermal grain-boundary grooves imaged using atomic-force microscopy (AFM) for compacts made from powders with $x = 0.95$, 1.0, and 1.5 and with $x \sim 1.05$ with and without 1 wt% LiF.

Grain-boundary grooving can be used to extract interface energies from thermally-etched polished surfaces. When a surface intersected by a grain boundary is exposed to temperatures where diffusion occurs, interface energies equilibrate to form a groove bounded by accommodating ridges, which deepen the groove by continually flattening to minimize surface energy.[276] If surface energy is isotropic, the grain boundary perpendicular, and torque terms are disregarded, the groove profile is described by;

$$\gamma_{gb} = 2\gamma_s \cos(\Psi/2), \qquad (3.17.1)$$

where γ_{gb} and γ_s are the grain boundary and surface energies per unit area, respectively, and Ψ is the internal dihedral angle.[276] Thus, finding Ψ permits determining γ_{gb}/γ_s. The dihedral angle can also be found from;

$$s \approx 4.73 d \tan(\Psi/2), \qquad (3.17.2)$$

where s is the inter-ridge distance and d is the groove depth.[276]

Ψ, s, and d can be determined from surface topography maps made using AFM. However, AFM resolution is limited by the probe-tip radius. Due to groove convexity, slope measurements overestimate Ψ, underestimating γ_{gb}/γ_s. Although d can also be underestimated, the error associated with measuring s and d is less than for measuring Ψ at the groove root.[276] To reduce the relative depth measurement error, deeper grooves are preferable. However, since surface reconstruction occurs concurrently with grooving, the optimal thermal treatment is a balance between maximizing groove depth using long anneal times or high temperatures and minimizing surface reconstruction using short anneal times or low temperatures.

Ψ varies considerably as it depends on (i) inter-grain lattice misorientation, (ii) grain-boundary plane orientation, (iii) surface plane orientations, (iv) proximity to triple lines where grooves widen, (v) interface stoichiometry, (vi) precipitates, (vii) impurity content, (viii) and thermal treatment time, temperature, and atmosphere.[135,277] Thus, valid statistics require sufficient grain boundary groove profiles.

Hydroxide powders with $x = 0.95$, 1.0, and 1.5 (S.A. ~10-20 m^2/g, Ca ~30-35, Na ~0-460, K ~20-640, Si ~60-155 ppm) were hot-pressed at 1600°C and 35 MPa for 5 h under a vacuum of $5{\cdot}10^{-2}$ Pa and hot-isostatic pressed at 1850°C and 200 MPa for 5 h in argon to ensure complete solid solution.[11] Dense, transparent compacts were ground with SiC papers, polished with diamond slurries to 1 μm, and final polished with 0.05 μm colloidal silica. To maximize groove depth, minimize surface reconstruction, and replicate typical processing conditions, polished compacts were thermally-etched for 1 h at 1450°C in argon and rapidly cooled. Thermal grain-boundary grooves were imaged by AFM (XE-100, Park Systems, Santa Clara, CA, USA) in intermittent contact mode with aluminum-plated pyramidal silicon cantilever tips (910M, ACTA, AppNano, Mountain View, CA, USA) with a radius of curvature <10 nm. AFM resolution was verified using a silicon grid (TGX01P, MikroMasch, Sofia, Bulgaria) with 1.15 x 3 μm lateral and 0.110 ± 0.004 μm vertical features. Polished surfaces prior to etching had a root-mean-squared roughness of <5.00 nm.

At least fifteen acceptable boundaries were mapped for each stoichiometry. Groove profiles were rejected when grain-height or groove-slope differentials on either side of boundaries were excessive (>40 nm and >20°, respectively) or when grooves were shallower than the AFM tip radius. AFM maps, typically <30 x 30 μm, were corrected for tilt and at least three perpendicular line profiles were acquired for each boundary (XEP software, Park Systems), resulting in at least 45 profiles per stoichiometry. Dihedral angles were determined using best-fit tangents on either side of grooves and also by measuring inter-ridge widths and groove depths. The γ_{gb}/γ_s ratio was calculated using Eqs. 3.17.1 and 3.17.2 and values were averaged for each boundary and stoichiometry.

Polished sulfate powder compacts hot-pressed with and without 1 wt% LiF using the standard using were thermally etched for 15 min at 800°C in a vertical drop-down furnace and quenched in air. Surface roughness maps were generated at selected sites by AFM (Nanoscope 310D, Digital Instruments, Tonawanda, NY, USA). Dihedral angles were measured from line scans generated using the AFM software. Due to inadequate thermal etch parameters and excessive surface roughness for samples without LiF, only five grain boundaries were examined for each condition. Electrostatic-force microscopy (EFM) was performed on polished compacts hot-pressed with and without LiF to try to detect changes in dielectric constant across grain boundaries. However, no changes were detected, either due to low instrument sensitivity or because the chemical gradients were too small, too shallow, or non-existent.

3.18 Electrochemical Impedance Spectroscopy Experiments

Electrochemical impedance spectroscopy (EIS) can be used to probe the dielectric properties of solids and interfaces.[278] The motivation for performing EIS was to characterize interfaces and gain insights into the cause of grain-boundary embrittlement[1] and short-wavelength scatter[1,216] in compacts processed with LiF from a defect-chemistry perspective. Degraded properties were tentatively attributed to LiF-induced MgO-depletion[78] as the smaller lattice parameter for MgO-deficient stoichiometry[161] was expected to cause strain and refractive index variation at grain boundaries. Since 20 – 50 nm wide Mg-depleted zones have been observed at boundaries without LiF, even for MgO-rich stoichiometry (Section 2.4.2),[81,86,89,161,162] the reaction of LiF with spinel forming volatile MgF_2[1] was expected to exacerbate MgO-depleted grain boundaries to the extent where they affected fracture properties and scattered visible wavelengths. Few EIS studies were found for polycrystalline spinel,[152,157,163,279] and none for fully-dense or transparent spinel, and so EIS was conducted between 500°C and 900°C in oxidizing and reducing atmosphere on fully-dense polycrystalline spinel compacts hot-pressed with different powders and with and without LiF, and the dielectric properties determined were related to intrinsic microstructure.

Four compacts hot-pressed using the standard processing were analyzed; an apparently more oxidized, cream-colored ("white") sulfate powder compact, an identically processed but apparently more reduced ("dark") sulfate powder compact, a transparent sulfate powder compact hot-pressed with 1 wt% LiF, and a transparent alkoxide powder compact (Section 3.1). Polished (to 0.05 μm grit-size) cylindrical (~12.7 x 2 mm) hot-pressed compacts were glued with Crystalbond^{TM} to a steel plate placed on a magnetic-bed surface grinder and ground with a 600-grit diamond grinding wheel to ~1.0 mm thickness. The ground side was re-polished to ~0.7 mm thickness using successively finer Al_2O_3 media to 0.05 μm grit-size. Compact thickness was measured at five locations with a micrometer. Gold electrodes ~7 mm or ~10 mm in diameter were magnetron sputtered on each side through a circular stencil using a setting of 20 mA for 8 min. Silver or platinum wire leads were tied to silver mesh, which was glued to the electrodes using silver adhesive paint cured at 200°C for 30 min. Electrode leads were threaded through a 2-bore alumina tube, leaving the sample hanging freely at one end. The 2-bore alumina tube was inserted through an UltraTorr^{TM} fitting mounted on a ported steel flange attached to a larger-diameter closed-end alumina tube. A type-K thermocouple was inserted through an UltraTorr^{TM} fitting and positioned adjacent to the sample. Gas inlet and outlet alumina tubes were fitted through two other UltraTorr^{TM} fittings. The assembled EIS rig was placed in a tube furnace and thermocouple leads were connected to a thermocouple reader. The gas inlet tube was connected to a synthetic air cylinder or argon with 2% H_2, set to a flow rate of 70 cm^3/m controlled by a mass-flow controller. The furnace was ramped to 900°C and sequentially cooled at 50°C intervals to 500°C with temperature allowed to stabilize at each interval. A potentiostat (Reference 3000, Gamry, Warminster, PA, USA) applied an alternating voltage (AC) of 100 mV rms from 0.1 Hz to 1 MHz at ten points per decade and recorded impedance (Fig. 3.2).

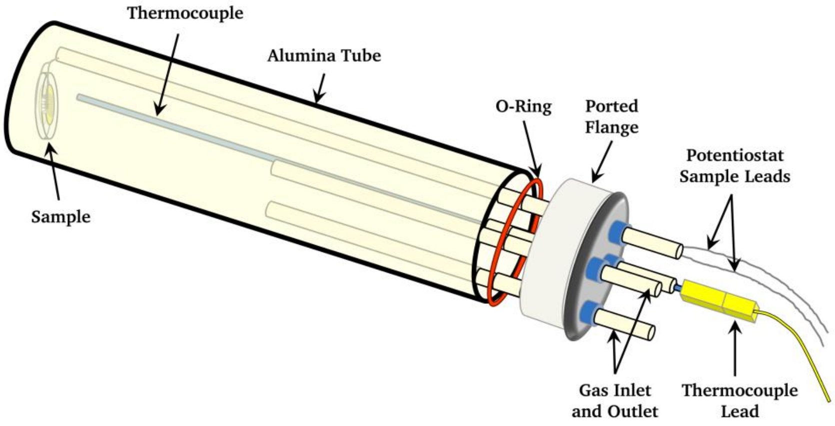

Fig. 3.2: Schematic of EIS Apparatus.

Impedance is given by;

$$Z = Z_0 e^{j\omega t} = Re[Z] - Im[Z] = \frac{V_0 cos(\omega t)}{i_0 cos(\omega t - \varphi)}, \qquad (3.18.1)$$

where Z is impedance, $j = \sqrt{-1}$, V_0 is voltage amplitude, i_0 is current amplitude, $\omega = 2\pi f$ is angular frequency, f is AC frequency, t is time, and ϕ is phase shift. The real and imaginary impedance components were normalized for sample-electrode geometry by multiplying by A/L (where A and L are the electrode cross-sectional area and separation, respectively) and plotted on Nyquist (Cole-Cole) plots, yielding resistivity on the real axes. Impedance arcs were simulated and fitted using Zview® (Scribner Associates, Southern Pines, NC, USA) electrochemistry software by modeling samples as two parallel resistor-capacitor (RC) circuits and a Warburg element in series, representing bulk, grain-boundary, and sample-electrode impedances (Fig. 3.3).[278] Capacitors were replaced with constant phase elements (CPE's) to model impedance non-linearity, with CPE impedance given by;

$$Z(\omega) = Q^{-1}(j\omega)^{-n_c}, \qquad (3.18.2)$$

where Q and n_c are CPE parameters, and the response is purely capacitive when $n_c = 1$.[278,280,281] Fitted equivalent-circuit resistances and CPE parameters were used to calculate resistivity;

$$\rho = RA/L, \qquad (3.18.3)$$

conductivity;

$$\sigma = 1/\rho, \qquad (3.18.4)$$

and effective capacitance;

$$C_{eff} = R^{((1-n_c)/n_c)}Q^{(1/n_c)\,282} \tag{3.18.5}$$

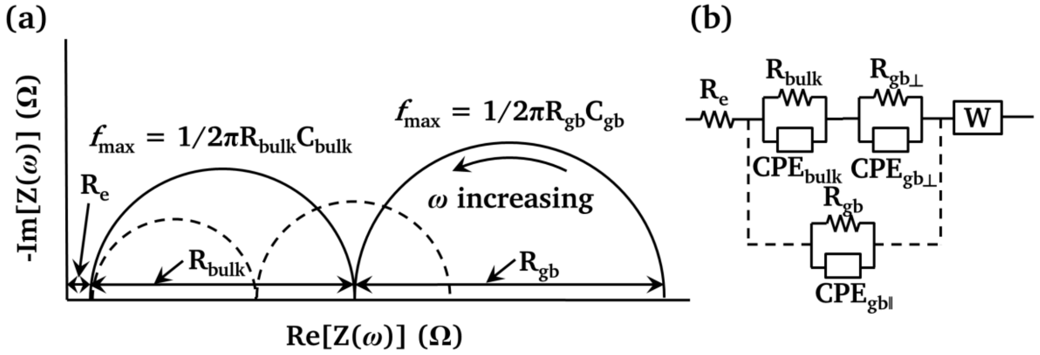

Fig. 3.3: Idealized Nyquist plot (a) and equivalent circuit representing a polycrystalline solid with electrodes (b), dashed line represents additional parallel grain-boundary conductivity and its effect. Z is impedance, f is AC frequency, ω is angular frequency, R is resistance, C is capacitance, and subscripts 'e' refer to electrode, 'gb' to grain boundaries, and '⊥' to field-perpendicular and '∥' to field-parallel boundaries.

Separate arcs were attributed to different impeding mechanisms based on their time constants or capacitances.[283] Time constants were determined from arc maxima, where;

$$\omega_{max}\tau = 2\pi f_{max}\tau = 1, \tag{3.18.6}$$

where ω_{max} is the resonant angular frequency at the maximum, τ is the time constant, and f_{max} is the resonant frequency at the maximum.[278] Since $\tau = RC$ for parallel RC-circuits, capacitance was also calculated from resonant frequency and resistance values using;

$$2\pi f_{max} = 1/RC \tag{3.18.7}$$

Modulus plots of Im(M) versus f (where $M = j\omega C_c Z$, $C_c = \varepsilon_0 A/L$ is the empty cell capacitance and ε_0 is the vacuum permittivity) were also constructed to emphasize components with smaller capacitances when separate arcs were not resolved in Nyquist plots.[278,283]

Specific conductivities were calculated using the series brick-layer model (series model), which assumes cubic grains with intervening boundaries and $\sigma_{gb} << \sigma_{bulk}$, ignores parallel conductance, and since resistivities add for series elements gives;

$$\rho_t = \rho_{bulk} + \rho_{gb\perp} \quad or \quad \frac{1}{\sigma_t} = \frac{1}{\sigma_{bulk}} + \frac{v_{gb}}{3\sigma_{gb\perp sp}}, \qquad (3.18.8)$$

where $\sigma_t = 1/\rho_t = 1/(R_t(A/L))$ is total conductivity, $\sigma_{bulk} = 1/\rho_{bulk} = 1/(R_{bulk}(A/L))$ is specific bulk conductivity, the bulk volume fraction is assumed to equal unity, $v_{gb} \approx 3d/D$ is the grain-boundary volume fraction (where d is grain-boundary width and D is grain size), $\sigma_{gb\perp\ sp} = 1/\rho_{gb\perp\ sp}$ is *specific* conductivity across field-perpendicular grain boundaries, and the 1/3 in the last term corresponds to the fraction of perpendicular grain boundaries (the 2/3 parallel boundaries are ignored).[278,284] The v_{gb} calculated in this model underestimated that calculated considering tetrakaidecahedral grains, especially for samples with bi-modal grain-size distributions. The effective impeding perpendicular grain-boundary width ($d_\perp$) was assumed to correspond to the grain-boundary core and estimated at ~1 nm by TEM for all compacts. Where grain-boundary arcs were well-resolved, $d_\perp$ was also estimated using;

$$d/D \approx C_{\mathrm{bulk}}\varepsilon_{\mathrm{bulk}}/C_{\mathrm{gb}\perp}\varepsilon_{\mathrm{gb}}, \qquad (3.18.9)$$

assuming $\varepsilon_{\mathrm{bulk}} \approx \varepsilon_{\mathrm{gb}}$.[278] Using this relation and $\varepsilon_{bulk}\varepsilon_0 = C_{bulk}(L/A)$, bulk permittivity was estimated using;

$$\varepsilon_{bulk} = C_{gb\perp}(d/D)(L/A)(1/\varepsilon_0)^{278} \qquad (3.18.10)$$

Activation energies for conductivity were calculated using;

$$\sigma = (\sigma_0/T)e^{-Ea/kT}, \qquad (3.18.11)$$

where σ is conductivity, σ_0 is a pre-exponential constant, E_a is the activation energy for conductivity, k is Boltzmann's constant, and T is temperature.[120]

Higher than expected conductivities compared to single crystals of similar stoichiometry, both in this study using the series model (Eq. 3.18.8) and in the literature, suggested the presence of enhanced conductivity *along* field-parallel grain-boundaries (dashed lines in Fig. 3.3), while still assuming reduced conductivity *across* boundaries. The *specific* conductivity along field-parallel grain boundaries ($\sigma_{gb\parallel\ sp}$) that would be required to reduce bulk conductivity from comparable single-crystal values (σ_{sc}) to observed values using the series model ($\sigma_{bulk\ series}$) was estimated using the complete brick-layer model, in which conductivities add for parallel elements and resistivities add for series elements, giving;

$$\sigma_t = \sigma_{series} + \sigma_{parallel} \quad or \quad \sigma_t = \frac{1}{\dfrac{1}{\sigma_{bulk}} + \dfrac{v_{gb}}{3}\dfrac{1}{\sigma_{gb\perp sp}}} + \frac{2v_{gb}\sigma_{gb||sp}}{3}, \tag{3.18.12}$$

where σ_t is observed total conductivity, σ_{series} is conductivity across the bulk and intervening boundaries, $\sigma_{parallel}$ is conductivity along grain boundaries, σ_{bulk} was set equal to σ_{sc}, $\sigma_{gb\perp\ sp}$ was set equal to $\sigma_{sc}(\sigma_{gb\perp\ sp\ obs}/\sigma_{bulk\ series})$ (assuming the series model ratio valid), v_{gb} is the grain-boundary volume fraction, and $\sigma_{gb\|\ sp}$ is the specific field-parallel grain-boundary conductivity. The effective grain-boundary width contributing to parallel conduction ($d_{\|}$) was assumed to correspond to higher conductivity in Mg-depleted regions and estimated at 20 nm for samples without LiF based on STEM-EDS studies on slightly Al_2O_3-rich[86,89,162] and MgO-rich[86] compacts. Although a wider effective grain-boundary width was expected due to increased Mg-deficiency in the sample with LiF, the same 20 nm width was used as literature estimates were unavailable.

CHAPTER 4 RESULTS AND DISCUSSION

This chapter presents combined results and discussion for starting powders (Section 4.1), bulk samples (Section 4.2), and interfaces (Section 4.3). A general discussion tying together the conclusions from this chapter is given in Chapter 5.

4.1 Starting Powders

Since they largely determine the sintering and densification behavior, microstructure evolution, and properties of polycrystalline ceramics and their interfaces, starting powders were characterized to enable making inferences on processing-structure-property relationships. Sulfate and alkoxide-derived powders were examined by X-ray diffraction (XRD), polarized-light microscopy, scanning electron microscopy (SEM) in combination with energy-dispersive X-ray spectroscopy (EDS), transmission electron microscopy (TEM) in combination with selected-area diffraction (SAD), carbon-sulfur and nitrogen determination, inductively-coupled plasma in combination with mass and optical-emission spectroscopy (ICP OES/MS), particle-size analysis by laser scattering, Zeta potential analysis (Section 4.1.1), and simultaneous thermal analysis in combination with mass spectroscopy (STA-MS) (Section 4.1.2), with chemical interactions verified by thermodynamic simulations (Section 4.1.3). Sintering behavior was assessed by dilatometry and by examining hot-press displacement (Section 4.1.4). Hydroxide-derived powders were only used for thermal grain-boundary grooving experiments and their properties were obtained from the group who synthesized them.

4.1.1 Powder Characterization

Properties for aqueous sulfate-derived (“sulfate”), alkoxide-derived flame-spray (“alkoxide”), and reaction-sintered hydroxide-derived (“hydroxide”) powders are shown in Table 4.1.

Table 4.1: Spinel Powder Properties.[a]

Property	**Sulfate**	**Alkoxide**	**Hydroxide**
Crystallite Size (nm)	50, 35[h]	58, 30[h]	-
Agglomerate Size (d_{50}, μm)	0.2, 0.3[h]	0.1-0.3[h]	2.7-3.2[e]
Surface Area (BET, m^2/g)	30	29	12-20[e]
Stoichiometry	n ~1.05[b]	n ~0.995[d]	n ~0.95, 1.0, 1.5[e]
Element/Detection Method	ICP (ppm)	GDMS (ppm)	ICP (ppm)
B	88	0.4	-
C	592[f]	1,267[f]	-
N	46,620[f]	-	-
F	-	<10	-
Na	39	2.3	<460[e]
Si	40, 71[b]	17	60-155[e]
P	-	2.0	-
S	800[g], 890[b] 1,034[f]	7, 154[f]	-
Cl	-	13	-
K	39	1.4	20-640[e]
Ca	10, 19[b]	3	30-35[e]
Ti	2	1.6	-
Cr	1	0.8	-
Mn	-	5.7	20[e]
Fe	5, 4[b]	8-16	-
Cu	2, 9[c]	<1	-
Zn	1, 5[c]	<10	-
Ga	30[c]	0.9	-
Y	-	1.1	-
Zr	3[c]	-	-
I	11[c]	-	-
Ba	228[c]	-	-
Total Volatiles	-	32	-

[a] Manufacturer’s data.[285,286]

[b] Estimate based on ICP-OES,[287] ICP-MS and LA-ICP-OES/MS.

[c] ICP OES/MS estimate normalized to 30 ppm Ga counts.

[d] Estimate based on image analysis of MgO precipitates.

[e] Estimate based on values for $x = 1.0$ and 1.2.[55,77]

[f] Carbon-sulfur and nitrogen determination.

[g] Private communication.[288]

[h] SEM and TEM.

ICP OES/MS for sulfate powder indicated similar trace impurities (Si, S, Ca, Cr, Fe Cu, Zn) to reported values and also trace amounts of Li, V, Ni, Ga, Sr, Zr, I, and Ba.[287] However, some results are not shown due to uncertainty in dilutions and normalization standards. Carbon and sulfur content measured by infrared absorption were higher than reported, attributed to remnant organic synthesis and sulfate species for alkoxide and sulfate powder, respectively. High nitrogen content for sulfate powder was attributed to atmospheric nitrogen adsorption on the high surface-area powders and the analysis was not repeated for alkoxide powder. Values for hydroxide powders were based on communications with the researchers who manufactured them.[55,77] XRD for sulfate and alkoxide powders showed only peaks corresponding to spinel, indicating stoichiometric composition within the instrument resolution of ~1%. However, sulfate powder was determined Al_2O_3-rich (~$MgO:1.06Al_2O_3$) based on LA-ICP OES/MS (Section 4.1.2) and alkoxide powder MgO-rich (~$MgO:0.995Al_2O_3$) based on image analysis of MgO nodules in hot-pressed compacts (Section 4.3.2).[287] Particulate and filamentous contaminants up to millimeters in size were observed by optical and polarized-light microscopy and micron-sized agglomerates (Fig. 4.1) by SEM in sulfate and alkoxide powders. Crystallites varied from rounded to facetted and had an average size of ~35 nm for sulfate and ~30 nm for alkoxide powder, with few crystallites up to 100 nm in diameter (especially alkoxide powder) and agglomerates joined by sinter-necks up to ~300 nm in diameter (Fig. 4.2 and Fig. 4.3). Intensities, positions, and calculated lattice spacings of indexed SAD ring patterns for both powders matched spinel ICDD PDF Files 00-021-1152 and 00-005-0672[289] (Fig. 4.4).

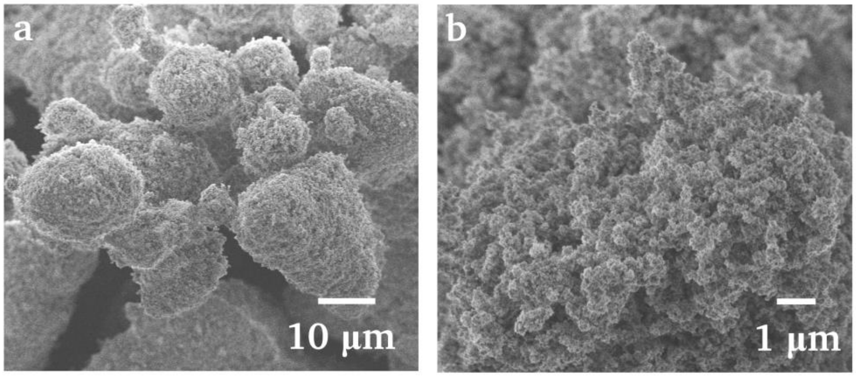

Fig. 4.1: Sulfate powder (a) agglomerates and (b) crystallites (SEM).

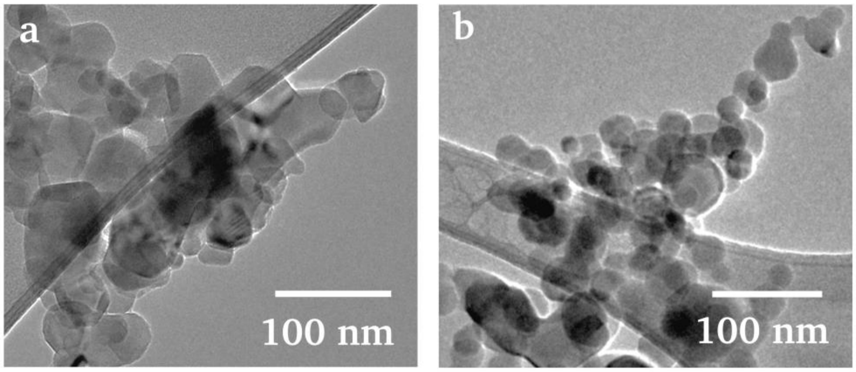
a
100 nm
b
100 nm

Fig. 4.2: Sulfate (a) and alkoxide (b) powder crystallites (TEM-BF).

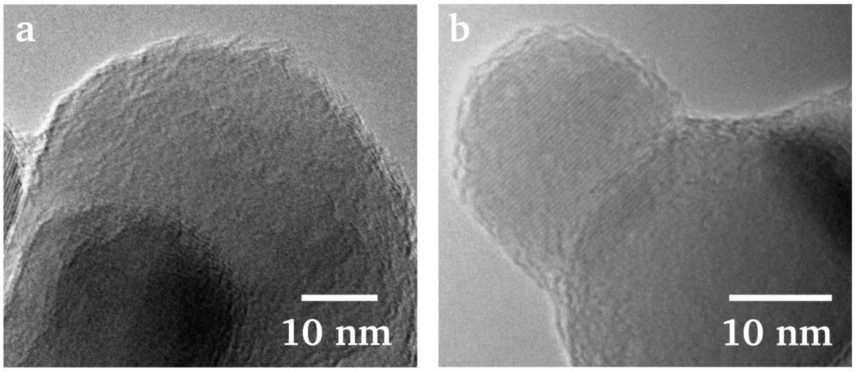
a
10 nm
b
10 nm

Fig. 4.3: Sulfate (a) and alkoxide (b) powder crystallites (HRTEM).

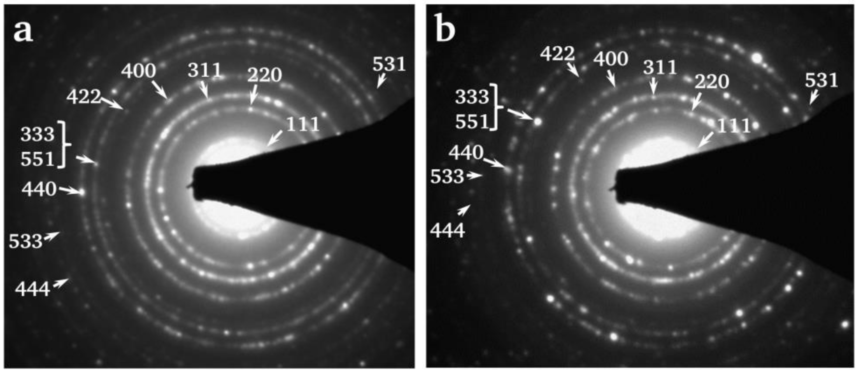
a
400
311
220
531
422
111
333
551
440
533
444
b
422
400
311
220
531
333
551
111
440
533
444

Fig. 4.4: Indexed electron-diffraction patterns for (a) sulfate and (b) alkoxide powder (TEM).

Laser-scattering particle-size results varied widely depending on dispersion, but were similar to reported values. Mercury pycnometry results are not shown as values were unreasonable, likely because the chamber volume was much larger than the powder samples. Sulfate powder had a Zeta potential of +13.5 mV and alkoxide powder -0.6 mV, the low values indicating both powders formed an unstable colloidal suspension and had a tendency to flocculate. SEM indicated LiF was well-dispersed by the various mixing methods, although LiF crystallites were significantly larger than spinel crystallites (Fig. 4.5).

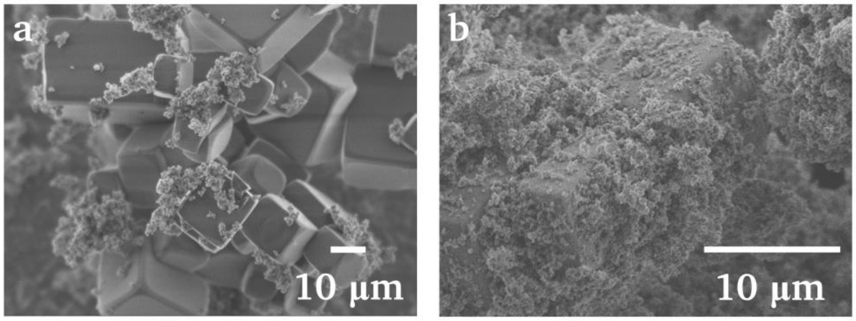

Fig. 4.5: Sulfate powder mixed with LiF (a,[221] b) (SEM).

Sulfate powder with LiF coarsened when heated in air above 900°C, whereas no coarsening was observed when heating with or without LiF under vacuum, even up to 1200°C (Fig. 4.6). This indicated a vapor-phase transport that was consistent with delayed sintering onset observed by dilatometry (Section 4.1.4) and larger grain-size in compacts hot-pressed with LiF addition (Sections 4.3.1 – 4.3.2).

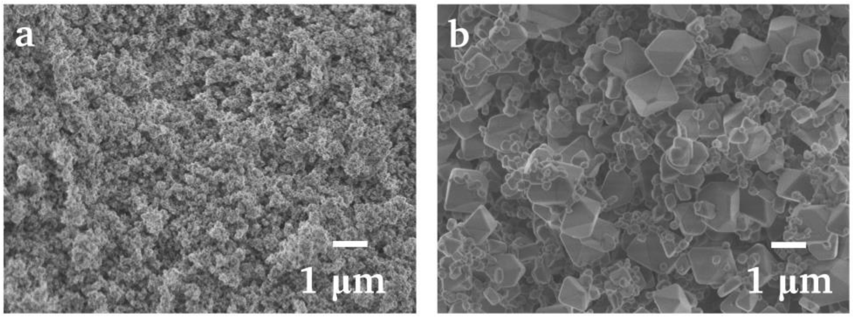

Fig. 4.6: Sulfate powder with 1 wt% LiF heated at 1200°C for 1 h in (a) vacuum and (b) air[221] (SEM).

Although sulfate and alkoxide powders had similar stoichiometry and particle-size characteristics, higher impurity content, agglomeration, and slight Al_2O_3-rich stoichiometry for sulfate powder rendered it less prone to attaining theoretical density and high transparency. Whereas, the high carbon content of alkoxide powder rendered it more likely to exhibit absorption. Sulfate powder could be improved by processing in H_2 to remove sulfur, and alkoxide powder by annealing in oxygen to combust remnant carbon.

4.1.2 Thermal Analysis

Sulfate and alkoxide powders exhibited minimal thermal activity and lost <2% and <1% of their initial mass, respectively, attributed mainly to adsorbed water vaporization (Fig. 4.7).

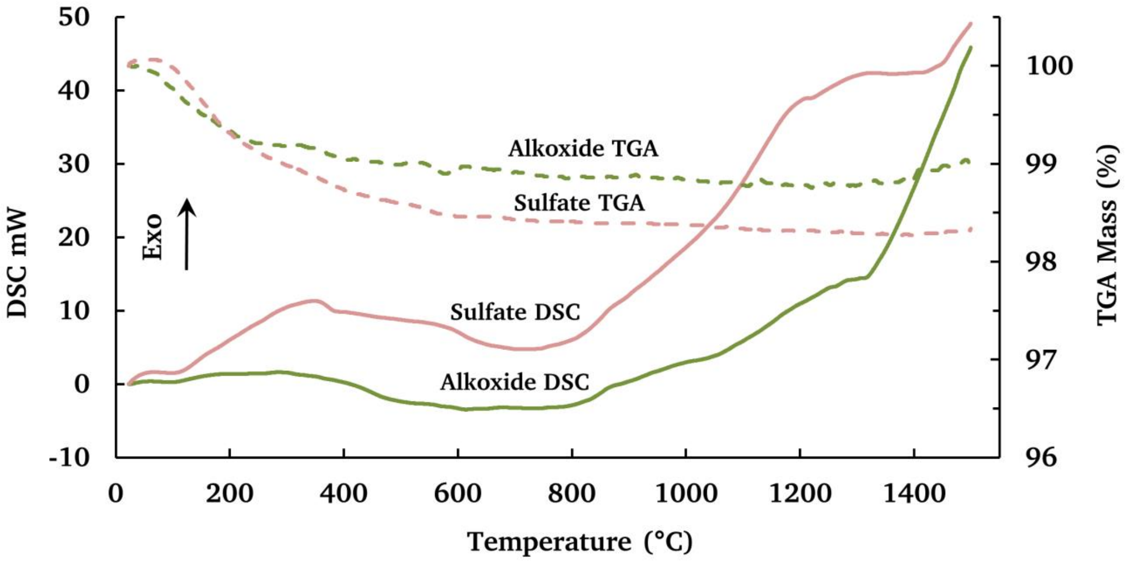

Fig. 4.7: STA (DSC + TGA) for sulfate and alkoxide powders in argon at 5K/min ramp.

Sulfate powder with LiF lost mass concomitant with the amount added plus adsorbed water (Fig. 4.8). The LiF melting and vaporization endotherms were discernible, especially for 10 wt% LiF addition, for which the vaporization endotherm was split into peaks at 1100°C and 1175°C, possibly indicating an exotherm in between. The reason for the slight initial mass increase noted for samples with LiF is unknown. Simultaneous thermal analysis (STA) of pure LiF in argon showed melting (850°C) and vaporization (1000°C – 1400°C) endotherms, the latter concomitant with complete mass loss, consistent with reports in the literature.[216] STA of MgF_2 and $LiAlO_2$, by-products of the reaction between LiF and spinel, in argon indicated 15% mass loss between 1000°C and 1350°C, corresponding to the 16 wt% LiF calculated to form along with spinel (Fig. 4.9). An endotherm at 740°C was likely the formation the eutectic liquid MgF_2:LiF, an exotherm at 760°C may have been the formation of spinel, and a small endotherm at 1270°C was consistent with the melting of unreacted MgF_2 (T_M 1263°C).

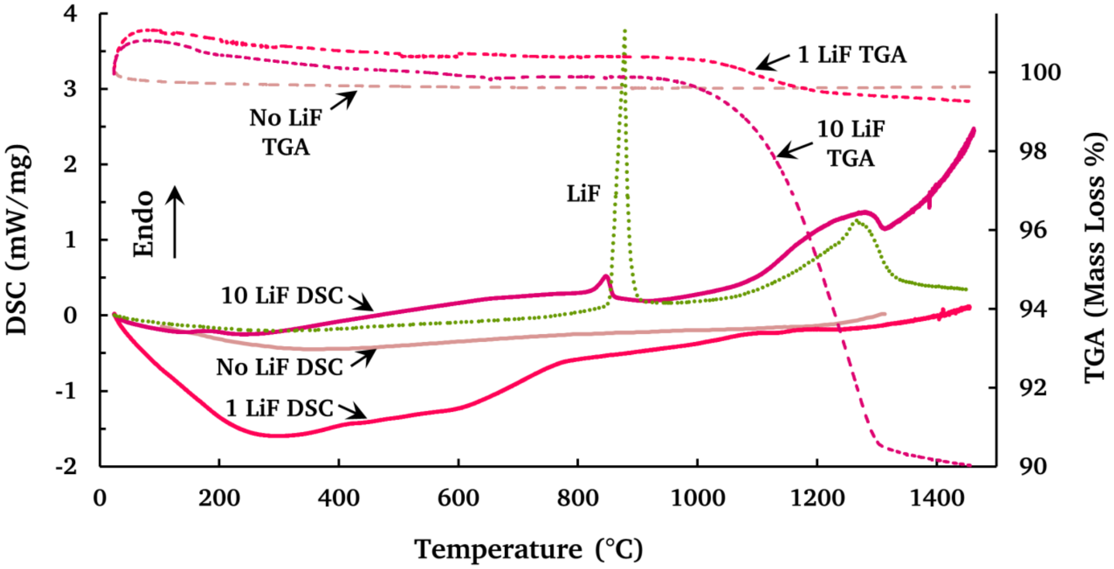

Fig. 4.8: STA for sulfate powders with 0, 1, and 10 wt% LiF addition in argon at 5-20 K/min with LiF DSC at 20% scale superimposed for reference.

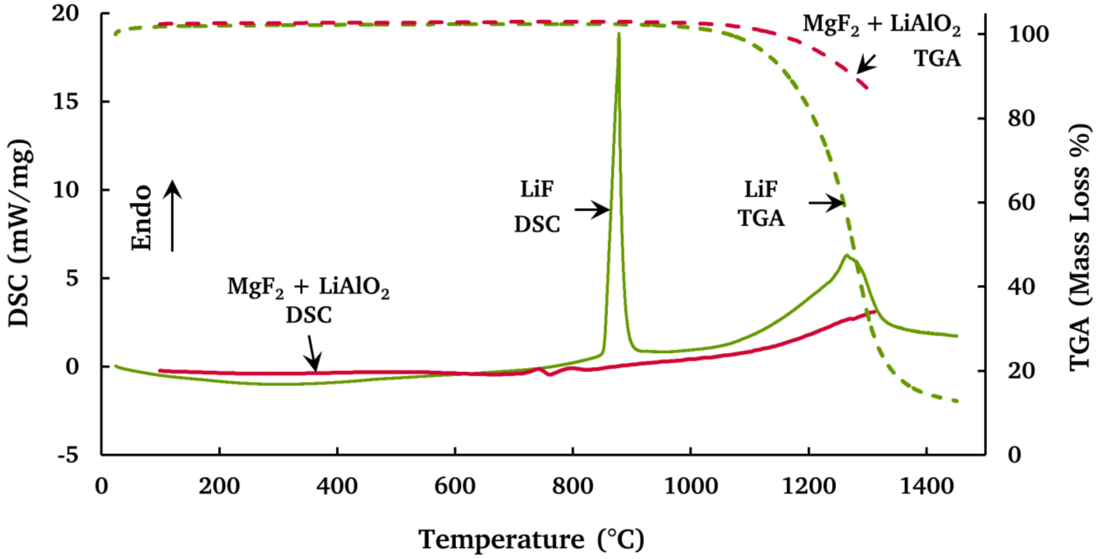

Fig. 4.9: STA for LiF and MgF_2 + $LiAlO_2$ in argon at 10-20 K/min.

STA combined with mass spectroscopy (STA-MS) for pure LiF in argon indicated argon isotopes and trace water vapor, the latter consistent with the hygroscopy of LiF. Weak signals for *m/z* 16 (O+) and 44 (CO_2+, N_2O+) >700°C and between 1150°C and 1500°C were coincident with the melting and vaporization of LiF, respectively. Signals for *m/z* 7 (Li+), 19 (F+), and 26 (LiF+) were not detected despite complete mass loss, suggesting LiF condensed on the vapor-transfer capillary, reacted with the crucible or atmospheric gases, passed through undetected, or formed species that were neutral, negatively-charged, or with greater molecular weight than the detection limit (*m/z* = 100). Lithium may have outgassed as masses 16 (O, Li_2H_2), 30 (NO, Li_2O), and 44 (N_2O, CO_2, Li_4O^{2+}) detected within its vaporization range and fluorine gas may not have ionized and been obscured by ^{38}Ar. STA-MS for MgF_2 and $LiAlO_2$ in argon indicated argon isotopes and trace atmospheric gases and water vapor. Weak (30 ppmv) *m/z* 2 (H_2) peaks at 675°C and 975°C were of unknown origin. As for pure LiF, no signals were observed for *m/z* 7 (Li+), 19 (F+), 26 (LiF+), 38 (F_2+), or 62 (MgF_2+).

STA-MS for alkoxide powder in argon indicated argon isotopes and trace atmospheric gases and water vapor. Weak *m/z* 44 (CO_2+) signals <400°C indicated residual organics or carbon, possibly flame-spray pyrolysis synthesis remnants. STA-MS for sulfate powder in argon indicated mainly argon isotopes and trace atmospheric gases and water vapor, which yielded distinct peaks up to 0.4 vol% at 100°C and 150°C upon vaporization. Weak (<100 ppmv) *m/z* 44 (CO_2+) peaks at 150°C and 675°C were likely evaporation or combustion of organic contamination. Similar results were obtained in air for alkoxide and sulfate powders with mainly atmospheric gases detected. STA-MS for sulfate powder with 1 wt% LiF in argon indicated mainly argon isotopes and trace atmospheric gases and water vapor. Water vapor signals occurred throughout, with peaks up to 0.2 vol% between 100°C and 350°C consistent with vaporization. A secondary peak with an associated endothermic rise between 650°C and 750°C may have been LiF-assisted decomposition of a magnesium or aluminum hydrate. A weak *m/z* 44 (CO_2+) signal <800°C peaking at 300°C (50 ppmv), associated with weak *m/z* 16 (O+, CH_4+) and 32 (O_2+, CH_3OH+) signals, was likely the evaporation or combustion of methanol used in mixing. Distinct *m/z* 32 (O_2+, S+), 48 (SO+), and 64 (SO_2+) peaks (20 ppmv, 20 ppmv, and 150 ppmv, respectively) coincident with the vaporization endotherm of LiF at 1075°C (Fig. 4.10), along with their fragmentation patterns, were consistent the decomposition of the intermediate synthesis product (Mg,Al)SO_4 and the release of SO_2, consistent with thermodynamic simulations (Section 4.1.3).

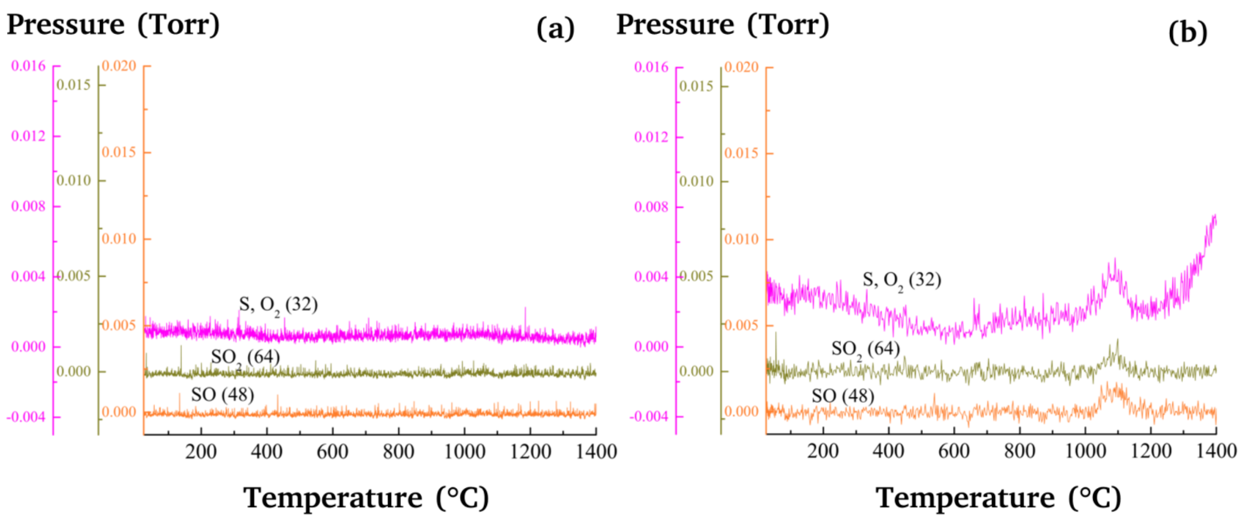

Fig. 4.10: STA-MS for *m/z* 32, 48, and 64 shown at a finer scale for (a) sulfate-derived powder without LiF and (b) with 1 wt% LiF in argon.

STA-MS correctly indicated *m/z* signals for atmospheric gases and water vapor and argon and its isotopes throughout the runs. However, some species were likely obscured by outgassing of species of the same mass, such as Ar-40 and MgO, and neither LiF nor its constituents were detected. Nevertheless, STA-MS helped identify chemical reactions with LiF and determine the outgassing behavior of volatiles (including LiF by TGA). A main finding was the repeatable obtainment of *m/z* signals consistent with the fragmentation of SO_2 within a narrow temperature range centered at 1075°C, and concomitant with an endothermic rise, only for sulfate powder with LiF. This confirmed a vapor-phase reaction between LiF and unreacted magnesium and/or aluminum sulfates and was corroborated by thermodynamic simulations (Section 4.1.3) and ICP (Section 4.2.2). This reaction identified the cleansing mechanism of LiF, whereby it reacts with impurities to form volatile species that can be removed, and partially answered why LiF was required to obtain transparency with sulfate powders. The outgassing behavior of LiF and volatiles such as water vapor helped direct the proper pressure-temperature regime to ensure their removal and enable attaining transparency.

4.1.3 Thermodynamic Simulations

Gibb's energy minimization equilibrium composition simulations in vacuum and air using HSC predicted the reaction of $MgAl_2O_4$ and LiF to form MgF_2 and $LiAlO_2$, consistent with reports in the literature (Eq. 4.1).[50,212] In air, the products were predicted to form above 1000°C along with LiF gas and trace amounts of AlF_3, and Li_2F_2 above 1200°C. Simulations with equal amounts of LiF and spinel in vacuum (replicating the hot-press environment) indicated a lower reaction temperature of ~750°C, consistent with the formation of a eutectic with MgF_2 and lower-temperature sintering onset indicated by dilatometry (Section 4.1.3). Simulations with MgF_2 and $LiAlO_2$ in vacuum predicted the reformation of spinel, consistent with reports in the literature.[50,212] Simulations with $Mg(SO_4)$, $Al_2(SO_4)_3$, and LiF in vacuum predicted the formation of MgF_2, $LiAlO_2$, $MgAl_2O_4$, and SO_2 (Eq. 4.2), consistent with STA-MS. Although, it is likely these reactions involved mixed-metal sulfides (Eq. 4.3 and 4.4), which HSC does not simulate. Simulations also confirmed the reaction of LiF or MgF_2 with calcium and iron (Eq. 4.5 and 4.6) were energetically favorable, consistent with lower concentrations for these impurities observed by ICP in compacts hot-pressed with LiF (Section 4.2.2). Simulations with spinel and carbon indicated the formation of aluminum oxy-carbides, which hot-press experiments with Al_2O_3 additions indicated are likely partly responsible for absorption (Section 4.2.3).

$$2LiF + MgAl_2O_4 \rightarrow MgF_2 + 2LiAlO_2 \tag{4.1}$$

$$2MgSO_4 + 2Al_2(SO_4)_3 + 2LiF \rightarrow MgF_2 + 2LiAlO_2 + MgAl_2O_4 + 6SO_2 + 2O_2 \tag{4.2}$$

$$(Mg, Al)SO_4 + 2LiF_{(g)} \rightarrow (Mg, Al)O + SO_{2(g)} + Li_2O_{(g)} + F_{2(g)} \tag{4.3}$$

$$(Mg, Al)O + SO_{2(g)} + Li_2O_{(g)} + F_{2(g)} \rightarrow (Mg, Al)O + SO_{2(g)} + 2LiF_{(g)} + \tfrac{1}{2}O_{2(g)} \tag{4.4}$$

$$MgF_2 + CaO \rightarrow CaF_2 + MgO \tag{4.5}$$

$$Fe_2O_3 + 4LiF \rightarrow 2FeF_2 + 2Li_2O + \tfrac{1}{2}O_{2(g)} \tag{4.6}$$

4.1.4 Dilatometry

Despite using the same cold-pressing conditions, 55% green density was achieved with alkoxide powder and only 51% with sulfate powder (Fig. 4.11). Cold-pressed alkoxide powder densified more readily and reached near-theoretical density, aided by the higher green density, the small size of samples, and the slow ramp rates during dilatometry. Whereas, cold-pressed sulfate powder samples reached <95% density and <60% with LiF addition. Densification curves for oxidizing and reducing atmosphere showed little difference, but alkoxide powder samples sintered in H_2 were more transparent than air-sintered samples.

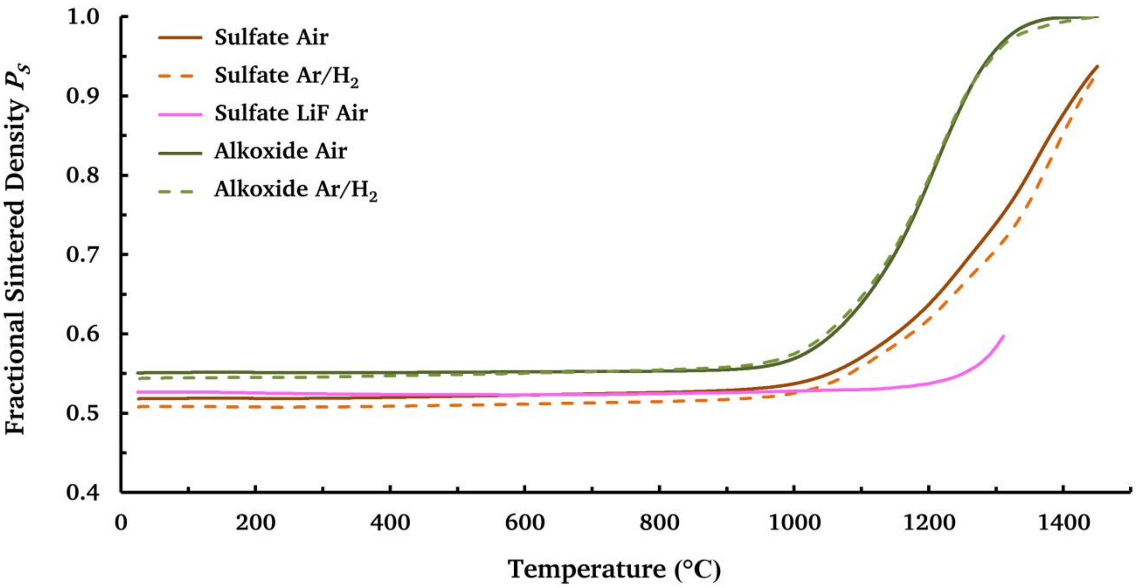

Fig. 4.11: Fractional sintered density relative to theoretical as a function of temperature for dilatometry with cold-pressed sulfate and alkoxide powder samples (inset).

Fractional theoretical sintered density (Fig. 4.12) calculated from displacement corrected for thermal expansion mismatch and pressure strain during hot-pressing indicated sulfate and alkoxide powder compacts deviated from pure thermal expansion at ~1000°C, with alkoxide powder compacts shrinking more. Significant shrinkage occurred upon pressure application (sharp drops at 900°C and 1200°C), lowering the temperature at which closed porosity was attained (92% density - dashed line in Fig. 4.12). Compacts hot-pressed with LiF deviated from pure thermal expansion at ~600°C, 400°C lower than without LiF, with a sintering onset at ~800°C. The latter was consistent with the formation of the MgF_2:LiF eutectic and its lower onset temperature in reducing conditions, as indicated by thermodynamic simulations. The ~200°C lower sintering onset compared to dilatometry (>1000°C) indicated the nominal 3 MPa pressure applied prior to full pressure application, as opposed to negligible pressure for dilatometry, was enough to overcome coarsening and force densification to lower temperatures.

Dilatometry confirmed the detrimental effect lower green density on densification for sulfate powder compacts, the former attributed to non-optimal particle coordination and agglomeration. Incomplete densification was also attributed to swelling caused by volatile impurities and coarsening due to Al_2O_3-rich stoichiometry. These shortcomings demonstrated why sulfate powder required LiF to remove impurities and pressure-assisted sintering to close inter-agglomerate pores. Dilatometry also demonstrated that pressure-assisted sintering was required with LiF addition due to the coarsening it induces. Higher green densities for alkoxide powder compacts and densification-enhancing MgO-rich stoichiometry resulted in complete densification and highly-transparent compacts. Although less accurate than dilatometry, hot-press displacement showed that pressure causes significant shrinkage and lowers the temperature at which closed porosity is attained, potentially trapping impurities and additives with higher volatilization temperatures. Whereas LiF-induced coarsening retarded densification without pressure during dilatometry, only 3 MPa was enough to overcome coarsening and lower densification temperature by several hundred degrees. This finding, in combination with observed coarsening behavior, suggests spinel compacts hot-pressed with LiF densify by pressure directing surface and vapor transport from inter-particle contacts to voids, contrary to the detrimental nature of these transport mechanisms without pressure.

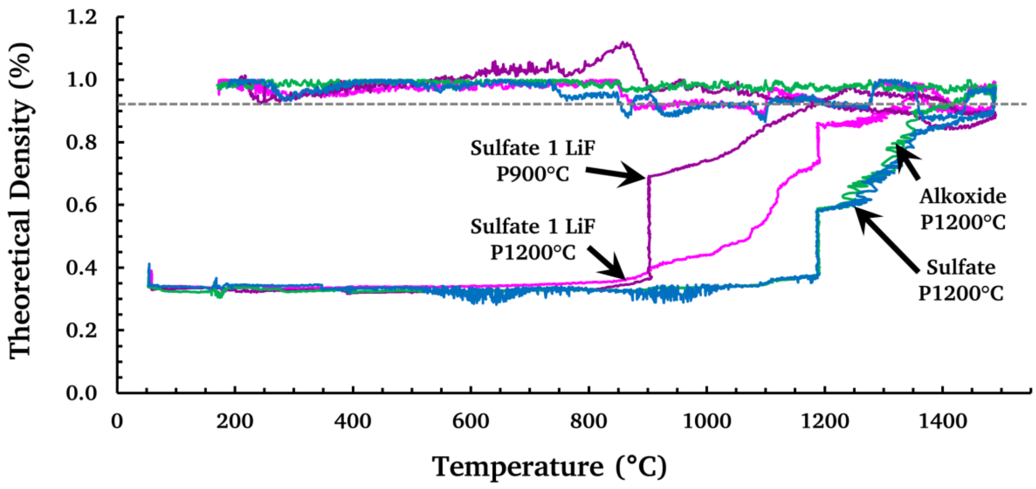

Fig. 4.12: Hot-press fractional theoretical sintered density versus temperature corrected for pressure and thermal expansion as a function of powders and LiF addition. Dashed line indicates closed porosity at 92% theoretical density (~1250-1350°C).

4.2 Bulk Compacts

Bulk compacts were characterized to relate bulk properties to starting powders, processing, microstructure, and interfaces. The stoichiometry, impurity content, microstructure, grain size, fracture mode, and optical properties of bulk samples made by pressureless sintering and hot-pressing, sometimes in combination with hot-isostatic pressing (HIP), using powders with varying stoichiometries and impurity contents derived from sulfates, alkoxides, and hydroxides, with and without LiF and Al_2O_3 additions, were characterized (Sections 4.2.1 – 4.2.4) and correlated with interface properties and behaviors (Section 4.3).

4.2.1 Dense Compacts

Detailed examination was conducted on compacts hot-pressed with 35 MPa applied at 1200°C using (i) sulfate powder, (ii) sulfate powder with pressure applied at 900°C instead of 1200°C, (iii) sulfate powder with 1 wt% LiF, (iv) alkoxide powder, and (v) alkoxide powder with 0.25 wt% LiF, and compacts hot-pressed and HIPed using hydroxide powders with (vi) $x = 0.95$, (vii) $x = 1.0$, and (viii) $x = 1.5$ (Fig. 4.13 and Fig. 4.14). All compacts were >99.5% dense based on Archimedes density measurement and porosity was not observed.[23]

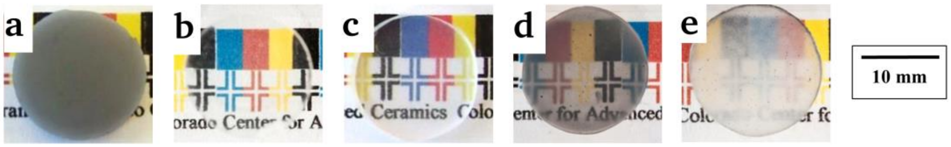

Fig. 4.13: Compacts hot-pressed using the standard profile with (a) sulfate powder, (b) sulfate powder with 1 wt% LiF, (c) sulfate powder with 1 wt% LiF but with pressure applied at 900°C, (d) alkoxide powder and (e) alkoxide powder with 0.25 wt% LiF (compacts 10 mm above template).

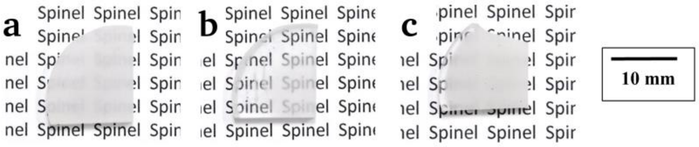

Fig. 4.14: Samples cut from hot-pressed and HIPed hydroxide powder compacts with $x = 0.95$ (a), 1.0 (b), and 1.5 (c) (10 mm above template).

Despite similar or greater impurity content compared to sulfate powder, compacts made using hydroxide powders were transparent, likely due partly to the presence of different impurity species and HIPing, which sometimes also increased transparency in sulfate powder compacts. Stoichiometric hydroxide powder compacts had the highest transparency, with scatter in non-stoichiometric compacts likely caused by MgO and Al_2O_3 precipitates.

Sulfate compacts were opaque, whereas identically-processed higher-purity alkoxide compacts were transparent (Fig. 4.15). Since porosity was not observed, impurities likely caused opacity. When processed with 1 wt% LiF, sulfate powder compacts were clear and transparent (Fig. 4.16). However, every processing variable impacted the transparency of compacts with LiF. Acoustic mixing or ball milling, ramping at 10°C/min instead of 6°C/min during hot-pressing, and larger sample size (especially thickness), all increased scatter, suggesting impurities and/or LiF as the source of degraded transparency. Applying pressure at too low a temperature also degraded transparency (Fig. 4.17) and yielded opaque compacts when applied below 900°C. This also pointed to impurities and/or LiF since pressure can force densification to occur below the volatilization temperature of some species. The best results were obtained by adding 1 wt% LiF by ultrasonic mixing in ethanol followed by rotary evaporation, ramping at 6°C/min, and applying pressure at 1200°C during hot-pressing ("standard profile").

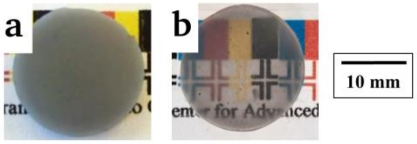

Fig. 4.15: Sulfate (a) and alkoxide (b) powder compacts hot-pressed using the standard profile (10 mm above template).

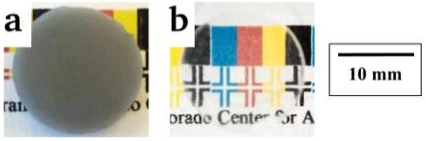

Fig. 4.16: Sulfate powder compacts (a) without and (b) with 1 wt% LiF hot-pressed using the standard profile (10 mm above template).

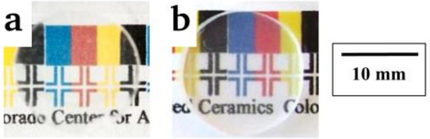

Fig. 4.17: Sulfate powder compacts with 1 wt% LiF hot-pressed with pressure applied at (a) 1200°C and (b) 900°C (10 mm above template).

The highest transparency for alkoxide powder compacts was obtained using a maximum sintering temperature of 1400°C, and in contrast to sulfate powder compacts, by applying pressure at 900°C instead of 1200°C during hot-pressing. These observations support that without volatile transparency-inhibiting impurities, densification can be forced to lower temperature without adverse effect. Despite better results using these processing parameters, compacts made using the standard hot-press profile were examined in detail to compare with sulfate powder compacts. LiF addition eliminated absorption, but it increased scatter much more than for sulfate powder compacts (Fig. 4.18), strongly suggesting the lower densification temperature for alkoxide powders trapped more LiF. LiF addition was scaled to S, Fe, and Ca impurity content, with the calculated optimal of 0.05 wt% yielding the least scatter.

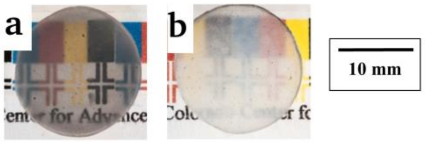

Fig. 4.18: Alkoxide powder compacts hot-pressed using the standard profile with (a) 0 and (b) 0.25 wt% LiF addition (10 mm above template).

Transparency differences between compacts strongly suggested (i) impurities in sulfate powder caused scatter (opacity) and absorption (grey tint), (ii) trapped LiF or its by-products caused scatter, (iii) ball or acoustic mixing caused agglomeration, (iv) higher temperature ramps and pressure application forced densification to lower temperature, trapping species with higher volatilization temperatures, and (v) precipitation in astoichiometric powders increased scatter.

4.2.2 Laser-Ablation Inductively-Coupled Plasma (LA-ICP OES/MS)

ICP-OES/MS by laser ablation on compacts hot-pressed using the standard profile with sulfate powder with and without 1 wt% LiF showed a decreasing concentration of iron, sulfur, and calcium from the geometric center to exterior surfaces (Table 4.2). This gradient may also have been present for species below the detection limit of ICP. In compacts processed with LiF, magnesium content was lower, impurity concentrations were lower (sometimes by an order of magnitude), and approximately half of the added lithium remained. STA-MS, TEM (Section 4.3.2), and SIMS (Section 4.3.5) indicated that most of the fluorine left the system, with only minor amounts remaining as MgF_2 in isolated triple junctions. Thus, the remnant lithium was likely not LiF. The high silica concentration suggested contamination from glassware during processing, although no detectable correlation was found with microstructure or optical and electronic properties.

Table 4.2: LA ICP-OES/MS at the Geometric Center and Exterior Surface of Compacts Hot-Pressed with Sulfate Powder with and without LiF and Pressure Applied at 1200°C.

Species	Units	No LiF Center	No LiF Surface	LiF Center	LiF Surface
Al_2O_3	wt%	73.6	72	74	74.2
MgO	wt%	26.2	27.8	25.4	25.3
CaO	ppm	93	32	19	4
SiO_2	ppm	1,211	1,428	1,208	764
Fe_2O_3	ppm	323	81	16	25
S	ppm	272	468	339	34
LiF	ppm	-	-	14,545	11,794
$MgO{:}nAl_2O_3$	Ratio	1.10	1.02	1.15	1.16

Lower impurity and magnesium concentrations with LiF addition were consistent with reactions forming volatile fluorides indicated by STA-MS and thermodynamic simulations. Impurity gradients were consistent with differential sintering, in which compact exteriors attained closed porosity before interiors (in part due to volatile impurity outgassing), trapping remnant impurities and LiF in compact interiors. Lower iron, calcium, and sulfur concentration with LiF addition was consistent with SEM-EDS of precipitate found on the exterior surfaces of compacts after hot-pressing, which were found to be composed of iron, calcium, and sulfur. Lower impurity content was also consistent with the disappearance of impurity-decorated aggregates of submicrometer grains (Section 4.3.2) and increased transmittance (Section 4.2.3) in sulfate powder compacts. Lower iron concentration was consistent with the disappearance of an iron-rich phase in alkoxide powder compacts with LiF. Lower magnesium content with LiF addition was consistent with the formation and evaporation of MgF_2 and the coarsening behavior of the resulting Al_2O_3-rich composition. The results also showed why applying pressure at lower temperatures when hot-pressing compacts with LiF addition resulted in opacity (Section 4.2.1), as it forces densification to lower temperatures, trapping LiF and its reaction products.

4.2.3 Spectrophotometry

Transmittance, reflectance, scatter, and absorptance for hot-pressed and HIPed hydroxide powder compacts, and for selected sulfate and alkoxide powder compacts hot-pressed with 1.5 g of powder with and without LiF and with pressure applied at 1200°C are shown in Fig. 4.19 – Fig. 4.22 up to 750 nm, with transmittance relatively constant in the IR (not shown). For sulfate powder compacts without LiF, in-line transmittance was negligible, forward scatter increased in the visible, reaching up to ~40% in the IR, and absorptance peaked to 95% at 250 nm and remained above ~45% in the IR. For sulfate powder compacts with 1 wt% LiF, in-line transmittance was greater than 80% (theoretical ~87%)[290] between 500 nm and 2500 nm, forward scatter was up to ~40% at 200 nm, and absorptance was negligible. For alkoxide powder compacts without LiF, forward scatter peaked at 20% at 270 nm and was negligible at longer wavelengths, whereas absorptance was significant over the visible, peaking near 90% at 210 nm and remaining above 35% in the IR. Sulfate powder compacts hot-pressed with 1.5 g of powder with pressure applied at 900°C displayed much lower in-line transmittance than when pressure was applied at 1200°C, being greater than 80% only between 1200 and 2500 nm. Compacts hot-pressed with 3.5 g of powder displayed significantly lower in-line transmittance. Sulfate powder compacts hot-pressed with LiF and standard processing subjected to UV-laser irradiation exhibited fluorescence that fit one Gaussian peak at 710 nm and a smaller one at 757 nm (Fig. 4.23), similar to some reports.[291]

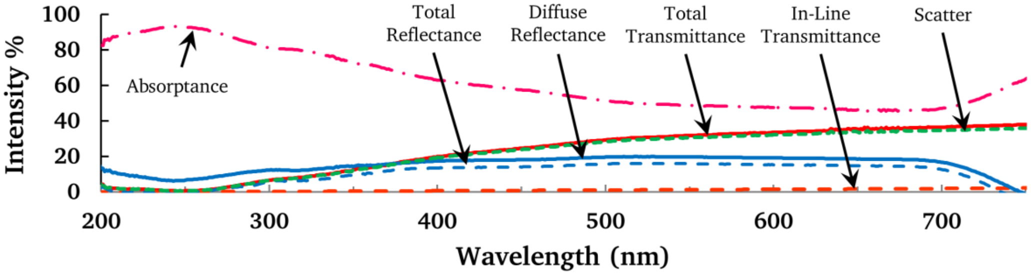

Fig. 4.19: Total (red) and in-line (dashed red) transmittance, total (blue) and diffuse (dashed blue) reflectance, scatter (dashed green), and absorptance (dashed pink) versus wavelength for sulfate powder compacts hot-pressed with the standard profile.

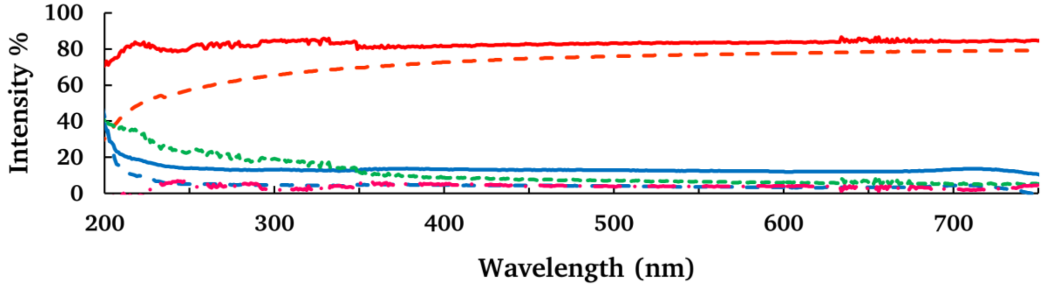

Fig. 4.20: Total (red) and in-line (dashed red) transmittance, total (blue) and diffuse (dashed blue) reflectance, scatter (dashed green), and absorptance (dashed pink) versus wavelength for sulfate powder compacts with 1 wt% LiF hot-pressed with the standard profile.

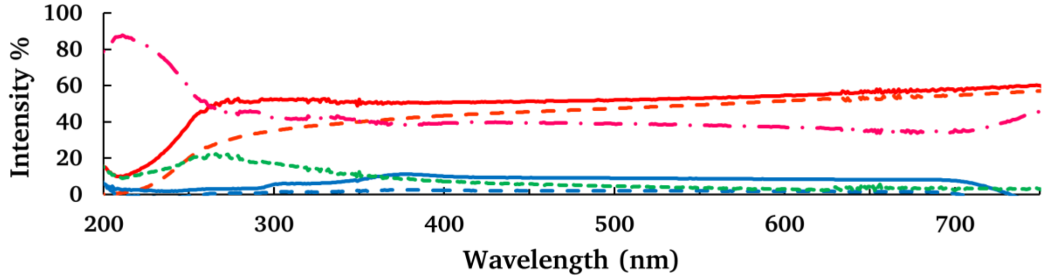

Fig. 4.21: Total (red) and in-line (dashed red) transmittance, total (blue) and diffuse (dashed blue) reflectance, scatter (dashed green), and absorptance (dashed pink) versus wavelength for sulfate powder compacts with 1 wt% LiF hot-pressed with pressure applied at 900°C instead of 1200°C.

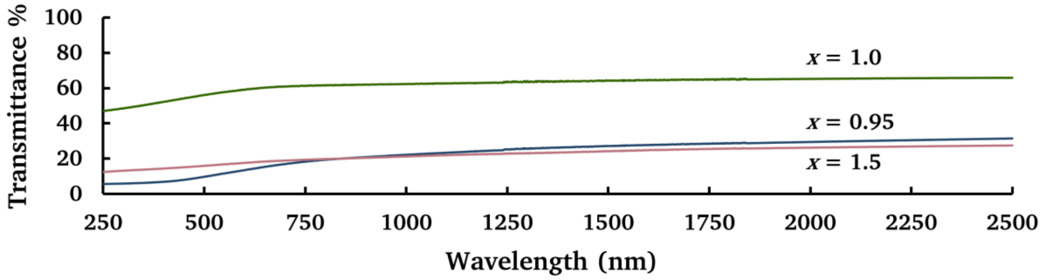

Fig. 4.22: Total transmittance for hot-pressed and HIPed hydroxide powder compacts with x = 0.95 (blue), 1.0 (green), and 1.5 (purple).

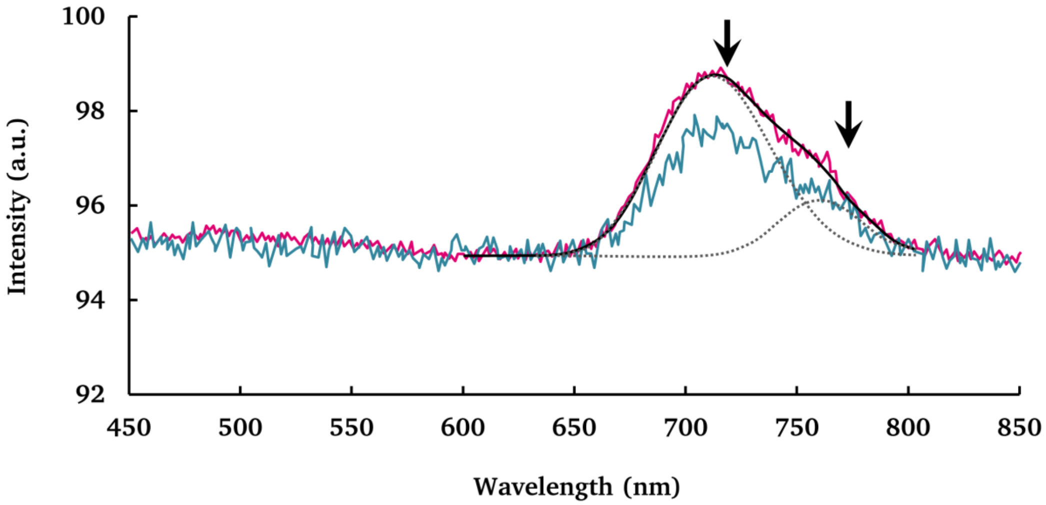

Fig. 4.23: UV-laser induced fluorescence for a sulfate powder compact hot-pressed with 1 wt% LiF performed with shorter (blue) and longer (pink) integration time. Gaussian fit (black) deconvolution (dotted) yielded two peaks at 710 nm and 757 nm (arrows).

Low transmittance for sulfate powder compacts without LiF was consistent with an amorphous impurity phase of varying areal extent decorating grain-boundaries in aggregates of submicrometer grains (Section 4.3.2). For sulfate powder compacts with LiF, scatter at short wavelengths was consistent with isolated impurity phases and pockets of remnant MgF_2 of the same size as the wavelength of the scattered light (Section 4.3.2). Ramping at 10°C/min, application of pressure at 900°C, or using 3.5 g of powder instead of using 1.5 g of powder, ramping at 6°C/min, and applying pressure at 1200°C, trapped more LiF and impurities (Section 4.2.2, 4.3.2), increasing scatter enough to cause opacity in some compacts. The fluorescence observed with LiF addition was not consistent with that observed for common impurities in spinel, LiF, or MgF_2. Scatter at short wavelengths in alkoxide powder compacts was consistent with MgO nodules and strain fields that surrounded them (Section 4.3.2), while absorption was consistent with carbon contamination (Sections 4.2.1 and 4.2.4).

4.2.4 Raman Spectroscopy

Raman spectra for transparent hot-pressed sulfate and alkoxide powder compacts and a stoichiometric single-crystal matched reported spectra for spinel (Fig. 4.24).[100,101] Sulfate powder compacts exhibited a peak at 525 cm^{-1}, which was absent in compacts with LiF, suggesting the removal of an impurity species (Fig. 4.24a). These compacts also exhibited fluorescence at higher wave numbers. The broad shoulder at 350 cm^{-1} and peak at 680 cm^{-1} in

Fig. 4.24b are associated with a low inversion parameter[292] and these were more prominent for the single crystal. Raman spectra for alkoxide and sulfate powder compacts without LiF closely matched the single-crystal spectrum, whereas those with LiF had features associated with a higher inversion parameter. Spectra for dark spots in sulfate and alkoxide powder compacts with and without LiF matched spectra for graphite foil and pyrolytic graphite, indicating these features were caused by carbon or organic contamination.

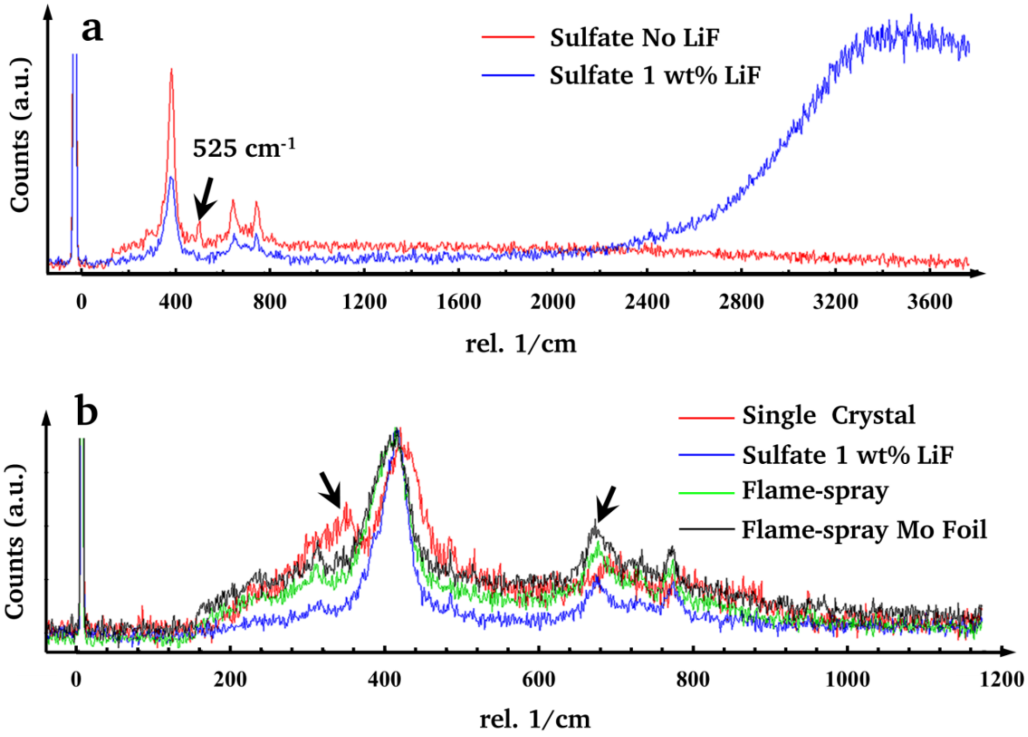

Fig. 4.24: Raman spectra for (a) compacts hot-pressed with sulfate powder with and without 1 wt% LiF, and (b) a spinel single crystal and compacts hot-pressed with sulfate powder with 1 wt% LiF and with alkoxide ("flame-spray") powder (arrows indicate features associated with low inversion).

4.3 Interfaces

The surfaces and grain boundaries of transparent spinel compacts made using powders with different stoichiometries and additives were examined by optical and polarized-light microscopy (Section 4.3.1), scanning electron microscopy (SEM) in conjunction with energy-dispersive X-ray spectroscopy (EDS) and electron-backscatter diffraction (EBSD) (Section 4.3.2), transmission (TEM) and scanning TEM (STEM) in conjunction with selected-area diffraction (SAD), convergent-beam electron diffraction (CBED) (Section 4.3.4), EDS, and electron-energy loss spectroscopy (EELS) (Section 4.3.3), time-of-flight secondary-ion mass spectroscopy (TOF-SIMS) (Section 4.3.5), parallel-ion electron spectroscopy (PIES) (Section 4.3.6), atomic-force (AFM) (Section 4.3.7), and electrochemical impedance spectroscopy (EIS) (Section 4.3.8). Interface properties were correlated to stoichiometry, impurity and additive content, microstructure, processing conditions, and bulk properties.

4.3.1 Optical Microscopy

The microstructure of compacts hot-pressed with the standard profile (35 MPa applied at 1200°C) consisted of equiaxed micron-sized matrix grains with an average size of 10 μm for sulfate powders (Fig. 4.25a) and 4 μm for alkoxide powders (Fig. 4.25b), and abnormal grains up to hundreds of microns in diameter that were more prevalent near surfaces (Fig. 4.26). Addition of 1 wt% LiF to sulfate powders more than doubled grain size to 24 μm (Fig. 4.27) and 0.25 wt% LiF to alkoxide powders quadrupled it to 16 μm (Fig. 4.28). For compacts hot-pressed with sulfate powder with 1 wt% LiF, applying pressure at 900°C instead of 1200°C resulted in a bi-modal matrix grain-size distribution with smaller average grain size (Fig. 4.29). Some abnormal grains in sulfate and alkoxide powder compacts with and without LiF appeared to radiate from a point-source and the interface between these and matrix grains was planar (Fig. 4.30), suggesting the presence of an impurity liquid phase at processing temperature.

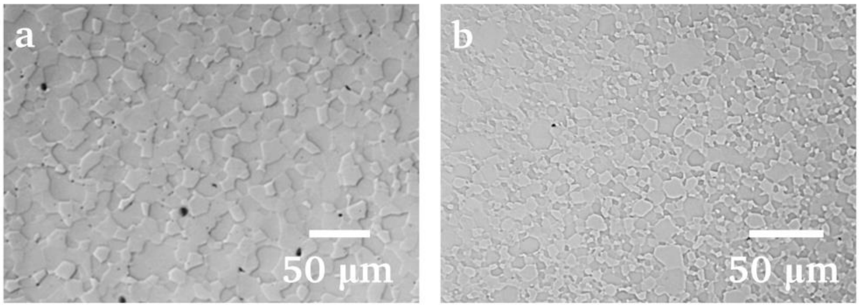

Fig. 4.25: Matrix grains in compacts hot-pressed with pressure applied at 1200°C using (a) sulfate powder and (b) alkoxide powder (optical microscopy 10X, 20X obj.).

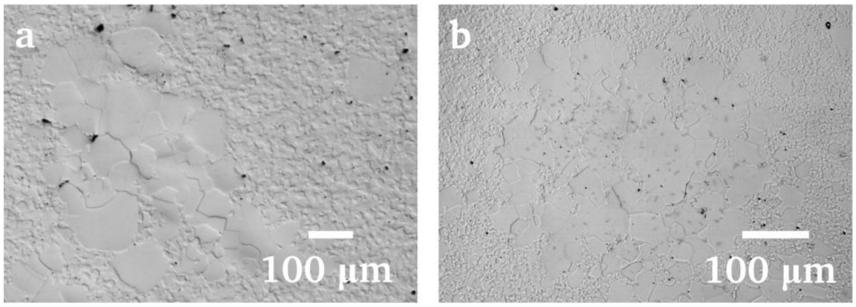

Fig. 4.26: Abnormal grains in compacts hot-pressed with pressure applied at 1200°C using (a) sulfate powder and (b) alkoxide powder (optical microscopy 10X obj.).

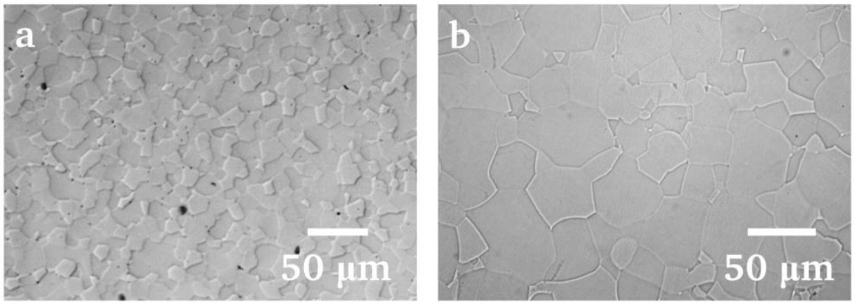

Fig. 4.27: Matrix grains in compacts hot-pressed with pressure applied at 1200°C using sulfate powder (a) without and (b) with 1 wt% LiF (optical microscopy 10X, 20X obj.).

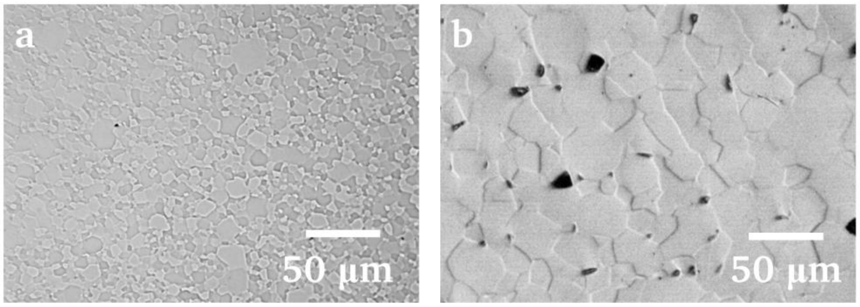

Fig. 4.28: Matrix grains in compacts hot-pressed with pressure applied at 1200°C using alkoxide powder (a) without and (b) with 0.25 wt% LiF (optical microscopy 20X obj.).

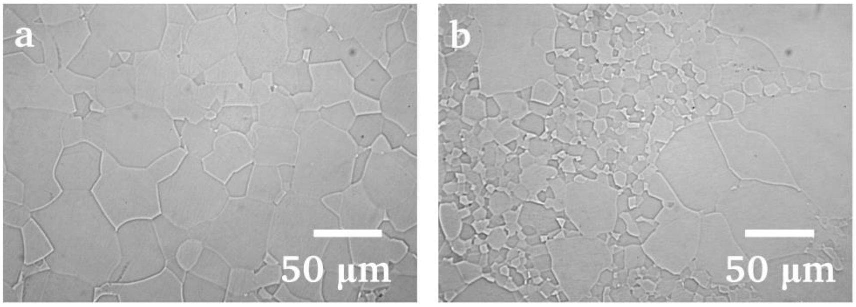

Fig. 4.29: Microstructure of compacts hot-pressed using sulfate powder with 1 wt% LiF with pressure applied at (a) 1200°C and (b) 900°C (optical microscopy 20X obj.).

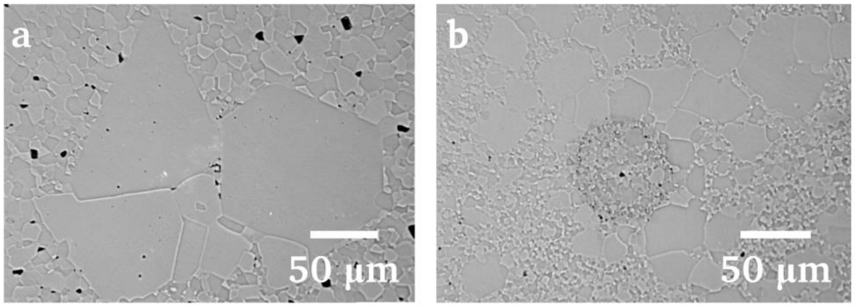

Fig. 4.30: Abnormal grains in compacts hot pressed with (a) sulfate powder with 1 wt% LiF (note planar interfaces) and (b) alkoxide powder appearing to originate from a point-source (optical microscopy 20X, 10X obj.).

Submicrometer-sized defects were observed at grain boundaries of sulfate powder compacts hot-pressed with the standard profile (Fig. 4.31a). These features were not observed with 1 wt% LiF addition (Fig. 4.31b). However, similar defects were observed (Fig. 4.32a), as were larger acicular micron-sized grain-boundary defects (Fig. 4.32b), when sulfate powder with 1 wt% LiF was hot-pressed with pressure applied at 900°C. This strongly suggested trapping of impurity and additive species by the lower temperature pressure application. By focusing into transparent compacts hot-pressed with LiF, grain boundaries were visible throughout the thickness due to optical scatter (Fig. 4.31b inset), requiring scattering features spanning hundreds of nanometers. Finding the cause of this scatter was a main motivation for examining grain-boundaries in greater detail using TEM (Sections 4.3.2 – 4.3.4), SIMS (Sections 4.3.5 and 4.3.6), AFM (Section 4.3.7), and EIS (Section 4.3.8).

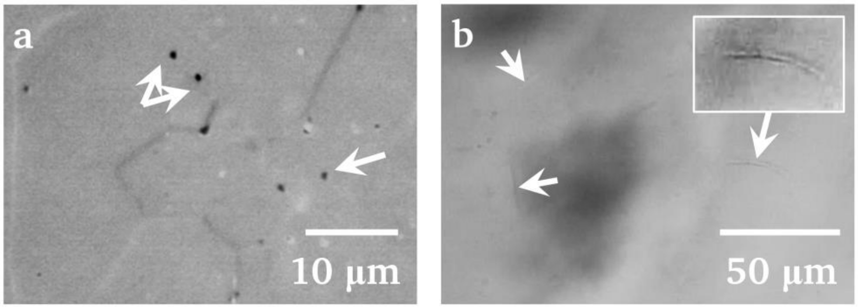

Fig. 4.31: (a) Submicrometer-sized grain-boundary inclusions in compact hot-pressed with sulfate powder using the standard profile and (b) grain-boundary scatter (arrows) in identically-processed compact with 1 wt% LiF (optical microscopy 10X obj.).

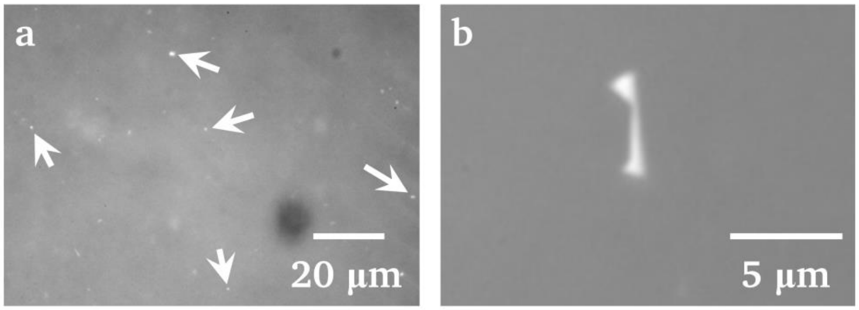

Fig. 4.32: (a) Submicrometer-sized inclusions and (b) grain-boundary phase in compact hot-pressed with sulfate powder with 1 wt% LiF and pressure applied at 900°C (optical microscopy 50X obj.).

Secondary phases were not detected by optical microscopy in alkoxide powder compacts, likely due to the low impurity content. However, micron-sized optical defects such as inclusions and pore clusters were observed by focusing into transparent sulfate and alkoxide powder compacts. Alkoxide powder compacts contained spherical opaque defects that degraded transparency (Fig. 4.33a). These were typically associated with abnormal grains, which appeared to radiate outwards from the defects, suggesting an impurity source. Local strain fields associated with these defects were indicated by polarized-light microscopy. Although care was taken during preparation, flakes from the graphite liners were observed and pore-clusters (Fig. 4.33b) appeared to be the advanced stage of decomposition of these flakes or of other organic-based contaminants.

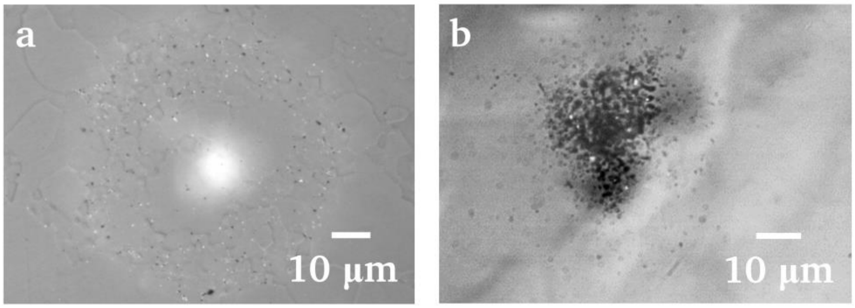

Fig. 4.33: (a) Spherical optical defect surrounded by abnormal grains in alkoxide powder compact without LiF, and (b) pore-cluster in sulfate powder compact with LiF (optical microscopy 10X obj.)

A crack in one compact hot-pressed with alkoxide powder and 0.05 wt% Al_2O_3 addition was surrounded by a zone of reduced absorption (Fig. 4.34). The color-change adjacent to the crack under polarized light indicated uniaxial tensile strain, which was estimated to be in the single-digit MPa's using a Michel-Levy chart and also by applying enough pressure to make the birefringence vanish. The grain-size near the crack was larger than in the surrounding matrix and the boundaries of grains adjacent to the crack were decorated by a second phase (Fig. 4.35). Since no major impurities were detected by SEM-EDS and TEM-EDS, the second phase was attributed to porosity caused by MgO vaporization or by CO/CO_2 formation arising from carbon contamination from the graphite foil or hot-press fixtures. Similar tensile strain was indicated under polarized light at surfaces of compacts hot-pressed with sulfate and alkoxide powders with and without LiF. The cause of the strain was not conclusively determined, but may have been associated with MgO evaporation or differential sintering.

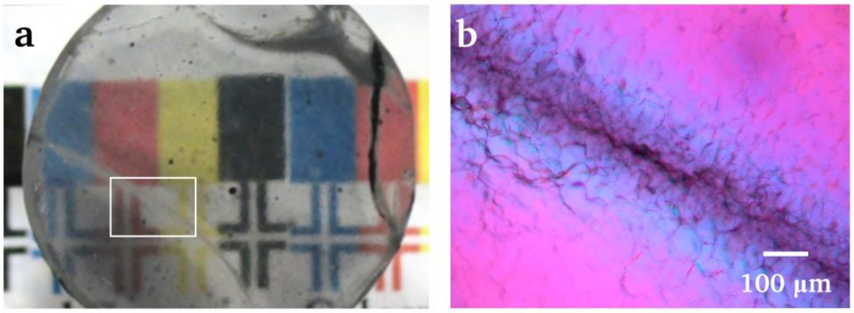

Fig. 4.34: Crack exhibiting reduced absorption that occurred while hot-pressing an alkoxide powder compact (a, white box), with color-change under polarized light indicating strain birefringence (b) (optical microscopy, 5X obj., full-wavelength filter).

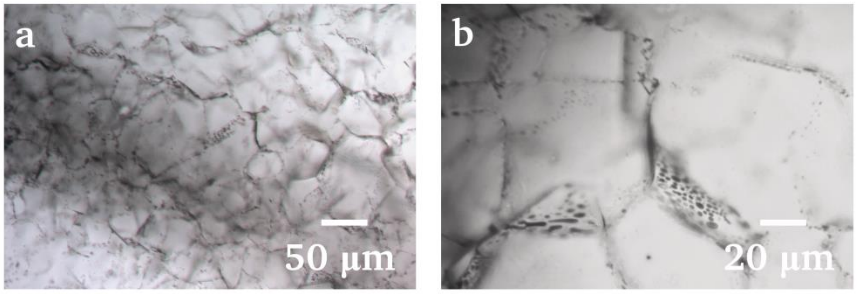

Fig. 4.35: Grain-size in the crack region was larger (a, 20X obj.) and boundaries were decorated by a secondary phase (b, optical microscopy, 50X obj.).

4.3.2 Electron Microscopy

Compacts hot-pressed with sulfate powder and pressure applied at 1200°C (dark and opaque, Section 4.2.1, Fig. 4.13a) displayed a bi-modal grain size distribution consisting of ~20 μm matrix grains and ~6 vol% aggregates with an average size of ~5 μm composed of grains with an average size of ~0.4 μm (Fig. 4.36). By modeling grains as tetrakaidecahedrons, the total grain-boundary area of the submicrometer grains was estimated to be more than twice that of the matrix grains. The fracture mode was predominantly transgranular for matrix grains and intergranular for submicrometer grains and for the interface between matrix grains and submicrometer-grain aggregates (Fig. 4.36b). FIB lift-outs (Fig. 4.37) confirmed this interface was planar (Fig. 4.38) and electron-diffraction and EDS showed it was decorated by a partially-wetting impurity-rich (C, S, Si, K) amorphous phase (Fig. 4.39) that also occupied all or part of triple junctions within the aggregates (Fig. 4.40). Roughly 120-degree dihedral angles indicated similar grain-grain and grain-amorphous phase interface energies within aggregate triple junctions. However, boundaries of submicrometer grains intersected the submicrometer-grain-aggregate matrix-grain interfaces nearly perpendicularly (Fig. 4.41), suggesting wetting by the amorphous phase along the entire interface. Boundaries of submicrometer grains exhibited strain-contrast resembling dislocation arrays (Fig. 4.42), whereas matrix grain-boundaries were generally clean (Fig. 4.43). Grain-boundary impurity concentration outside of the amorphous phase was below the detection limit of TEM-EDS, typically <1,000 ppm per species.

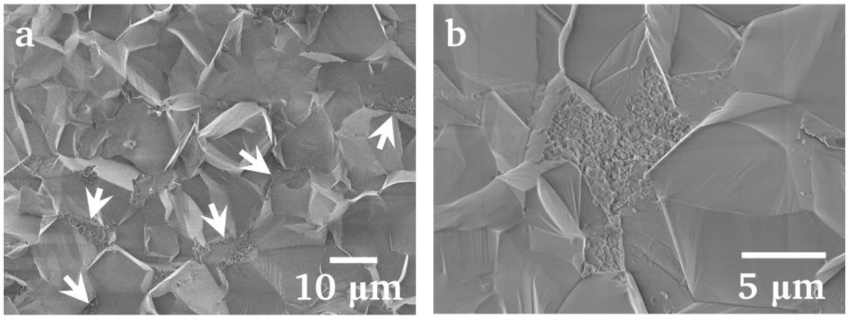

Fig. 4.36: Fracture surface of compact hot-pressed with sulfate powder with pressure applied at 1200°C exhibiting (a) transgranular fracture (arrows show submicrometer-grain aggregates) and (b) submicrometer-grain aggregate (SEM).

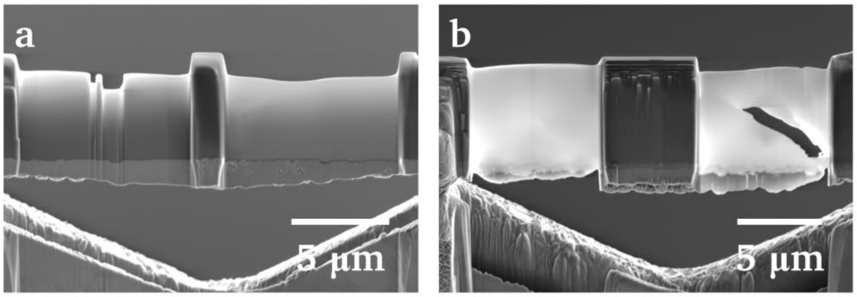

Fig. 4.37: Focused ion-beam lift-outs, with only one window usable in each, from compacts hot-pressed at 1200°C with sulfate powder (a) and (b) with 1 wt% LiF (SEM).

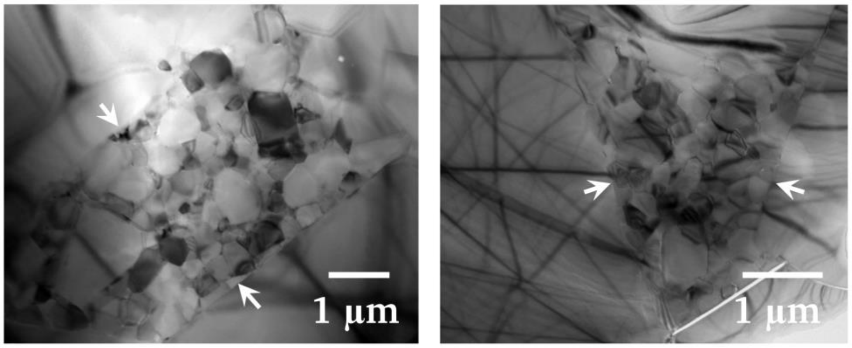

Fig. 4.38: Submicrometer-grain aggregates in compacts hot-pressed with sulfate powder and pressure applied at 1200°C showing planar interfaces between aggregates and larger matrix grains (arrows) (TEM-BF).

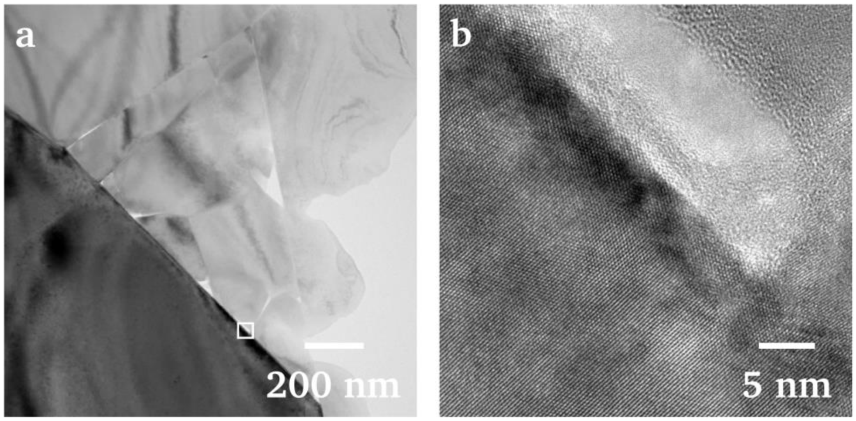

Fig. 4.39: Submicrometer-grain aggregate in compact hot-pressed with sulfate powder and pressure applied at 1200°C (a) with amorphous phase at submicrometer grain aggregate-matrix grain interface (white box, b) (TEM-BF).

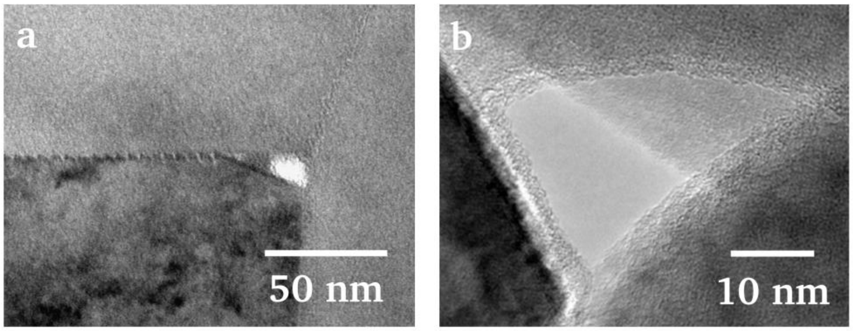

Fig. 4.40: Partially-filled triple-junction phase in submicrometer grain aggregate in compact hot-pressed with sulfate powder and pressure applied at 1200°C (a, b) (TEM-BF).

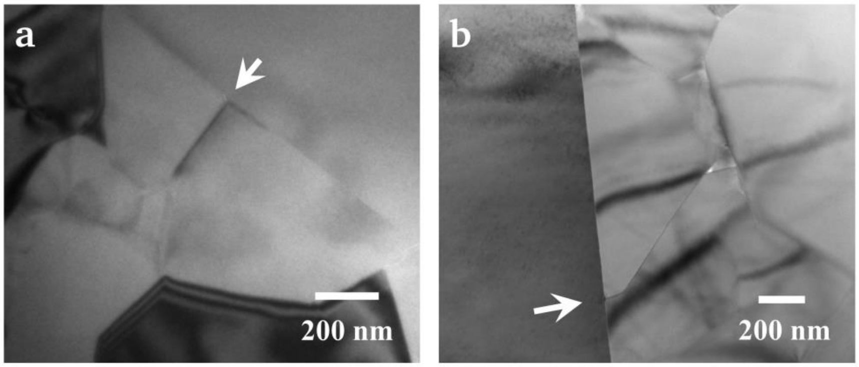

Fig. 4.41: Near-perpendicular intersection of submicrometer-grain boundary with the interface between matrix grains and submicrometer-grain aggregates (a, arrow) in sulfate powder compact with boundary deviating to intersect at right angles (b, arrow) (TEM-BF).

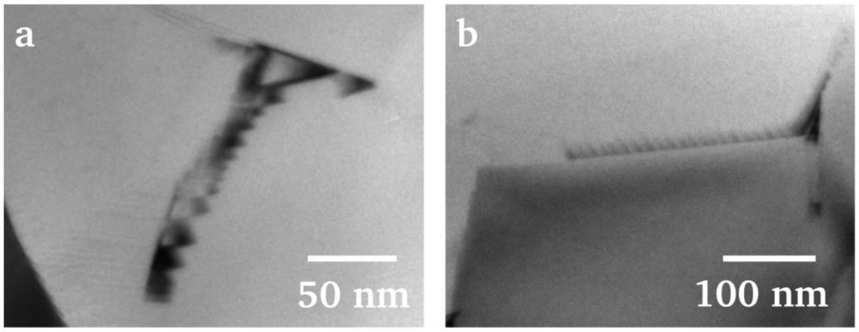

Fig. 4.42: Dark-contrast features resembling dislocation arrays at boundaries of submicrometer grains in compact hot-pressed with sulfate powder and pressure applied at 1200°C (a, b) (TEM-BF).

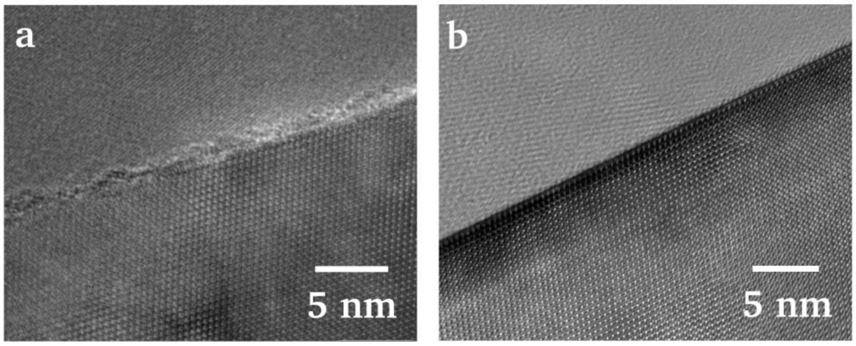

Fig. 4.43: Clean, (a) atomically-rough and (b) smooth matrix grain boundaries in compact hot-pressed with sulfate powder and pressure applied at 1200°C (HRTEM).

Compacts hot-pressed with 1.5 g of sulfate powder with 1 wt% LiF and pressure applied at 1200°C (transparent, Section 4.2.1, Fig. 4.13b) displayed predominantly intergranular fracture (Fig. 4.44a). The grain-size distribution was uniform, but aggregates of small grains remained (Fig. 4.44b). The grains within the aggregates were micrometer-size, as opposed to submicrometer-size for compacts without LiF. Due to reduced grain-boundary area associated with grain growth, impurities in the aggregates concentrated into polyhedral submicrometer-sized Fe, Ni, C, and Ga-rich triple junction and grain-boundary phases that were detectable by SEM-EDS (Fig. 4.45c,d). Matrix grain-boundaries were generally clean (Fig. 4.46a) but a wetting amorphous phase was occasionally observed (Fig. 4.46b).

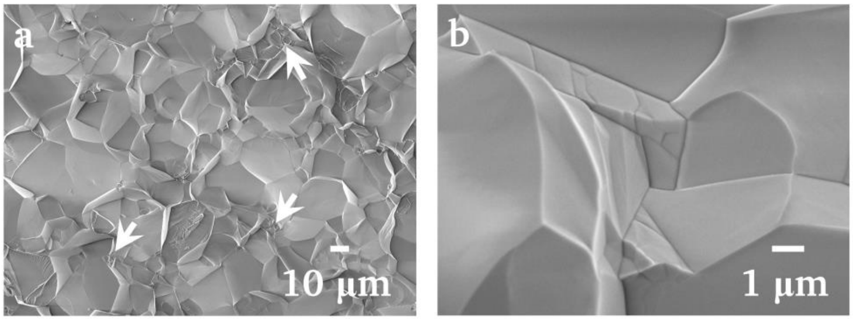

Fig. 4.44: Fracture surface of compact hot-pressed with sulfate powder with 1 wt% LiF and pressure applied at 1200°C showing (a) matrix grains with interspersed smaller-grain aggregates (arrows, b) (fracture surface, SEM).

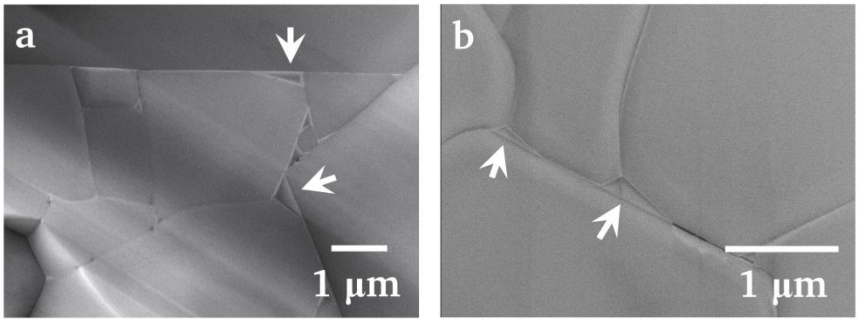

Fig. 4.45: Polyhedral (a) and partially-wetting (b) Fe, Ni, C, and Ga-rich secondary phases (arrows) in smaller-grain aggregates of compact hot-pressed with sulfate powder with 1 wt% LiF and pressure applied at 1200°C (fracture surface, SEM).

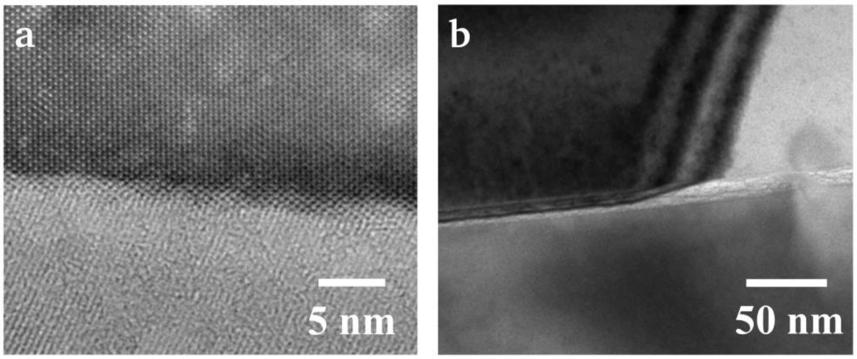

Fig. 4.46: Clean grain-boundary (a) and with amorphous phase (b) in compact hot-pressed with 1.5 g of sulfate powder with 1 wt% LiF and pressure applied at 1200°C (HR-TEM, TEM-BF).

Compacts hot-pressed with 1.5 g of sulfate powder and 1 wt% LiF and with pressure applied at 900°C (hazy, Section 4.2.1, Fig. 4.13c) were shown by chemical analysis to contain more impurities and additives. Occasional mottled-contrast fluorine-rich phases at triple-junctions were determined to be MgF_2 by electron diffraction (Fig. 4.47b). Matrix grain-boundaries were generally clean, but a 1 nm thick disordered zone (Fig. 4.48) suggested the presence of a wetting phase, and this was supported by through-focus Fresnel ridge imaging indicating the presence of two parallel interfaces (Fig. 4.49). TEM of matrix grain-boundaries occasionally showed strain contrast, more so than in compacts hot-pressed without LiF (Fig. 4.50) and dislocation arrays were also occasionally observed within grains. STEM-EDS across matrix grain boundaries indicated S, Ca, and C segregation at the boundary core (Fig. 4.51).

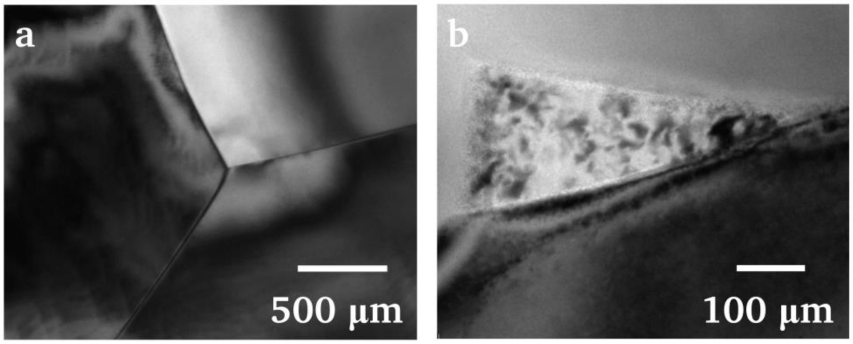

Fig. 4.47: Clean (a) and mottled-contrast fluorine-rich (MgF_2) phase (b) at matrix-grain triple junctions in compact hot-pressed with sulfate powder with 1 wt% LiF and pressure applied at 900°C (TEM-BF).

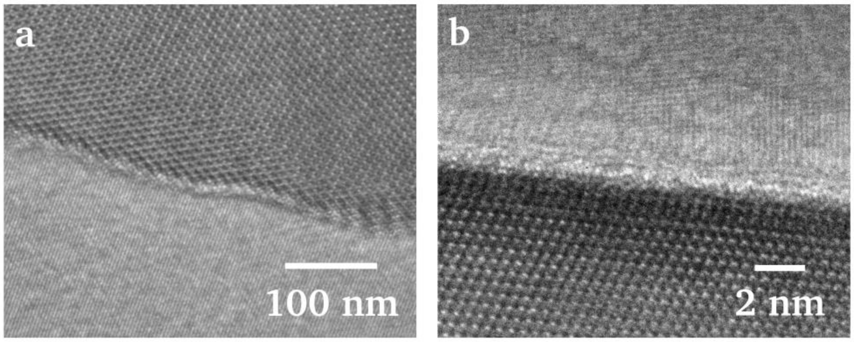

Fig. 4.48: Matrix grain-boundaries of compact hot-pressed with sulfate powder with 1 wt% LiF and pressure applied at 900°C showing disorder at the interface (a, b) (HRTEM)

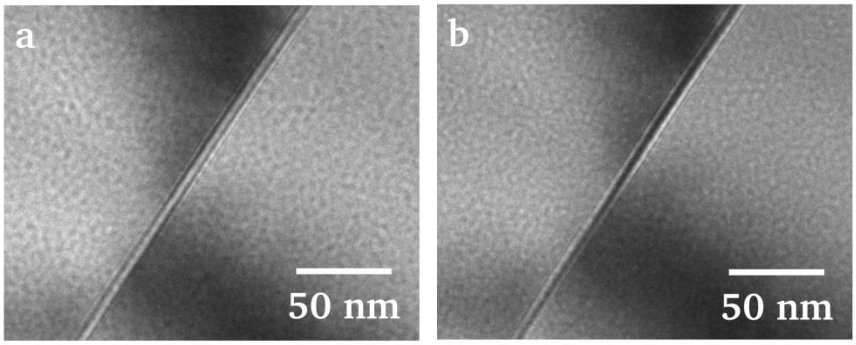

Fig. 4.49: De-focus (± 3.5 μm) of a grain-boundary of compact hot-pressed with sulfate powder with 1 wt% LiF and pressure applied at 900°C showing Fresnel fringes with reversed contrast (a, b) (TEM)

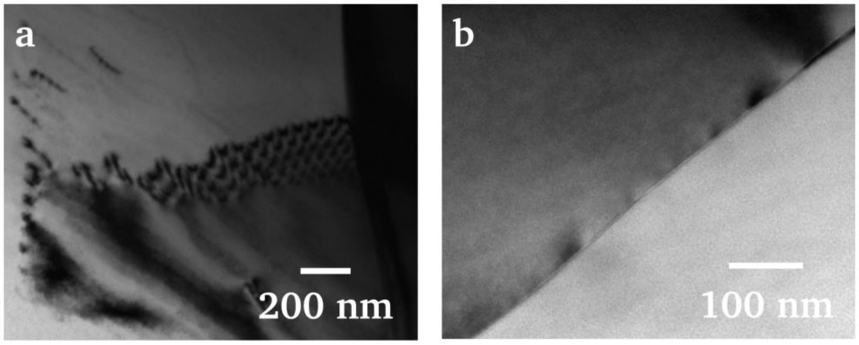

Fig. 4.50: Dislocation arrays (a) and strain-contrast at a grain-boundary (b) in a compact hot-pressed with sulfate powder with 1 wt% LiF and pressure applied at 900°C (TEM)

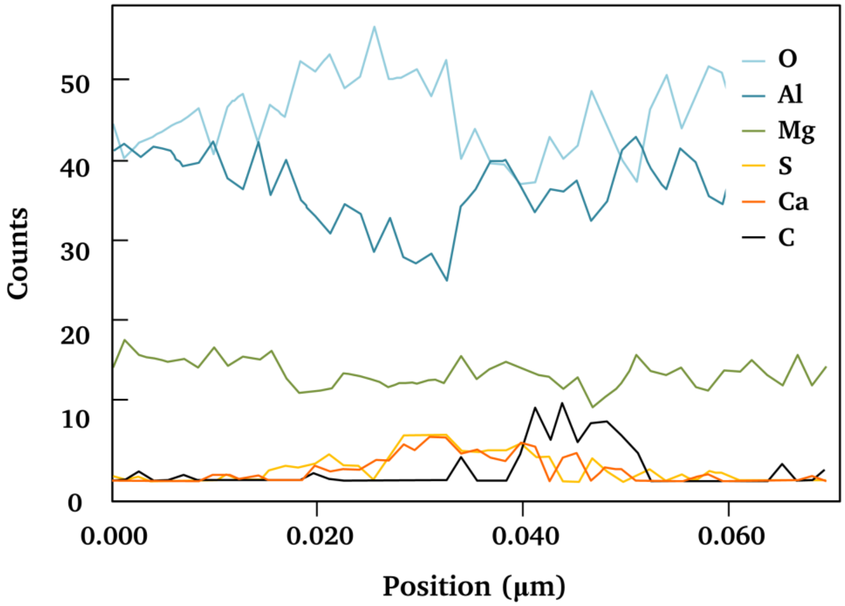

Fig. 4.51: Drift-corrected STEM-EDS profile scan across a matrix grain boundary of a compact hot-pressed with sulfate powder with 1 wt% LiF and pressure applied at 900°C showing C, Ca, and S segregation at the core (~0.035 μm).

The fracture surfaces of compacts hot-pressed with alkoxide powder with pressure applied at 1200°C (Fig. 4.13b,d) were predominantly transgranular (Fig. 4.52a), whereas they were intergranular for compacts with LiF addition (Fig. 4.52b), as observed for sulfate powder compacts. In compacts without LiF, irregularly-disseminated clusters of white-contrast particles ~100 nm in diameter and occupying less than 0.5 vol% were determined by SEM-WDS to be iron-rich (Fig. 4.53a) and were attributed to steel flaking-off from the flame-spray nozzle. This phase was absent in compacts hot-pressed with LiF (Fig. 4.53b), indicating iron removal, as observed for sulfate powder compacts. Nodules ~125 nm in diameter were determined by SEM-WDS to be at least 88% MgO and confirmed by TEM-EDS and TEM-SAD to be pure MgO (Fig. 4.54), indicating LiF exacerbated MgO-rich stoichiometry in alkoxide powders. The nodules were more prevalent at grain boundaries and in compacts with LiF, occupying ~0.9% of the grain boundaries (0.27 vol% or 0.08 wt%). Lighter contrast surrounding the nodules in SEM-BS suggested the adjacent matrix may have been Mg-depleted (Fig. 4.54a). The spherical shape of the nodules indicated a high interface energy between the nodules and the spinel matrix, despite both having similar cubic crystal structures and primitive unit cell lattice parameters ($\alpha_{Magnesia}$ = 4.212, α_{Spinel} = 4.404 nm).[272]

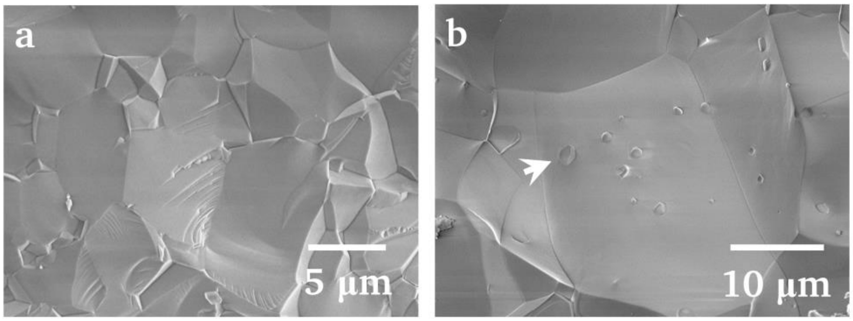

Fig. 4.52: Fracture surfaces of compacts hot-pressed with pressure applied at 1200°C with (a) alkoxide powder (a) and alkoxide powder with 0.25 wt% LiF (b) with arrows showing MgO nodules (SEM).

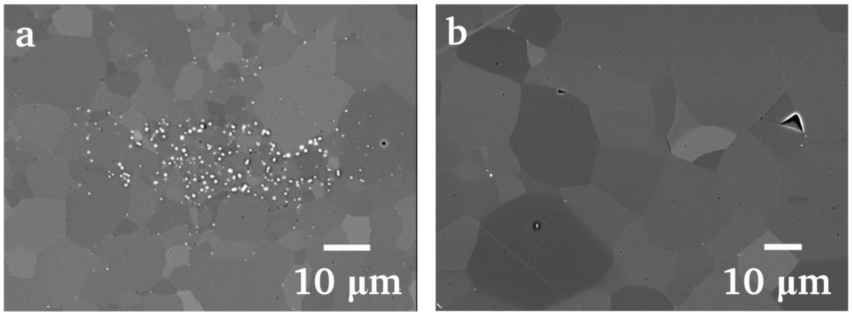

Fig. 4.53: Fe-rich phase in compact hot-pressed with alkoxide powder (a) and larger grain-size and absence of Fe-phase in compact hot-pressed with alkoxide powder with 0.25 wt% LiF (b) (SEM).

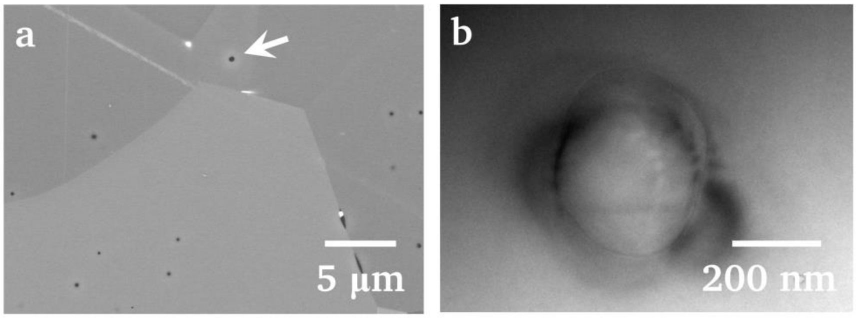

Fig. 4.54: MgO nodules (arrow) surrounded by light-contrast indicative of Mg-depletion in compact hot-pressed with alkoxide powder with 0.25 wt% LiF (SEM) and high-magnification of MgO nodule (b) (TEM-BF).

Fracture surfaces of quenched sulfate and alkoxide powder compacts hot-pressed with LiF exhibited a larger fraction of transgranular fracture than un-quenched compacts (Fig. 4.55 and 4.56), possibly indicating additives and impurities diffused from grain boundaries into the lattice.

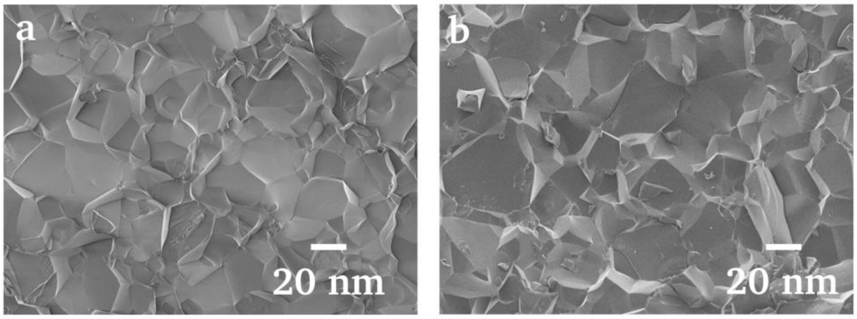

Fig. 4.55: Fracture surfaces for (a) hot-pressed compact with sulfate powder with 1 wt% LiF and (b) same compact after quenching (SEM).

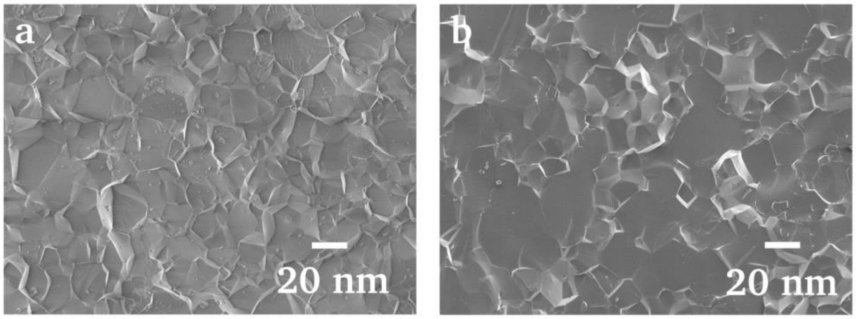

Fig. 4.56: Fracture surfaces for (a) hot-pressed alkoxide powder compact with 0.25 wt% LiF and (b) same compact after quenching (SEM).

No preferential grain orientation was observed for sulfate or alkoxide powder compacts with or without LiF by SEM-EBSD (Fig. 4.57). Grain-sizes were consistent with those calculated from optical and SEM images and the average misorientation angle was 45° (Fig. 4.58, Fig. 4.59).

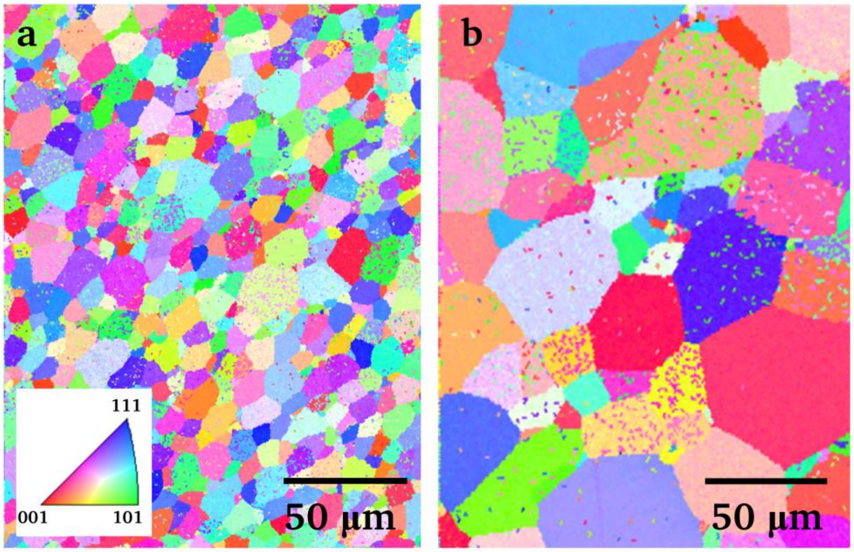

Fig. 4.57: EBSD pole maps for polished sulfate-powder compacts without (a) and with 1 wt% LiF (b) oriented perpendicular to the hot-pressing direction (inset: color-coded pole orientation).

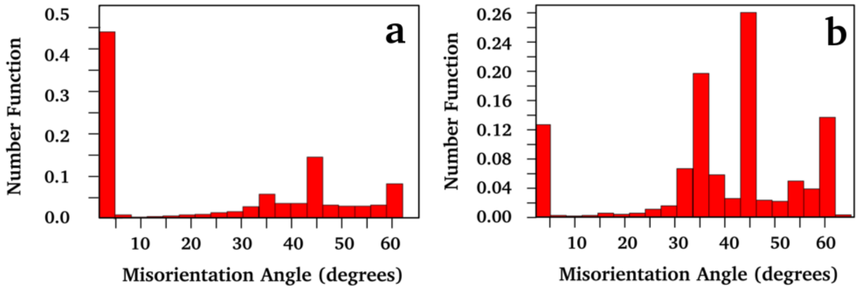

Fig. 4.58: EBSD grain misorientation angles for compact hot-pressed with sulfate powder (a) without LiF and (b) with 1 wt% LiF, both showing preferred 45° orientation (first bar in graphs is instrument noise).

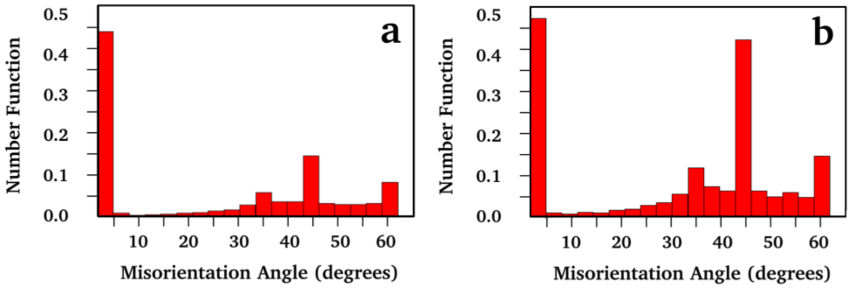

Fig. 4.59: EBSD grain misorientation angles for compact hot-pressed with sulfate powder without LiF (a) and alkoxide-powder compact with 0.25 wt% LiF (b), exhibiting strikingly similar orientation profiles with preferred 45° orientation (first bar in graphs is instrument noise).

Impurity-phase filled triple-junctions and intergranular fracture of grains in submicrometer-grain aggregates in hot-pressed sulfate powder compacts indicated impurities were present at the boundaries, even though they were not detected by TEM-EDS (but detected by STEM-EDS). The glassy structure and distribution of the secondary-phase at interfaces between aggregates and matrix grains suggested it formed from a eutectic liquid that partially de-wet upon cooling. Partially-filled triple-junctions in the aggregates suggested the unfilled portions were previously occupied by a vapor associated with the eutectic melt. In turn, the impurity phase and its vapor at triple-junctions were expected to pin grain boundaries and inhibit densification at processing temperature, explaining the small grain size. Planar interfaces between the aggregates and matrix grains along which fracture propagated, combined with the amorphous phase where submicrometer-grain boundaries intersected the interface and the near-perpendicular orientation of the intersections, suggested remnants of the wetting phase remained along the entirety of the interfaces. The varied areal extent of these wetted or partially-wetted interfaces made them likely candidates responsible for scatter causing opacity, with amorphous-phase filled triple junctions contributing to scatter at shorter wavelengths. Transgranular fracture of matrix grains in these compacts and in hot-pressed alkoxide compacts was consistent with those grain boundaries having lower impurity content.

The larger grain-size in compacts hot-pressed with sulfate powder with LiF was consistent with coarsening caused by LiF-induced (i) impurity removal, (ii) increased surface and vapor transport, and (iii) shifting of stoichiometry to Al_2O_3-rich. The distribution of small-grain regions in these compacts indicated they corresponded to submicrometer-grain aggregates in compacts without LiF. However, the grains within these regions coarsened due impurity removal and enhanced mass transport associated with LiF. Concomitantly, even though total impurity content decreased (at least for S, Ca, and Fe), local impurity concentration increased with decreasing grain-boundary area associated with coarsening for both small and matrix grains, resulting in secondary-phases visible by SEM. The change in matrix-grain fracture from transgranular to intergranular with LiF addition was consistent with a wetting-phase occasionally observed at boundaries. Application of pressure at a lower temperature during hot-pressing trapped more impurities, LiF, and their by-products. As a consequence, impurities became detectable at grain-boundaries by STEM-EDS, triple-junctions filled with MgF_2 were observed, and the wetting grain-boundary phase was more prevalent. Where the wetting phase could not be discerned by HRTEM, through-focus Fresnel fringes indicated it was present and <1 nm thick. Considerably more strain contrast was observed at boundaries in these compacts (how LiF affects this is unknown), which together with the wetting phase likely contributed to grain-boundary scatter visible by optical microscopy. LiF resulted in similar coarsening and embrittlement in alkoxide powder compacts. Moreover, since the alkoxide powder was slightly MgO-rich, reaction of LiF with spinel caused the formation of MgO nodules, which along with their associated strain fields contributed to short-wavelength scatter observed by spectrophotometry.

4.3.3 Electron Energy-Loss Spectroscopy (STEM-EELS)

A typical zero-loss extracted, background-subtracted STEM-EELS spectrum from a grain-boundary area scan of a FIB lift-out from a compact hot-pressed with sulfate powder with 1 wt% LiF and standard processing is shown in Fig. 4.60. The extracted zero-loss peak was ~2 eV at full-width half-maximum, indicating limited energy resolution. The low-loss spectrum indicated the Mg-$L_{2,3}$ (51 eV), Al-$L_{2,3}$ (73 eV), and Mg-L_1 edges (88 eV) (Fig. 4.61), and the high-loss spectrum the C-K (284 eV) and O-K edges (532 eV) (Fig. 4.62). The Li-K edge (55 eV) was not resolvable, likely due to low signal and overlap with the Mg-$L_{2,3}$ edge. The F-K, Mg-K, and Al-K edges were not observed. STEM-EDS indicated strong Mg, Al, and O peaks and weaker C, S, Si, and possibly Fe, K, and Ca peaks. Ratios of integrated intensities for typical STEM-EDS peaks and STEM-EELS edges for Mg, Al, and O (Fig. 4.63) did not indicate stoichiometry gradients, contrary to literature reports of Mg-depletion in compacts processed without LiF. Chemical gradients had been expected based on the wetting phase and Fresnel fringe and strain contrast observed by TEM in these compacts. It is possible gradients were shallower and larger than the

~50 nm STEM scans. Indeed, light-scattering at boundaries observed by optical microscopy (Section 4.3.1) indicated the causing features were on the order of visible wavelengths.

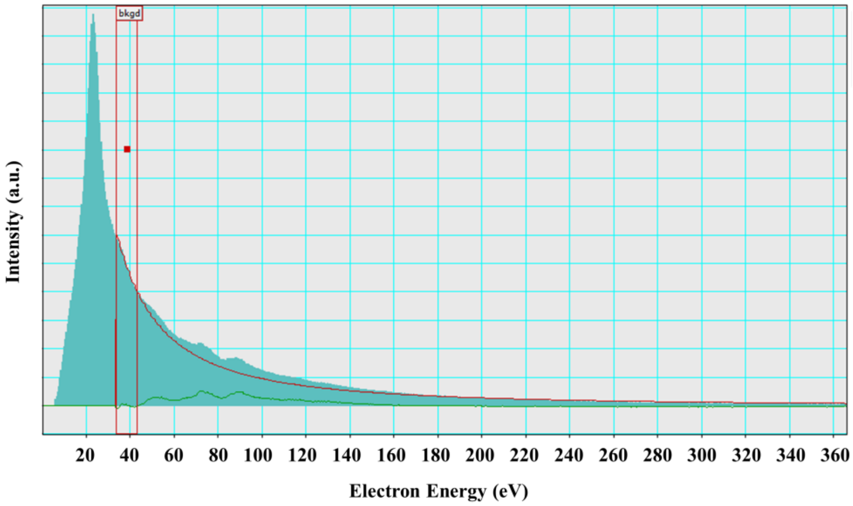

Fig. 4.60: Typical zero-loss removed, background-corrected (green line) EELS spectrum with the Mg-$L_{2,3}$ (51 eV), Al-$L_{2,3}$ (73 eV), and Mg-L_1 (88 eV) edges visible (red rectangle indicates selected fit region for background subtraction).

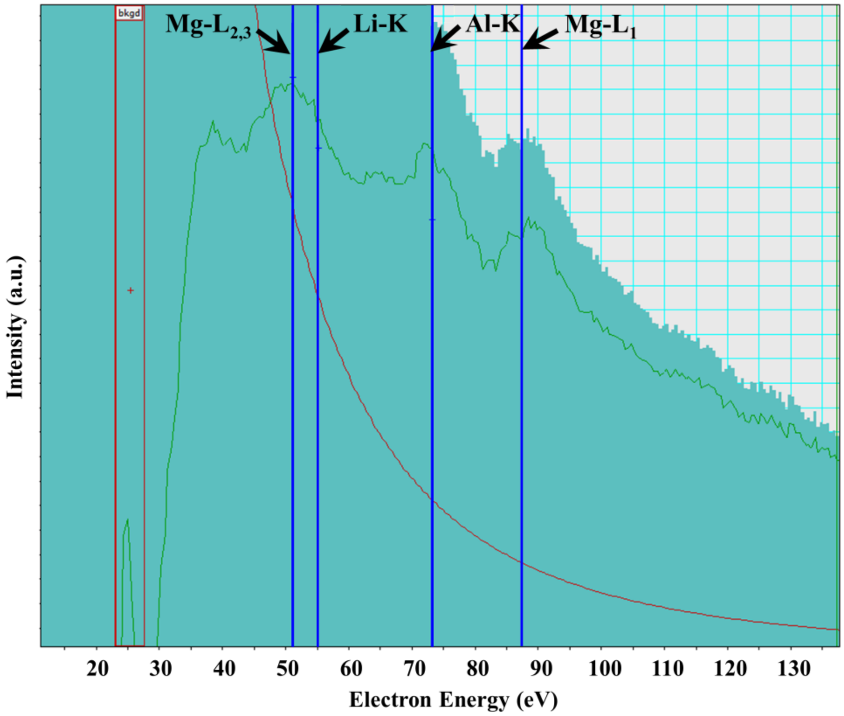

Fig. 4.61: Typical low-loss region of zero-loss removed, background-corrected EELS spectrum showing the Mg-$L_{2,3}$ (51 eV), Al-$L_{2,3}$ (73 eV) and Mg-L_1 (88 eV) edges.

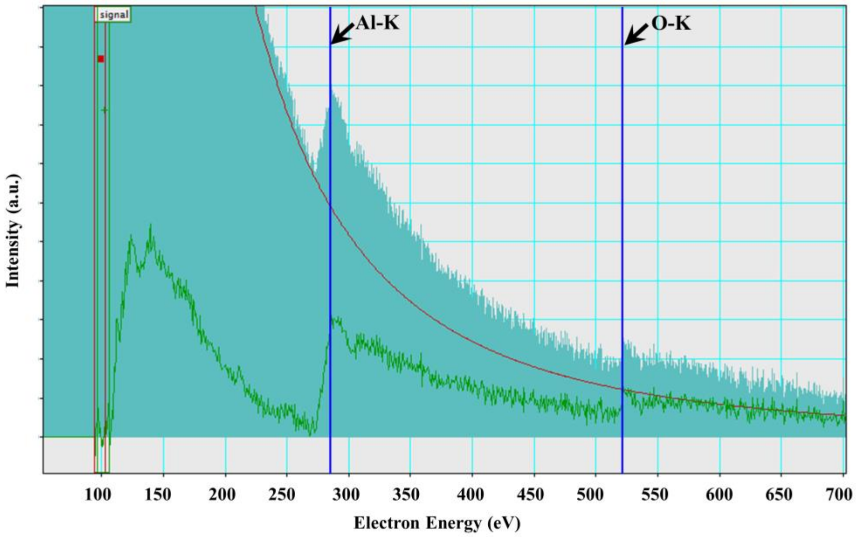

Fig. 4.62: Typical high-loss region of zero-loss removed, background-corrected EELS spectrum showing well-defined C-K (284 eV) and O-K (532 eV) edges.

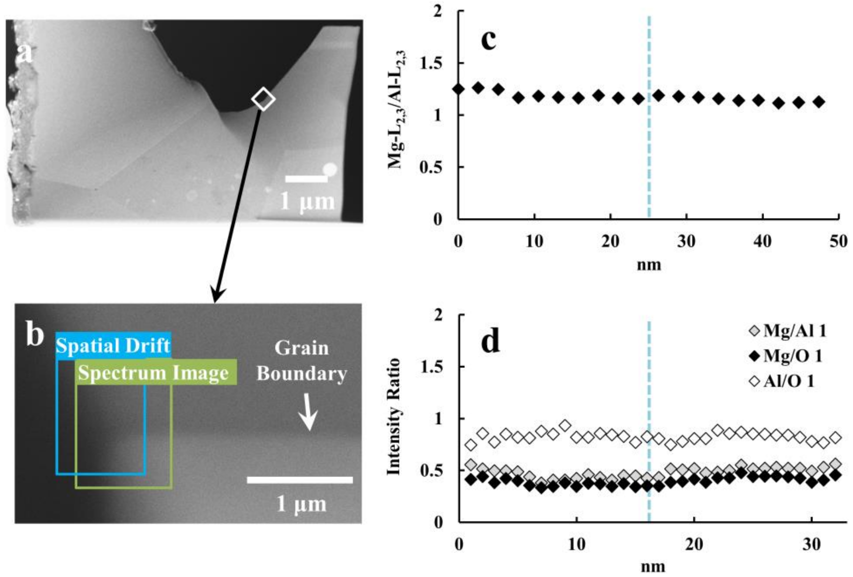

Fig. 4.63: FIB lift-out (a) from a compact hot-pressed with sulfate powder with 1 wt% LiF and standard processing, grain-boundary area scan (b), and STEM-EELS (c) and STEM-EDS (d) intensity ratios across the boundary (dashed line indicates boundary core).

4.3.4 Convergent-Beam Electron Diffraction (TEM-CBED)

TEM-CBED (TEM convergent-beam electron diffraction) patterns taken from grain interiors and boundaries of FIB lift-outs (Fig. 4.64, Fig. 4.65) from compacts hot-pressed with sulfate powder with and without 1 wt% LiF are shown in Fig. 4.66 and Fig. 4.67. The calculated lattice parameters were significantly larger than reported values for spinel (8.0898 Å), attributed to microscope parameters (voltage, camera length) used for calculations that changed after the calibration to determine these parameters was performed. Additionally, even with optimal convergence, the beam probe-size was wider than the grain-boundary core, resulting in contributions from adjacent grains. Moreover, beam-circularity anisotropy manifested by aspherical first-order Laue zones (FOLZ) patters decreased measurement accuracy. Nevertheless, the results are included because microscope parameter calibration error similarly affected all measurements, allowing comparative analysis. Moreover, the results were consistent within samples and indicated a smaller lattice parameter for the sample with LiF, consistent with MgO-depleted stoichiometry, and possibly a slightly smaller lattice parameter at grain boundaries, indicative of a stoichiometry gradient.

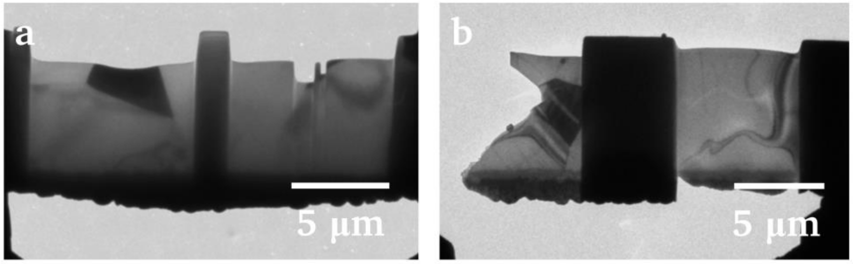

Fig. 4.64: FIB lift-outs from compacts hot-pressed with sulfate powder without LiF (a) and with 1 wt% LiF (b).

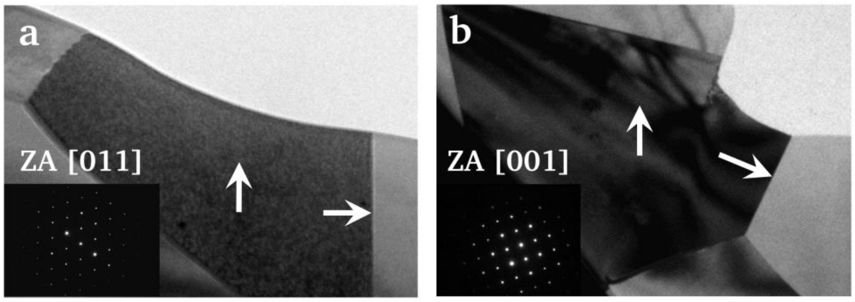

Fig. 4.65: FIB lift-outs from compacts hot-pressed with sulfate powder without LiF oriented along the [011] zone axis (a) and with sulfate powder with 1 wt% LiF oriented along the [001] zone axis (b), with arrows indicating CBED locations.

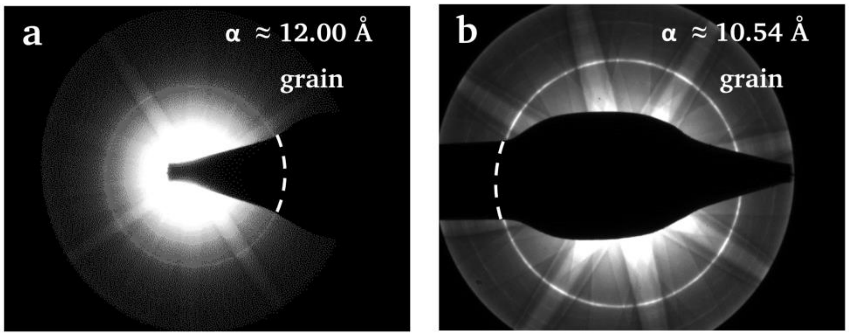

Fig. 4.66: CBED patterns from grain interiors and grain-boundaries for compacts hot-pressed with sulfate powder (a,b), the first-order Laue zones are indicated by the white dashed lines.

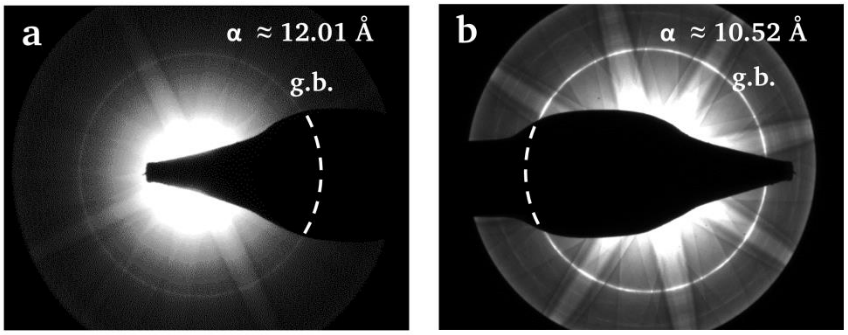

Fig. 4.67: CBED patterns from grain interiors and grain-boundaries for compacts hot-pressed with sulfate powder with 1 wt% LiF (a,b), the first-order Laue zones are indicated by the white dashed lines.

4.3.5 Secondary-Ion Mass Spectroscopy (TOF-SIMS)

TOF-SIMS $^{7}Li^{+}$ maps of polished surfaces of samples hot-pressed with sulfate powder with; (i) the standard profile with 35 MPa applied at 1200°C, (ii) 1 wt% LiF addition and pressure applied at 1100°C, and (iii) 1 wt% LiF addition and pressure applied at 900°C are shown in Fig. 4.68 and Fig. 4.69. Lithium segregation was not detected within the instrument resolution of ~1 μm. In compacts with LiF addition, applying pressure at 900°C forced densification to occur below the temperature of LiF volatilization (~1100°C), resulting in higher lithium content (Fig. 4.69b). Apart from an initial instrument-related decrease, lithium concentration was unchanged with depth-profiling (Fig. 4.70), indicating uniform lithium distribution within grain interiors.

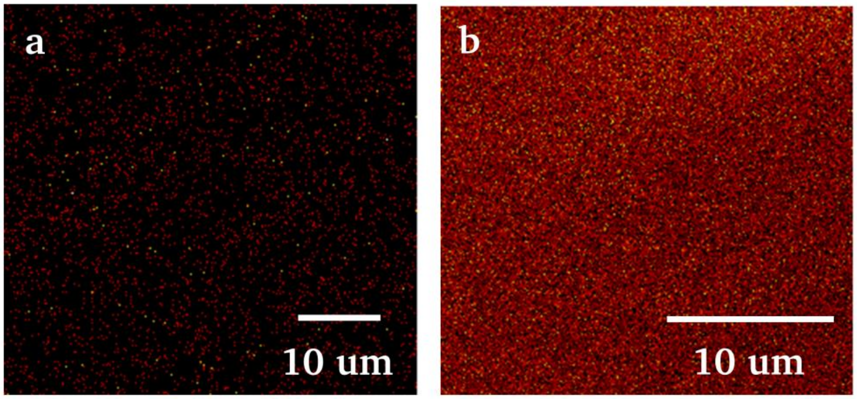

Fig. 4.68: SIMS $^{7}Li^{+}$ maps for a 50 x 50 μm area of a sample hot-pressed with sulfate powder without LiF using the standard profile (a), and a 25 x 25 μm area of a sample hot-pressed with sulfate powder with 1 wt% LiF (b).

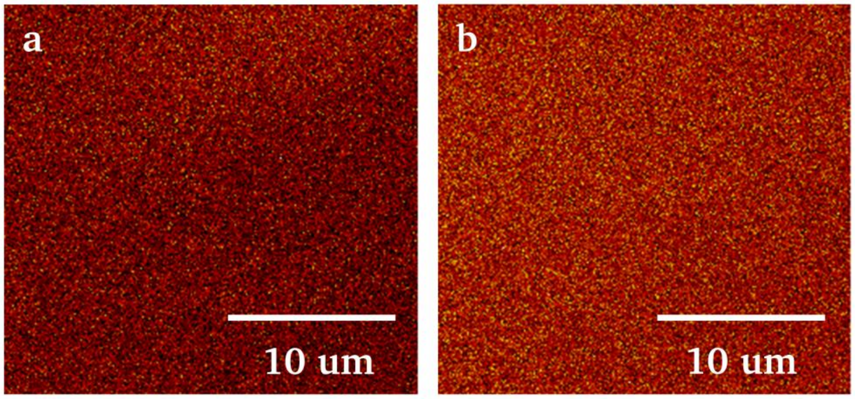

Fig. 4.69: SIMS $^{7}Li^{+}$ maps for 25 x 25 μm areas of sample hot-pressed with sulfate powder with 1 wt% LiF with pressure applied at 1100°C (a) and at 900°C (b) during hot-pressing.

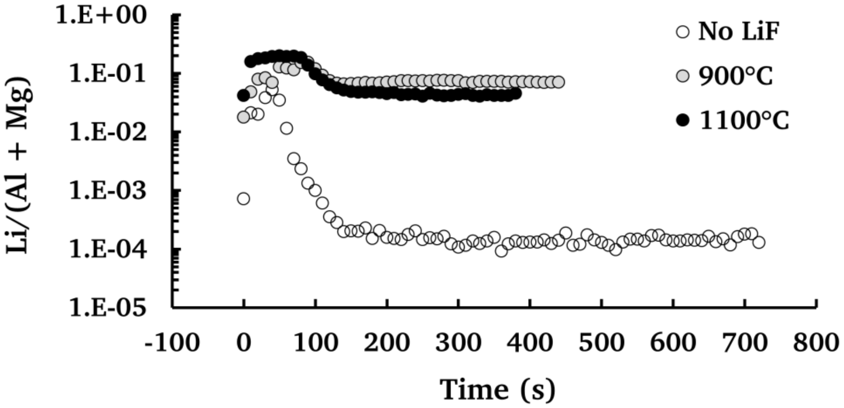

Fig. 4.70: SIMS $^{7}Li^{+}$ depth profiles corresponding to maps in Fig. 4.68 and Fig. 4.69.

SIMS $^{7}Li^{+}$, $^{25}Mg^{2+}$, and $^{27}Al^{3+}$ mapping performed with a different instrument (IMS 6f, Cameca, France) on the polished surface of a sample hot-pressed with sulfate powder and 1 wt% LiF addition using the standard profile (Fig. 4.71, the same sample as for Fig. 4.68b) indicated no Li, Mg, or Al segregation observable within the instrument resolution.

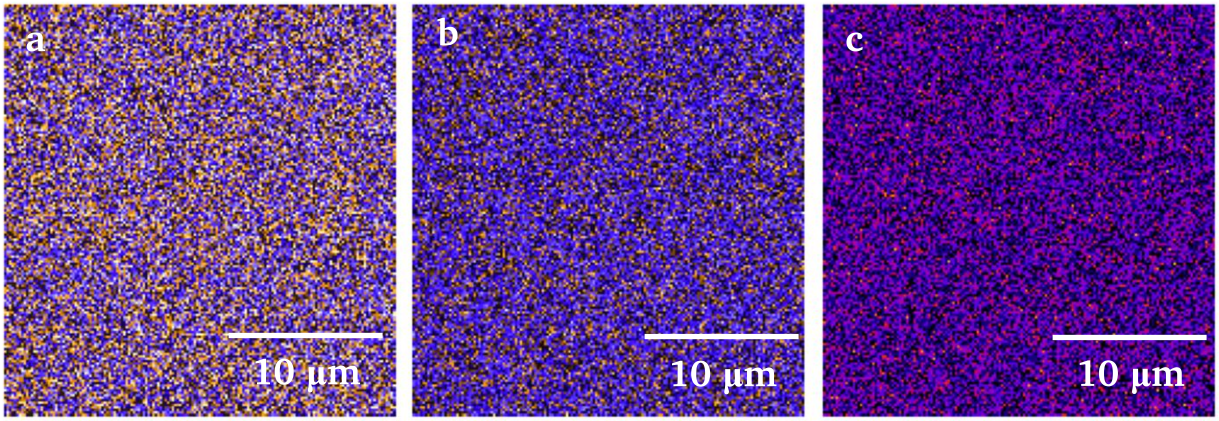

Fig. 4.71: 50 x 50 μm SIMS (a) $^{7}Li^{+}$, (b) $^{25}Mg^{2+}$, and (c) $^{27}Al^{3+}$ maps for sulfate powder sample with 1 wt% LiF hot-pressed using the standard profile.

SIMS performed on a 50 x 50 μm area on the polished surface of a sample hot-pressed with sulfate powder and 1 wt% LiF addition using the standard profile (the same sample as for Fig. 4.68b and Fig. 4.71) using an instrument with a higher lateral resolution of 50 nm (Nano-SIMS 50L, Cameca, France) revealed lower-intensity features indicative of lower lithium content on the $^{7}Li^{+}$ map, which were consistent with the size and morphology of grain-boundaries for this sample ($\overline{GS}$ ~12 μm) (Fig. 4.72a, arrows). Unfortunately, these features could not be directly correlated to the microstructure of the scanned area. No similar signal-intensity features were detected for $^{25}Mg^{2+}$ (Fig. 4.72b).

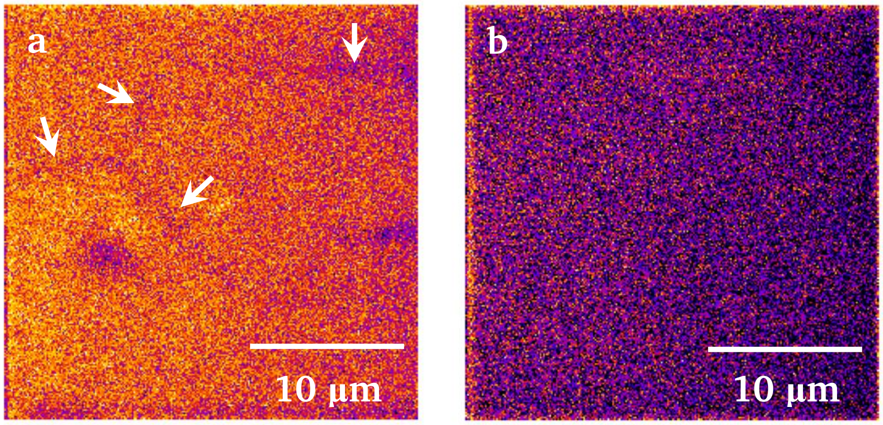

Fig. 4.72: Nano-SIMS (a) $^{7}Li^{+}$ and (b) $^{25}Mg^{+}$ maps of a 50 x 50 μm area on the polished surface of a sample hot-pressed with sulfate powder and 1 wt% LiF addition using the standard profile, arrows indicate features consistent with grain-boundaries.

4.3.6 Parallel-Ion Electron Spectroscopy (PIES)

PIES (Parallel-ion electron spectroscopy; LIMS, Esch-sur-Alzette, Luxembourg) conducted on a FIB lift-out from a sample hot-pressed with sulfate powder and 1 wt% LiF using the standard profile is shown in Fig. 4.73. $^{7}Li^{+}$ distribution appeared uniform and no grain-boundary or triple-junction segregation was detected (Fig. 4.73b). However, the resolution of this method is currently below that of nano-SIMS. TEM-EDS of the triple-junction at the lower left of the FIB lift-out in Fig. 4.73a only indicated signals for Mg, Al, and O and only one composition was detected by principle component analysis (Fig. 4.74b).

SIMS confirmed increased lithium content when pressure was applied at a lower temperature during hot pressing, consistent with LA ICP-OES/MS and TEM observations. The uniform distribution of lithium indicated by depth-profiling was contrary to studies indicating the presence of lithium and fluorine only at grain boundaries.[204] However, this finding was consistent with studies suggesting lithium and/or LiF is distributed throughout grains[212] and with thermal-grooving experiments (Section 4.3.7) suggesting LiF-induced defects were present in the bulk. Nano-SIMS suggested possible lithium depletion at grain-boundaries, although this could not be verified separately. Although instrument resolution was limiting, the results had important implications for conductivity (Section 4.3.8).

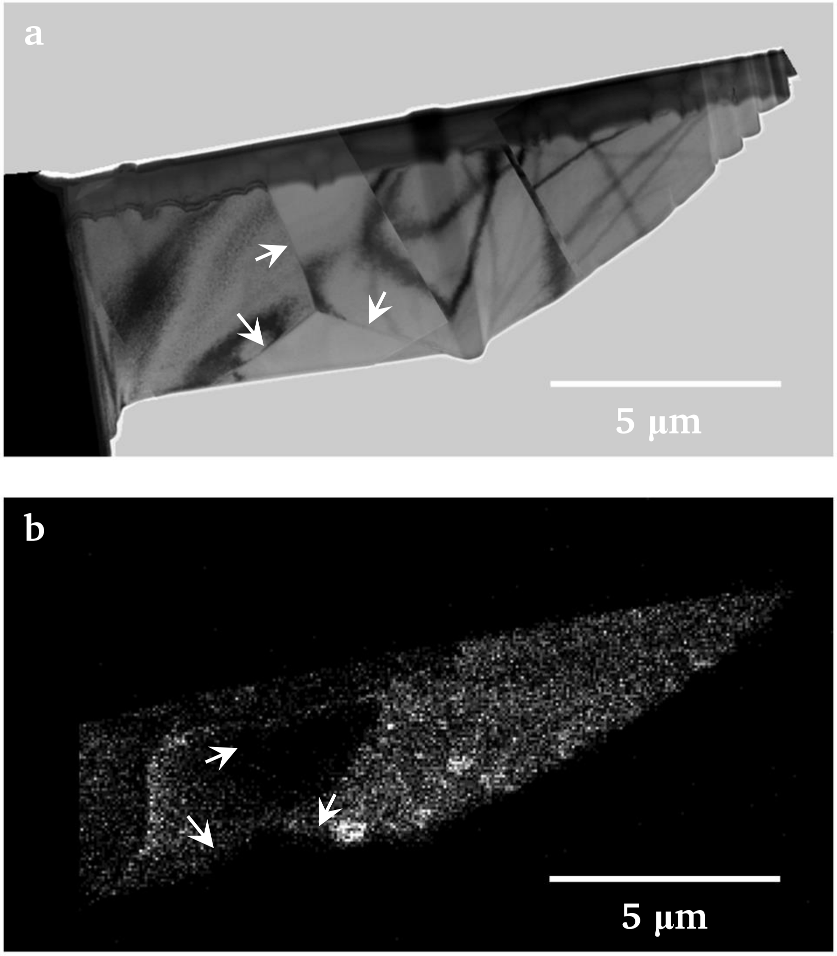

Fig. 4.73: (a) Composite TEM brightfield image of a FIB lift-out from sample hot-pressed with sulfate powder with 1 wt% LiF using the standard profile, grain boundaries indicated by arrows, and (b) PIES $^{7}Li^{+}$ map.

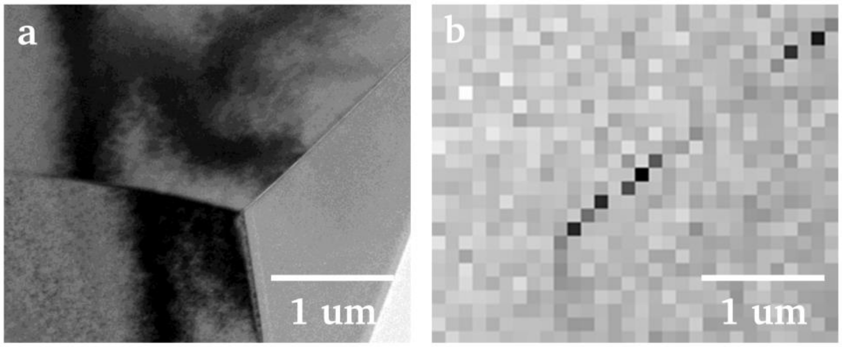

Fig. 4.74: (a) TEM brightfield image of triple-junction at lower left of FIB lift-out in Fig. 4.73, and (b) intensity map of triple-junction area.

4.3.7 Atomic-Force Microscopy (AFM)

AFM tips accurately replicated test grid features (Fig. 4.75a) and polished compact surfaces exhibited minimal roughness (Fig. 4.75b). Thermal etching revealed grain boundaries and the grain size of hot-pressed and HIPed compacts using hydroxide powders with x = 0.95, 1.0, and 1.5 (Section 4.2.1, Fig. 4.14) used for analysis ranged from 0.5 – 5 μm. Many boundaries were unusable because of (i) shallowness, (ii) grain-height differentials caused by tilted boundaries, (iii) waviness caused by surface reconstruction, and (iv) grain-boundary precipitates in astoichiometric compositions, which obscured groove slopes and ridges. Results based on acceptable boundaries (Fig. 4.76) are shown in Table 4.3. Thermal-grooves were also imaged for compacts hot-pressed with sulfate powder (n ~1.05) with and without LiF (not shown).

Interface-energy ratios and standard deviations were similar to reported values.[129,135] However, they were likely all somewhat similarly affected by starting powder impurities. Compared to stoichiometric, γ_{gb}/γ_s was 28% lower for MgO-rich and 51% lower for Al_2O_3-rich powder compacts. The Mullins approach yielded expected[135,276] ~17-36% higher γ_{gb}/γ_s values. Based on reported γ_s for lower-energy {100} planes,[123-127,129] direct groove-slope measurements indicated γ_{gb} ranged from 0.8 to 1.8 J/m^2 (1.0 – 2.2 J/m^2 for the Mullins approach) with lower values corresponding to MgO-rich and higher values to stoichiometric compacts.

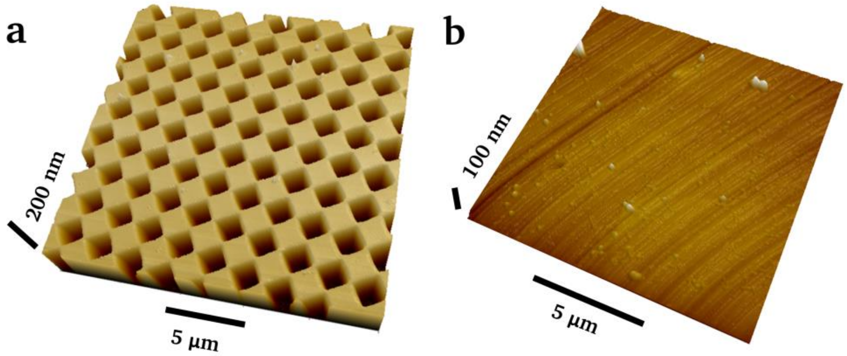

Fig. 4.75: AFM topography images of (a) calibration grid, showing excellent feature replication, and (b) polished sample surface with minimal roughness.

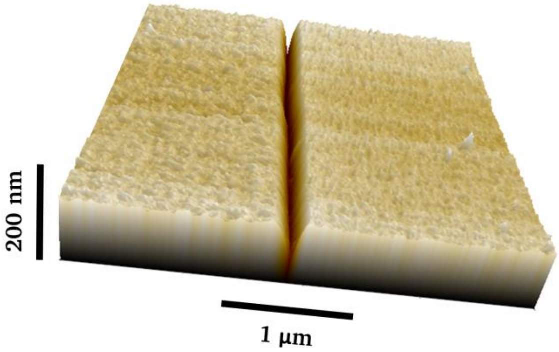

Fig. 4.76: AFM topography image of an optimal thermal grain-boundary groove (x = 1.0).

Table 4.3: Grain-boundary to Surface Energy Ratio (γ_{gb}/γ_s) as a Function of Stoichiometry for Hydroxide-powder Compacts.

x	Direct slope measurement	Mullins approximation
0.95	0.52 ± 0.23	0.63 ± 0.23
1.0	0.77 ± 0.22	0.94 ± 0.27
1.5	0.38 ± 0.13	0.58 ± 0.37

Pressureless sintering studies in reducing and oxidizing atmosphere indicate enhanced densification for MgO-rich spinel (suggesting lower γ_{gb}/γ_s)[121,186] and coarsening for Al_2O_3-rich spinel (suggesting higher γ_{gb}, and thus higher γ_{gb}/γ_s[121,186]).[2,94] Although γ_{gb}/γ_s was lower for MgO-rich spinel compared to stoichiometric, it was lower yet for Al_2O_3-rich spinel. This lack of correlation for Al_2O_3-rich spinel suggested factors other than interface energies may have dominated densification.

Lower γ_{gb}/γ_s for MgO-rich spinel, along with increased bulk diffusion attributed to oxygen vacancies[94] and grain-boundary drag caused by intrinsic defects[86,161] and precipitates,[2] likely contributes to enhanced densification. However, only limited grain-boundary stoichiometry variation was expected. Although complete solubility exists for $x = 0.95$ at the processing temperature of 1850°C,[72] MgO precipitation, which is preferentially at boundaries,[2] likely occurred during cooling. Moreover, MgO solubility is <1 mol% (n ~0.96) at the thermal-grooving temperature of 1450°C,[72] and boundary precipitates were observed. In addition, MgO-depletion at boundaries[86,161,162] likely further shifted stoichiometry. Thus, spinel in the groove region was likely near-stoichiometric, suggesting γ_{gb}/γ_s is strongly sensitive to MgO-rich stoichiometry. However, it is not known whether lower γ_{gb}/γ_s was due to lower γ_{gb} or higher γ_s.

Near-stoichiometric boundaries were not expected in Al_2O_3-rich spinel. Despite some observed precipitation, Al_2O_3 solubility is still ~59 mol% (n ~1.44) at 1450°C.[72] Moreover, MgO-depletion was expected to further shift boundary stoichiometry to Al_2O_3-rich. The lower γ_{gb}/γ_s suggests either lower γ_{gb}, or that γ_{gb} increases are accompanied by proportionally larger γ_s increases. Reports indicate impurities lower γ_{gb},[129] and it may be similarly lowered by intrinsic defects ($\mathrm{Al}^{\bullet}_{\mathrm{Mg}}$, $\mathrm{V}'''_{\mathrm{Al}}$, $\mathrm{V}''_{\mathrm{Mg}}$) [86,89,98,103,162] that accommodate boundary strain energy. Moreover, higher γ_s for Al_2O_3-rich spinel is suggested by reports indicating Al-terminated surfaces have higher energy.[123,125-128] Since γ_s correlates with modulus and fracture, higher γ_s is also suggested by higher elastic constants and fracture toughness for Al_2O_3-rich single crystals.[124] Thus, lower γ_{gb}/γ_s may be due to higher γ_s and possibly lower γ_{gb}, but the latter is not associated with coarsening. If not interface energies, increased surface diffusion is a prime candidate to explain coarsening. Studies indicate higher grain-boundary diffusion and higher O^{2-} bulk diffusion in Al_2O_3-rich spinel,[139,145,293] and surface diffusion may similarly be higher. However, increased surface diffusion presumably also affects groove profiles and γ_{gb}/γ_s measurements, especially when using the Mullins approach, shedding some uncertainty on the results.

Thermal grooves for the compact hot-pressed with sulfate powder were poorly-formed, suggesting an insufficient thermal etch, which along with differential grain etching and high roughness precluded accurate grain-boundary groove-slope determination. The contrastingly smooth surface of the compact hot-pressed with sulfate powder with 1 wt% LiF indicated a much higher surface energy and/or surface diffusion, consistent with observations of coarsening of powder crystallites that were thermally-treated in air with LiF addition. That smooth surfaces were observed several hundred micrometers away from boundaries suggested defects associated with LiF contributing to surface-energy changes or enhanced surface transport were present in the bulk, with relevance to TOF-SIMS results (Section 4.3.5) and EIS (Section 4.3.8).

4.3.8 Electrochemical Impedance Spectroscopy (EIS)

Properties of EIS samples prepared from compacts hot-pressed with alkoxide and sulfate powders with and without LiF (Fig. 4.77) were described in Sections 4.1 – 4.3, but they are repeated here to emphasize structure-property relationships. Samples were estimated to have a theoretical density >99.5% and less than 0.05% porosity based on optical microscopy, SEM, TEM, and spectrophotometry. Hot-pressed sulfate-powder samples were opaque and one was darker ("dark") than the other ("white") due to reduction caused by vacuum fluctuations during hot-pressing. Stoichiometry was estimated slightly Al_2O_3-rich (x ~1.06) by LA-ICP OES/MS. Microstructure consisted of matrix grains ($\overline{GS}$ = 12 μm) and ~6 vol% aggregates of sub-micron grains ($\overline{GS}$ <0.5 μm) accounting for ~70% of the grain-boundary area and in which grain boundaries were decorated with an impurity phase. The sample hot-pressed with sulfate powder with LiF was transparent and stoichiometry was estimated at x ~1.16. Grain-size ($\overline{GS}$ = 25 μm) was uniform with areas of smaller micron-sized grains comprising <1 vol% and occasional secondary-phases at triple junctions. Whereas fracture was transgranular for samples without LiF, it was intergranular for the sample with LiF, indicative of chemical differences at the boundaries. Grain boundaries were devoid of secondary-phases, but grain-boundary scatter was observed by optical microscopy, Fresnel fringes and strain contrast were observed by TEM, and STEM-EDS indicated higher grain-boundary impurity content (C, Ca, S, Si) compared to matrix grains of compacts without LiF. However, LA-ICP OES/MS indicated lower total impurity content and ~0.5 wt% remnant lithium, while TEM-EDS indicated fluorine, especially at triple junctions, and SIMS indicated uniform lithium distribution in the bulk. Unlike compacts without LiF, grain-boundary stoichiometry gradients were not observed by STEM-EDS/EELS over the ~50 nm wide scans. The hot-pressed alkoxide-powder sample was transparent but dark with uniform grain size ($\overline{GS}$ = 4 μm), occasional MgO nodules ~150 nm in diameter, and slightly MgO-rich stoichiometry estimated at x ~0.995 based on the volume fraction of MgO nodules.

EIS results for sulfate-powder samples are shown in Fig. 4.78 – Fig. 4.80, a comparison at 850°C is shown in Fig. 4.81, and insets show high-frequency regions and Zview® simulation fits for higher temperatures. All EIS spectra were depressed semi-circles with centers below the real axis, indicating distributed capacitance, with good fits simulated using CPE's with $0.75 < n_C < 1$ (n_C refers to the CPE parameter). The spectra displayed increasing low-frequency tails with good fits simulated using Warburg elements with phase angles varying from $\pi/5$ to $\pi/8$. The sample hot-pressed with LiF displayed two well-resolved arcs at higher temperatures. Samples hot-pressed without LiF displayed single arcs, but bulges were noted below ~$50\cdot10^3$ Hz and better fits were obtained using two parallel RC-circuits in series, one representing grain boundaries. High-frequency arc intercepts were consistently near zero, indicating negligible electrode resistance, whereas low-frequency intercepts decreased with increasing temperature, indicating increasing conductivity following an Arrhenius relation (Fig. 4.82). The alkoxide-powder sample displayed single elongated arcs with much higher impedance (Fig. 4.83). Unresolved, elongated arcs were also noted for the sulfate-powder sample with LiF at lower temperatures. Unfortunately, the equipment did not permit high enough temperatures to resolve separate arcs for the alkoxide-powder sample. All sample spectra were unchanged in reducing conditions, indicating oxygen ions were not the main charge-carriers, consistent with other reports.[154] However, degradation of the gold electrodes in reducing conditions sometimes erroneously indicated lower impedance. Modulus plots did not reveal any additional arcs or features. Calculated properties based on both the series and complete brick-layer models are shown in Table 4.4.

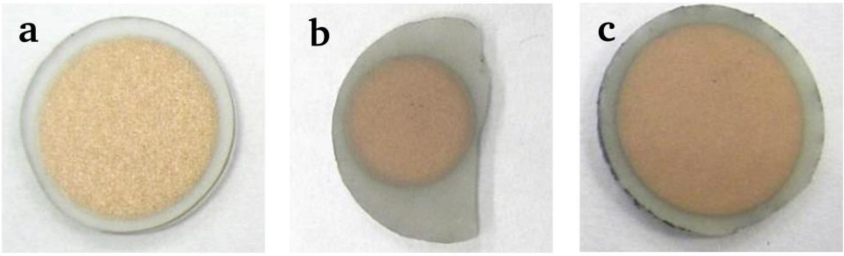

Fig. 4.77: Hot-pressed sulfate powder EIS samples with sputtered gold electrodes (without leads) made from (a) transparent compact with 1 wt% LiF, (b) dark-grey ("dark") opaque compact without LiF (note smaller electrode), and (c) light-grey ("white"), opaque compact without LiF. The alkoxide-powder sample had nearly-identical geometry to (a) and (c).

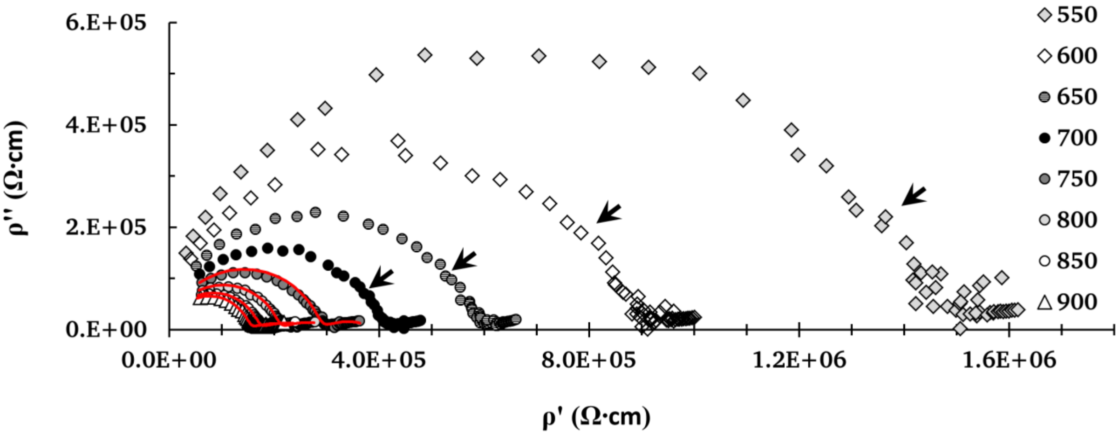

Fig. 4.78: EIS spectra for the dark sulfate-powder sample. Impedance is normalized for geometry (indicating resistivity on the real axis), arrows indicate low-frequency bulges, and Zview® simulation fits are shown as solid red lines.

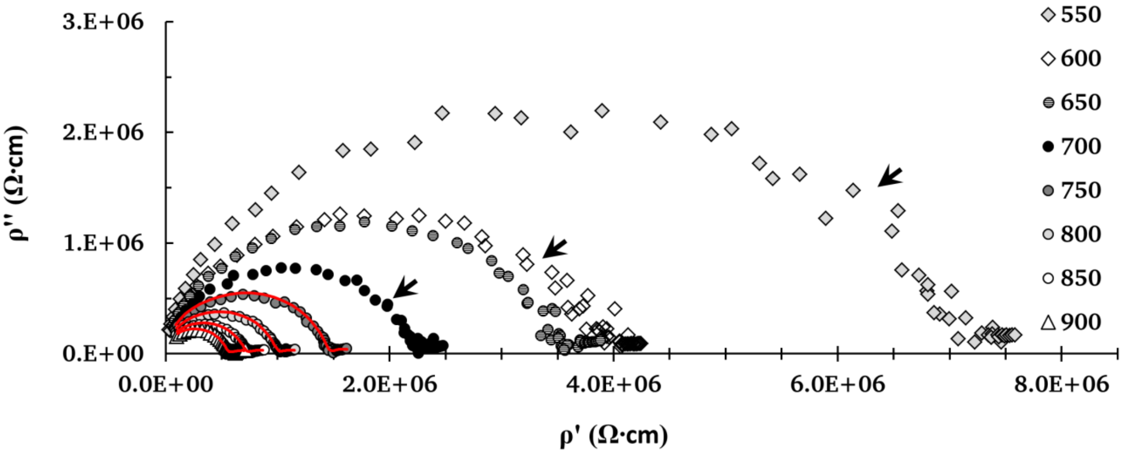

Fig. 4.79: EIS spectra for the light-colored sulfate-powder sample. Arrows show low-frequency bulges and Zivew® simulation fits are shown as solid red lines.

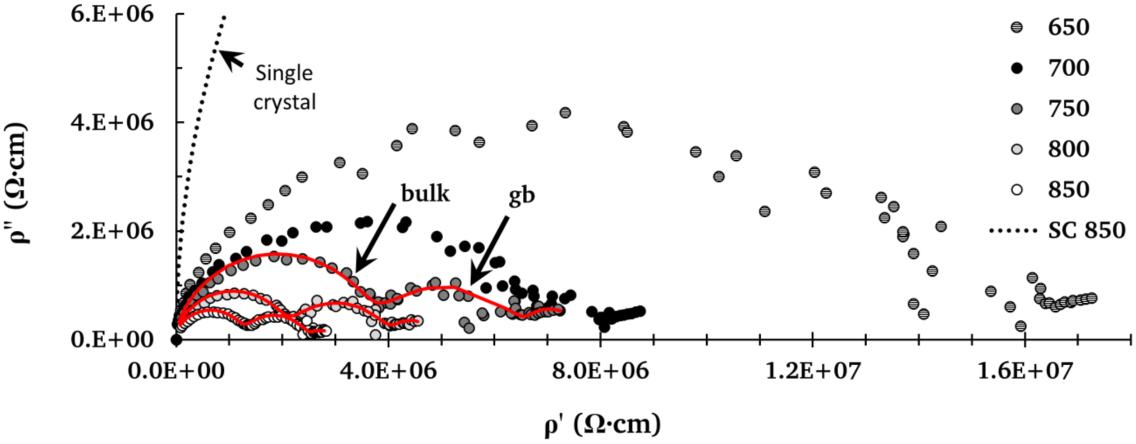

Fig. 4.80: EIS spectra for the transparent sulfate-powder sample with 1 wt% LiF. The simulated single-crystal impedance is based on $\sigma = 2.5 \cdot 10^{-8}$ S/cm at 850°C,[154] Zview® simulation fits are shown as solid red lines with bulk and grain-boundary components noted, and spectra for lower temperatures are not shown due to high scatter.

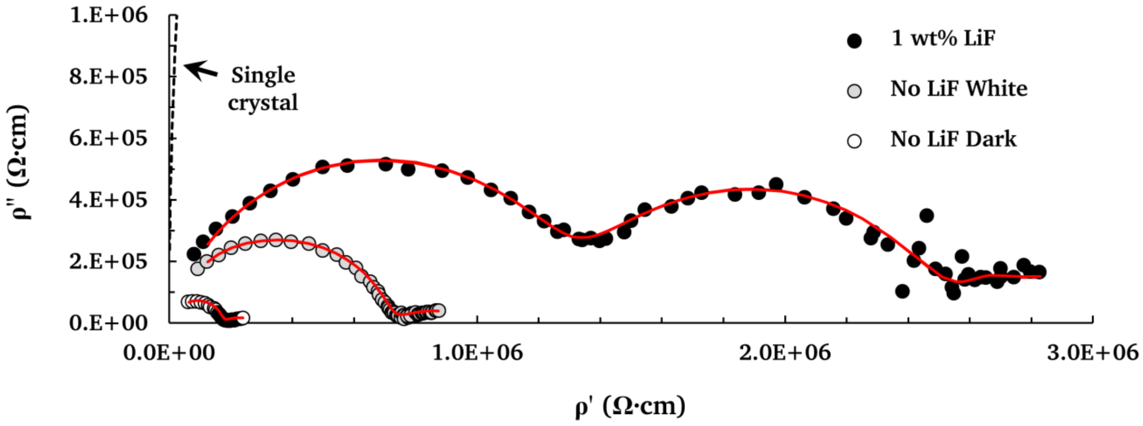

Fig. 4.81: Comparison of EIS spectra for sulfate-powder samples at 850°C showing Zview® simulation fits (solid lines) using the series model (ignoring dashed line in equivalent circuit in the inset) and simulated single-crystal impedance based on $\sigma = 2.5 \cdot 10^{-8}$ S/cm at 850°C (fine dashed line).[154]

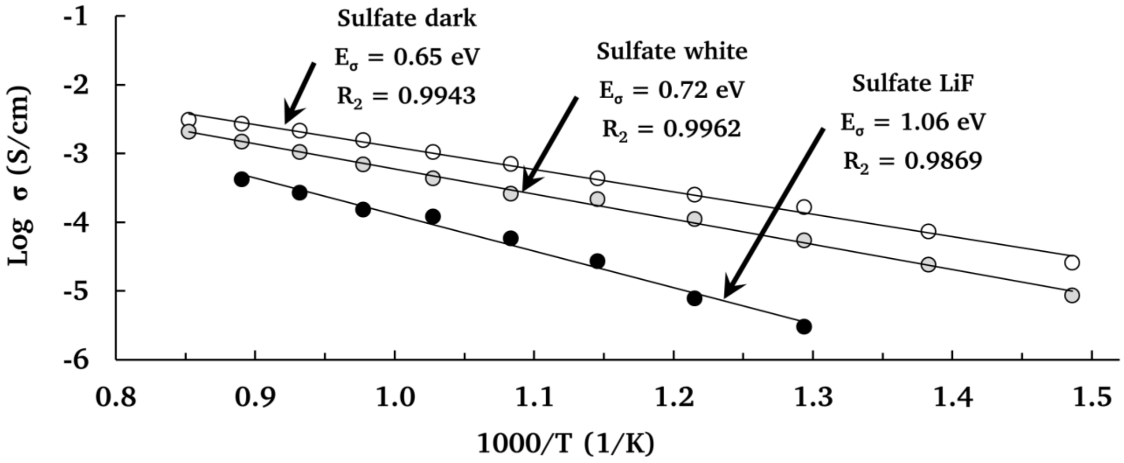

Fig. 4.82: Activation energies for total conductivity for sulfate-powder samples.

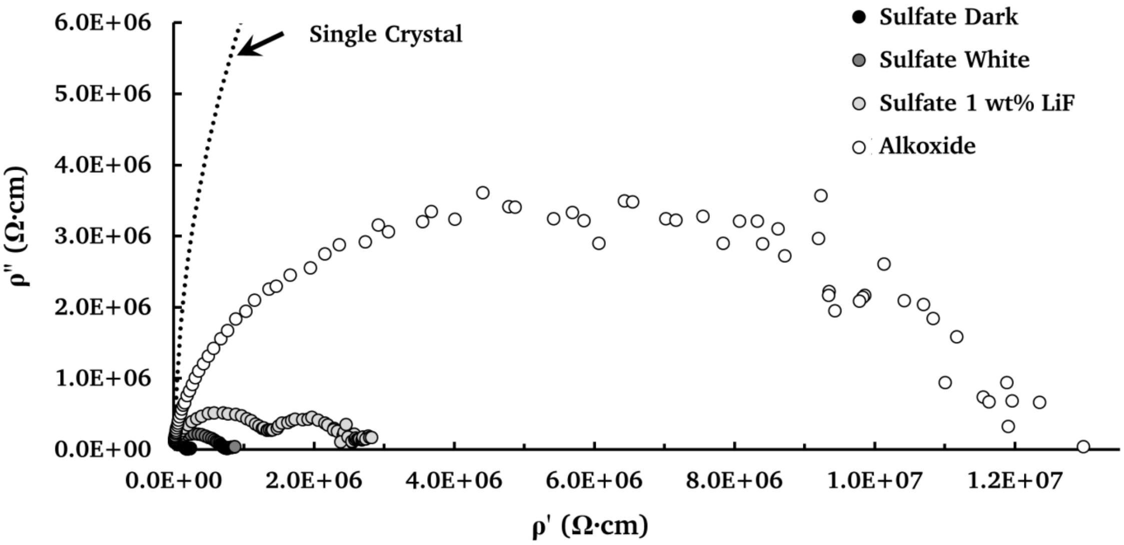

Fig. 4.83: EIS spectrum for the transparent alkoxide-powder sample at 850°C with EIS spectra for sulfate-powder samples shown for comparison. Spectra for lower temperatures are not shown due to high scatter.

Total conductivities for all samples were one decade or higher than reported values for single crystals of similar stoichiometry.[141,142,154] Although consistent with reported polycrystalline values,[154] lower values were expected due to impeded conduction across stoichiometry gradients, space-charge layers, and especially the core of grain boundaries.[86,89,161] Electrodes were well-aligned, and leakage and surface transport were not expected to increase conductivity to such extent.[278,294] This suggested higher bulk conductivity than for comparable single crystals and/or a parallel grain-boundary conductance contribution. Impurities and carbon contamination from the graphitic furnace could have contributed to the former, but higher than expected conductivity was also observed in the high-purity alkoxide-powder sample and carbon contamination alone would not explain the decades conductivity differences between samples subjected to similar hot-pressing conditions. Furthermore, impurities and carbon should have greater impact on grain-boundary conductivity, where they have been detected.[1,2]

Table 4.4: Selected Dielectric Properties of Polycrystalline Samples at 850°C.

Powder Additive Appearance	Sulfate No LiF Opaque, dark	Sulfate No LiF Opaque, white	Sulfate 1 wt% LiF Transparent	Alkoxide No LiF Transparent
Grain size D (μm)	11.5	11.5	25.1	4.3
σ_{sc}[a] (S/cm)	~3.0×10^{-8}	~3.0×10^{-8}	~3.0×10^{-8}	~1.0×10^{-8}
Series Brick-Layer Model				
gb width $d_{gb\perp}$[b] (nm)	1	1	1	1
$v_{gb\perp}$	8.70^{-5}	8.70^{-5}	3.98^{-5}	2.33^{-4}
σ_{total} (S/cm)	6.1×10^{-6}	1.4×10^{-6}	4.0×10^{-7}	1.1×10^{-7}
σ_{bulk}[c] (S/cm)	6.3×10^{-6}	2.2×10^{-6}	7.8×10^{-7}	1.1×10^{-7}
$\sigma_{gb\ total}$[c] (S/cm)	*2.3×10^{-4}*	*3.9×10^{-6}*	8.3×10^{-7}	*9.5×10^{-6}*
$\sigma_{gb\perp\ sp}$[d] (S/cm)	*2.0×10^{-8}*	*3.4×10^{-10}*	3.3×10^{-11}	*2.2×10^{-9}*
$E_{\sigma\ total}$[e] (eV)	0.63	0.71	1.07	-
$E_{\sigma\ bulk}$[f] (eV)	-	-	1.07	-
$E_{\sigma\ gb\perp}$[f] (eV)	-	-	*1.04*	-
$C_{eff\ bulk}$[g] (F)	-	-	9.8×10^{-12}	-
$C_{eff\ gb}$[g] (F)	-	-	1.8×10^{-9}	-
Complete Brick-Layer Model				
[h]gb width $d_{gb\parallel}$ (nm)	20	20	20	20
$v_{gb\parallel}$	1.74×10^{-4}	1.74×10^{-4}	7.97×10^{-5}	4.65×10^{-4}
[i]$\sigma_{gb\parallel\ sp}$ (S/cm)	*1.8×10^{-3}*	*4.0×10^{-4}*	2.4×10^{-4}	*1.0×10^{-5}*

[a] Estimated stoichiometry-adjusted single-crystal conductivities; $\sigma_{sc\ stoich}$ ~2.5×10^{-8} S/cm.[154]
[b] g.b. width contributing to impedance across g.b. core estimated by TEM.
[c] σ_{bulk} and $\sigma_{gb\ total}$ based on R_{bulk} and R_{gb} from series RC-circuit Zview® simulation fits.
[d] $\sigma_{gb\perp\ specific}$ based on series model using $d_{gb\perp} = 1$ nm.
[e] Activation energies calculated from slope of Arrhenius plots.
[f] Limited data points for bulk and g.b. activation energies.
[g] $C_{eff} = R^{((1-n)/n)} * Q^{(1/n)}$ calculated from CPE values from Zview® simulation fits.[282]
[h] Width contributing to parallel conductivity estimated from STEM-EDS of MgO-deficient boundaries.[86,89,162]
[i] $\sigma_{gb\parallel\ specific}$ for complete brick-layer model with $d_{gb\perp} = 1$ nm, $d_{gb\parallel} = 20$ nm; overestimate for 1 wt% LiF value.
Values in italics are uncertain due to poorly-resolved grain-boundary arcs.

In contrast, parallel grain-boundary conductance was suggested by small grain-size in some samples and high reported grain-boundary ionic conductivity.[160] Grain-boundary conductivity is typically discounted due to a small conductive width, but wider Mg-depleted grain-boundary zones would result otherwise. Moreover, higher conductivity at boundaries is not unexpected for normal ionic materials without significant defect concentrations typical of solid electrolytes, and enhanced conductivity along field-parallel grain-boundaries has been observed in other ceramics[295-297] and should be accentuated by current-line detouring along easy paths (Fig. 4.84).[298] Parallel conductance decreases calculated values for bulk and grain-boundary conductivity if unaccounted for by considering only a series model (Eq. 3.18.8), but the resulting equivalent circuit (Fig. 3.3b) and Eq. 3.18.12 cannot be solved without knowing at least two specific conductivities. However, assuming bulk conductivities were unchanged (equal to comparable single-crystals), estimating the intervening grain-boundary conductivity based on this value and the series model bulk to grain-boundary conductivity ratio, and using Eq. 3.18.12 with grain sizes and boundary widths from Table 4.4, the specific field-parallel grain-boundary conductivity required to reduce total conductivity to that observed was estimated at $\sim 2 \times 10^{-3} - 1 \times 10^{-5}$ S/cm for samples without LiF and $\sim 2.4 \times 10^{-4}$ S/cm for the sample with LiF. Although parallel conductance could not be unequivocally confirmed, the results strongly suggest it was responsible for the high observed conductivity, perhaps with a contribution from an impurity-related increase in bulk conductivity.

Near-zero high-frequency arc intercepts, arc capacitances consistent with bulk values for oxides,[78,283] and the absence of other high-frequency arcs in modulus plots, imply the single arcs in sulfate-powder samples without LiF were mainly due to bulk impedance. Intervening grain-boundary impedance was not expected to contribute to the arcs at higher frequencies due to the larger time-constant, with differences of less than one decade typically required for merging arcs.[278] Two decades higher than expected bulk conductivity calculated using the series model was attributed to conduction along Mg-depleted, field-parallel grain boundaries, likely accentuated by current-line detouring through impurity-rich regions of submicrometer grains.[298] The contribution from impurities was deemed likely due to their concentration at boundaries. Increased magnesium loss due to reducing conditions in the graphitic furnace[2,75,79-81,83] and carbon contamination likely also contributed to increased grain-boundary conductivity, especially for the darker sample.

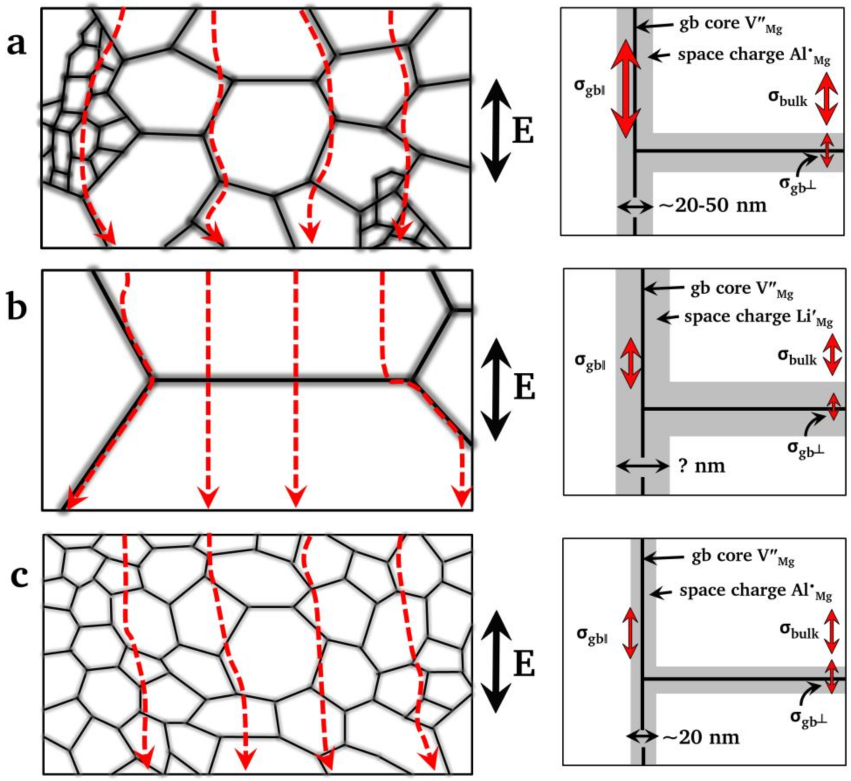
a
E
gb core V''_{Mg}
space charge $Al^{\bullet}_{Mg}$
σ_{gbl}
σ_{bulk}
$\sigma_{gb\perp}$
~20-50 nm
b
E
gb core V''_{Mg}
space charge Li'_{Mg}
σ_{gbl}
σ_{bulk}
$\sigma_{gb\perp}$
? nm
c
E
gb core V''_{Mg}
space charge $Al^{\bullet}_{Mg}$
σ_{gbl}
σ_{bulk}
$\sigma_{gb\perp}$
~20 nm

Fig. 4.84: Possible conduction mechanisms in polycrystalline spinel, "E" represents the AC field direction. (a) sulfate-powder sample without LiF, (b) sulfate-powder sample with 1 wt% LiF, (c) alkoxide-powder sample without LiF. Dashed arrows indicate current lines. Vertical arrows besides conductivity symbols indicate relative magnitudes. Shaded regions indicate relative effective grain-boundary widths and differing conductivities due to Mg-depletion, V''_{Mg}, and/or Li'_{Mg}.

Bulk impedance arcs in sulfate-powder samples without LiF imply intervening field-perpendicular grain-boundary impedance, even if parallel conduction exists, as suggested by low-frequency arc bulges. It is unlikely the bulges were due to sample-electrode effects, such as partial blocking, as bulge capacitances were similar to those for grain-boundary arcs in samples with LiF and to expected values for grain boundaries in oxides.[278,283] Simulations using the series model confirmed good fits with a larger bulk impedance and a smaller series grain-boundary impedance ($C_{bulk} = 10^{-12}$ F and $C_{gb} = 10^{-9}$ F at 850°C). Assuming an effective resistive width of 1 nm, *specific* resistivity *across* field-perpendicular grain-boundaries (using the series model) was several decades lower than for the bulk, attributed to poor transport across the core. However, as separate arcs were not fully-resolved, grain-boundary properties for these samples involve uncertainty and grain-boundary capacitances were not used to independently calculate grain-boundary widths. Arc non-linearity in these and other samples was attributed to microstructural variation, with possible contributions from surface and coating heterogeneities, slow adsorption reactions, and non-uniform potential and current distribution.[278,280] The low-frequency tails were attributed to sample-electrode effects.[279]

Different dielectric properties for the sulfate-powder sample with LiF were expected given microstructure, fracture, and optical property differences compared to without LiF addition. The two well-resolved arcs at higher temperatures were attributed to bulk and grain-boundary impedances as capacitances matched typical values for these components.[278,283] Higher than expected total conductivity than for comparable single crystals using the series model was attributed to field-parallel grain-boundary conduction. However, lower total conductivity compared to without LiF addition was partly attributed to larger grain-size and lower impurity content per unit volume (even though matrix grain-boundary impurity content was higher). Larger grain-size was expected to reduce the field-parallel grain-boundary contribution, thus increasing the conductance contribution across (and corresponding impedance from) the bulk and intervening grain boundaries. Although bulk conductivity was lower than without LiF addition, arc capacitances were similar and high-frequency intercepts were still near zero.

Higher activation energy for bulk conductivity and a different ratio of bulk to grain-boundary conductivity in the sulfate-powder sample with LiF compared to without LiF suggested other factors besides grain size and parallel conductance affected conductivity. Lower bulk and especially grain-boundary conductivities were also attributed to scatter and point-defect trapping caused by the incorporation of lithium. Although LiF shifts stoichiometry to more conductive Al_2O_3-rich composition, lithium was expected to replace magnesium by $2LiF \rightarrow 2Li'_{Mg} + 4Al_{Al}^{x} + 7O_{O}^{x} + V_{O}^{\bullet\bullet} + MgF_2 + MgO,$ rather than by forming conductivity-enhancing V''_{Mg}.[215] Although the defect chemistry is speculative, possible lower lithium concentration at boundaries suggested by nano-SIMS could either increase conductivity at boundaries due to higher magnesium content or decrease conductivity if lithium occupies magnesium vacancies. The counteraction of absorption by LiF also indicated a lower charge-carrier concentration. As for the sample without LiF, decades lower *specific* conductivity *across* grain-boundaries than for the bulk was attributed to poor ionic transport across the core. Based on EIS between 750°C and 850°C, where arcs were well-resolved, activation energies for bulk and field-perpendicular grain-boundary conductivity using the series model for the sulfate-powder sample with 1 wt% LiF were estimated at 1.07 eV and 1.04 eV, respectively, but a higher value had been expected for the boundaries.

If conductivity is predominantly ionic in spinel, decreased bulk and grain-boundary conductivity (perpendicular and parallel) with LiF addition does not necessarily contradict the enhanced densification observed with LiF addition attributed to increased bulk or interface diffusion. This is because O^{2-} is the rate limiting species for densification and its diffusivity and ionic conductivity are decades lower than for the cations, and it is likely cation conductivities (and hence diffusivities) are also affected by LiF. In addition, most densification studies with LiF have been conducted with pressure-assisted sintering, which provides an additional driving force for transport from surfaces and grain boundaries to voids, subjecting ion diffusion to different driving forces than conductivity.

Higher total conductivity than for comparable single crystals for the alkoxide-powder sample was also primarily attributed to field-parallel grain-boundary conductance. Although impurity concentration was low, grain-boundary charge-carriers were still expected. The presence of isolated MgO nodules was not expected to contribute significantly to impedance. Lower total conductivity compared to sulfate-powder samples was attributed to MgO-rich stoichiometry and cleaner grain boundaries, and also demonstrated that greater grain-boundary area alone does not necessarily increase conductivity and that carbon contamination likely has less effect than stoichiometry and impurities, as this sample was subjected to identical hot-pressing conditions.

Determining the effective grain-boundary width for calculating specific conductivities was problematic. The effective width of 1 nm deemed to contribute to impedance across grain-boundaries was an approximation of assumed mechanisms near the core. When the effective width was calculated using $d \approx D(C_{\mathrm{bulk}}/C_{\mathrm{gb}})$ and capacitance values from the series model,[299] a value of 135 nm was obtained for the sample with LiF (where distinct grain-boundary arcs were observed). However, this assumed equal bulk and grain-boundary permittivities, which is unlikely due to grain-boundary stoichiometry, impurity, and additive gradients. Although, the value of $\varepsilon_{bulk} = 9.0$, calculated from $\varepsilon_{bulk} = C_{gb\perp}(d/D)(A/L)(1/\varepsilon_0)$ using a grain-boundary width of 135 nm compared favorably with $\varepsilon_{spinel} = 8\text{-}9.2$.[2] The effective width contributing to enhanced conduction along grain-boundaries of 20 nm was also an approximation, as stoichiometry and impurity gradients differ between samples. For the sample with LiF, the lack of detection of Mg-depleted grain-boundary zones with STEM (at least over the ~50 nm widths examined) may indicate stoichiometry gradients were shallower and wider than for samples without LiF rather than absent. This was suggested by observable grain-boundary scatter by optical microscopy (in the absence of grain-boundary phases), in which case using an effective grain-boundary width of 20 nm overestimated parallel conductivity (consistent with lithium incorporation decreasing conductivity).

Although high conductivity along grain-boundaries due to stoichiometry gradients and impurities was suggested, their respective contributions and the specific impurities and point-defects responsible could not be unequivocally determined. Analysis was complicated as conduction mechanisms and transference numbers as a function of stoichiometry and temperature in spinel are not known with certainty. EIS studies varying grain size, stoichiometry, and grain-boundary impurities while keeping other variables fixed, and using blocking and non-blocking electrodes, combined with measurement of grain-boundary conductivities with microelectrodes would help determine respective conductivity contributions. Decoration with cathodoluminescence combined with SEM and TEM to identify and quantify resistive features such as secondary-phases at triple junctions and grain boundaries would also be valuable.

CHAPTER 5 GENERAL DISCUSSION

This chapter provides a general discussion of the results. Section 5.1 summarizes the results of powder and bulk compact characterization, Sections 5.2, 5.3, and 5.4 discuss the effects of stoichiometry, impurities, and LiF on interfaces and on mechanical, optical, and electronic properties, and Section 5.5 discusses combined effects on interfaces, mainly relating to electronic properties.

5.1 Interfaces and Starting Powders

The interfaces of spinel compacts made from powders with different stoichiometries, impurity contents, and LiF additions were probed by optical and electron microscopy, atomic-force microscopy, and various diffraction and spectroscopic methods. In order to relate interface properties to processing and properties, starting powders and bulk properties were also characterized. Although starting powders had similar crystallite, particle, and agglomerate size characteristics, sulfate-derived powders were slightly alumina-rich (x ~1.05) and had more impurities (>1000 ppm, mainly sulfur), whereas alkoxide powders were slightly MgO-rich (x ~0.995) and had less impurities (<100 ppm). These small differences in stoichiometry and impurity content, as well as small changes in LiF additions, were found to affect the free energy, diffusion, lattice parameter, stress state, and mechanical, optical, and electronic properties of interfaces, which in turn affected sintering, densification, microstructure evolution and bulk properties. Although hydroxide-derived powders were not directly compared to sulfate and alkoxide-derived powder compacts, small, deliberately induced differences in stoichiometry in these compacts had similar effects on interfaces and properties.

5.2 Interfaces, Stoichiometry, and Microstructure Evolution

Effect of MgO-rich stoichiometry on densification

Compacts made with Al_2O_3-rich hydroxide-derived powders ($x = 1.5$) were found to have the lowest grain-boundary to surface energy ratio ($\gamma_{gb}/\gamma_s = 0.38$), followed by MgO-rich hydroxide-powder compacts ($x = 0.95$, $\gamma_{gb}/\gamma_s = 0.52$) and stoichiometric hydroxide-powder compacts ($x = 1.0$, $\gamma_{gb}/\gamma_s = 0.77$). The low γ_{gb}/γ_s for MgO-rich compacts, combined with reported grain-boundary drag from intrinsic defects and higher bulk conductivity due to oxygen vacancies, was expected to favor densification over coarsening, consistent with dilatometry results and reported enhanced densification for MgO-rich spinel. However, due to precipitation and local depletion of MgO, interfaces in these compacts were expected to be closer to stoichiometric than the bulk, suggesting interface energy may be sensitive to even smaller stoichiometry differences. Grain-boundary MgO-depletion was suggested by a smaller lattice parameter than grain interiors by convergent-beam electron diffraction (CBED). Unfortunately, chemical gradients associated with stoichiometry gradients were not observed by electron-energy loss spectroscopy (EELS), possibly because they were too shallow to be detected.

Effect of Al_2O_3-rich stoichiometry on coarsening and densification

The low γ_{gb}/γ_s ratio for Al_2O_3-rich spinel compacts appeared inconsistent with reports indicating delayed sintering for these compositions and with dilatometry results, with the explanation lying in the densification mechanism. Compared to stoichiometric, Al_2O_3-rich spinel reportedly exhibits higher bulk, grain-boundary, and likely surface diffusion, the latter favoring coarsening, which is typically observed. Thus, although interface energies favor densification for Al_2O_3-rich spinel, it is opposed by coarsening due to higher surface transport. However, during pressure-assisted sintering, pressure directs mass transport from areas of higher stress at interparticle contacts to areas of lower stress at intervening pores, allowing surface transport to contribute to densification. Under these conditions, Al_2O_3-rich compositions are expected to enhance densification.

Effect of non-stoichiometry on compact surface stress state

Astoichiometry also affected compact surfaces, which were Al_2O_3-rich compared to the bulk due to MgO evaporation during sintering. Al_2O_3-rich spinel has a smaller lattice parameter, a slightly lower thermal expansion, and is associated with a volume reduction compared to stoichiometric spinel. However, it is unclear how these affected the stress state at surfaces. Differential sintering of compact surfaces and the slightly lower thermal expansion of Al_2O_3-rich spinel were expected to result in surface compression. However, polarized-light microscopy indicated low single-digit MPa surface tension, possibly because the volume reduction associated with the stoichiometry change offset the thermal expansion difference.

Effect of stoichiometry on properties

Al_2O_3-rich compositions exhibited larger grain sizes due to increased interface transport and associated coarsening. Although not conclusively demonstrated, stoichiometry gradients at internal interfaces such as grain boundaries were expected to affect fracture, optical, and electronic properties. Grain-boundary MgO-depletion was expected to (i) result in residual stress due to thermal-expansion mismatch and/or volume change compared to grain interiors, (ii) to cause optical scatter due to refractive index variation, and (iii) to affect electronic conductivity (Sections 5.4 and 5.5).

5.3 Interfaces, Impurities, and Microstructure Evolution

Effect of impurities on densification and microstructure evolution

Impurities (~1000 ppm) in sulfate-derived powder compacts segregated at grain boundaries, especially within aggregates of submicrometer-sized grains, which were interspersed between larger micron-sized matrix grains. The only features that corresponded to the well-dispersed nature of the aggregates were crystallite-size variation and agglomeration. These were expected to result in inhomogeneous green bodies and associated grain-size variations, and assumed to have contributed to the formation of the aggregates.

Segregated impurities in sulfate-powder compacts formed a eutectic melt with spinel at processing temperatures and upon cooling solidified into glassy C, S, Si, and K-rich phases at triple junctions within submicrometer-grain aggregates and along interfaces between the aggregates and matrix grains. The morphology of the glassy phase, its location along the interface between matrix grains and submicrometer-grain aggregates, and the planarity of this interface, suggested the phase wet this interface at processing temperatures and de-wet upon cooling. The phase was expected to have an associated vapor at processing temperatures, which was expected to fill or partially-fill triple junctions. Impurities and the glassy phase were expected to restrict grain-growth by solute drag and Zener pinning, respectively, while the associated vapor was expected to oppose both grain growth and densification, explaining the small grain size within the submicrometer grain aggregates. While the glassy phase restricted grain-growth in the aggregates, it stabilized the interface between the aggregates and larger matrix grains, allowing the latter to grow at the expense of the former. Submicrometer grain boundaries intersected larger adjoining matrix boundaries at high angles, indicating a high relative surface energy for the matrix grains, which in turn is a driving force for coarsening. The uniform grain-size observed in compacts hot-pressed with higher-purity alkoxide-derived powders (which also exhibited agglomeration) was attributed to a lack of impurities and demonstrated that agglomeration alone does not necessarily cause bi-modal grain-size distributions.

Effect of impurities on fracture properties

Bi-modal grain-size distributions caused by a combination of agglomeration and impurities in sulfate-derived powder compacts were associated with large grains, which serve as fracture origins and lower strength. Matrix grains in these compacts fractured trans-granularly, whereas grains within submicrometer grain aggregates fractured inter-granularly due to the presence of impurities and glassy phases.

Effect of impurities on optical properties

Absorption over the entire visible spectrum, due to carbon contamination in the starting powders and from the graphitic furnace, was the main source of reduced light transmission in sulfate and alkoxide powder compacts. In sulfate-powder compacts, the additional scatter from glassy phases caused by less than ~1000 ppm impurities contributed to opacity. Glassy phases at triple-junctions scattered wavelengths on the order of their sizes, grain-boundary phases perpendicular to the incident light scattered shorter wavelengths, and those near-parallel to the incident light were expected to scatter longer wavelengths, especially phases with a larger areal extent, like the interfaces between matrix grains and submicrometer grain aggregates. The size-range and large extent of the glassy phases (submicrometer grains constituted the majority of the grain-boundary area) resulted in scatter from the near-UV to the visible and lower transmittance in the infrared. Impurities were also deemed to increase grain-boundary conductivity, as discussed in Section 5.5.

5.4 Interfaces, LiF, and Microstructure Evolution

LiF was found to have a complex and profound effect on the free-energy, diffusion, fracture, optical and electronic properties of interfaces, thereby affecting sintering, densification, microstructure and final properties. LiF addition (i) caused spinel crystallites to coarsen during the initial stages of sintering, (ii) shifted stoichiometry towards Al_2O_3-rich composition, (iii) lowered the impurity content, (iv) lowered the densification temperature, (v) increased grain size and homogeneity, (vi) increased transparency, and (vii) decreased conductivity, but it also (viii) embrittled grain boundaries and (ix) caused scatter at grain-boundaries at shorter visible wavelengths.

Reaction of LiF with spinel to form MgO

The coarsening of loose spinel crystallites during thermal treatment, observed only with LiF addition, indicated vapor-phase transport, which in turn required the formation of volatile magnesium and aluminium-containing species. Thermodynamic simulations indicated that LiF reacted with spinel to form MgF_2, $LiAlO_2$ and AlF_3, with MgF_2 indicated as the prevalent volatile reaction species. Thus, and also partly because of the formation of the LiF:MgF_2 eutectic (at ~740°C), MgF_2 was expected to evaporate more prevalently than volatile aluminium species during processing. Chemical analysis confirmed compacts processed with LiF were magnesium-deficient, especially at surfaces, shifting stoichiometry from x ~1.05 to x ~1.15 in sulfate powder compacts. Although pure LiF melts at ~850°C, STA-MS, dilatometry, and thermodynamic simulations indicated it reacted with spinel at as low as ~650°C. This partially explained the lower sintering onset of 800°C with LiF, 200°C below that observed without LiF. With added pressure, some densification occurred at 600°C, up to 400°C lower than without LiF, with only 200°C of this attributable to the nominal 3 MPa applied below 1200°C during hot-pressing.

Reaction of LiF with impurities

In addition to lowering magnesium content, chemical analysis indicated lower impurity (C, Ca, S, Si, Fe) content in compacts hot-pressed with LiF, especially at surfaces and by orders of magnitude for some impurities. STA-MS of sulfate-derived spinel powders with LiF showed LiF catalyzed the decomposition of remnant magnesium and aluminum sulfates to volatile SO_x species at ~1075°C in argon, air, or vacuum. Thermodynamic simulations indicated fluorine and MgF_2 reacted with calcium, iron, and likely other impurities, to form volatile fluorides. In turn, SO_x species and impurity fluorides could be removed during hot pressing by applying pressure at a temperature above that at which these species outgassed. Whereas, applying pressure at lower temperatures forced densification to lower temperatures, trapping volatiles within compacts.

Incorporation of LiF in the lattice

While LiF reduced impurity content, approximately half of the original lithium (~15,000 ppm for 1 wt% addition) remained in the compacts. Whereas fluorine from LiF reacted to form fluorides, secondary-ion mass spectroscopy (SIMS) showed lithium was uniformly distributed within spinel grains. The increased inversion parameter indicated by Raman spectroscopy suggested lithium incorporated via a lattice replacement. Moreover, fluorescence observed by

Raman spectroscopy and under ultraviolet laser irradiation suggested lithium incorporation was associated with the formation of point-defects. Lithium likely replaced Mg^{2+} since the ionic radius is similar and the charge difference is smaller than for Al^{3+}, with charge likely compensated by oxygen vacancies and/or Al^{3+} on Mg^{2+} sites and the replaced magnesium and free oxygen forming MgO. The latter was indicated by magnesium depletion in sulfate powders and MgO nodule formation in (MgO-rich) alkoxide powders hot-pressed with LiF. Hence, in addition to magnesium depletion from MgF_2 formation, lithium likely contributed to magnesium depletion by MgO formation, some of which likely evaporated during processing due to its higher vapor pressure.

Effect of LiF on interface energies

Atomically-smooth surfaces observed by atomic-force microscopy (AFM) in thermally-etched polished compacts hot-pressed with LiF, as opposed to atomically-rough surfaces in those without LiF, indicated LiF increased surface transport and/or energy. Increased surface transport due to LiF was indicated by facetted growth in loose crystallites and increased densification with applied pressure. Lower lithium content at grain boundaries suggested by nano-SIMS could not be confirmed with other methods. However, it would be consistent with magnesium-deficient grain boundaries indicated by CBED, as these would have fewer sites for lithium to replace magnesium, in which case, $Al_{Mg}^{\bullet}$ rather than Li_{Mg}' would charge-compensate V_{Mg}''.

Effect of LiF on densification

Increased surface and vapor transport and the shifting of stoichiometry towards Al_2O_3-rich composition, which exhibits higher diffusion and causes coarsening, precluded densification of spinel powders with added LiF without pressure, as confirmed by dilatometry. However, as explained above, increased surface and vapor transport enhanced densification and lowered its onset temperature during pressure-assisted sintering, as demonstrated by hot-press displacement curves for compacts processed with LiF. Since densification is controlled by the slowest species along the fastest path, which reports suggest is grain-boundary oxygen-ion diffusion, the uniform distribution of lithium and the associated point defects were expected to increase densification, especially if at least some of the defects were present at interfaces. Moreover, the lower yield stress associated with Al_2O_3-rich stoichiometry likely also contributed to densification.

Effect of LiF on microstructure evolution

LiF-induced coarsening and the removal of eutectic-forming impurities prevented the formation of submicrometer-grain aggregates and resulted in a larger and more uniform grain size. The formation of spherical MgO nodules in alkoxide powders hot-pressed with LiF suggested a high interface energy and the nodules likely restricted grain size by pinning boundaries. However, depending on the amount of LiF added, excess MgF_2, and likely LiF, accumulated at triple junctions and pinned grain boundaries, as demonstrated by the gradient in impurity and lithium concentration from compact geometric center to exterior surface that was concomitant with increased grain-size and transmittance.

Effect of LiF on fracture

Compacts processed with LiF exhibited intergranular fracture, as opposed to transgranular fracture without if. However, the cause of intergranular fracture could not be determined with certainty. The shifting of stoichiometry towards Al_2O_3-rich composition by LiF was expected to be greater at boundaries due to higher evaporation and outward diffusion of MgO in the late stages of sintering. However, this should have been at least partially counter-balanced by MgO diffusion from grain interiors to boundaries. If present, Al_2O_3-rich boundaries would be expected to result in residual tensile stress due to the lower thermal expansion compared to stoichiometric or near-stoichiometric grain interiors (as grain interiors with higher shrinkage would exert an inward traction on the boundaries).

Grain-boundary embrittlement by LiF

CBED possibly suggested a smaller lattice parameter at boundaries and the reversing contrast of lattice-fringe patterns observed by de-focus transmission electron microscopy (TEM) indicated a chemical or lattice variation at boundaries, both more prominently in compacts with LiF addition. However, apart from possibly lower lithium content at boundaries suggested by nano-SIMS, significant chemical gradients were not observed by STEM-EDS or STEM-EELS. It is possible that species contributing to chemical gradients were below the resolution of the instrument or that chemical gradients were too wide and shallow for the small length scales examined (<50 nm). Strain contours observed by TEM in compacts hot-pressed with LiF suggested the presence of stress, but it could not be determined whether it was tensile of compressive. The low grain-boundary to surface-energy ratio indicated for Al_2O_3-rich compositions by AFM would be expected to result in stronger, rather than weaker boundaries. However, these results were for compacts processed without LiF; the results for compacts with LiF were ambiguous.

STEM-EDS confirmed grain boundaries in samples processed with LiF had higher impurity contents and this was attributed to impurity concentration with decreasing grain-boundary area associated with coarsening. However, embrittlement was also observed in high-purity (<100 ppm total) alkoxide-derived flame-spray pyrolysis powder compacts hot-pressed with as little as 0.25 wt% LiF. Quenching experiments indicated a transition from intergranular to transgranular fracture after quenching, suggesting solute species or point-defects at boundaries were re-dissolved in the bulk during thermal treatment. It is possible that a combination of defect chemistry variation, residual tensile stress, and a lower work of fracture caused the embrittlement observed in compacts processed with LiF.

Effect of LiF on optical properties

LiF addition enabled transparency by removing impurities. However, when added in higher concentration (>1 wt% for the typical hot-pressing regime) or if densification was forced to occur below the vaporization range (1000°C – 1200°C) of LiF or its by-products by pressure application or by using spinel powders with higher sintering activity, then LiF and/or its by-products (MgF_2) accumulated at triple junctions and became the main source of optical scatter. However, even for lower concentrations (1 wt%), chemical analysis indicated half of the added lithium remained, and this concentration was higher than all of the other impurities combined. Despite high remnant lithium in compacts with 1 wt% LiF addition, only scarce triple-junctions with MgF_2 and/or LiF were observed, confirming SIMS results indicating lithium incorporated within the spinel lattice. However, optical scatter made grain boundaries within the thickness of these compacts visible by optical microscopy. Even though this required scattering features on the order of the scattered light (500 – 750 nm), no such scattering features were identified. Similar to the preceding discussion on embrittlement, it is likely that strain or shallow stoichiometry or point-defect gradients were responsible.

Hot-press experiments, electron microscopy, and spectrophotometry indicated scatter at short wavelengths in MgO-rich alkoxide-derived powder compacts with added LiF was caused by the refractive index variation associated with MgO nodules (n = 1.735 versus 1.710 for spinel) and their surrounding strain fields, while absorption was caused by carbon contamination. Indeed, absorption was completely eliminated by shielding compacts with molybdenum foil and using alumina dies. Moreover, absorption correlated with Al_2O_3-rich stoichiometry and thermodynamic simulations indicated aluminum oxy-carbides as a source. The specific light-absorbing impurity or point-defect removed by lithium fluoride was not determined with certainty. However, it was most likely carbon, as this was identified as the source of absorption in compacts hot-pressed without LiF and its concentration was lower with LiF addition. Doping experiments with Li_2O and AlF_3 suggested lithium, rather than fluorine, was responsible for counteracting absorption, although the specific mechanism was not identified. It is possible lithium reacted with carbon to form volatile lithium-carbon compounds or that the presence of lithium altered the behavior or light-absorbing defects or impurities. Although impurities concentrated at boundaries in compacts with LiF, electrochemical impedance spectroscopy indicated the larger grain-size resulted in a lower volume-fraction of conductive boundaries (Section 5.5).

5.5 Interfaces and Combined Effects

Stoichiometry, impurities, and LiF had combined effects on internal and external interfaces and sintering, densification, microstructure evolution, and bulk properties, especially optical and electronic properties. LiF reduced impurities and shifted stoichiometry towards Al_2O_3-rich compositions and entrained gradients in these quantities and in properties they affected. Moreover, the effects of LiF were compounded by its entrapment within compacts under certain conditions, for example when using MgO-rich powders which sintered more readily or when applying pressure at lower temperatures during hot-pressing. For MgO-rich powders, LiF-precipitation of MgO nodules affected microstructure evolution and optical properties. The effect of LiF was more dramatic when more impurities were present in starting powders.

Conductivity was also affected by the interaction of stoichiometry, impurities, and LiF with interfaces. Compact conductivities were found to be more than one decade higher than reported values for single-crystals of similar stoichiometry and the activation energies for conductivity were lower. Higher conductivity was attributed to conductance and current-line detouring along magnesium-depleted, impurity-rich, field-parallel grain-boundaries with specific conductivities decades higher than the bulk. Whereas, specific conductivity across boundaries was decades lower than the bulk, attributed to poor transport across the core. However, the presence of parallel conductivity precluded determining specific bulk and grain-boundary dielectric properties with certainty. Carbon contamination from the starting powders and the graphitic furnace, and magnesium loss due to reduction likely contributed to increased bulk and especially grain-boundary conductivities. LiF addition decreased bulk and grain-boundary conductivities and increased the activation energies for conductivity, attributed to larger grain size caused by LiF-induced coarsening, less grain-boundary area and current-line detouring, lower total impurity and charge-carrier concentration, and lithium replacing magnesium (the main charge carrier) in the lattice. Conductivity of low-impurity, fine grain-size, MgO-rich (alkoxide powder) compacts was one decade or lower than higher-impurity, larger grain-size, Al_2O_3-rich (sulfate powder) compacts, attributed to MgO-rich stoichiometry and cleaner grain boundaries. The results suggest conductivity in polycrystalline spinel is a highly sensitive function of stoichiometry, stoichiometry gradients, impurities, carbon contamination, defect chemistry and gradients, and grain-boundary area.

CHAPTER 6 SUMMARY

This chapter provides a condensed summary of the experiments, results, the main findings, and also guidance for future work.

The interfaces of transparent polycrystalline magnesium aluminate spinel compacts made by a variety of methods and using powders with different stoichiometries, impurities and LiF sintering additive contents were characterized using a variety of analytical methods, with emphasis placed on how they affected densification, microstructure evolution and electro-optical properties. Small variations in starting powder stoichiometry, parts-per-million impurities, and minor additions of LiF were found to significantly affect the free energy, diffusion, lattice parameter, stress state, and mechanical, optical, and electronic properties of grain boundaries and surfaces, in turn affecting densification, microstructure evolution, and bulk properties.

For the first time, by using atomic-force microscopy, the ratio of grain-boundary to surface energy as a function of stoichiometry for spinel was determined. Astoichiometric compositions exhibited a lower grain-boundary to surface energy ratio, favoring densification. However, increased interface transport for Al_2O_3-rich compositions favored coarsening, precluding densification without pressure. Preferential MgO evaporation resulted in compact-scale and grain-boundary stoichiometry gradients, which affected fracture behavior, caused optical scatter, and affected conductivity, with Al_2O_3-rich compositions exhibiting higher conductivity, attributed to increased magnesium vacancies.

The specific mechanisms by which impurities modified interfaces to yield observed microstructures and the specific causes of optical scatter and absorption were determined. Starting powder impurities segregated at grain boundaries, restricting grain-growth by solute drag. Where present in higher concentration, they formed a eutectic melt with spinel at processing temperatures that wet grain boundaries, stabilizing interfaces between abnormal and adjacent smaller grains and contributing to bi-modal grain-size. When present at triple-junctions, the eutectic phase pinned grain boundaries, while its associated vapor opposed grain growth and densification. Combined with starting powder particle-size variation and agglomeration, the net effect was the formation of micron-sized grains interspersed with aggregates of sub-micrometer grains.

The impurity phase de-wet boundaries upon cooling and solidified into a glassy phase, especially at triple-junctions, resulting in intergranular fracture, optical scatter over the entire visible spectrum and into the infrared, and increased conductivity. Impurity-related scatter combined with absorption caused by carbon contamination from the graphitic hot-press fixtures resulted in opacity.

The multi-facetted effects and mechanisms associated with LiF were described for the first time. The mechanism by which LiF enhances pressure-assisted sintering was explained, and the mechanism by which fluorine reacts with impurities and magnesium was confirmed by simultaneous thermal analysis combined with mass spectroscopy, chemical analysis, and thermodynamic simulations. The incorporation of lithium into the lattice was conclusively demonstrated by secondary-ion mass spectroscopy, and the formation of stoichiometry and impurity gradients and associated embrittlement and optical scatter were explained. For the first time, the variation of lattice parameter at grain boundaries due to LiF-induced stoichiometry gradients was characterized using convergent-beam electron diffraction. Moreover, a new characterization tool; secondary-ion mass spectroscopy combined with transmission electron microscopy (PIES) was validated.

LiF reacted with spinel, increasing surface energy and/or transport, and forming volatile species that contributed to vapor-phase transport and coarsening. LiF also reacted to form volatile MgF_2 and MgO, which evaporated preferentially and shifted stoichiometry to Al_2O_3-rich, especially at interfaces. For MgO-rich compositions, increased MgO formation resulted in precipitation of MgO nodules, which restricted grain growth and caused optical scatter. While lithium incorporated into the lattice, fluorine reacted with impurities to form volatile fluorides, which could be removed by evaporation with careful processing. The net effect of LiF was to enhance densification, reduce its onset temperature, and result in coarsening, which with added pressure resulted in fully-dense compacts. Reduced impurity content combined with enhanced densification due to increased surface and grain-boundary transport during pressure-assisted sintering resulted in transparency. However, stoichiometry and point-defect gradients embrittled grain boundaries, caused optical scatter, and reduced electronic conductivity. Moreover, when present in higher concentration, LiF and its by-products were the main sources of optical scatter.

For the first time, the dielectric properties of fully-dense transparent polycrystalline compacts and their grain boundaries were quantified. Higher conductivity compared to single crystals was attributed to conductance along impurity-rich, magnesium-depleted grain boundaries. LiF was found to decrease conductivity by reducing grain-boundary area due to coarsening, reducing total impurity content, and by forming conductivity-reducing defects by replacing magnesium in the lattice.

The work highlighted the importance and complexity of interfaces. From a practical standpoint, the key variables (particle-size characteristics, stoichiometry, and impurities and additives) involved in the processing of transparent spinel were identified and guidance given as how to improve transmittance. The work demonstrated that fabrication of highly-transparent spinel, and likely transparent ceramics in general, requires a holistic approach that considers all variables and their interactions over length scales ranging from the atomic- to the compact-scale and occurring throughout the entirety of processing, but especially during sintering. However, although many of the questions asked at the outset were answered, the specific cause of grain-boundary embrittlement, grain-boundary optical scatter, and the specific point-defects caused by lithium incorporation were not conclusively determined.

Although significant advances have been made in the understanding and technological development of transparent polycrystalline spinel in the last fifty years, work still remains. Stoichiometry is a potentially powerful tool to modify densification, microstructure, and nearly all bulk properties. Yet there remains a lack of understanding of stoichiometry and of ability to manipulate it, especially stoichiometry gradients. Moreover, the ion diffusivities of astoichiometric compositions at grain boundaries, the effect of grain-boundary and surface stoichiometry gradients on properties, the role of point defects and grain-boundary space-charge, and the transference numbers as a function of stoichiometry are either not fully-understood or not known. Much progress also remains with respect to manufacturing, especially up-scaling fine grain-size technologies, strengthening grain boundaries, and lowering costs. However, the outlook for transparent spinel, and for transparent ceramics in general, remains bright. This is in part due to the unique properties that allow applications no other materials can fulfill, and in part due to the accumulation of sufficient scientific and technical know-how to produce high-quality components.

REFERENCES

1. M. Rubat du Merac, I. E. Reimanis, C. Smith, H.-J. Kleebe, M. M. Müller, 'Effect of Impurities and LiF Additive in Hot-Pressed Transparent Magnesium Aluminate Spinel', *Int. J. App. Ceram. Tech.*, **10** [1] 33-48 (2013).

2. M. Rubat du Merac, H.-J. Kleebe, M. M. Müller, I. E. Reimanis, '50 Years of Research and Development Coming to Fruition; Unraveling the Complex Interactions during Processing of Transparent Magnesium Aluminate ($MgAl_2O_4$) Spinel', *J. Am. Ceram. Soc.*, **96** [11] 3341-3365 (2013).

3. M. Rubat du Merac, I. E. Reimanis, and H.-J. Kleebe, 'Electrochemical Impedance Spectroscopy of Transparent Polycrystalline Magnesium Aluminate ($MgAl_2O_4$) Spinel', *J. Am. Ceram. Soc.*, **98** [7] 2130-2138 (2015).

4. D. C. Harris, 'History of Development of Polycrystalline Optical Spinel in the U.S.', Window and Dome Technologies and Materials IX, *Proc. SPIE*, **5786** [1] 1-22 (2005).

5. D. D. Silva, A. R. Boccaccini, 'Industrial Developments in the Field of Optically Transparent Inorganic Materials: A Survey of Recent Patents', Recent Patents in Materials Science 2008, [1] 56-73 (2008).

6. M. Suárez, A. Fernández, R. Torrecillas, J. L. Menéndez, 'Sintering to Transparency of Polycrystalline Ceramic Materials', *Sintering of Ceramics - New Emerging Techniques*, Ed. A. Lakshmanan, InTech 527-552 (2012).

7. J. A. Salem, 'Transparent Armor Ceramics as Spacecraft Windows', *J. Am. Ceram. Soc.*, **96** [1] 1-9 (2013).

8. A. Goldstein, 'Correlation between $MgAl_2O_4$-Spinel Structure, Processing Factors and Functional Properties of Transparent Parts (Progress Review)', *J. Eur. Ceram. Soc.*, **32** 2869-2886 (2012).

9. R.-J. Xie, H. T. Hintzen, 'Optical Properties of (Oxy)Nitride Materials: A Review', *J. Am. Ceram. Soc.*, **96** [3] 665-687 (2013).

10. M. Ramisetty, S. Sastri, U. Kashalikar, L. M. Goldman, N. Nag, 'Transparent Polycrystalline Cubic Spinels Protect and Defend', *Am. Ceram. Soc. Bull.*, **92** [2] 20-25 (2013).

11. S. F. Wang, J. Zhang, D. W. Luo, F. Gu, D. Y. Tang, Z. L. Dong, G. E. B. Tan, W. X. Que, T. S. Zhang, S. Li, L. B. Kong, 'Transparent Ceramics: Processing, Materials and Applications', *Prog. Solid State Chem.*, 1-35 (2013).

12. M. C. L. Patterson, J. E. Caiazza, D. W. Roy, 'Transparent Spinel Development', *Inorganic Optical Materials II, Proc. SPIE,* **4102** 59-68 (2000).

13. A. A. DiGiovanni, L. Fehrenbacher, D. W. Roy, 'Hard Transparent Domes and Windows From Magnesium Aluminate Spinel', *Window and Dome Technologies and Materials IX, Proc. SPIE,* **5786** 56-63 (2005).

14. *U.S. Army ManTech Manufacturing Technology 2012 Brochure*, U.S. Army, www.armymantech.com (2012).

15. Technology Assessment and Transfer Inc., *www.techassess.com (*2013).

16. MER Corp., *www.mercorp.com (*2013).

17. Armorline Corp., *www.armorline.com. (*2013).

18. M. Rubat du Merac, 'Sintering Theory, Practice & Applications, Case Study: Transparent $MgAl_2O_4$', 353-395, (Netzsch) *Ceramic & Nuclear Focused Workshop*, Albuquerque, NM, May 8-9 (2012).

19. I. Ganesh, 'A Review on Magnesium Aluminate ($MgAl_2O_4$) Spinel: Synthesis, Processing, and Applications', *Int. Mater. Rev.*, **58** [2] 63-112 (2013).

20. J. F. W. Bowles, R. A. Howie, D. J. Vaughan, J. Zussman, *Rock-Forming Minerals, Non-Silicates Oxides, Hydroxides, and Sulphides, Second Edition,* The Geological Society, Bath, UK, **5A** 363 (2011).

21. S. Klemme, "The Influence of Cr on the Garnet-Spinel Transition in the Earth's Mantle: Experiments in the System $MgO\text{-}Cr_2O_3\text{-}SiO_2$ and Thermodynamic Modelling"*, Lithos*, **77** 639-646 (2004).

22. K. E. Sickafus, J. M. Wills, N. W. Grimes, 'Structure of Spinel', *J. Am. Ceram. Soc.*, **82** [12] 3279-3292 (1999).

23. D. C. Harris, *Materials for Infrared Windows and Domes, Properties and Performance*, SPIE Optical Engineering Press, NY, (1999).

24. A. Krell, J. Klimke, T. Hutzler, 'Transparent Compact Ceramics: Inherent Physical Issues', *Opt. Mater.*, **31** 1144-1150 (2009).

25. A. Krell, T. Hutzler, J. Klimke, 'Transmission Physics and Consequences for Materials Selection, Manufacturing, and Applications', *J. Eur. Ceram. Soc.*, **29** 207-221 (2009).

26. G. Bernard-Granger, C. Guizard, L. San Miguel, 'Sintering Behavior and Optical Properties of Yttria', *J. Am. Ceram. Soc.*, **90** [9] (2007).

27. R. Johnson, P. Biswas, P. Ramavath, R. S. Kumar, G. Padmanabham, 'Transparent Polycrystalline Ceramics: An Overview', *Trans. Ind. Ceram. Soc.*, **71** [2] (2012).

28. J. M. Dodson, J. R. Brandon, H. K. Dhilon, I. Friel, S. L. Goeghegan, T. P. Mollart, P. Santini, G. A. Scarsbrook, D. J. Twitchen, A. J. Whitehead, J. J. Wilman, H. de Wit, 'Single Crystal and Polycrystalline CVD Diamond for Demanding Optical Applications', *Proc. SPIE* **8016** (2011).

29. D. C. Harris, 'Review of Navy Program to Develop Optical Quality Diamond Windows and Domes' (Report), *Naval Air Systems Command*, China Lake, CA (2002).

30. P. Hogan, T. Stefank, C. Willingham, R. Gentilman, 'Transparent Yttria for IR Windows and Domes - Past and Present. Andover' (Report), *Raytheon Integrated Defense Systems*, Andover, MA (2004).

31. M. C. L. Patterson, A. A. DiGiovanni, L. Fehrenbacher, D. W. Roy, 'Spinel: Gaining Momentum in Optical Applications', *Window and Dome Technologies VIII, Proc. SPIE*, **5078** 71-79 (2003).

32. G. R. Parsons, F. C. Mooney, United States Statutory Invention Registration, Appl. No. 667,624, Reg. No. H1567 (1967).

33. D.W. Roy, J.L. Hastert, United States Patent No. 4,930,731 (1990).

34. T. J. Mroz, T. M. Hartnett, J. M. Wahl, L. M. Goldman, J. Kirsch, W. R. Lindbert, 'Recent Advances in Spinel Optical Ceramic', *Window and Dome Technologoes and Materials IX, Proc. SPIE*, **5786** (2005).

35. J. H. Burnett, 'High-index Materials for 193-mm Immersion Lithography', *2nd International Conference on Immersion Lithography*, Burgess, Belgium, 15 September (2005).

36. I. E. Reimanis, H.-J. Kleebe, 'A Review on the Sintering and Microstructure Development of Transparent Spinel ($MgAl_2O_4$)', *J. Am. Ceram. Soc.*, **92** [7] 1472-1480 (2009).

37. J. S. Sanghera, G. Villalobos, W. Kim, S. Bayya, I. D. Aggarwal, ‚Transparent Spinel Ceramic', *NRL Review 2009*, 215-217 (2009).

38. J. Zhang, T. Lu, X. Chang, N. Wei, W. Xu, 'Related Mechanism of Transparency in $MgAl_2O_4$ Nano-Ceramics Prepared by Sintering Under High Pressure and Low Temperature', *J. Phys. D: Appl. Phys.*, **42** 1-5 (2009).

39. J. Sanghera, S. Bayya, G. Villalobos, W. Kim, J. Frantz, B. Shaw, B. Sadowski, R. Miklos, C. Baker, M. Hunt, I. Aggarwal, F. Kung, D. Reicher, S. Peplinski, A. Ogloza, P. Langston, C. Lamar, P. Varmette, M. Dubinskiy, L. DeSandre, 'Transparent Ceramics for High-Energy Laser Systems', *Opt. Mater.* (2010).

40. C. F. Chen, F. P. Doty, R. J. T. Houk, R. O. Loutfy, H. M. Volz, P. Yang, 'Characterizations of a Hot-Pressed Polycrystalline Spinel:Ce Scintillator', *J. Am. Ceram. Soc.*, **93** [8] 2399-2402 (2010).

41. K. Nassau, *Gems Made by Man,* Chilton Book Co., Radnor, PA, 247 (1980).

42. C. A. Schacht, *Refractories Handbook,* Marcel Dekker Inc., NY (2004).

43. A. Gatti, 'Development of a Process for Producing Transparent Spinel Bodies', *Report*, General Electric Company, Space Division, Contract to Naval Air Systems Command, Washington, D.C. (1969).

44. G. Gilde, P. Patel, M. Patterson, 'A Comparison of Hot-Pressing, Rate-Controlled Sintering, and Microwave Sintering of Magnesium Aluminate Spinel for Optical Applications', *Window and Dome Technologies and Materials VI, Proc. SPIE*, **3705** 94-104 (1999).

45. A. Krell, T. Hutzler, J. Klimke, A. Potthoff, 'Fine-Grained Transparent Spinel Windows by the Processing of Different Nanopowders', *J. Am. Ceram. Soc.*, **93** [9] 2656-2666 (2010).

46. R. J. Bratton, 'Translucent Sintered $MgAl_2O_4$', *J. Am. Ceram. Soc.*, **57** [7] 283-286 (1974).

47. P. Hing, 'Fabrication of Translucent Magnesium Aluminate Spinel and its Compatibility in Sodium Vapour', *J. Mater. Sci.*, **11** 1919-1926 (1976).

48. J.-G. Li, T. Ikegami, J.-H. Lee, T. Mori, 'Fabrication of Translucent Magnesium Aluminum Spinel Ceramics', *J. Am. Ceram. Soc.*, **83** [11] 2866-2868 (2000).

49. R. Cook, M. Kochis, I. E. Reimanis, H.-J. Kleebe, ‘A New Powder Production Route for Transparent Spinel Windows: Powder Synthesis and Window Properties’, *Window and Dome Technologoes and Materials IX, Proc. SPIE,* **5786** 41-47 (2005).

50. K. Rozenburg, I. E. Reimanis, ‘Sintering Kinetics of a $MgAl_2O_4$ Spinel Doped with LiF’, *J. Am. Ceram. Soc.*, **92** [2] 444-450 (2008).

51. A. F. Dericioglu, Y. Kagawa, ‘Effect of the Grain Boundary Microcracking on the Light Transmittance of Sintered Transparent $MgAl_2O_4$’, *J. Eur. Ceram. Soc.*, **23** 951-959 (2003).

52. A. F. Dericioglu, A. R. Boccaccini, I. Dlouhy, Y. Kagawa, ‘Effect of Chemical Composition on the Optical Properties and Fracture Toughness of Transparent Magnesium Aluminate Spinel Ceramics’ 5, 2005, *Mater. Trans.*, **46** [5] 996-1003 (2005).

53. G. Gilde, P. Patel, J. Sands, P. Patterson, D. Blodgett, D. Duncan, D. Hahn, ‘Evaluation of Hot Isostatic Pressing Parameters on the Optical and Ballistic Properties of Spinel for Transparent Armor’, *J. Am. Ceram. Soc.*, **88** [10] 2747-2751 (2006).

54. M.-Y. Lei, C.-X. Huang, J.-L. Sun, ‘Effect of HIP on the Properties and Microstructure of Transparent Polycrystalline Spinel’, *Key Eng. Mat.*, **336-338** 1200-1202 (2007).

55. A. C. Sutorik, G. Gilde, J. J. Swab, C. Cooper, R. Gamble, E. Shanholtz, ‘The Production of Transparent $MgAl_2O_4$ Ceramic Using Calcined Powder Mixtures of $Mg(OH)_2$ and y-Al_2O_3 or AlOOH’, *Int. J. App. Ceram. Tech.*, **9** [3] 575-587 (2011).

56. MER Corp., ‘High Strength, Transparent, Edge Bonded IR Spinel Windows’, *NAVAIR Public Release* 11-119, MER Corp. (2011).

57. L. Esposito, A. Piancastelli, S. Martelli, ‘Production and Characterization of Transparent $MgAl_2O_4$ Perpared by Hot Pressing’, *J. Eur. Ceram. Soc.*, **33** 737-747 (2013).

58. M. Shimada, T. Endo, T. Saito, T. Sato, ‘Fabrication of Transparent Spinel Polycrystalline Materials’, *Mater. Lett.*, **28** 413-415 (1996).

59. K. Tsukuma, ‘Transparent $MgAl_2O_4$ Spinel Ceramics Produced by HIP Post-Sintering’, *J. Ceram. Soc. Jpn.*,**114** [10] 802-806, (2006).

60. A. Krell, J. Klimke, T. Hutzler, ‘Advanced Spinel and sub-um Al_2O_3 for Transparent Armor Applications’, *J. Eur. Ceram. Soc.*, **29** 275-281 (2009).

61. A. C. Sutorik, G. Gilde, C. Cooper, J. Wright, C. Hilton, “The Effect of Varied Amounts of LiF Sintering Aid on the Transparency of Alumina Rich Spinel Ceramic with the Composition MgO-1.5 Al_2O_3’, *J. Am. Ceram. Soc.*, **95** [6] 1807-1810 (2012).

62. B.-N. Kim, K. Morita, J.-H. Lim, K. Hiraga, H. Yoshida, ‘Effects of Preheating of Powder before Spark Plasma Sintering of Transparent $MgAl_2O_4$ Spinel’, *J. Am. Ceram. Soc.*, **93** [8] 2158-2160 (2010).

63. N. Frage, S. Cohen, S. Meir, S. Kalabukhov, M. P. Dariel, ‘Spark Plasma Sintering (SPS) of Transparent Magnesium-Aluminate Spinel’, *J. Mater. Sci.*, **42**, 3273-3275 (2007).

64. K. Morita, B.-N. Kim, K. Hiraga, H. Yoshida, ‘Fabrication of Transparent $MgAl_2O_4$ Spinel Polycrystal by Spark Plasma Sintering Process’, *Scripta Mater.*, **58** 1114-1117 (2008).

65. S. Meir, S. Kalabukhov, N. Froumin, M. P. Dariel, N. Frage, ‘Synthesis and Densification of Transparent Magnesium Aluminate Spinel by SPS Processing’, *J. Am. Ceram. Soc.*, **2** 358-364 (2009).

66. C. Wang, Z. Zhao, ‘Transparent $MgAl_2O_4$ Ceramic Produced by Spark Plasma Sintering’, *Scripta Mater.*, **61** 193-196 (2009).

67. G. Bonnefont, G. Fantozzi, S. Trombert, L. Bonneau, ‘Fine-Grained Transparent $MgAl_2O_4$ Spinel Obtained by Spark Plasma Sintering of Commercially Available Nanopowders’, *Ceram. Int.*, **38** 131-141 (2012).

68. E. A. Maguire, R. L. Gentilman. United States Patent 4,347,210 (1982).

69. G. Liu, J. Li, Z. Yang, ‘Melt-Casting of Translucent $MgAl_2O_4$ Ceramics by Combustion Synthesis Under High Gravity’, *Mater. Manuf. Process.*, **27** [6] 689-693 (2012).

70. A. Goldstein, L. Giefman, S. Bar Ziv, ‘Susceptor Assisted Microwave Sintering of $MgAl_2O_4$ Powder at 2.45 GHz’, *J. Mater. Sci. Lett.*, **17** 977-979 (1998).

71. H. Palmour III, W. W. Kriegel, R. D. McBrayer, ‘Research on Growth and Deformation Mechanisms in Single Crystal Spinel’, North Carolina State College, *Report No. ASD-TDR-62-1086*, Contract No. AF33(616)-7820 (1963).

72. B. Hallstedt, ‘Thermodynamic Assessment of the System MgO-Al_2O_3’, *J. Am. Ceram. Soc.*, **75** [6] 1497-1507 (1992).

73. I.-H. Jung, S. A. Decterov, A. D. Pelton, 'Critical Thermodynamic Evaluation and Optimization of the MgO-Al_2O_3, CaO-MgO-Al_2O_3, and MgO-Al_2O_3-SiO_2 Systems', *J. Phase Equilib. Diff.*, **25** [4] 329-345 (2004).

74. C. Wagner, 'The Mechanism of Formation of Ionic Compounds of Higher Order', *Z. Phys. Chem.*, **B34** 309-316 (1936).

75. A. D. Mazzoni, M. A. Sainz, A. Caballero, E. F. Aglietti, 'Formation and Sintering of Spinels ($MgAl_2O_4$) in Reducing Atmospheres', *Mater. Chem. Phys.*, **78** 30-37 (2002).

76. Y. M. Chiang, W. D. Kingery, 'Grain-Boundary Migration in Nonstoichiometric Solid Solutions of Magnesium Aluminate Spinel: I, Grain Growth Studies', *J. Am. Ceram. Soc.*, **72** [2] 271-277 (1989).

77. A. C. Sutorik, G. Glide, J. J. Swab, C. Cooper, R. Gamble, 'Transparent Solid Solution Magnesium Aluminate Spinel Polycrystalline Ceramic with the Alumina-Rich Composition MgO-1.2 Al_2O_3', *J. Am. Ceram. Soc.*, **95** [2] 636-643 (2012).

78. T. Sasamoto, H. Hara, T. Saya, 'Mass-Spectroscopic Study of the Vaporization of Magnesium Oxide from Magnesium Aluminate Spinel', *Bull. Chem. Soc. Jpn.*, **64** 3327-3333 (1981).

79. M. A. Sainz, A. D. Mazzoni, E .F. Aglietti, A. Caballero, 'Thermochemical Stability of Spinel (MgO-Al_2O_3) Under Strong Reducing Conditions', *Mater. Chem. Phys.*, **86** 399-408 (2004).

80. M. Matsui, T. Takahashi, I. Oda, 'Influence of MgO Vaporization on the Final-Stage Sintering of MgO-Al_2O_3 Spinel', pp. 562-73 in *Advances in Ceramics, Structure and Properties of MgO and Al_2O_3 Ceramics*, Edited by W. D. Kingery, American Ceramic Society, Columbus, OH (1984).

81. C.-J. Ting, H.-Y. Lu, 'Deterioration in the Final-Stage Sintering of Magnesium Aluminate Spinel', *J. Am. Ceram. Soc.*, **83** [7] 1592-1598 (2000).

82. V. L. K. Lou, T. E. Mitchell, A. H. Heuer, 'Review - Graphical Displays of the Thermodynamics of High-Temperature Gas-Solid Reactions and Their Application to Oxidation of Metals and Evaporation of Oxides', *J. Am. Ceram. Soc.*, **68** [2] 49-58 (1985).

83. A. D. Mazzoni, M. A. Sainz, E. F. Aglietti, A. Caballero, 'Carbon Coating and Reaction on Magnesia-Alumina Spinel', *Mater. Chem. Phys.*, **101** 211-216 (2007).

84. S. Meir, S. Kalabukhov, N. Frage, M. P. Dariel, ‘Fabrication of Transparent Magnesium Aluminate Spinel’ (Presentation), *32nd International Conference on Advanced Ceramics and Composites*, Daytona Beach, FL (2008).

85. E. J. W. Verwey, E. L. Heilmann, ‘Physical Properties and Cation Arrangement of Oxides with Spinel Structures’, *J. Chem. Phys.*, **15** 174-180 (1947).

86. Y. M. Chiang, W. D. Kingery, ‘Grain-Boundary Migration in Nonstoichiometric Solid Solutions of Magnesium Aluminate Spinel: II, Effect os Grain-Boundary Nonstiochiometry’, *J. Am. Ceram. Soc.*, **73** [5] 1153-58 (1990).

87. C.-J. Ting, H.-Y. Lu, ‘Hot-Pressing of Magnesium Aluminate Spinel - I. Kinetics and Densification Mechanism’, *Acta. Mater.*, **47** [3] 817-830 (1999).

88. C.-J. Ting, H.-Y. Lu, ‘Hot-Pressing of Magnesium Aluminate Spinel - II. Microstructure Development’, *Acta Mater.*, **47** [3] 831-840 (1999).

89. N. Nuns, F. Beclin, J. Crampon, ‘Grain-Boundary Characterization in a Nonstoichiometric Fine-Grained Magnesium Aluminate Spinel: Effects of Defect Segregation at the Space-Charge Layers’, *J. Am. Ceram. Soc.*, **92** [4] 870-875 (2009).

90. Y. Okuyama, N. Kurita, N. Fukatsu, ‘Defect Structure of Alumina-Rich Nonstoichiometric Magnesium Aluminate Spinel’, *Solid State Ionics*, **177** 59-64 (2006).

91. V. Šepelák, S. Indris, I. Bergmann, A. Feldhoff, K. D. Becker, P. Heitjans, ‘Nonequilibrium Cation Distribution in Nanocrystalline $MgAl_2O_4$ Spinel Studied by ^{27}Al Magic-Angle Spinning NMR’, *Soild State Ionics*, **177** 2487-2490 (2006).

92. K. E. Sickafus, A. C. Larson, N. Yu, M. Nastasi, G. W. Hollenberg, F. A. Garner, R. C. Bradt, ‘Cation Disorder in High-Dose, Neutron-Irradiated Spinel’, *J. Nucl. Mater.*, **219** 123-134 (1995).

93. H. Maekawa, S. Kato, K. Kawamura, T. Yokokawa, ‘Cation Mixing in Natural $MgAl_2O_4$ Spinel: A High-Temperature ^{27}Al NMR Study’, *Am. Mineral.*, **82** 1125-1132 (1997).

94. C.-J. Ting, H.-Y. Lu, ‘Defect Reactions and the Controlling Mechanism in the Sintering of Magnesium Aluminate Spinel’, *J. Am. Ceram. Soc.*, **82** [4] 841-848 (1999).

95. G. B. Andreozzi, F. Princivalle, H. Skogby, A. Della Giusta, ‘Cation Ordering and Structural Variations with Temperature in $MgAl_2O_4$ Spinel: An X-Ray Single-Crystal Study’, *Am. Mineral.*, **85** 1164-1171 (2000).

96. B. J. Wood, R. J. Kirkpatrick, B. Montez, 'Order-Disorder Phenomena in $MgAl_2O_4$ Spinel', *Am. Mineral.*, **71** 999-1006 (1986).

97. U. Schmocker, H. R. Boesch, F. Waldner, 'A Direct Determination of Cation Disorder in $MgAl_2O_4$ Spinel by ESR', *Phys. Lett.*, **40A** [3] 237-238 (1972).

98. R. I. Sheldon, T. Hartmann, K. E. Sickafus, A. Ibarra, B. L. Scott, D. N. Argyriou, A. C. Larson, R. B. Von Dreele, 'Cation Disorder and Vacancy Distribution in Nonstoichiometric Magnesium Aluminate Spinel, $MgO\text{-}xAl_2O_3$', *J. Am. Ceram. Soc.*, **82** [12] 3293-3298 (1999).

99. V. T. Gritsnya, I. V. Afansyev-Charkin, V. A. Kobyakov, K. E. Sickafus, 'Structure and Electronic States of Defects in Spinel of Different Compositions $MgO\text{-}nAl_2O_3$:Me', *J. Am. Ceram. Soc.*, **82** [12] 3365-3373 (1999).

100. P. Barpanda, S. K. Behera, P. K. Gupta, S. K. Pratihar, S. Bhattacharya, 'Chemically Induced Order Disorder Transition in Magnesium Aluminum Spinel', *J. Eur. Ceram. Soc.*, **26** 2603-2609 (2006).

101. D. Gosset, D. Simeone, M. Dutheil, S. Bouffard, M. Beauvy, 'Structural Evolutions of Spinels under Ions Irradiations', *J. Eur. Ceram. Soc.*, **25** 2677-2681 (2005).

102. M. C. Warren, M. T. Dove, S. A. T. Redfern, 'Disordering of $MgAl_2O_4$ Spinel from First Principles', *Mineral. Mag.*, **64** [2] 311-317 (2000).

103. R. Dupree, M. H. Lewis, M. E. Smith, 'A Study of the Vacancy Distribution in Non-Stoichiometric Spinels by Magic-Angle Spinning NMR', *Philos. Mag. A*, **53** [2] L17-20 (1986).

104. R. J. Bratton, 'Initial Sintering Kinetics of $MgAl_2O_4$', *70th Annual Meeting*, The American Ceramic Society, Basic Sciences Division, Chicago, Il (1968).

105. T. A. Bazilevskaya, V. T. Gritsnya, D. V. Orlinski, L. V. Udalova, A. V. Voitsenya, 'The Effect of Composition, Processing Conditions, and Irradiation, on Lattice Defects in Spinel Ceramics', *J. Nucl. Mater.*, **253** 133-140 (1998).

106. C. A. Gilbert, R. Smith, S. D. Kenny, S. T. Murphy, R. W. Grimes, J. A. Ball, 'A Theoretical Study of Intrinsic Point Defects and Defect Clusters in Magnesium Aluminate Spinel', 2009, *J. Phys.: Condens. Matter*, **21** 275406-275412 (2009).

107. J. A. Ball, S .T. Murphy, R. W. Grimes, D. Bacorisen, R. Smith, B. P. Uberuaga, K. E. Sickafus, 'Defect Processes in $MgAl_2O_4$ Spinel', *Solid State Sci.*, **10** 717-724 (2008).

108. Z. Lodziana, J. Piechota, 'Ab initio Thermodynamic Properties of Point Defects and O-Vacancy Diffusion in Mg Spinels', *Phys. Rev. B*, **74** 1-11 (2006).

109. G. P. Summers, G. S. White, K. H. Lee, J. H. Crawford Jr., 'Radiation Damage in $MgAl_2O_4$', *Phys. Rev. B*, **21** [6] 2578-2584 (1980).

110. V. T. Gritsnya, Y. G. Kazarinov, V. A. Kobyakov, I. E. Reimanis, 'Radiation-Induced Luminescence in Magnesium Aluminate Spinel Crystals and Ceramics', *Nucl. Instrum. Meth. B*, **250** 342-348 (2006).

111. J. He, L.-B. Lin, T.-C. Lu, P. Wang, 'Effects of Electron- and/or Gamma-Irradiation upon the Optical Behavior of Transparent $MgAl_2O_4$ Ceramics: Different Color Centers Induced by Electron-Beam and γ-Ray', *Nucl. Instrum. Meth. B*, **191** 596-599 (2002).

112. V. T. Gritsnya, I. V. Afanasyev-Charkin, V. A. Kobyakov, K. E. Sickafus, 'Neutron Irradiation Effects in Magnesium-Aluminate Spinel Doped with Transition Metals', *J. Nucl. Mater.*, **283-287** 927-931 (2000).

113. M. H. Lewis, 'The Defect Structure and Mechanical Properties of Spinel Single Crystals', *Philos. Mag.*, **17** [147] 481-499 (1968).

114. E. J. Haney, G. Subhash, 'Rate Sensitive Indentation Response of a Coarse-Grained Magnesium Aluminate Spinel', *J. Am. Ceram. Soc.*, **94** [11] 3960-3966 (2011).

115. S. S. de Souza, A. G. Blak, 'Defect Simulations in $MgAl_2O_4$ Spinels', *Radiat. Eff. Defect. S.*, **146** 123-129 (1998).

116. B. P. Uberuaga, D. Bacorisen, R. Smith, J. A. Ball, R. W. Grimes, A. F. Voter, K. E. Sickafus, 'Defect Kinetics in Spinels: Long-Time Simulations of $MgAl_2O_4$, $MgGa_2O_4$, and $MgIn_2O_4$', *Phys. Rev. B*, **75** 104116;1-13 (2007).

117. G. S. White, R. V. Jones, J. H. Crawford Jr.,'Optical Spectra of $MgAl_2O_4$ Crystals Exposed to Ionizing Radiation', *J. Appl. Phys.*, **53** [1] 265-270 (1982).

118. M. L. Bortz, R. H. French, D. J. Jones, R. V. Kasowski, F. S. Ohuchi , 'Temperature Dependence of the Electronic Structure of Oxides: MgO, $MgAl_2O_4$, and Al_2O_3', *Phys. Scripta*, **41** 537-541 (1990).

119. D. M. Saylor, B. El Dasher, Y. Pang, H. M. Miller, P. Wynblatt, A. D. Rollett, G. S. Rohrer, 'Habits of Grains in Dense Polycrystalline Solids', *J. Am. Ceram. Soc.*, **87** [4] 724-726 (2004).

120. W. D. Kingery, H. K. Bowen, D. R. Uhlmann, *Introduction to Ceramics*, 2nd Edition, John Wiley & Sons, NY (1976).

121. S.-J. L. Kang, *Sintering: Densification, Grain Growth, and Microstructure*, Elsevier Butterworth-Heinamann, Burlington, MA (2005).

122. R. J. Mishra, G. Thomas, 'Surface Energy of Spinel', *J. Appl. Phys.*, **48** [11] 4576-4580 (1977).

123. M. J. Davies, S. C. Parker, G. W. Watson, 'Atomistic Simulation of the Surface Structure of Spinel', *J. Mater. Chem.*, **4** [6] 813-816 (1994).

124. R. L. Stewart, R. C. Bradt, 'Fracture of Polycrystalline $MgAl_2O_4$', *J. Am. Ceram. Soc.*, **63** [11-12] 619-623 (1980).

125. C. M. Fang, S. C. Parker, G. de With, 'Atomistic Simulation of the Surface Energy of Spinel $MgAl_2O_4$', *J. Am. Ceram. Soc.*, **83** [8] 2082-2084 (2000).

126. N. J. van der Laag, C. M. Fang, and G. de With, 'Geometry of {100} Surfaces of Spinel ($MgAl_2O_4$): First-Principles Simulations and Experimental Measurements', *J. Am. Ceram. Soc.*, **88** [6] 1544-1548 (2005).

127. M. K. Rasmussen, A. S. Foster, B. Hinnemann, F. F. Canova, S. Helveg, K. Meinander, N. M. Martin, J. Knusden, A. Vlad, E. Lundgren, A. Stierle, F. Besenbacher, and J. V. Lauristen, 'Stable Cation Inversion at the $MgAl_2O_4$ (100) Surface', *Phys. Rev. Letters*, **107** [3] 036012 3-4 (2011).

128. F. R. Massaro, M. Bruno, F. Nestola, 'Configurational and Energetical Study of the (100) and (110) Surfaces of the $MgAl_2O_4$ Spinel by means of Quantum-Mechanical and Empirical Techniques', *CrystEngComm*, **16** 9224-9235 (2014).

129. MD M. Hasan, 'Spinel Surface and Interface Thermodynamics: Effect of Dopant Segregation', *PhD Thesis*, University of California Davis (2016).

130. W. H. Bragg, *Atomic Structure of Minerals*, 3rd Ed., Springer-Verlag, Vienna (1943).

131. H. A. Miers, *Mineralogy, 2nd Ed.*, 51, Macmillan and Co. Ltd., London (1929).

132. C. C. Wang, P. J. Zanzucchi, 'Dielectric and Optical Properties of Stoichiometric Magnesium Aluminate Spinel Single Crystals', *J. Electrochem. Soc.*, **118** [4] 586-591 (1971).

133. M. K. Rasmussen, K. Meinander, F. Besenbacher, and J. V. Lauritsen, 'Noncontact Atomic Force Microscopy Study of the Spinel $MgAl_2O_4$ (111) Surface', *Bielstein J. of Nanotechnology*, **3** 192-197 (2012).

134. T. N. Jensen, M. K. Rasmussen, J. Knudsen, A. Vlad, S. Volkov, E. Lundgren. A. Stierle, and J. V. Lauritsen, 'Correlation between Stoichiometric and Surface Structure of the Polar $MgAl_2O_4$ (100) Surface as a function of Annealing Temperature', *Phys. Chem. Chem. Phys.*, **17** 5795-5804 (2015).

135. J. Teevan, 'The Effect of Titanium Dioxide Doping on the Grain Growth and Grain-Boundary Energy of Magnesium Aluminate Spinel', *MSc. Thesis*, Lehigh University (2010).

136. S. Drev, A. Reĉnik, N. Daneu, 'Twinning and Epitaxial Growth of Taaffeite-type Modulated Structures in BeO-doped $MgAl_2O_4$', *CrystalEngComm*., 15 2640-2647 (2013).

137. J. R. Martinelli, E. Sonder, R. A. Weeks, R. A. Zuhr, 'Mobility of Cations in Magnesium Aluminate Spinel', *Phys. Rev. B*, **33** 5698-5701 (1986).

138. S. T. Murphy, B. P. Uberuaga, J. B. Ball, A. R. Cleave, K. E. Sickafus, R. Smith, R. W. Grimes, 'Cation Diffusion in Magnesium Aluminate Spinel', *Solid State Ionics*, **180** 1-8 (2009).

139. N. Benameur, G. Bernard-Granger, A. Addad, S. Raffy, C. Guizard, 'Sintering Analysis of a Fine-Grained Alumina-Magnesia Spinel Powder', *J. Am. Ceram. Soc.*, **94** [5] 1388-1396 (2011).

140. T. Mathews, K. T. Jacob, J. P. Hajra, 'Electrical Transport in Magnesium Aluminate', *Bull. Mater. Sci.*, **13** [4] 293-300 (1990).

141. R. A. Weeks, E. Sonder, 'Electrical Conductivity of Pure and Fe-Doped Magnesium-Aluminum Spinel,' *J. Am. Ceram. Soc.,* **63** [1-2] 92-95 (1980).

142. J. L. Bates, J. E. Garnier, 'Electrical Conductivity of $MgAl_2O_4$ and $Y_3Al_5O_{12}$', *Communications of the American Ceramic Society,* C138-141 (1981).

143. K. Ando, Y. Oishi, 'Self-Diffusion Coefficients of Oxygen Ion in Single Crystals of MgO-nAl_2O_3 Spinels', *J. Chem. Phys.*, **61** [2] 625-629 (1974).

144. K. Ando, Y. Oishi, 'Effect of Ratio of Surface Area to Volume on Oxygen Self-Diffusion Coefficients Determined for Crushed MgO-Al_2O_3 Spinels', *Communications of the American Ceramic Society*, C131-132 (1983).

145. K. P. R. Reddy, A. R. Cooper, 'Oxygen Diffusion in Magnesium Aluminate Spinel', *J. Am. Ceram. Soc.*, **64** [6] 368-371 (1981).

146. V. S. Stubican, G. Huzinec, D. Damjanović, 'Diffusion of ^{51}Cr in Surface Layers of Magnesia, Alumina, and Spinel', *J. Am. Ceram. Soc.*, **68** [4] 181-184 (1985).

147. R. J. Bratton, 'Sintering and Grain-Growth Kinetics of $MgAl_2O_4$', *J. Am. Ceram. Soc.*, **54** [3] 141-143 (1971).

148. S.-D. Mo, W. Y. Ching, 'Electronic Structure of Normal, Inverse, and Partially Inverse Spinels in the $MgAl_2O_4$ System,' *Phys. Rev. B,* **54** [23] 551-561 (1996).

149. S. M. Hosseini, 'Structural, Electronic and Optical Properties of Spinel $MgAl_2O_4$ Oxide,' *Phys. Stat. Sol. B,* **245** [12] 2800-2807 (2008).

150. M. Hachemaoui, F. Semari, R. Khenata, A. Bouhemadou, M. Rabah, 'Structural, Elastic and Electronic Properties of XAl_2O_4 (X=Mg, Zn) Compounds,' *Journal of Scientific Research,* **0** [1] 112-116 (2010).

151. T. E. Bradburn, G. R. Rigby, 'The Electrical Conductivity of Spinels,' *Transactions of the Journal of the British Ceramic Society,* **52** [8] 417-435 (1953).

152. E. Sonder, 'Ionic Transference Numbers and Electrical Conduction in $MgAl_2O_4$ Spinel,' *J. Amer. Ceram. Soc.,* **66** [1] 50-53 (1983).

153. N. Fukatsu, 'Incorporation of Hydrogen into Magnesium Aluminate Spinel,' *Solid State Ionics,* **152-153** 809-817 (2002).

154. M. Lee, 'Ionic Conductivity Measurement in $MgAl_2O_4$ Spinel and Solid State Galvanic Cell with $MgAl_2O_4$ Electrolyte,' *PhD Thesis,* University of Colorado at Boulder, Boulder, CO (2007).

155. R. Lindner, 'Diffusion von Ni^{63} in Nickelspinellen,' *Zeitschrift fur Physicalische Chemie,* **18** 303-307 (1958).

156. W. P. Whitney, 'Self-Diffusion Coefficients of Al^{3+} in $MgAl_2O_4$,' *American Ceramic Society*

Bulletin, 388 (1970).

157. S. Saha, B. Das, N. Mazumder, A. Bharati, K. Kumar Chattopadhyay, 'Effect of Cr Doping on the AC Electrical Properties of $MgAl_2O_4$ Nanoparticles,' *J. Sol-Gel Sci. Technol.,* **61** 518-526 (2012).

158. H. Roegner, 'Direct Current Resistance of Ceramic Materials,' *Z. Elektrochem.,* **46** 25-27 (1940).

159. D. M. Shakhtin, T. L. Pivovar, 'Measuring the Electrical Resistance of Oxide Ceramics at High Temperatures,' *Ogneupory,* **12** [8] 59-62 (1971).

160. Y. Oishi, K. Ando, 'Self-Diffusion Coefficients of Oxygen Ion in Single Crystals of MgO-$n$$Al_2O_3$ Spinels,' *J. Chem. Phys.,* **61** [2] 625-629 (1974).

161. Y. M. Chiang, W. D. Kingery, 'Grain-Boundary Migration in Nonstoichiometric Solid Solutions of Magnesium Aluminate Spinel: I, Grain Growth Studies', *J. Am. Ceram. Soc.*, **72** [2] 271-277 (1989).

162. N. Nuns, F. Béclin, J. Crampon, 'Space Charge Characterisation by EDS Microanalysis in Spinel $MgAl_2O_4$', *J. Eur. Ceram. Soc.*, **25** 2809-2811 (2005).

163. A. Laobuthee, S. Wongkasemjit, E. Traversa, R. M. Laine, '$MgAl_2O_4$ Spinel Powders from Oxide One Pot Synthesis (OOPS) Process for Ceramic Humidity Sensors,' *J. Eur. Ceram. Soc.,* **20** 91-97 (2000).

164. Y. Shimizu, H. Arai, T. Seiyama, 'Theoretical Studies on the Impedance-Humidity Characteristics of Ceramic Humidity Sensors,' *Sensors and Actuators,* **7** 11-22 (1985).

165. Spinel - Material Specifications, Technical Data Sheet, Technology Assessment & Transfer, Annapolis, MD, www.techassess.com (2013).

166. S. Kochawattana, A. Stevenson, S.-H. Lee, M. Ramirez, V. Gopalan, J. Dumm, V. K. Castillo, G. J. Quarles, G. L. Messing, 'Sintering and Grain Growth in SiO_2 Doped Nd:YAG. 2008', *J. Eur. Ceram. Soc.*, **28** 1527-1534 (2008).

167. R. Apetz, M. P. B. van Bruggen, 'Transparent Alumina: A Light-Scattering Model', *J. Am. Ceram. Soc.*, **86** [3] 480-486 (2003).

168. H. C. Van de Hulst, *Light Scattering by Small Particles*, Dover Publ. Inc., NY (1957).

169. A. Krell, T. Hutzler, J. Klimke, A. Potthoff, 'Nano-Processing for Larger Fine-Grained

Windows of Transparent Spinel', in *Advances in Ceramic Armor VI: Engineering and Science Proceedings*, **31** 167-182 (2010).

170. A. Krell, K. Waetzig, J. Klimke, 'Influence of the Structure of MgO-nAl$_2$O$_3$ Spinel Lattices on Transparent Ceramics Processing and Properties', *J. Eur. Ceram. Soc.*, **32** 2887-2898 (2012).

171. R. L. Stewart, R. C. Bradt, 'Fracture of Polycrystalline MgAl$_2$O$_4$', *J. Am. Ceram. Soc.*, **63** [11-12] 619-623 (1980).

172. A. Ghosh, K. W. White, M. G. Jenkins, A.S. Kobayashi, R. C. Bradt, 'Fracture Resistance of a Transparent Magnesium Aluminate Spinel', *J. Am. Ceram. Soc.*, **74** [7] 1624-1630 (1991).

173. O. Tokariev, L. Schnetter, T. Beck, J. Malzbender, 'Grain Size Effect on the Mechanical Properties of Transparent Spinel Ceramics', *J. Eur. Ceram. Soc.*, 1-9 (2012).

174. T. Mroz, L. M. Goldman, A. D. Gledhill, D. Li, N. P. Padture, 'Nanostructured, Infrared-Transparent Magnesium-Aluminate Spinel with Superior Mechanical Properties', *Int. J. Appl. Ceram. Technol.*, **9** [1] 83-90 (2012).

175. A. Goldstein, A. Goldenberg, M. Hefetz, 'Transparent Polycrystalline MgAl$_2$O$_4$ Spinel with Submicron Grains, by Low Temperature Sintering', *J. Ceram. Soc. Jpn*., **117** [11] 1281-1283 (2009).

176. K. Morita, B.-N. Kim, H. Yoshida, K. Hiraga, 'Spark-Plasma-Sintering Condition Optimization for Producing Transparent MgAl$_2$O$_4$ Spinel Polycrystal', *J. Am. Ceram. Soc.*, **92** [6] 1208-1216 (2009).

177. A. Krell, A. Bales, 'Grain Size-Dependent Hardness of Transparent Magnesium Aluminate Spinel', *Int. J. Appl. Ceram. Technol.*, **8** [5] 1108-1114 (2011).

178. A. Rothman, S. Kalabukhov, N. Sverdlov, M. P. Dariel, N. Frage, 'The Effect of Grain Size on the Mechancial and Optical Properties of Spark Plasma Sintering-Processed Magnesium Aluminate Spinel MgAl$_2$O$_4$', *Int. J. Appl. Ceram. Technol.*, 1-8 (2012).

179. A. Muller, D. J. Green, 'Comparison of the Elastic-Plastic Indentation Response of MgAl$_2$O$_4$, AlON, and AlN', *J. Am. Ceram. Soc.*, **96** 4 1263-1270 (2013).

180. J. W. McCauley, E. Strassburger, P. Patel, B. Paliwal, K. T. Ramesh, 'Experimental Observations on Dynamic Response of Selected Transparent Armor Materials', *Exp. Mech*., **53** 3-29 (2013).

181. D. C. Harris, ‘Multi-Spectral Transparent Materials Technologies’, American Ceramic Society (*Presentation*), Baltimore, MD (2010).

182. Spinel Technical Data Sheet, Surmet Corp., www.surmet.com (2013).

183. R. Gentilman, E. Maguire, J. Pappis, ‘High Durability Missile Domes’, *Interim Technical Report*, Contract N00014-76-C-0635, Raytheon Company (1977).

184. A. V. Belyakov, A. N. Sukhozhak, ‘Production of Transparent Ceramics (Review)’, *Science for Ceramics Manufacture*, **52** [1-2] 14-19 (1995).

185. A. Wajler, H. Tomaszewski, H. Weglarz, R. Diduszko, ‘Influence of Processing on Magnesium Aluminate Precursors Morphology Prepared by Co-Precipitation’, *Ceramic Matrials*, **63** [1] 104-108 (2011).

186. R. A. German, *Sintering Theory and Practice*, John Wiley & Sons Inc., New York (1996).

187. B. Tu, H. Wang, X. Liu, W. Wang, and Z. Fu, ‘Theoretical Predictions of Composition-Dependent Structure and Properties of Alumina-Rich Spinel’, *J. Eur. Ceram. Soc.*, **36** [4] 1073-1079 (2016).

188. C. Baudin, P. Pena, ‘Influence of Stoichiometry on Fracture Behavior of Magnesium Aluminate Spinels at 1200°C’, *J. Eur. Ceram. Soc.*, **17** 1501-1511 (1997).

189. C. Zografou, P. Reynen, D. V. Mallinckrodt, ‘Nonstoichiometry and the Sintering of Magnesium Oxide and Magnesium Aluminate ($MgAl_2O_4$)’, *Interceram*, **32** [5] 40-43 (1983).

190. S. Kanzaki, Z. Nakagawa, K. Hamano, K. Saito, ‘Effect of Nonstoichiometry on Microstructure and Mechanical Strength of Mg-Al Spinel Ceramics’, *Yogyo Kyokaishi*, **87** [5] 230-237 (1979).

191. R. Duclos, N. Doukham, B. Escaig, ‘Study of the Origin of the Composition Influence on the Mechanical Properties of $MgO\text{-}nAl_2O_3$ Spinels’, *Acta Mater.*, **30** [7] 1381-1388 (1982).

192. C. Huang, T. Lu, L. Lin, M. Lei, C. Huang, ‘A Study on Toughening and Strengthening of Mg-Al Spinel Transparent Ceramics’, *Key Eng. Mat.*, **336-338** 1207-1210 (2007).

193. R. Ahuja, J. M. Osorio-Guillen, J. Souza de Almeida, B. Holm, W. Y. Ching, B. Johansson, 'Electronic and Optical Properties of γ-Al_2O_3 from ab initio Theory', *Journal of Condensed Physics: Condensed Matter*, **16** 2891-2900 (2004).

194. F. Nestola, L. Secco, M. Bruno, M. Prencipe, F. Matrignago, F. Princivalle, A. Dal Negro, 'The Effect of Non-Stoichiometry on the High-Temperature Behavior of $MgAl_2O_4$ Spinel', *Mineralogical Magazine*, **73** [2] 181-186 (2009).

195. W. T. Baker, J. G. Lindsay, 'Reactive Magnesia Spinel, Preparation and Properties', *Am. Ceram. Soc. Bull.*, **46** [11] 1094-1097 (1967).

196. R. D. Bagley, 'Optical Properties of Sintered Magnesium Aluminate Spinel', *Am. Ceram. Soc. Bull.*, **55** 882 (1976).

197. K. Uematsu, R. M. Cannon, R. D. Bagley, M. F. Yan, U. Chowdry, H. K. Bowen, 'Microstructure Evolution Controlled by Dopants and Pores at Grain Boundaries', 190-205, *Proceedings of an International Symposium on Factors in Densification and Sintering of Oxide and Non-Oxide Ceramics*, Tokyo Institute of Technology, Tokyo, Japan (1979).

198. M. F. Yan, R. M. Cannon, H. K. Bowen, 'Grain Boundary Migration in Ceramics', *Ceramic Microstructures*, 276-307, Westview Press, Boulder, CO (1977).

199. J. T. Bailey, J. R. Russel, 'Sintering Spinel Ceramics', *Am. Ceram. Soc. Bull.*, **47** [11] 1025-29 (1968).

200. G. Gottstein, A. H. King, L. S. Shvindlerman, 'The Effect of Triple-Junction Drag on Grain Growth', *Acta Mater.*, **48** 397-403 (2000).

201. G. Gottstein, L. S. Shvindlerman, 'A Novel Concept to Determine the Mobility of Grain Boundary Quadruple Junctions', *Scripta Mater.*, **52** 863-866 (2005).

202. G. Bernard-Granger, N. Benameur, C. Guizard, M. Nygren, 'Influence of Graphite Contamination on the Optcial Properties of Transparent Spinel Obtained by Spark Plasma Sintering', *Scripta Mater.*, **60** 164-167 (2009).

203. S. J. Bennison, M. P. Harmer, 'Swelling of Hot-Pressed Al_2O_3', *J. Am. Ceram. Soc.*, **68** [11] 591-97 (1985).

204. W. C. Johnson, D. F. Stein, R. W. Rice, 'Analysis of Grain-Boundary Impurities and Fluoride Additives in Hot-Pressed Oxides by Auger Electron Spectroscopy', *J. Am. Ceram. Soc.*, **57** [8] 342-344 (1974).

205. A. D. Gledhill, D. Li, T. Mroz, L. M. Goldman, N. P. Padture, 'Strengthening of Transparent Spinel/Si_3N_4 Nanocomposites', *Acta Matrialia*, **60** 1570-1575 (2012).

206. I. Ganesh, K. A. Teja, N. Thiyagarajan, R. Johnson, B. M. Reddy, 'Formation and Densification Behavior of Magnesium Aluminate Spinel: The Influence of CaO and Moisture in the Precursors', *J. Am. Ceram. Soc.*, **88** [10] 2752-2761 (2005).

207. G. R. Villalobos, J. S. Sanghera, I. D. Aggarwal, R. Miklos, 'Analysis of Scattering Sites in Transparent Magnesium Aluminate Spinel', Advances in Ceramic Armor: A Collection of Papers Presented at the 29th International Conference on Advanced Ceramics and Composites, Cocoa Beach, Florida, January 23-28, *Ceramic Engineering and Science Proceedings*, **26** [7], John Wiley & Sons, Inc., Hoboken, NJ (2005).

208. J.-L. Huang, S.-Y. Sun, Y.-C. Ko, 'Investigation of High-Alumina Spinel: Effect of LiF and $CaCO_3$ Addition', *J. Am. Ceram. Soc.*, **80** [12] 3237-3241 (1997).

209. J.-L. Huang, S.-Y. Sun, C.-Y. Chen, 'Investigation of High Alumina-Spinel: Effects of LiF and $CaCO_3$ Addition (Part 2)', *Mater. Sci. Eng. A*, **259** 1-7 (1999).

210. I. Ganesh, S. Bhattacharjee, B. P. Saha, R. Johnson, Y. R. Mahajan, 'A New Sintering Aid for Magnesium Aluminate Spinel', *Ceram. Int.*, **27** 773-779 (2001).

211. S.-K. Chen, M.-Y. Cheng, S.-J. Lin, 'Reducing the Sintering Temperature for MgO-Al_2O_3 Mixtures by Additions of Cryolite (Na_3AlF_6)', *J. Am. Ceram. Soc.*, **85** [3] 540-544 (2002).

212. K. Rozenburg, I. E. Reimanis, H.-J. Kleebe, R. L. Cook, 'Chemical Interactions Between LiF and $MgAl_2O_4$ Spinel During Sintering', *J. Am. Ceram. Soc.*, **90** [7] 2038-2042 (2007).

213. M. W. Benecke, N. E. Olson, J. A. Pask, 'Effect of LiF on Hot-Pressing of MgO', *J. Am. Ceram. Soc.*, **50** [7] 365-368 (1967).

214. F. F. Lange, D. R. Clarke, 'Morphological Changes of an Intergranular Thin Film in a Polycrystalline Spinel', *J. Am. Ceram. Soc.*, **65** [10] 502-506 (1982).

215. I. E. Reimanis, H.-J. Kleebe, 'Reactions in the Sintering of $MgAl_2O_4$ Spinel Doped with LiF', *Int. J. Mat. Res.*, **98** [12] 1273-1278 (2007).

216. G. R. Villalobos, J. S. Sanghera, I. D. Aggarwal, 'Degradation of Magnesium Aluminum Spinel by Lithium Fluoride Sintering Aid', *J. Am. Ceram. Soc.*, **88** [5] 1321-1322 (2005).

217. M. Müller, H.-J. Kleebe, 'Sintering Mechanism of LiF-Doped Mg-Al Spinel', *J. Am. Ceram. Soc.*, **95** [10] 3022-3024 (2012).

218. V. T. Gritsnya, Y. G. Kazarinov, A. O. Moskvitin, I. E. Reimanis, 'Point Defects in Magnesium Aluminate Spinel Ceramics Doped with Lithium Fluoride', *Acta Phys. Pol. A*, **117** 161-165 (2010).

219. F. J. Alvarez, D. M. Pasquevich, A. E. Bohe, 'Formation of Magnesium Spinel in the Presence of LiCl', *J. Mater. Sci.*, **40** 1193-1200 (2005).

220. T. Nakajima, 'Carbon-Fluorine Compounds as Battery Materials', *J. Fluorine Chem.*, **100** 57-61 (1999).

221. I. E. Reimanis, *Unpublished Work*, Colorado School of Mines, Golden, CO (2008-2014).

222. I. E. Reimanis, H.-J. Kleebe, ' Transparent Spinel Fabricated from Novel Powders: Synthesis, Microstructure and Optical Properties', *10th DoD Electromagnetic Windows Symposium*, Norfolk, VA, May 18-20 (2004).

223. T. C. Lu, X. H. Chang, J. Q. Qi, X. J. Luo, Q. M. Wei, S. Zhu, K. Sun, J. Lian, L. M. Wang, 'Low-Temperature High-Pressure Preparation of Transparent Nanocrystalline $MgAl_2O_4$ Ceramics', *Appl. Phys. Lett.*, **88** 213120;1-3 (2006).

224. W. T. Donlon, T. E. Mitchell, A. H. Heuer, 'Work Softening in Stoichiometric Spinel ($MgAl_2O_4$)', *Philos. Mag. A*, **45** [6] 1013-1036 (1982).

225. P. C. Panda, R. Raj, P. E. D. Morgan, 'Superplastic Deformation in Fine-Grained MgO-$2Al_2O_3$ Spinel', *J. Am. Ceram. Soc.*, **68** 522-529 (1985).

226. F. Beclin, R. Duclos, J. Crampon, F. Valin, 'Superplasticity of HIP MgO-Al_2O_3 Spinel: Prospects for Superplastic Forming', *J. Eur. Ceram. Soc.*, **17** 439-445 (1997).

227. K. Morita, K. Hiraga, B.-N. Kim, T.S. Suzuki, Y. Sakka, 'Strain Softening and Hardening during Superplastic-Like Flow in a Fine-Grained $MgAl_2O_4$ Spinel Polycrystal', *J. Am. Ceram. Soc.*, **87** [6] 1102-1109 (2004).

228. T. Shiono, H. Ishitomi, Y. Okamoto, T. Nishida, 'Mechanism of Fine-Grained Magnesium Aluminate Spinel Prepared Using an Alkoxide Precursor', *J. Am. Ceram. Soc.*, **83** [3] 645-647 (2000).

229. D. M. Choi, H. Palmour III, ‘Second Technical Report: Flow and Fracture of Hot-Pressed Polycrystalline Spinel at Elevated Temperature’, *Report*, North Carolina State University (1965).

230. D. M. Chay, H. Palmour III, W. W. Kriegel, ‘Microstructure and Room-Temperature Mechanical Proerties of Hot-Pressed Magnesium Aluminate Spinel as Described by Quadratic Multivariable Analysis’, *J. Am. Ceram. Soc.*, **51** [1] 10-16 (1968).

231. T. E. Mitchell, ‘Dislocations and Mechanical Properties of MgO-Al_2O_3 Spinel Single Crystals’, *J. Am. Ceram. Soc.*, **82** [12] 3305-3316 (1999).

232. E. A. Olevsky, S. Kandukuri, L. Froyen, ‘Consolidation Enhancement in Spark-Plasma Sintering: Impact of High Heating Rates’, *J. Appl. Phys.*, **102** 114913;1-12 (2007).

233. J. R. Groza, M. Garcia, J. A. Schneider, ‘Surface Effects in Field-Assisted Sintering.’, *J. Mater. Res.*, **16** [1] 286-292 (2001).

234. R. Raj, M. Cologna, J. S. C. Francis, ‘Influence of Externally Imposed and Internally Generated Electrical Fielad on Grain Growth, Diffusional Creep, Sintering, And Related Phenomena in Ceramics’, *J. Am. Ceram. Soc.*, **94** [7] 1941-1965 (2011).

235. Y. Kodera, C. L. Hardin, J. E. Garay, ‘Transmitting, Emitting and Controlling Light: Processing of Transparent Ceramics using Current-Activated Pressure-Assisted Densification’, *Scripta Mater.,* (2013).

236. H. Conrad, ‘Thermally Activated Plastic Flow of Metals and Ceramics with an Electric Field or Current’, *Mater. Sci. Eng.*, **A322** 100-107 (2002).

237. G. Bernard-Granger, N. Benameur, A. Addad, M. Nygren, C. Guizard, S. Deville Phenomenological Analysis of Densification Mechanism During Spark Plasma Sintering of $MgAl_2O_4$’, *J. Mater. Res.*, **24** [6] (2009).

238. U. Anselmi-Tamburini, J. E. Garay, Z. A. Munir, A. Tacca, F. Maglia, G. Chiodelli, G. Spinolo, ‘Spark Plasma Sintering and Characterization of Bulk Nanostructured Fully Stabilized Zirconia: Part II. Characterization Studies’, *J. Mater. Res.*, **19** [11] 3263-3269 (2004).

239. X. J. Chen, K. A. Khor, S. H. Chan, L. G. Yu, ‘Preparation Yttria-Stabilized Zirconia Electrolyte by Spark-Plasma Sintering’, *Mater. Sci. Eng. A*, **A341** 43-48 (2003).

240. K. Morita, B.-N. Kim, H. Yoshida, H. Zhang, K. Hiraga, Y. Sakka, ‘Effect of Loading Schedule on Densification of $MgAl_2O_4$ Spinel during Spark Plasma Sintering (SPS) Processing’, *J. Eur. Ceram. Soc.*, **32**, 2303-2309 (2012).

241. A. DiGiovanni, ‘Improved IR Windows for Severe Aerothermal Environments’, *Report*, Contract #N00167-04-C-0018, Naval Air Warfare Division, China Lake, CA (2004).

242. Z. Li, C. A. Black, R. C. Bradt, ‘Dimensional Stability, Optical and Elastic Properties of $MgAl_2O_4$ Spinel Irradiated in FFTF to Very High Exposures’, *J. Nucl. Mater.*, **212-215** 1087-1090 (1994).

243. V. T. Gritsnya, I. V. Afanasyev-Charkin, V. A. Kobyakov, T. I. Voitsenya, K. E. Sickafus, ‘Charge Carrier Rearrangement in Spinel Crystals Irradiated at Low Temperatures’, *Nucl. Intrum. Meth. B.*, **166-167** 244-249 (2000).

244. A. Ibarra, D. Bravo, F. J. Lopez, F. A. Garner, ‘High-Dose Neutron Irradiation of $MgAl_2O_4$ Spinel: Effects of Post-Irradiation Thermal Annealing on EPR and Optical Absorption’, *J. Nucl. Mater.*, **336** 156-162 (2005).

245. M. Müller, *Unpublished Research*, Technische Universität Darmstadt (2012).

246. P. P. Krivoruchko, B. G. Alapin, E. V. Degtyareva, ‘Oxygen Partial Pressure in the Atmosphere of Sintering Furnaces’, *Sov. Powder Metal +*, **17** [8] 631-634 (1978).

247. *Engineered Materials Handbook, Ceramics and Glasses, Vol. 4*, ASM International, Materials Park, OH, 185-284 (1991).

248. P. Miranzo, L. Tabernero. J.S. Moya, J.R. Jurado, ‘Effect of Sintering Atmosphere on the Densification and Electrical Properties of Alumina’, *J. Am. Ceram. Soc.*, **73** 2119-21 (1990).

249. M. Gonzalez, A. R. Landa-Canovas, M. T. Hernandez, ‘Pyrolytic and Graphitic Carbon: Pressure Induced Phases Segregated in Polycrystalline Corundum’, *Appl. Phys. A*, 865-869 (2005).

250. G. Villalobos, S. Bayya, W. Kim, J. Sanghera, B. Sadowski, R. Miklos, C. Florea, I. Aggarwal, M. Hunt, ‘Transparent Spinel Directly from the Hot Press’, *Advances in Ceramic Armor VIII: Ceramic Engineering and Science Proceedings*, **33** 105-108 (2012).

251. A. Ikesue, Transparent Spinel Ceramics, Method for Production Thereof, and Optical Material Using the Transparent Spinel Ceramics, European Patent, EP2112127A1 (2008).

252. M. Tanaka, T. Takahashi, S. Hatamoto, Int. Patent Appl., WO-2009/128269A1 (2009).

253. A. Goldstein, A. Goldengerg, Y. Yeshurun, M. Hefetz, 'Transparent $MgAl_2O_4$ Spinel from a Powder Prepared by Flame Spray Pyrolysis.', *J. Am. Ceram. Soc.*, **91** [12] 4141-4144 (2008).

254. A. Goldstein, A. Goldenberg, M. Vulfson, 'Development of a Technology for the Obtainment of Fine Grain Size Transparent $MgAl_2O_4$ Spinel Parts', *J. Ceram. Sci. Technol.*, **2** 1-8 (2011).

255. O. Tokariev, R. W. Steinbrech, L. Schnetter, J. Malzbender, 'Micro- and Marco-Mechanical Testing of Transparent MgAl2O4 Spinel', *J. Materi. Sci.*, **47** 4821-4826 (2012).

256. K. Hamano, S. Kanzaki, 'Fabrication of Transparent Spinel Ceramics by Reactive Hot-Pressing', *J. Ceram. Soc. Jpn.*, **85** 225-230 (1997).

257. D. S. Tsai, C. T. Wang, S. J. Yang, S. E. Hsu, 'Hot Isostatic Pressing of $MgAl_2O_4$ Spinel Infrared Windows', *Mater. Manuf. Proc.*, **9** 709-719 (1994).

258. J.E. Sanonetti, W.C. Martin, S.L. Young. 'Handbook of Basic Atomic Spectroscopic Data' , *NIST Physics Reference Data Handbook*, National Institute of Standards and Technology (NIST), Gaithersburg, MD (2005).

259. J. R. de Laeter, J. K. Böhlke, P. de Bièvre, H. Hidaka, H. S. Peiser, K. J. R. Rosman, P. D. P. Taylor, 'Atomic Weights of the Elements: Review 2000', *Pure Appl. Chem.*, **75** [6] 683-800 (2003).

260. R. S. Houk, V. A. Fassel, G. D. Flesoh, H. J. Svec, 'Inductively Coupled Argon Plasma as an Ion Source for Mass Spectroscopic Determination of Trace elements', *Anal. Chem.*, **52** 2283-2289 (1980).

261. A. N. Shcheglov, A. V. Kovalchiuk, T. I. Yuranova, V. N. Vasilets, A. N. Ponomarev, 'A Study of Gas Phase Processes in RF Plasma in the Mixture of Ar and Methyl-methacrylate', 12th *International Symposium on Plasma Chemistry*, **1** 191-195 (1995).

262. T. W. Schlatter, 'Amospheric Composition and Vertical Structure', *NOAA Earth Systems Research Laboratory*, Boulder, CO (2009).

263. '*Mass Spectra*' by NIST Mass Spectra Data Center in NIST Chemistry WebBook, NIST Standard Reference Database Number 69, Eds. P. J. Linstrom and W. G. Mallard,

National Institute of Standards and Technology (NIST), Gaithersburg, MD 20899, Retrieved 2013.

264. M. Schrod, J. Semel, R. Steiner, 'Verfahren zur Minderung von NO_x-Emissionen in Rauchgasen', *Chem.-Ing.-Tech.*, **57** [9] 717-727 (1985).

265. S. M. Correa, 'A Review of NO_x Formation Under Gas-Turbine Combustion Conditions', *Combust. Sci. and Tech.*, **87** 329-362 (1992).

266. W. R. May, 'Reduction of Thermal and Prompt NO_x in Exhausts of Natural Gas Fueled Boilers', *SFA International Inc.,* 1-19 (2012).

267. D. Smith, R. A. Fouracre, 'The Temperature Dependence of the Reaction Rate Coefficients of O^+ Ions with Molecular Oxygen and Nitrogen', *Planet. Space Sci.*, **16** 243-252 (1968).

268. R. G. Munro, 'Evaluated Material Properties for a Sintered alpha-Al_2O_3', *J. Am. Ceram. Soc.*, **80** 1919-1928 (1997).

269. K. Rozenburg, 'An Investigation of the Role of Lithium Fluoride the Sintering of Magnesium Aluminate Spinel'*, PhD Thesis*, Colorado School of Mines, Golden, CO, USA (2009).

270. *NIST Type C Reference Tables*, Monograph 175 Revised to ITS-90, NIST.

271. *Grade ISO 63 Datasheet*, Mersen Corp., Greenville-MI, USA.

272. *Handbook of Chemistry and Physics, 90th Edition,* D. R. Lide, Ed. in Chief, CRC Press, Boca Raton (2009).

273. A. Schwartz, D. Lassila, E. Baker, 'Analysis of Intergranular Impurity Concentration and the Effects on the Ductility of Copper Shaped Charge Jets,' *Ballistics '98, 17th International Symposium on Ballistics*, Midrand, South Africa, March 23-27, 1998.

274. D. B. Williams, C. B. Carter, *'Transmission Electron Microscopy',* Springer, NY (1996).

275. S. Griffiths, *Unpublished Work,* Colorado School of Mines, Golden, CO, USA (2012).

276. W. W. Mullins, "Theory of Thermal Grooving", *J. of Appl. Phys.*, 1957, **28** [3] 333-339 (1957).

277. G. S. Rohrer, "Grain Boundary Energy Anisotropy: a Review", *J. Mater. Sci.*, **46** 5881-5895 (2011).

278. E. Barsoukov, J. R. MacDonald J. M. E. Barsoukov, Ed., *Impedance Spectroscopy: Theory, Experiment, and Applications*, 2nd Ed., Hoboken, Wiley-Interscience, NJ, 1-537 (2005).

279. G. Gusmano, G. Montesperelli, P. Nunziante, E. Traversa, 'Study of the Conduction Mechanism of $MgAl_2O_4$ at Different Environmental Humidities,' *Electrochemica Acta,* **38** [17] 2617-21 (1993).

280. J.-B. Jorcin, M. E. Orazem, N. Pebere, B. Tribollet, 'CPE Analysis by Local Electrochemical Impedance Spectroscopy,' *Electrochimica Acta,* **51** 1473-79 (2006).

281. J. R. MacDonald, 'Note on the Parametrization of the Constant-Phase Admittance Element,' *Solid State Ionics,* **13** 147-9 (1984).

282. C. M. Gore, J. O. White, E. D. Wachsman and V. Thangadurai, 'Effect of Composition and Microstructure on Electrical Properties and CO_2 Stability of Donor-Doped, Proton Conducting $BaCe_{1-(x+y)}Zr_xNb_yO_3$,' *J. Mater. Chem. A,* **2** 2363-2373 (2014).

283. D. C. Sinclair, 'Characterization of Electro-materials using AC Impedance Spectroscopy,' *Bol. Soc. Esp. Ceram. Vidrio,* **34** [2] 55-65 (1995).

284. N. M. Beekmans, L. Heyne, 'Correlation between Impedance, Microstructure, and Composition of Calcia-Stabilized Zirconia,' *Electrochimica Acta,* **4** 303-310 (1976).

285. Baikowski, S30CR Technical Information Pamphlet, Baikowski (2009).

286. Nanocerox Nano-Powder Analysis Magnesium Aluminum Oxide, Nanocerox (2008).

287. T. Jochum (Collaboration) *Unpublished Work*, Colorado School of Mines, Golden, CO, (2011).

288. Baikowski Technical Data Sheet (Private Communications, J. Otto), Baikowski International Corp. (2010-2013).

289. ICDD PDF 2, International Center for Diffraction Data, Newton Square, PA, USA, 1996.

290. *CRC Handbook of Chemistry and Physics*, 84th Ed., Ed. In Chief D.R. Lide, CRC Press, 149-156 (2004).

291. A. Ibarra, R. Vila, F. A. Garner, 'Optical and Dielectric Properties of Neutron Irradiated $MgAl_2O_4$ Spinels', *J. Nucl. Mater.*, 233-237 1336-1339 (1996).

292. S. Saeseaw, W. Wang, K. Scarratt, J.L. Emmett, T.R. Douthit, "Distinguishing Heated

Spinels from Unheated Natural Spinels and from Synthetic Spinels", *Gemological Institute of America* (2009).

293. M. F. Ashby and H. J. Forst, Olivines and Spinels: Mg_2SiO_4 and $MgAl_2O_4$ (Chapter 15), *Deformation-Mechanism Maps, the Plasticity and Creep of Metals and Ceramics*; Pergamon Press, Oxford, UK (1982).

294. J. Oijerholm, J. Pan, and C. Leygraf, 'In-Situ Measurements by Impedance Spectroscopy of Highly Resistive a-Alumina', *Corrosion Science*, **48** 243-257 (2006).

295. X. Guo and Y. Ding, 'Grain Boundary Space Charge Effect in Zirconia,' *J. Electrochem. Soc.,* **151** [1] J1-J7 (2004).

296. A. Peters, C. Korte, D. Hesse, N. Zakharov and J. Janek, 'Ionic Conductivity and Activation Energy for Oxygen Ion Transport in Superlattices - The Multilayer System CSZ (ZrO_2 + CaO)/Al_2O_3,' *Solid State Ionics,* **178** 67-76 (2007).

297. M. G. Bellino, D. G. Lamas and N. E. Walsöe de Reca, 'Enhanced Ionic Conductivity in Nanostructured, Heavily Doped Ceria Ceramics,' *Advanced Functional Materials,* **16** 107-13 (2006).

298. J. Fleig, 'The Influence of Non-Ideal Microstructures on the Analysis of Grain Boundary Impedances,' *Solid State Ionics,* **131** 117-27 (2000).

299. J. R. MacDonald, 'Impedance Spectroscopy', *Annals of Biomedical Engineering*, **20** 289-305 (1992).

PERSONAL INFORMATION

Curriculum Vitae

Personal

Name	Marc Rubat du Merac
Born	03.08.1968 in Montreal, Quebec, Canada
Status	Married

Education

1994-1999	B.Sc. Mechanical Engineering, University of Calgary, Calgary, AB, Canada
2000-2005	M.Sc. Materials Science, University of Calgary, Calgary, AB, Canada
2012-2014	Ph.D. Materials Science, Technische Universität Darmstadt, Darmstadt, Germany

Vocational

1994-2005	Private/Commercial Pilot Training, Southern Aero and Westpoint Aviation, Springbank/Calgary, AB, Canada

Work Experience

2000-2005	Teacher’s assistant, University of Calgary, Calgary, AB, Canada
2006-2008	Materials engineer (failure analysis, manufacturing support, materials consulting), Acuren Inc./Rubat du Merac Engineering Inc., Calgary, AB, Canada
2008-2012	Research assistant (transparent ceramic research), Colorado School of Mines, Golden, CO, USA
2012-2014	Research assistant (transparent ceramic research), Technische Universität Darmstadt, Darmstadt, Germany
2015-2016	Research scientist (transparent yttria-zironia laminates), Forschungszentrum Jülich, Jülich, Germany
2016-2018	Scientist (ceramics, transparent ceramics), CeramTec GmbH, Plochingen, Germany

Publications

M. Rubat du Merac, I. E. Reimanis, C. Smith, H.-J. Kleebe, M. M. Müller, 'Effect of Impurities and LiF Additive in Hot-Pressed Transparent Magnesium Aluminate Spinel', *Int. J. App. Ceram. Tech.*, 10 [1] 33-48 (2013).

M. Rubat du Merac, H.-J. Kleebe, M. M. Müller, I. E. Reimanis, '50 Years of Research and Development Coming to Fruition; Unraveling the Complex Interactions during Processing of Transparent Magnesium Aluminate ($MgAl_2O_4$) Spinel', *J. Am. Ceram. Soc.*, 96 [11] 3341-3365 (2013).

M. Rubat du Merac, I. E. Reimanis, H.-J. Kleebe, 'Electrochemical Impedance Spectroscopy of Transparent Polycrystalline $MgAl_2O_4$ Spinel Hot-Pressed with and without LiF', *J. Am. Ceram. Soc.*, 98 [7] 2130-2138 (2015).

J. A. Miller, I. E. Reimanis, M. Rubat du Merac, 'Enhanced Fracture Toughness in Non-stoichiometric Magnesium Aluminate Spinel through Controlled dissolution of Second Phase Alumina', *J. Am. Ceram. Soc.*, 101 [2] 812-820 (2017).

M. Rubat du Merac, I. E. Reimanis, J. A. Miller and H.-J. Kleebe, 'Interface Energies in Non-stoichiometric Transparent $MgAl_2O_4$ Spinel Determined by Thermal Grain-Boundary Grooving', to be submitted to the Journal of the European Ceramic Society, August, 2018.

Conferences

M. Rubat du Merac, I. E. Reimanis, H.-J. Kleebe, C. Smith, “Effect of Impurities in Hot-Pressed Transparent $MgAl_2O_4$”, 34th International Conference and Exposition on Advanced Ceramics and Composites, Daytona Beach, FL, USA, January 27, 2010 (Presentation).

M. Rubat du Merac, I. E. Reimanis, C. Smith, H.-J. Kleebe, “The Role of LiF and the Effect of Impurities in Hot-Pressed Transparent $MgAl_2O_4$”, Gordon Conference on Solid State Studies in Ceramics, New London, NH, USA, August 15-20, 2010 (Poster).

M. Rubat du Merac, I. E. Reimanis, H.-J. Kleebe, “Role of LiF & Effect of Impurities in Hot-Pressed Transparent $MgAl_2O_4$”, 35th International Conference and Expo on Advanced Ceramics and Composites, Daytona Beach, FL, USA, January 26, 2011 (Presentation).

M. Rubat du Merac, I. E. Reimanis, H.-J. Kleebe, C. S. Smith, “The Role of Chemical Interactions and Point-Defects on the Sintering and Optical Properties of Hot-Pressed Transparent $MgAl_2O_4$”, 36th International Conference and Exposition on Advanced Ceramics and Composites, Daytona Beach, FL, USA, January 26, 2012 (Presentation).

M. Rubat du Merac, I. E. Reimanis, “Sintering, Theory, Practice, and Applications. Case Study: Transparent $MgAl_2O_4$”, Netzsch Symposium Ceramic Nuclear Focused Workshop, Albuquerque, NM, USA, May 9, 2012 (Invited Presentation).

M. Rubat du Merac, I. E. Reimanis, “Grain-Boundary Embrittlement in Transparent $MgAl_2O_4$ Hot-Pressed with LiF”, Gordon Conference on Solid State Studies in Ceramics, South Hadley, MA, USA, August 12-17, 2012 (Poster).

M. Rubat du Merac, M. Müller, H.-J. Kleebe, I. E. Reimanis, “The Role of Point-Defects in the Sintering of Transparent Polycrystalline $MgAl_2O_4$”, 37th International Conference and Exposition on Advanced Ceramics and Composites, Daytona Beach, FL, USA, January 30, 2013 (Presentation).

M. Rubat du Merac, H.-J. Kleebe, I. E. Reimanis, “Electrochemical Impedance Spectroscopy of Transparent Polycrystalline $MgAl_2O_4$”, Gordon Conference on Solid State Studies in Ceramics, South Hadley, MA, USA, July 20-25, 2014 (Poster).